The formation of Kiruna-type iron oxide-apatite deposits – a new genetic model

Von der Naturwissenschaftlichen Fakultät
der Gottfried Wilhelm Leibniz Universität Hannover
zur Erlangung des Grades

Doktorin der Naturwissenschaften
Dr. rer. nat.

genehmigte Dissertation von

M.Sc. Jaayke Lynn Fiege (geb. Knipping)

Erscheinungsjahr 2019

Referent: Prof. Dr. François Holtz (Leibniz Universität Hannover)

Koreferent: Prof. Dr. Adam C. Simon (University of Michigan)

Koreferent: Prof. Dr. Stefan Weyer (Leibniz Universität Hannover)

Tag der Pomotion: 13.08.2019

Acknowledgements

First, I would like to thank my advisors François Holtz, Jim Webster and especially Adam Simon, who introduced me into the exciting world of economic geology. Without the unrestricted support of each of these researches, the whole project would not have been possible, since this was not a DFG or NSF funded project and it was completely based on several stipends, scholarships and prizes, which I only received with their help and support! It was an honor to work on this very interesting project that developed into different directions over the past years and which was conducted at mainly three different great institutions.

Many thanks to the whole Simon-lab-family in the Earth and Environmental Science Department at the University of Michigan (2013-2015), especially Liz, Laura, Tom, Brian, Tristan and Xiaofei! I had a great time with awesome colleagues that became all good friends! I also would like to thank Jim Webster for the full-time support at the IHPVs in the Earth and Planetary Science Department at the American Museum of Natural History in New York (2017-2018) and Shuo Ding (Echo) for fellowship in this lab! Of course I want to thank all colleagues at my home institution - Institut for Mineralogy - at Leibniz University Hannover! Special thanks to Stefan Linsler, Robert Balzer and David Neave for support at the IHPVs in Hannover, Martin Oeser for assistance at the LA-ICP-MS for in-situ Fe isotope analyses as well as discussions and Julian Feige for preparation of IR-sections! The support by Harald Behrens throughout my career - from being a Bachelor student in his lab until today - is also much appreciated!

Further, I would like to thank my collaboration partners outside of these three institutions: Many thanks to Martin Reich and Fernando Barra from

Abstract

Kiruna-type iron oxide-apatite (IOA) deposits are important sources for Fe, necessary for steel production, and other elements such as REE, crucial for new technologies. IOA deposits occur worldwide (Sweden, Chile, USA, China, Iran etc.) and range in age from Late Archean (2.5 Ga) to the present. However, their formation is still under debate. Hypotheses vary from a (magmatic-) hydrothermal origin to direct crystallization from an immiscible Fe-rich melt. In order to investigate which hypotheses works best, we measured trace element concentrations and Fe-isotope ratios *in-situ* in magnetites (Fe_3O_4) from the Cretaceous Los Colorados IOA deposit (~350 Mt Fe) in the Chilean Iron Belt. Analyses showed that magnetite cores have an igneous texture and chemistry, while the surrounding magnetite rims indicate lower temperature (magmatic-) hydrothermal formation conditions. Since a coactive cooperation between both processes could not be explained by one of the existing models, we developed a completely novel formation model for Kiruna-type IOA deposits.

In our proposed scenario the decompression of an oxidized, andesitic and volatile-rich magma, typical for arc-volcanism, results in degassing of volatiles such as H_2O and Cl. The exsolved fluid bubbles are expected to nucleate preferentially on surfaces of oxide crystals such as magnetite where surface tension is lower. The bulk density of these bubble-magnetite pairs is expected to be lower than the surrounding magma and will thus float upwards as a bubble-magnetite suspension that is additionally enriched in dissolved Fe due to complexation with Cl. This suspension will cause the formation of massive magnetite deposits in regional-scale transcurrent faults with magmatic-hydrothermal as well as with igneous characteristics.

High temperature decompression experiments confirmed that the flotation model is physically possible and clearly showed upward accumulation of magnetite upon decompression and fluid exsolution in contrast to gravitational settling of these dense minerals expected without exsolved fluids. This flotation scenario is in agreement with the geochemical and isotopic signatures observed at Los Colorados and other Kiruna-type IOA deposits. Mineral flotation on exsolved fluid bubbles may also change classical views on crystal fractionation and thus the formation of monomineralic layers in mafic layered intrusions (e.g., Skaergaard, Bushveld complex), where dense magnetite layers overlie less dense anorthosite layers.

Zusammenfassung

Kiruna-typ Eisenoxid-Apatit (IOA) Lagerstätten sind wichtige Quellen für Eisen und sind deshalb essentiell für die Stahlproduktion, als auch entscheidend für die Förderung von Seltenen Erden (REE), die verstärkt in neuen Technologien eingesetzt werden. IOA Lagerstätten existieren weltweit (Schweden, Chile, USA, China, Iran, etc.) und haben sich zwischen dem späten Archaikum (2.5 Ga) und der Gegenwart gebildet. Jedoch ist die Art der Entstehung dieser Lagerstätten immer noch stark umstritten. Hypothesen variieren von (magmatisch-) hydrothermalen Szenarien zu rein magmatischer Kristallisation aus Eisen-reichen Schmelzen, die sich von Silikat-Schmelzen abgetrennt haben. Um die Frage nach der tatsächlichen Entstehung letztendlich zu klären, wurden in dieser Studie Magnetite (Fe_3O_4) der kreidezeitlichen Los Colorados IOA Lagerstätte (~350 Mt Fe) im Chilean Iron Belt *in-situ* auf Spurenelemente und Fe-Isotopenverteilung ausführlich untersucht. Die analytischen Ergebnisse implizieren eine rein magmatische Bildung der Kerne, während die Kristallränder auf eine Bildung bei niedrigeren Temperaturen unter (magmatisch-) hydrothermalen Bedingungen hindeuten. Da ein direktes Zusammenwirken dieser beiden Prozesse nicht durch eines der existierenden Modelle erklärt werden konnte, haben wir ein komplett neues Modell für die Entstehung von Kiruna-typ IOA Lagerstätten entwickelt.

In unserem vorgeschlagenen Scenario führt die Druckentlastung eines oxidierten, andesitischen und volatil-reichen Magmas, typisch fuer Arc-Vulkanismus, zur Entgasung von Volatilen wie H_2O und Cl. Die herausgelösten Fluidblasen bilden sich bevorzugt an Oxidkristall-Oberflächen, wie z.B. Magnetit, wo die Oberflächenspannung geringer ist. Die Gesamtdichte dieser Fluidblasen-Magnetit-Paare ist geringer als das des umgebenden Magmas und würde deshalb als Fluidblasen-Magnetit-Suspension aufsteigen, welches aufgrund der Komplexierung von Fe und Cl zusätzlich an gelöstem Eisen angereichert ist. Diese Suspension wird sich als massive Magnetitlagerstätte in regionalen Blattverschiebungen niederschlagen, die sowohl (magmatisch-) hydrothermale, als auch rein magmatische Charakteristika aufweist.

Hochtemperatur-Dekompressionsexperimente belegen, dass das Flotations-Modell physikalisch möglich ist und, dass nach Druckentlastung und Entgasung eine nach oben gerichtete Magnetit Ansammlung statt findet, entgegen einer gravitationsbedingten Ablagerung dieser dichten Minerale, die ohne Fluidblasen erwartet würde. Dieses Flotations-Scenario stimmt mit den geochemischen und isotopischen Signaturen überein, die in Los Colorados und in anderen IOA Lagerstatten beobachtet wurden. Flotation von dichten Mineralen an Fluidblasen verändert möglicherweise auch klassische Ansichten zur Kristallfraktionierung. Somit muss eventuell auch die Entstehung von monomineralischen Lagen in mafischen Lagenintrusionen (z.B. Skaergaard, Bushveld Komplex) überdacht werden, wo dichte Magnetitlagen weniger dichte Anorthositlagen überlagern.

Table of Contents

Chapter 1: Introduction

Ore deposits are natural concentrations of certain metals in a wide range of geological settings, such as sedimentary, metamorphic, hydrothermal and magmatic systems. The exploration of new deposits, and thus the precise knowledge about the formation of known ore deposits, is crucial to today's society. Due to increasing steel production and the high demand for Cu and rare earth elements (REE) for new technologies, iron oxide-copper-gold (IOCG) deposits and Kiruna-type iron oxide-apatite (IOA) deposits are not just of scientific but also of great economic interest (e.g., Foose and McLelland, 1995; Chiaradia et al., 2006; Barton, 2014). IOA deposits are sometimes classified as the magnetite-rich (Fe_3O_4) and Cu-poor endmember of IOCG deposits, which occur globally and range in age from Late Archean (2.5 Ga) to the present (Williams et al., 2005). While IOCG deposits are mostly accepted to be formed by hydrothermal processes mainly due to a lack of clear igneous correlation (Barton, 2014), the origin of IOA deposits remains controversial and a fierce debate developed within the last years between different research teams.

Furthermore, Kiruna-type IOA deposits should not be shuffled together with nelsonites. The latter are characteristically enriched in Ti (as ilmenite or Ti-rich magnetite) and apatite (30-50 modal %), and are commonly associated with anorthosites (90-100 modal % plagioclase) (Philpotts, 1967). In contrast, Kiruna-type deposits, named after the Kiruna deposit in Sweden (Geijer, 1931), comprise less Ti (<1 wt%) present in magnetite and/or titanite instead of ilmenite. Apatite concentrations vary vastly and are mostly less abundant when compared with nelsonites. While some Kiruna-type deposits contain as much as 50% apatite (e.g., Mineville, New York; Foose and

McLelland, 1995), other deposits contain only accessory amounts (e.g., El Laco, Chile; Nyström and Henriquez, 1994). It is mostly accepted that nelsonites result from immiscibility between silicate-rich and Fe-P-rich melts, while the origin of Kiruna-type IOA deposits remains controversial due to the small amounts of Ti and P, which have been experimentally demonstrated to partition into an Fe-rich oxide melt (Philpotts, 1967; Naslund, 1983; Charlier and Grove, 2012, Chen et al., 2013, Fischer et al. 2016, Hou et al., 2018).

In order to achieve more certainty about the formation of the economically important Kiruna-type IOA deposits, natural samples from the Los Colorados Kiruna-type IOA deposit (350 Mt of iron) in Chile were here investigated as a case study with various petrological and geochemical methods.
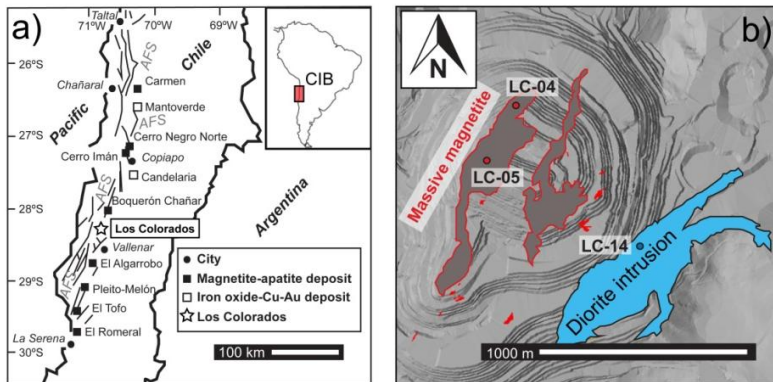
Figure 1.1: a) Map of the Coastal Cordillera (N Chile) and the location of the main Fe ore deposits associated to the Atacama Fault System (AFS). b) Plan view of the massive magnetite dike-like bodies of *Los Colorados*, the associated diorite intrusion and the location of the investigated drill cores LC-04, LC-05 and LC-14 (from Knipping et al. 2015b).

Los Colorados has experienced minimal postdepositional hydrothermal alteration that commonly obscures primary features in older IOA deposits and it is among the largest Kiruna-type iron ore deposits in the

8

Chilean Iron Belt, which is geologically coupled to the Atacama Fault System (Fig. 1.1a). The sinistral transcurrent Atacama Fault System is located along the Coastal Cordillera and was caused by tectonic changes in the Cretaceous period. While the South Atlantic Ocean opened as a result of the second major break-up phase of the supercontinent Pangaea, the subduction zone on the Pacific side of South America became the eponymous flat Andean-type subduction. Thus, the tectonic regime in the back-arc basin changed from transtensional to transpressional (Uyeda and Kanamori, 1979). This tectonic change induced the development of the Atacama Fault System – host to the Chilean Iron Belt. The here located iron deposits are mainly IOCG and Kiruna-type IOA deposits that are composed of large amounts of (low Ti-) magnetite, actinolite and variable amounts of apatite (Nyström and Henriquez, 1994).

About 50 Kiruna-type IOA deposits, including seven large deposits (>100 Mt high grade Fe-ore each), occur in the Chilean Iron Belt between latitudes 25° and 31° S (Nyström and Henriquez, 1994). The Los Colorados deposit is hosted in the volcanic rocks of the Punta del Cobre Formation along the southern segment of Atacama Fault System (Pincheira et al., 1990). The iron oxide ore occurs in two sub-parallel dikes, which are each about 500 m deep, 150 m wide and 1500 m long (Fig. 1.1b). Radiometric K-Ar dating indicates similar ages of ~110 Ma for the formation of the magnetite dikes and an adjacent brecciated dioritic intrusion (Pichon, 1981) which may imply a genetic association between the two systems. The paleo depth of the surface is estimated to be 3-4 km. Proven resources of up to 986 Mt with an average ore grade of 34.8% Fe (CAP-summary, 2013) are more than the total reported resources of the other IOA deposits in the CIB (e.g., El Romeral, El Algarrobo and Cerro Negro Norte).

In *Chapter 2*, *3* and *4* several samples from different depths of three drill cores from Los Colorados (Fig. 1.1b), two from the western massive magnetite dike (LC-04 and LC-05) and one from the associated diorite intrusion (LC-14), were investigated with several petrological and geochemical methods, such as microscopy, bulk rock analysis (ICP-OES), scanning electron microscopy (SEM), electron probe microanalysis (EPMA), laser ablation inductively coupled plasma mass spectrometry (LA-ICP-MS) and *in-situ* Fe-isotope analyses using multi collector (MC-) LA-ICP-MS. *Chapter 2* also includes (bulk) Fe- and O-isotope data collected by my colleague (Dr. Laura Bilenker).

The results of all studies revealed chemical zoning from the core to the edge of the magnetite grains. The magnetite cores are more similar to magnetite with an igneous origin (such as magnetite from nelsonites), while the surrounding magnetite rims are more similar to magnetite precipitated by magmatic-hydrothermal fluids (Dupuis and Beaudoin, 2011; Nadoll et al. 2014). This observation was compared with the published models existing to that date.

One model includes a solely hydrothermal origin resulting from non-magmatic deuteric fluids close to the surface that scavenges iron from surrounding dioritic plutons and metasomatically replaces volcanic rocks (Menard, 1995; Barton and Johnson, 1996, 2004; Haynes, 1995, 2000; Sillitoe and Burrows, 2002), while others assume a magmatic-hydrothermal fluid that sources Fe directly from magmas (Pollard, 2006, Tornos et al. 2016, Westhues et al, 2017). A third hypothesis invokes liquid immiscibility between Fe-rich oxide melt and Si-rich melt, with coalescence, separation and crystallization of the Fe-rich melt forming IOA deposits (e.g., Nyström and

Henríquez, 1994; Travisany et al., 1995; Naslund et al., 2002; Chen et al. 2010, Hou et al. 2018). The first two hypotheses allow the possibility for a genetic connection between IOA and IOCG deposits, which has been observed within the Chilean Iron Belt (Sillitoe, 2003) and in the Missouri iron province (Seeger, 2003), whereas the third hypothesis distinguishes IOA deposits completely from IOCG deposit systems (Williams et al., 2005; Nold et al., 2014). However, the first two models cannot explain the magnetite cores with igneous trace element and Fe-isotope signatures measured at Los Colorados, while the third one is incapable of explaining the precipitation of (magmatic-) hydrothermal magnetite directly surrounding the igneous formed magnetite grains. Therefore, we propose in *Chapter 2*, *3* and *4* a fourth and completely new formation model for Kiruna-type IOA deposits that further allows a connection between those and IOCG deposits.

In our model primary igneous magnetite crystallizes from silicate melt in a crustal magma reservoir. During decompression, e.g. an eruption, saline fluid exsolves and bubbles nucleate on these magnetite crystals due to favorable wetting properties (e.g., Hurwitz and Navon, 1994). Thus, magnetite-bubble pairs will form and buoyantly ascend, coalesce and separate as a magnetite-fluid suspension within the magma. When extensional tectonic stress opens crustal fractures above the magma reservoir, this suspension can escape and precipitate at lower pressures and temperatures secondary magmatic-hydrothermal magnetite surrounding primary igneous magnetite crystals.

To test if magnetite flotation on exsolved fluid bubbles is really possible in a silicate melt and if the density of a magnetite-fluid suspension would be low enough to efficiently segregate and accumulate magnetite at the top of residual silicate magma, we conducted in *Chapter 5* decompression experiments at magmatic reasonable conditions. All experimental parameters

were set to suit those of arc-magmatic conditions expected within the Chilean Iron Belt. Image analysis of the quenched decompression (+annealing) experiments revealed an efficient accumulation of the dense magnetite crystals at the top of the experimental capsules overlaying less dense silicate melt in contrast to static experiments without an exsolved fluid phase, where magnetite settles - as expected - gravitationally to the bottom. This observation is direct experimental evidence for our new formation model.

Chapter 2: Giant Kiruna-type deposits form by efficient flotation of magmatic magnetite suspensions

Jaayke L. Knipping[1], Laura D. Bilenker[1], Adam C. Simon[1], Martin Reich[2], Fernando Barra[2], Artur P. Deditius[3], Craig Lundstrom[4], Ilya Bindeman[5], and Rodrigo Munizaga[6]

[1]*Department of Earth and Environmental Sciences, University of Michigan, 1100 North University Avenue, Ann Arbor, Michigan 48109-1005, USA*

[2]*Department of Geology and Andean Geothermal Center of Excellence (CEGA), Universidad de Chile, Plaza Ercilla 803, Santiago 8320198, Chile*

[3]*School of Engineering and Information Technology, Murdoch University, 90 South Street, Murdoch, Western Australia 6150, Australia*

[4]*Department of Geology, University of Illinois, 605 East Springfield Avenue, Champaign, Illinois 61820, USA*

[5]*Department of Geological Sciences, University of Oregon, 1275 E 13th Avenue, Eugene, Oregon 97403-1272, USA*

[6]*Compañia Minera del Pacífico (CAP) Brasil N 1050, Vallenar, Región de Atacama 1610000, Chile*

ABSTRACT

Kiruna-type iron oxide-apatite (IOA) deposits are an important source of Fe ore, and two radically different processes are being actively investigated for their origin. One hypothesis invokes direct crystallization of immiscible Fe-rich melt that separated from a parent silicate magma, while the other hypothesis invokes deposition of Fe oxides from hydrothermal fluids of either magmatic or crustal origin. Here, we present a new model based on O and Fe stable isotopes and trace and major element geochemistry data of magnetite from the ~350 Mt Fe Los Colorados IOA deposit in the Chilean Iron Belt that merges these divergent processes into a single sequence of events that explains all characteristic features of these curious deposits. We propose that

concentration of magnetite takes place by the preferred wetting of magnetite, followed by buoyant segregation of these early-formed magmatic magnetite-bubble pairs, which become a rising magnetite-suspension that deposits massive magnetite in regional-scale transcurrent faults. Our data demonstrate an unambiguous magmatic origin, consistent with the namesake IOA analogue in the Kiruna district, Sweden. Further, our model explains the observed coexisting purely magmatic and hydrothermal-magmatic features and allows a genetic connection between Kiruna-type IOA and iron oxide-copper-gold deposits, contributing to a global understanding valuable to exploration efforts.

2.1 INTRODUCTION

The Los Colorados (LC) deposit, in the Cretaceous Chilean Iron Belt (CIB) in the Coastal Cordillera of northern Chile (25–31°S) (Fig. 2.1), was formed during the breakup of Gondwana, which forced the Pacific margin into flat subduction (Chen et al., 2012). The inversion of extensional back-arc basins caused transcurrent crustal-scale fault zones (Atacama Fault System: AFS), which host ~50 iron oxide-apatite (IOA) deposits; seven each contain >100 Mt high-grade ore (Nyström and Henríquez, 1994). These deposits share characteristics with large IOA deposits in the giant Proterozoic Kiruna district (>100Mt Fe) of Sweden (Nyström and Henríquez, 1994; Jonsson et al., 2013) including similar tectonic stress changes in a former back-arc setting (Allen et al. 2008). However, deposits in the Kiruna district have been disturbed by later alteration and metamorphism that complicate mineralogical and geochemical investigations. The origin of Kiruna-type IOA deposits remains controversial, and fundamentally different formation processes have been suggested. Several working hypotheses, including magmatic-hydrothermal replacement (Sillitoe and Burrows, 2002), hydrothermal precipitation in the sense of iron oxide-copper-gold (IOCG) deposits (Barton, 2014), and liquid immiscibility

14

(Nyström and Henríquez, 1994; Naslund et al., 2002), have been invoked to explain, e.g., the vesiculated "magnetite lava flows" at the El Laco IOA deposit northeast of the CIB (Park, 1961; Nyström and Henríquez, 1994).
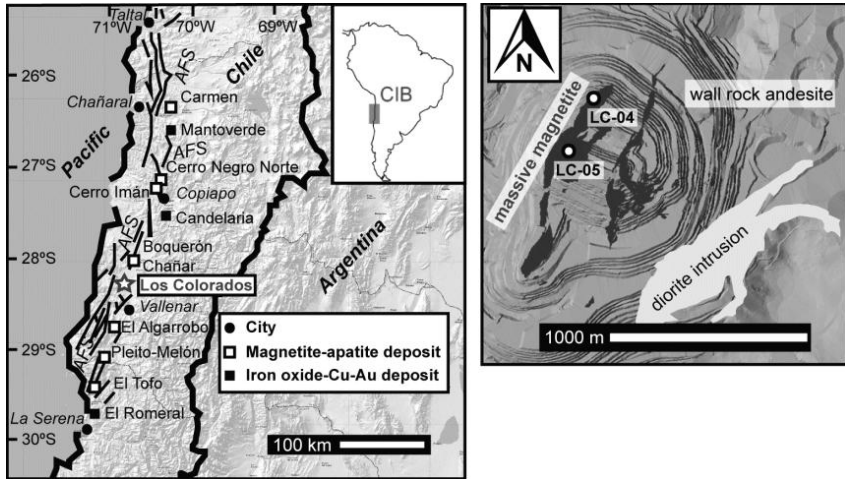
Figure 2.1: Map of Los Colorados within the Chilean Iron Belt. Right hand image shows the magnetite ore bodies, the adjacent diorite intrusion, and the location of the investigated drill cores (LC-04, LC-05).

Iron ore at LC consists of massive magnetite ($\leq$90% modal) in two km-scale subparallel "dikes" (110 Ma), which are exposed along the strike of the southern segment of the AFS and associated with a diorite intrusion (108 Ma) (Pincheira et al., 1990) (Fig. 2.1). Magnetite crystals contain polycrystalline silicate and halite-bearing fluid inclusions (<5 μm). Coeval actinolite, clinopyroxene and minor apatite are present, and the ore body lacks sodic and potassic alteration phases.

2.2 MAGMATIC STABLE ISOTOPE SIGNATURES AT LOS COLORADOS

We report stable Fe and O isotope pairs for 13 samples from two drill cores of LC (LC-04, LC-05), one representative sample from the extensively overprinted Fe oxide deposit at Mineville, New York (USA) (Valley et al., 2011), and one from the Kiruna deposit, Sweden. Iron isotope values were obtained following the double-spike method of Millet et al. (2012). The resulting $\delta^{56}Fe_{mgt}$ values for LC magnetite range from 0.09‰ to 0.24‰ (average $\delta^{56}Fe_{mgt}$ [±2σ] = 0.17‰ ± 0.05) and $\delta^{18}O_{mgt}$ values range from 1.92‰ to 3.17‰ (average $\delta^{18}O_{mgt}$ [±2σ] = 2.60‰ ± 0.04) (Fig. 2.2; Table S2.1, supplementary).
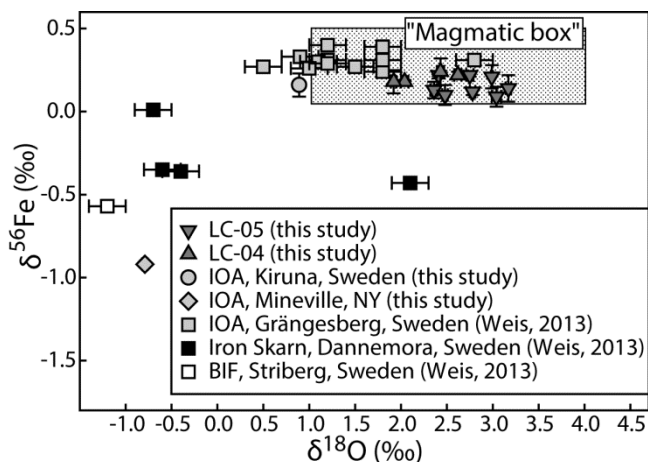
Figure 2.2: $\delta^{18}O$ vs. $\delta^{56}Fe$ isotope values of magnetite. Box shows the range for magmatic magnetite (Heimann et al., 2008; Taylor, 1967; Weis, 2013), within which the Los Colorados (LC) data distinctively plot . Data of a skarn, banded iron formation (BIF), and iron oxide-apatite (IOA) deposits in Sweden, and the altered IOA Mineville deposit (USA), are plotted for comparison. Non-magmatic deposits (skarn and BIF) plot outside of the magmatic box, reflecting a lighter Fe and O isotopic composition. Uncertainties are ± 2σ or smaller than symbol size.

Iron and O isotope compositions of magnetite precipitated from a silicate melt or magmatic-hydrothermal aqueous fluid range from 0.06‰ and

0.5‰ and 1.0–4.0‰, respectively, based on analyses of natural samples of known igneous origin (Heimann et al., 2008; Taylor, 1967). The isotopic signature of magnetite at LC overlaps these established magmatic values. The data also overlap the Fe and O isotope signature of magnetite from the Kiruna district (Jonsson et al., 2013; Weis, 2013), and eliminate a purely low-temperature (T) hydrothermal origin for the Fe ore. In contrast, data for magnetite from Mineville demonstrate that hydrothermal alteration-related mineralization (Valley et al. 2011) shifts $\delta^{56}Fe_{mgt}$ and $\delta^{18}O_{mgt}$ to lower values (Fig. 2.2).

2.3 MAGMATIC TO HYDROTHERMAL GEOCHEMICAL ZONING OF MAGNETITE

To distinguish between purely igneous and magmatic-hydrothermal signatures that are merged as "magmatic" in the previous section, high resolution trace element analyses were performed on individual magnetite grains. Electron probe microanalyses (Table S2.2 and S2.3, supplementarty) of most magnetite grains from the center of the western dike (LC-05) and its border zone (LC-04) indicate a high-T magmatic origin (porphyry type) according to discrimination diagrams (Ti+V vs. Al+Mn) of Dupuis and Beaudoin (2011) and Nadoll et al. (2014) (Fig. 2.3). However, some magnetite grains are zoned (Fig. 2.3) with euhedral cores rich in silicate inclusions (type 1) within a less porous magnetite matrix (type 2), which can be surrounded by a third generation of porous magnetite (type 3). The compositions of the magnetite cores (type 1) are consistent with Ti-rich magnetite in nelsonites (Fe-Ti, V-field), which are thought to form by purely magmatic processes, while type 2 magnetite has a high-T magmatic-hydrothermal fluid signature (Porphyry-field). Only samples distal from the dike center or distal from the grain cores (i.e., late growth zones) have Ti+V and Al+Mn as low as expected

for magnetite of the Kiruna-field (c.f. Dupuis and Beaudoin 2011) in Figure 2.3 (type 3 magnetite). The chemical patterns are therefore best interpreted to reflect a change from purely magmatic to magmatic-hydrothermal conditions during crystallization of the LC magnetite.
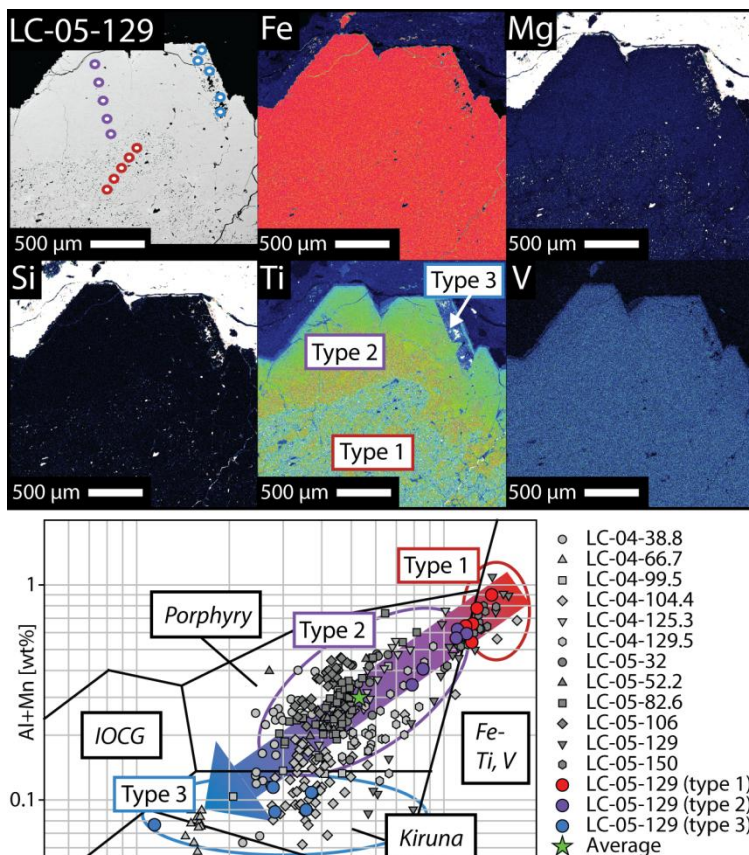
Figure 2.3: Elemental maps of LC magnetite and magnetite chemistry plotted on the discriminant diagram by Dupuis and Beaudoin (2011) and Nadoll et al. (2014). The elemental maps reveal core to rim zonation from igneous to magmatic-hydrothermal magnetite, and the Ti+V and Al+Mn diagram shows distribution of LC samples from high to low values. Star is the average of all LC magnetites.

2.4 A NEW MODEL: MAGNETITE SEGREGATION, SUSPENSION, AND TRANSPORT

The data presented here indicate that LC magnetite records a transition from purely magmatic conditions (type 1) to high-T magmatic-hydrothermal conditions (type 2) with decreasing T (type 3). This compositional change suggests that the formation of the LC magnetite ore resulted from a sequence of events involving a melt and a magmatic-hydrothermal fluid. We propose the following model to explain this process:

(1) In hydrous, oxidized arc-magmas, magnetite is the first liquidus phase at 200 MPa (Martel et al., 1999), which facilitates H_2O saturation (Hurwitz and Navon, 1994). To reduce surface energies, bubbles nucleate on crystal surfaces (heterogeneous bubble nucleation). However, fluids exclusively attach to magnetite microlites due to larger wetting angles between fluids and oxides (45–50°) compared to silicates (5–25°) (Gualda and Ghiorso, 2007; Edmonds et al., 2014) (Fig. 2.4a).

(2) Bubble-magnetite pairs (i.e., fluid bubbles attached to magnetite microlites) rise (Fig. 2.4b) when the buoyancy force $F^{\text{buoyancy}} > 0$ (Gualda and Ghiorso, 2007), which can be estimated by Equation (1):

$$F^{\text{buoyancy}} = \left(V_{\text{bubble}} \cdot \Delta\rho_{\text{bubble}} - V_{\text{mgt}} \cdot \Delta\rho_{\text{mgt}} \right) \cdot g \qquad \textbf{(1)}$$

Here, V_{bubble} and V_{mgt} are the volumes of bubble and magnetite, respectively, g is gravitational force, and $\Delta\rho$ is the density difference between melt and bubble ($\Delta\rho_{\text{Bubble}}$), or magnetite and melt ($\Delta\rho_{\text{mgt}}$). A magnetite-bubble pair will not ascend when $F^{\text{buoyancy}} \leq 0$. Thus, the critical ratio of $V_{\text{bubble}}/V_{\text{mgt}}$ at which these aggregates will ascend in the magma chamber can be calculated by Equation 2:

$$\frac{V_{\text{bubble}}}{V_{\text{mgt}}} = \left(\frac{\Delta\rho_{\text{mgt}}}{\Delta\rho_{\text{bubble}}} \right) \qquad \textbf{(2)}$$

We assume ρ_{mgt} = 5.20 g/cm^3 and ρ_{melt} = 2.27 g/cm^3 for a hydrous (6 wt% H_2O) andesite at 1000°C and 200 MPa (cf. Ochs and Lange, 1999). Our proposed model uses a fluid with a bulk salinity of 35 wt% $NaCl_{eq}$ based on the presence of euhedral halite in our magnetite-hosted fluid inclusions (Bodnar and Vityk, 1994), and contains 7.2 wt% Fe based on published magnetite solubility data (Simon et al., 2004). Using an equation of state for 1000°C and 200 MPa (Pitzer and Sterner, 1995; Driesner, 2007), and the aforementioned fluid chemistry, the ρ_{bubble} is 0.51 g/cm^3. These parameters allow $F^{buoyancy} > 0$ as long as magnetite comprises < 37 vol% of the magnetite-bubble aggregate. Experimental evidence for flotation of ore minerals by such a process is reported by Matveev and Ballhaus (2002) and Mungall et al. (2015).

(3) These aggregates grow, coalesce and sweep up other magnetite microlites during ascent, becoming a rising suspension with up to 37 vol% (=65 wt%) magnetite (Fig. 2.4c). Once magnetite microlites are enclosed within the suspension, their chemistry will be controlled by the aqueous fluid, and reflect partitioning of elements between melt, aqueous fluid and magnetite. Hence, the concentration of fluid-immobile elements such as Ti, V, Al, and Mn, among others, should decrease in magnetite that grows from the aqueous fluid component of the suspension, and the magnetite chemistry should become magmatic-hydrothermal (type 2 magnetite). Published experimental data demonstrate that Cl-bearing aqueous fluids can scavenge up to several wt% Fe from the melt as $FeCl_2$ (Simon et al., 2004; Bell and Simon, 2011) (Fig. 2.4c), allowing for type 2 and type 3 magnetite to grow during ascent and cooling (Fig. 2.4d). Abundant Cl in the melt can be explained by seawater recycling of the subducted slab (Philippot et al., 1998). Chlorine-bearing aqueous brine also effectively scavenges P, among other fluid-compatible elements, from silicate melt, with reported brine/melt partition coefficients for P ranging from 2 to 6

(Zajacz et al., 2008). The magnetite suspension ascends through the melt-dominated magma, owing to increasing V_{bubble} and thus decreasing ρ_{bubble} during ascent (decompression) and forms larger magnetite-suspension pockets (Fig. 2.4c).

(4) Instead of forming just magnetite-rich enclaves as described by Edmonds et al. (2014), we propose that tectonic stress changes caused here an efficient ascent of the magnetite-suspension. A sudden destabilization of the magma body results in rapid transport (5–20 m/s) through hydraulic fractures in a ductile crystal-mush regime (Hautmann et al., 2014), wherein high-flux permeable channels become well developed with increasing crystallinity (cf. Hersum et al., 2005). This is a plausible, repeatable scenario for the formation of LC, due to the tectonic activity along the AFS during the Lower Cretaceous, which also explains the spatial relationship between the CIB and AFS. Finally, the magnetite suspension(s) will accumulate in large crustal faults owing to decreasing pressure and T, trapping additional phases such as brine and silicates as inclusions (Fig. 2.4d). Euhedral actinolite, apatite and clinopyroxene may co-crystallize, similar to observations in decompression experiments for chromite deposits (Matveev and Ballhaus, 2002).

Incorporation of primary (type 1) magnetite into the exsolved magmatic-hydrothermal aqueous fluid phase would not only explain the detected geochemical signature, but would also decrease the magma volume required to produce the ~350 Mt Fe ore deposit at LC. For instance, for a hydrous (6 wt% H_2O) andesitic magma (ρ = 2.27 g/cm^3), the addition of 20 wt% primary magnetite into the fluid phase (mass proportion of magnetite in the suspension) would decrease the required magma chamber size from >150 to 50 km^3 when 20% degassing and a 50% depositional efficiency of dissolved Fe are assumed. In this case, the fluid that ascends after formation of the LC

deposit retains half of its original dissolved Fe. Notably, the parental magma loses only 0.7 wt% FeO (see Fig. S2.3 and S2.4, supplementary)
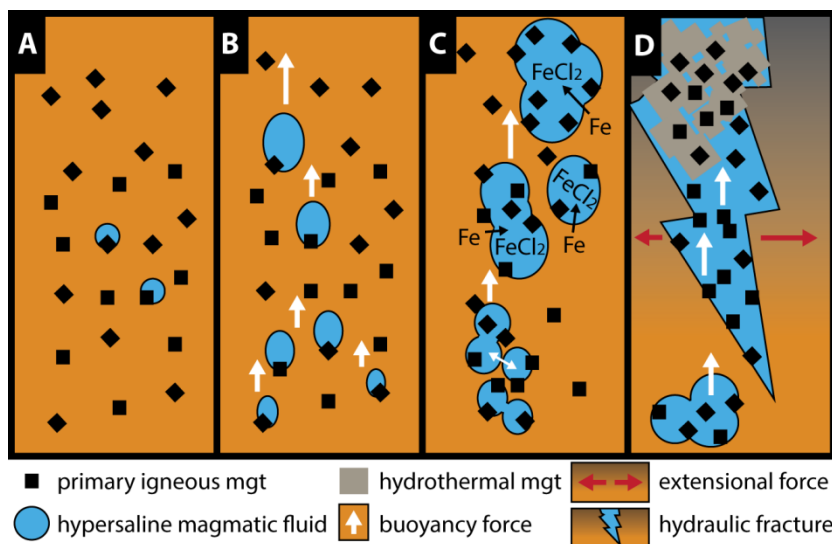
Figure 2.4: Model proposed showing preferred bubble nucleation on magnetite microlites crystallized from silicate melt (orange) (A), ascent of bubble-magnetite pairs due to positive $F^{buoyancy}$ (B), further ascent, growth, coalescence and accumulation of primary magnetite as well as scavenging of Fe into the high-salinity fluids (C), formation of hydraulic fractures (due to tectonic stress changes) allowing fast efficient segregation of magnetite-rich fluid (D), and the eventual growth of hydrothermal magnetite during progressive cooling. Panels represent scenarios becoming shallower from A to D. The color change in D implies increasing crystallinity.

2.5 A GENETIC LINK BETWEEN IOA AND IOCG DEPOSITS?

Our proposed magnetite suspension model accounts for the observed combination of primary igneous (type 1) and secondary high-T hydrothermal magnetite (type 2), and can also explain the lack of K and Na alteration at LC and potentially a genetic link between IOA and IOCG deposits. Simon et al. (2004) reported that the Fe concentration of a Cl-rich aqueous fluid decreases

slightly during decompression, while concentrations of Na and K strongly increase, allowing for magnetite precipitation without simultaneous Na and K mineralization. However, owing to retrograde solubility of metals such as Fe, Cu, and Au (Williams-Jones and Migdisov, 2014; Hurtig and Williams-Jones, 2014), the magmatic-hydrothermal fluid that precipitates magnetite will continue transporting significant amounts of dissolved Fe (plus Cu, Au) after IOA deposition. Further ascent and cooling promotes the precipitation of Cu-sulfides at T <420°C and at shallow levels within the crust, as observed for IOCG deposits. This is consistent with the proposed model in which IOA deposits represent the deeper roots of IOCG systems (e.g., Sillitoe, 2003) and may therefore be a step toward a systematic formation model for IOCG deposits.

2.6 CONCLUSION

The CIB experienced an amalgamation of several factors including: (1) the formation of a Cl-rich hydrous mafic magma due to recycling of sea-water during subduction; (2) crustal thinning in an extensional back-arc setting, allowing magma ascent into the shallow crust; and, (3) a stress change during the Lower Cretaceous that produced crustal-scale faults (AFS) to serve as conduits for magnetite-fluid suspensions. Our new magnetite-suspension model for the formation of Kiruna-type IOA deposits is supported by stable Fe and O isotope signatures and the contrasting magnetite geochemistry between silicate inclusion-rich igneous cores and the surrounding magmatic-hydrothermal magnetite matrix. The observed trend from high to low Ti+V and Al+Mn values (Fig. 2.3) can be explained by cooling magmatic-hydrothermal fluids since these elements become increasingly incompatible in magnetite and aqueous fluid at lower T. Eventually, further ascent and cooling reduces the ability of the fluid to maintain high concentrations of dissolved Fe and other

elements (e.g., Cu, Au), which promotes the precipitation of Cu-sulfides and Fe-oxides at shallower levels than IOA deposits, supporting a genetic link between IOA and IOCG deposits. Lastly, it is plausible that a magnetite-fluid suspension vented to the surface could have produced the strongly vesiculated magnetite "lava flows" observed at El Laco, Chile (Park, 1961), with magnetite trace element patterns guiding researchers to a high-T magmatic-hydrothermal origin (Dare et al., 2014).

Chapter 3: Trace elements in magnetite from massive iron oxide-apatite deposits indicate a combined formation by igneous and magmatic-hydrothermal processes

Jaayke L. Knipping[1,*], Laura D. Bilenker[1], Adam C. Simon[1], Martin Reich[2], Fernando Barra[2], Artur P.Deditius[3], Markus Wälle[4], Christoph A. Heinrich[4], François Holtz[5] and Rodrigo Munizaga[6]

[1]*Department of Earth and Environmental Sciences, University of Michigan, 1100 North University Ave, Ann Arbor, Michigan, USA*

[2]*Department of Geology and Andean Geothermal Center of Excellence (CEGA), Universidad de Chile, Plaza Ercilla 803, Santiago, Chile*

[3]*School of Engineering and Information Technology, Murdoch University, 90 South Street, Murdoch, Western Australia, Australia*

[4] *Institute of Geochemistry and Petrology, ETH Zurich, Clausiusstrasse 25, 8092 Zürich, Switzerland*

[5]*Institut für Mineralogie, Leibniz Universität Hannover, Callinstr. 3, 30167 Hannover, Germany*

[6]*Compañia Minera del Pacífico (CAP) Brasil N 1050, Vallenar, Región de Atacama, Chile.*

ABSTRACT

Iron oxide-apatite (IOA) deposits are an important source of iron and other elements (e.g., REE, P, U, Ag and Co) vital to modern society. However, their formation, including the namesake Kiruna-type IOA deposit (Sweden), remains controversial. Working hypotheses include a purely magmatic origin involving separation of an Fe-, P-rich, volatile-rich oxide melt from a Si-rich silicate melt, and precipitation of magnetite from an aqueous ore fluid, which is either of magmatic-hydrothermal or non-magmatic surface or metamorphic origin. In this study, we focus on the geochemistry of magnetite from the

Cretaceous Kiruna-type Los Colorados IOA deposit (~350 Mt Fe) located in the northern Chilean Iron Belt. Los Colorados has experienced minimal hydrothermal alteration that commonly obscures primary features in IOA deposits. Laser ablation-inductively coupled plasma-mass spectroscopy (LA-ICP-MS) transects and electron probe micro-analyzer (EPMA) wavelength-dispersive X-ray (WDX) spectrometry mapping demonstrate distinct chemical zoning in magnetite grains, wherein cores are enriched in Ti, Al, Mn and Mg. The concentrations of these trace elements in magnetite cores are consistent with igneous magnetite crystallized from a silicate melt, whereas magnetite rims show a pronounced depletion in these elements, consistent with magnetite grown from an Fe-rich magmatic-hydrothermal aqueous fluid. Further, magnetite grains contain polycrystalline inclusions that re-homogenize at magmatic temperatures (> 850 °C). Smaller inclusions (< 5μm) contain halite crystals indicating a saline environment during magnetite growth. The combination of these observations are consistent with a formation model for IOA deposits in northern Chile that involves crystallization of magnetite microlites from a silicate melt, nucleation of aqueous fluid bubbles on magnetite surfaces, and formation and ascent of buoyant fluid bubble-magnetite aggregates. Decompression of the fluid-magnetite aggregate during ascent along regional-scale transcurrent faults promotes continued growth of the magmatic magnetite microlites from the Fe-rich magmatic-hydrothermal fluid, which manifests in magnetite rims that have trace element abundances consistent with growth from a magmatic-hydrothermal fluid. Mass balance calculations indicate that this process can leach and transport sufficient Fe from a magmatic source to form large IOA deposits such as Los Colorados. Furthermore, published experimental data demonstrate that a saline magmatic-hydrothermal ore fluid will scavenge significant quantities of metals such as Cu and Au from a silicate melt, and when combined with solubility data for Fe,

Cu and Au, it is plausible that the magmatic-hydrothermal ore fluid that continues to ascend from the IOA depositional environment can retain sufficient concentrations of these metals to form iron oxide copper-gold (IOCG) deposits at lateral and/or stratigraphically higher levels in the crust. Notably, this study provides a new discrimination diagram to identify magnetite from Kiruna-type deposits and to distinguish them from IOCG, porphyry and Fe-Ti-V/P deposits, based on low Cr (< 100 ppm) and high V (>500 ppm) concentrations.

3.1 INTRODUCTION

Kiruna-type iron oxide-apatite (IOA) deposits are sometimes classified as the Cu-poor endmember of iron oxide copper-gold (IOCG) deposits, which occur globally and range in age from Late Archean (2.5 Ga) to the present (Williams et al., 2005). Iron oxide-apatite and IOCG deposits are of economic interest due to their mineable amounts of iron oxides (i.e., magnetite and/or hematite) and/or variable amounts of Cu, Au, REE, P, U, Ag and Co (e.g., Foose and McLelland, 1995; Chiaradia et al., 2006; Barton, 2014). While IOCG deposits are mostly thought to be formed by hydrothermal processes (Mumin et al. 2007; Barton, 2014), the origin of Kiruna-type IOA deposits remains controversial. Some authors invoke a hydrothermal origin, which can be either a non-magmatic surface derived deuteric fluid that scavenges iron from surrounding dioritic plutons and metasomatically replaces volcanic rocks (Menard, 1995; Rhodes and Oreskes, 1995, 1999; Barton and Johnson, 1996, 2004; Haynes, 1995, 2000; Rhodes et al., 1999; Sillitoe and Burrows, 2002), or a magmatic-hydrothermal fluid that sources Fe directly from magmas (Pollard, 2006). A third hypothesis invokes liquid immiscibility between a Fe-, P-rich oxide melt and a conjugate Si-rich melt, with coalescence, separation and crystallization of the Fe-, P-rich oxide melt forming IOA deposits (e.g.,

27

Nyström and Henríquez, 1994; Travisany et al., 1995; Naslund et al., 2002; Henríquez et al., 2003; Chen et al. 2010). The first two hypotheses allow the possibility for a genetic connection between Kiruna-type IOA and IOCG deposits, which have been observed within the same district (Sillitoe, 2003) and such as in the Missouri iron province (Seeger, 2003), whereas there is debate about the connection when applying the third hypothesis. Some authors distinguishe then Kiruna-type IOA deposits *sensu stricto* from IOCG deposits (Williams et al., 2005; Nold et al., 2014), while other assume the degassing of an iron oxide magma at depth as source for IOCG forming fluids (Naslund et al. 2002). Recently, Knipping et al. (2015) proposed a novel model, based on isotopic and trace element composition of magnetite of the Los Colorados IOA deposit, in which initially purely magmatic processes are combined with magmatic-hydrothermal precipitation of magnetite that further allows a connection between IOA and IOCG deposits. The aforementioned model involves crystallization of magnetite microlites from a silicate melt, wherein the magnetite serves as the nucleation surface for a subsequently exsolved magmatic-hydrothermal aqueous fluid. These magnetite-bubble pairs buoyantly segregate and become a rising magnetite-fluid suspension that deposits massive magnetite along or in proximity to regional-scale transcurrent faults.

Kiruna-type iron oxide-apatite deposits should not be confused with another type of IOA deposits: nelsonites. Nelsonites are characteristically enriched in Ti that is present as ilmenite and/or Ti-rich magnetite, and apatite (30-50 modal %), and are commonly associated with anorthosites complexes (90-100 modal % plagioclase) (Philpotts, 1967) and the upper parts of layered mafic intrusions (Tollari et al. 2008). In contrast, Kiruna-type deposits, named after the Kiruna deposit in Sweden (Geijer, 1931), comprise less Ti (<1 wt%)

contained in magnetite ± trace titanite, and apatite is generally less abundant compared to nelsonites. While some Kiruna-type deposits contain as much as 50% apatite (e.g., Mineville, New York; Foose and McLelland, 1995), other deposits contain only accessory amounts (e.g., El Laco, Chile; Nyström and Henriquez, 1994). While the origin of Kiruna-type IOA deposits is discussed controversially (hydrothermal versus magmatic), it is generally accepted that the origin of nelsonites is magmatic. Although these processes are also still debated and possible hypotheses are immiscibility between silicate-rich and Fe-P-rich melts (Philpotts, 1967; Naslund, 1983; Charlier and Grove, 2012, Chen et al., 2013) or simple crystallization and accumulation of ore minerals from an evolved melt (Tollari et al. 2008; Tegner et al. 2006).

In this study, we use high resolution electron probe micro analyzer (EPMA) and laser ablation inductively coupled mass spectroscopy (LA-ICP-MS) analyses of a large suite of trace elements in magnetite grains from different depths of the Kiruna-type Los Colorados IOA deposit (~350 Mt Fe) in the Chilean Iron Belt (CIB) to explore the processes leading to the formation of a typical Kiruna-type IOA deposit. The crystallization history of magnetite at Los Colorados is discussed on the basis of trace element concentration analyses using magnetite as a fingerprint of deposit types (Dupuis and Beaudoin, 2011; Nadoll et al. 2014a,b and Dare et al. 2014a), which further gives new insights on the classification of Kiruna-type IOA deposits.

3.2 GEOLOGICAL BACKGROUND

About 50 Kiruna-type IOA deposits, including seven large deposits (>100 Mt high grade Fe-ore each), occur in the Chilean Iron Belt (CIB) within the Coastal Cordillera of northern Chile between latitudes 25° and 31° S (Nyström and Henriquez, 1994) (Fig.1). The CIB was formed during the

opening of the Atlantic Ocean, when the transtensional back arc basin of the South American subduction zone changed to a transpressional regime (Uyeda and Kanamori, 1979). This change in tectonic environment facilitated development of the sinistral transcurrent Atacama Fault System (AFS). In this study, we focus on the formation and evolution of the iron deposits associated with the AFS, most of which are composed of large amounts of (low Ti-) magnetite, actinolite and variable amounts of apatite (Nyström and Henriquez, 1994).

The Los Colorados iron ore deposit lacks sodic and potassic alteration that is commonly observed in hydrothermally formed deposits (Barton, 2014) and thus provides an ideal natural laboratory to deconvolve the original geochemical signature of a world-class Kiruna-type deposit.

The Los Colorados deposit is located at 28° 18′18′′ S and 70° 48′28′′ W and is hosted in the andesitic volcanic rocks of the Punta del Cobre Formation along the southern segment of AFS (Pincheira et al.,1990). The iron oxide ore occurs in two sub-parallel dikes, which are each about 500 m deep, 150 m wide and 1500 m long (Fig. 3.1). Radiometric K-Ar dating indicates similar ages of ~110 Ma for the formation of the magnetite dikes and an adjacent brecciated dioritic intrusion (Pichon, 1981) which may imply a genetic association between the two systems. The depth of the deposit relative to the paleo surface is estimated by the mine geologists to be 3-4 km. Proven resources of up to 986 Mt with an average ore grade of 34.8% Fe (CAP-summary, 2013) are more than the total reported resources of the other IOA deposits in the CIB (e.g., El Romeral, El Algarrobo and Cerro Negro Norte).
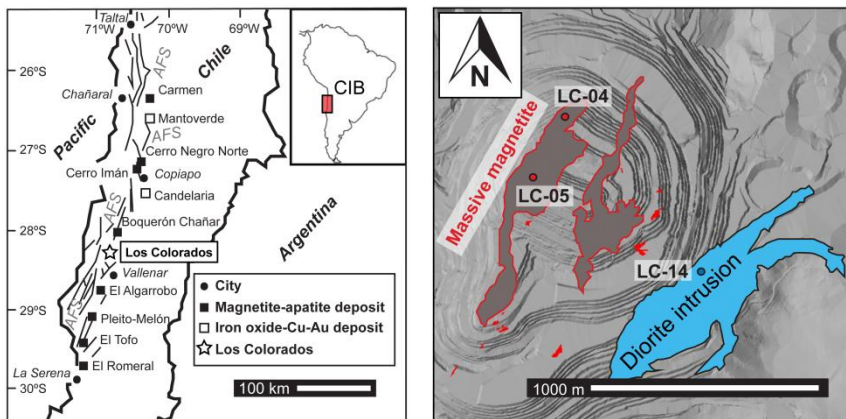
Figure 3.1: Map showing the location of the Los Colorados deposit within the Chilean Iron Belt (CIB), which is located along the Atacama Fault System (AFS) (left). Right-hand image (plan view) shows the massive magnetite ore bodies and the adjacent diorite intrusion that are both hosted in andesite of the Punta del Cobre formation and the location of the investigated drill cores (LC-04, LC-05 and LC-14).

3.3 SAMPLES FROM THE LOS COLORADOS IRON ORE DEPOSIT

Samples from different depths of three drill cores were analyzed in this study: LC-04, LC-05 and LC-14. LC-04 and LC-05 are drill cores taken from the western magnetite dike and LC-14 is taken from the adjacent (brecciated) diorite intrusion (Fig. 3.1). Six samples from different depth levels of LC-04 were taken, which is located in the northern part at the border zone of the western (main) dike. LC-04 reaches a relative depth of 146 m and crosscuts a diorite dike at 128 m. Six samples were studied from LC-05, which reaches a relative depth of 150 m in the center of the western dike (Fig. 3.1). The core LC-05 is composed only of massive magnetite ore. Four samples from different depths were studied from LC-14, which reaches a relative depth of 173 m into the brecciated dioritic intrusion south east of the ore body. Due to the topography of the area, the wells sink at different elevations (LC-04: 196 m, LC-05: 345 m, LC-14: 509 m) and thus samples from drill core LC-14 represent the upper part of the system relative to the ore body. The mineral

31

assemblage of the dike rocks at Los Colorados consists dominantly of magnetite (up to 94 wt%), actinolite and only minor apatite (< 0.7 wt%), which is mostly accumulated in veins in contact with actinolite (see Fig. S3.1, supplementary). The brecciated diorite intrusion contains up to 25 wt% iron.

3.4 METHODS

3.4.1 Bulk rock analysis

The bulk rock compositions of 15 samples derived from different depths of each drill core were determined by using inductively coupled plasma-optical emission spectroscopy (ICP-OES) for major elements (Thermo Jarrell-Ash ENVIRO II ICP) and inductively coupled plasma-mass spectroscopy (ICP-MS) for trace elements (Perkin Elmer Sciex ELAN 6000 ICP/MS) at Actlabs Laboratories, Ontario, Canada. In total, 70 elements or element oxides were analyzed (Table 3.1). Results of quality control are given in Table S3.1 (supplementary). Prior to ICP-OES or ICP-MS the powdered rocks were mixed with a flux of lithium metaborate and lithium tetraborate and fused in an induction furnace. Immediately after fusion, the generated melt was poured into a solution of 5% nitric acid containing an internal standard, and mixed continuously until completely dissolved (~30 minutes). This process ensured complete dissolution of the samples and allowed the detection of total metals, particularly of elements like REE, in resistant phases such as zircon, titanite, monazite, chromite and gahnite.

3.4.2 Microanalysis and mapping

The electron probe microanalysis (EPMA) was performed at the University of Michigan, USA (Electron Microbeam Analysis Laboratory, EMAL) and at the University of Western Australia (Centre of Microscopy, Characterisation and Analysis, CMCA), using a Cameca SX-100 and a JEOL

8530F, respectively. Magnesium, Al, Si, Ca, Ti, V, Mn and Fe were analysed in magnetite grains. Under similar analytical conditions (e.g., accelerating voltage, beam current, beam size, and wavelength dispersive crystals; Table 3.2), similar mean detection limits (~100 ppm) were achieved in both machines and reproducible quantitative WDS analyses were obtained. A focused beam (~1 μm) was used to avoid hitting any inclusions or exsolution lamellae within the magnetite. In addition to quantitative spot analyses along profiles, Wavelength Dispersive X-ray (WDX) maps were collected at the University of Western Australia by using an accelerating voltage of 20 kV, a beam current of 150 nA and a counting time of 20-40 ms/step. Interference corrections were carried out for Ti concentrations since V Kβ affects the Ti Kα signal. Qualitative elemental energy dispersive X-ray (EDX) maps of polycrystalline inclusions were generated by using a Hitachi S-3200N scanning electron microscope (SEM) at the University of Michigan.

3.4.3 Laser Ablation inductively coupled plasma   mass spectrometry (LA-ICP-MS)

Laser ablation-ICP-MS measurements were performed on 2-8 magnetite grains from each sample depth by using the 193 nm ArF excimer laser systems at ETH (Zürich). The coupled mass spectrometer was either a quadrupole (Elan 6100 DRC, PerkinElmer, Canada) for spot analyses or a highly sensitive sector field (Element XR, Thermo Scientific, Germany) ICP-MS for transect lines analyses. Both instruments were tuned to a high sensitivity and a simultaneous low oxide formation rate based on observation of ThO/Th signals. Since helium was used as carrier and argon as plasma gas, interferences with these elements as well as with oxides of these elements and double charged ions were taken into account when choosing representative isotopes for each element. Thus, ^{57}Fe was measured for the iron content,

instead of the more abundant ^{56}Fe that has an interference with ArO. Forty seconds of gas background were measured for background correction prior to sample analysis, and a sample-standard bracketing method (2 x standard, 20 x samples, 2 x standard) was used for instrumental drift correction. The NIST 610 standard was used following Nadoll and Koenig (2011) for magnetite analysis. Since the Fe content was well characterized in each sample by previous EPMA analysis, element concentrations in the unknowns were calculated from element to Fe ratios. The resulting concentrations of other elements such as Ti, V and Mn are in relatively good agreement with previous detected concentrations by EPMA (Fig. S3.2, supplementary), which makes NIST 610 as a standard suitable in this study. A laser spot size of 40 µm was used for standard measurements, while the spot size was decreased to 30 µm on unknowns, which was the best compromise between analyzing visually inclusion-free magnetite and measuring above the detection limit of most elements. In total, 39 elements were measured with dwell times of 10 ms, except for Zn, Ga, Sr, Sn (20 ms), Ni, Ge, Mo, Ba, Pb (30 ms) and Cr and Cu (40 ms) to achieve measureable concentration of these elements. Data were obtained by using a laser pulse of 5 Hz and a 60 s signal for spot analysis and velocity of 5 µm/s for transect measurements, which results in a depth resolution of 3-6 µm for the transects. To avoid the incorporation of possible surface contaminants, a "cleaning" with 25 % overlap per pulse was conducted directly before and along the transect of the actual measurement. The data were processed by using the software SILLS (Guillong et al., 2008), which calculates the detection limit after Pettke et al. (2012). Any exsolution lamellae of ilmenite and ulvöspinel in magnetite were incorporated into the LA-ICP-MS analyses to represent the initial composition of the Fe(-Ti) oxide (Dare et al. 2014a). The influence of micro- to nano-meter scale inclusions that were trapped in magnetite growth zones could not be avoided due to the analytical

34

beam size of LA-ICP-MS. Therefore, Si and Ca contents were taken from EPMA measurements for further interpretation following the protocol of Dare et al. (2014a) to avoid the influence of any silicate inclusion visible in BSE images.

3.5 RESULTS

3.5.1 Bulk content of major and trace elements

Major, minor and trace element compositions of the bulk rock samples are listed in Table 3.1. Total Fe is reported as Fe_2O_3, which varies significantly with depth. Drill core LC-04 includes a sharp contact between the magnetite dike and a crosscutting diorite dike with a sudden change from ~73 to 6 wt% Fe_2O_3 within 4 m (LC-04-125.3 vs. LC-04-129.5). The bulk rock data of the massive ore rock (LC-04 and LC-05) revealed very low Na and K-concentrations (Table 3.1), when excluding the diorite dike in drill core LC-04 (LC-04-129.5 and LC-04-143.1). This indicates the absence of sodic and potassic alteration products in the massive Fe-ore. The REE concentrations of the bulk rock of the diorite intrusion and the magnetite dikes are illustrated in Fig. 3.2. The brecciated diorite intrusion has distinctly higher REE concentrations than the magnetite dike and both have similar REE patterns, including a horizontal heavy REE distribution and a pronounced negative Eu-anomaly. However, the Eu-anomaly is distinctly larger (lower Eu/Sm) in the magnetite dike than in the brecciated diorite (Eu/Sm mag.dike = 0.12 ±0.06 vs. Eu/Sm diorite = 0.21 ± 0.07). Increasing Fe content is correlated with decreasing light REE. Two samples from the bottom of LC-04 have a dioritic composition and plot at higher REE values together with the diorite intrusion (LC-14).
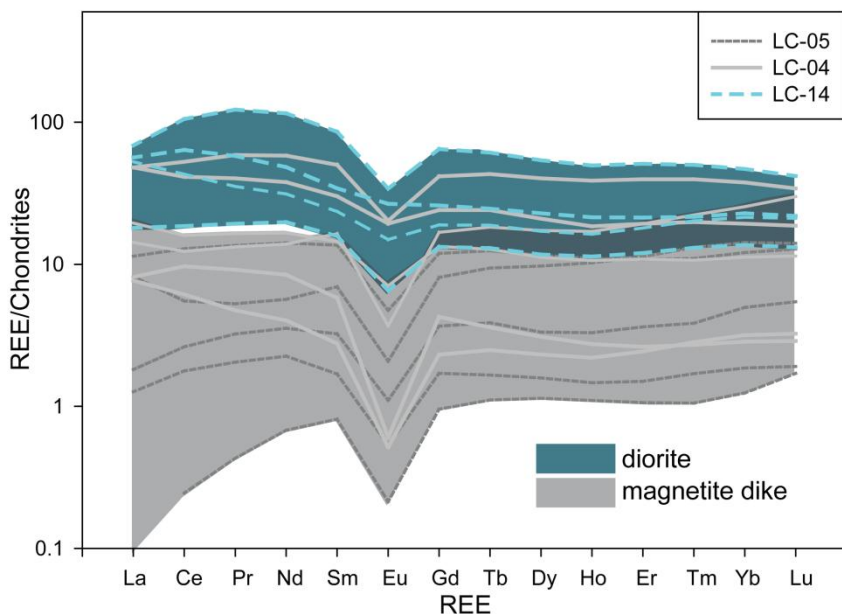
Figure 3.2: REE concentrations in the bulk rock samples of the magnetite dike (gray) and the diorite intrusion (blue) normalized to chondrite (Sun and McDonough, 1989). The diorite intrusion has distinctly higher REE concentrations, but shows in general a similar REE pattern (negative Eu-anomaly, horizontal HREE distribution), when compared to the magnetite dike. The two samples from drill core LC-04, which plot at higher values in the range of the diorite intrusion, have a dioritic composition, since they are from lower levels of this drill core, where it crosscuts a diorite dike.

3.5.2 Textures and trace element geochemistry of the Los

Colorados magnetite

The textures of the magnetite grains from the massive magnetite dike rock vary from pristine magnetite to inclusion-rich magnetite (Fig. 3.3a and b). The inclusions in magnetite vary from finely distributed micro- to nano-meter scale inclusions, to irregular, large ones (~tens of μm) that are randomly distributed. Sometimes ilmenite exsolution lamellae are observed in magnetite as well (e.g. LC-04-104). Zonation in back scattered electron (BSE) images is observed especially in some samples of drill core LC-04 (Fig. 3.3b), although selected samples of drill core LC-05 (150 m) also contain zoned magnetite

crystals (Fig. 3.3a). The magnetite in the brecciated diorite is more texturally diverse than magnetite in the massive magnetite dike, especially within sample LC-14-167. In this sample, magnetite grains exhibit oscillatory zoning, observed as different shades of gray in BSE images (Fig. 3.3c).
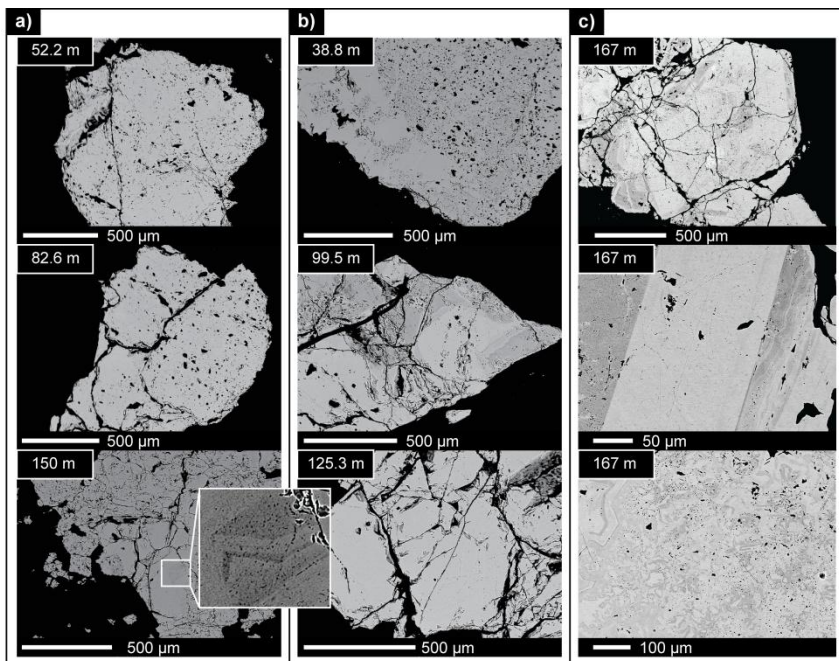
Figure 3.3: BSE-images of different magnetite grains from drill core LC-05 (column a), LC-04 (column b) and LC-14 (column c). a) randomly distributed inclusions in relatively pristine magnetite (depth 52.2 and 82.6 m) and inclusion-rich areas and inclusion-poor areas with some zoning (depth 150 m) b) pristine magnetite and inclusion-rich areas with small fine distributed inclusions to large randomly distributed irregular inclusions (depth 38.8 m), magnetite with different gray shades indicating different trace element concentration (depth 99.5 m) and pristine magnetite (depth 125.3 m). c) oscillatory zoned magnetite with different gray shades (depth 167 m), magnetite with crystallographically oriented spinel exsolutions in bright area and as small inclusions in dark gray areas (depth 167 m) and oscillatory zoning of bright and dark gray magnetite (depth 167 m).

3.5.2.1 Trace element profiles and maps by EPMA

Trace element profiles were measured from the core to rim of individual magnetite grains in order to assess possible chemical zonation.

Elements including Si, Al, Mg, Mn, Ca, Ti and V were measured with reasonable detection limits (~100 ppm) by EPMA. All analyzed EPMA data points of each magnetite grain from the different samples are listed in Table S3.2 (supplementary). Most of the analyzed individual magnetite grains from the magnetite dike show no variation in V (variations per measured profile are <0.01 wt%). The total V content of magnetite decreases upward and distal from the dike center. The highest V concentrations were detected in the deepest sample from the dike center (LC-05-150: 6720 ppm V), and V concentrations are generally higher in the more central drill core LC-05 (average $\pm$ 1σ: 3320 $\pm$ 1200 ppm) when compared to the more distal drill core LC-04 (average $\pm$ 1σ: 2460 $\pm$ 460 ppm). In contrast, magnetite from the brecciated adjacent diorite intrusion contains intensive zonation and generally lower V concentrations (average $\pm$ 1σ: 1640 $\pm$ 1000 ppm) with more pronounced changes in V contents of about several hundred to thousands of ppm within individual grains. Although the position of each focused analytical EPMA spot (ca. 1 μm) was set manually to avoid hitting inclusions and fine-scale exsolutions, some micro- and nano-impurities contaminated the signal and made the interpretation of the trace element profiles challenging. However, sometimes an enrichment of elements such as Si and Ca with a simultaneous depletion in Ti and Al was measured at the rim of the magnetite grains. Thus, trace element distributions within individual grains were also characterized by collecting WDS X-ray element maps. Figure 3.4a is a X-ray map of magnetite from the massive magnetite dike (LC-05-129) that shows distinct Ti-depletion from the grain core to its rim with three different zones (cf. Knipping et al. (2015)): Type 1) Ti-rich core with distinct Mg- and Si-inclusions; Type 2) Ti-poorer and more pristine transition zone and Type 3) Ti-depleted rim (Fig. 3.4a). Similar zoned magnetite grains with inclusion-free rims and inclusion-rich cores were also detected at the Proterozoic IOA deposit Pilot Knob (Missouri,

USA) and were interpreted as igneous phenocrysts (Nold et al., 2014). In contrast, Fig. 3.4b is a X-ray map of magnetite from the brecciated diorite intrusion (LC-14-167) that exhibits distinct oscillatory zoning, which is an indicator of fast crystal growth in a compositionally fluctuating hydrothermal system (Reich et al. 2013; Dare et al. 2015). The average Si and Ca concentrations (4500 and 1600 ppm, respectively) in these magnetites are similar to the data of Dare et al. (2015) for the El Laco ore, where also oscillatory zoning was observed.
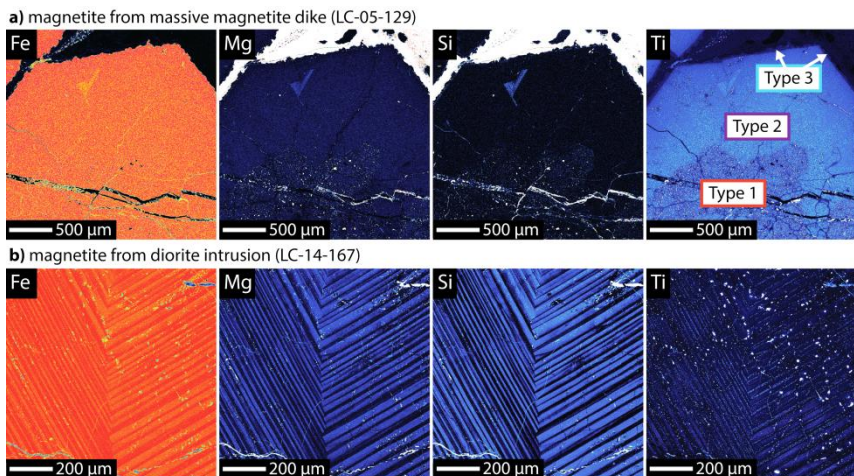
Figure 3.4: WDS elemental maps of selected trace elements in magnetite from Los Colorados: a) magnetite sample from the massive dike (LC-05-129) that contains a Ti- and inclusion-rich grain core (Type 1), which is surrounded by inclusion-poor magnetite that contains less Ti (Type 2) and a Ti-depleted rim (Type 3); b) magnetite from the brecciated diorite intrusion (LC-14-167) that exhibits oscillatory zoning, typical of crystal growth from a compositionally fluctuating fluid.

3.5.2.2 *Trace element profiles by LA-ICP-MS*

To obtain information about trace elements not detectable by EPMA, but which are of particular importance to discriminate ore deposit types (e.g., Cr, Ni, Co, Ga, Zn, Sn), transects were made by using LA-ICP-MS along the same profiles previously measured by EPMA. The Fe-content of magnetite

previously determined by using EPMA was used as the internal standard. The LA-ICP-MS technique also allows the continuous detection along a profile to better reveal cryptic chemical zoning. An example profile is shown for LC-05-82.6 in Fig. 3.5.
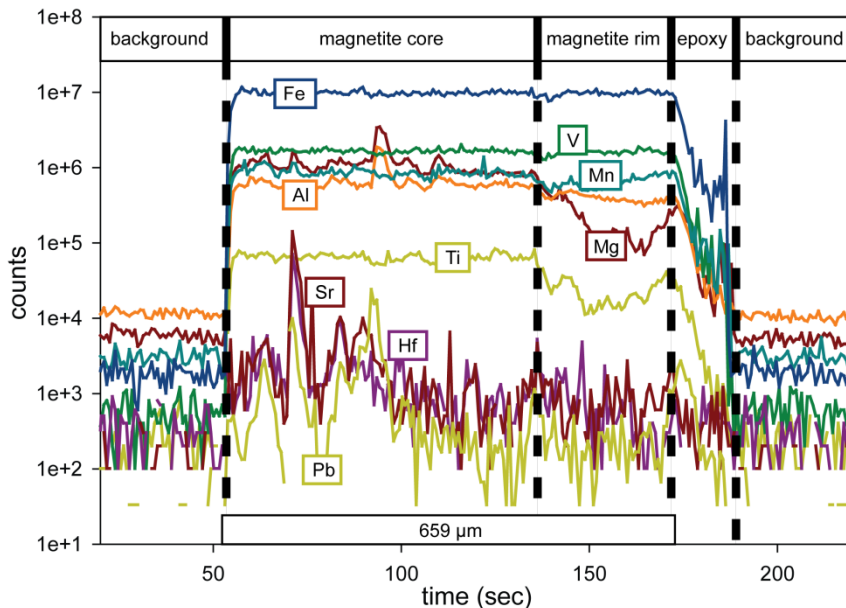
Figure 3.5: An example of a LA-ICP-MS profile across a magnetite grain from the dike sample LC-05-82.6, which did not show any zonation in BSE images. However, by using LA-ICP-MS, it is clear that particular elements such as Ti, Mg, Al and Mn are enriched in the core and depleted in the rim of the magnetite grain. Some elements, e.g., Mn, decrease in concentration at the core-rim boundary and then increase toward the outside of the grain. Some elements such as Sr, Hf and Pb exhibit more variability but are clearly enriched in the magnetite core. Elements such as Co, Ni (not illustrated) and V show no variation from core to rim.

Only a subtle zonation was detected by EPMA, and no zonation was evident by BSE images (Fig. 3.3a). However, the LA-ICP-MS transect demonstrates a clear change from high to low Ti, Al, Mg and Mn concentrations from core to rim. Manganese decreases in concentration at the core-rim boundary, but then increases toward the outside of the grain. Trace

40

elements such as Pb, Hf and Sr are rather enriched in the core of the grain, while the concentration of V seems to remain constant throughout the whole sample, as already observed in the majority of the EPMA profiles. It should be noted that LA-ICP-MS shows elemental changes from core to rim of grains, but EPMA (mapping) is definitely the better tool to discriminate different magnetite types (Type1, Type 2 and Type 3) due to its higher resolution (1 µm vs. 30 µm beam). For all analyzed magnetite grains, where zonation was observed by LA-ICP-MS, only the constant signal of the cores were considered for assumptions about original magnetite trace element contents. The measured concentrations of the cores from all transects (1-8 transects per sample) are averaged per sample and listed for 38 elements in Table 3.3, while Table 3.4 demonstrates the distinct variation of eleven selected elements between core and rim for one representative transect per sample.

3.5.3 Polycrystalline inclusions in massive magnetite

Magnetite-hosted inclusions are mostly polycrystalline and vary in size, but are present in almost all of the magnetite samples from Los Colorados. Larger inclusions (>10 µm) contain actinolite or clinopyroxene, titanite and an unspecified Mg-Al-Si-phase, while smaller inclusions (<10 µm) often contain additionally chlorine in the form of NaCl and KCl crystals. Figure 3.6 shows a BSE image and corresponding elemental EDX maps of the magnetite matrix with a small inclusion (<5 µm) containing a polycrystalline phase assemblage and a distinct euhedral halite crystal. According to Bodnar and Vityk (1994), and personnel communication with Robert Bodnar, a salinity of ~35 wt% NaCl can be estimated from the presence and relative size of the halite crystal, since the fluid must be over-saturated (>26 wt%) by several weight percent salt before a crystal nucleates in magnetite-hosted fluid inclusions. Even if no chlorine was detected in larger inclusions (>10 µm),

which can be due to sample preparation, the presence of euhedral salt crystals in small inclusions implies a saline environment. Broman et al. (1999) detected hydrous saline/silicate-rich inclusions in apatites and clinopyroxenes from the massive iron ores of the giant El Laco IOA deposit and reported homogenization temperatures (T_h) exceeding 800 °C.
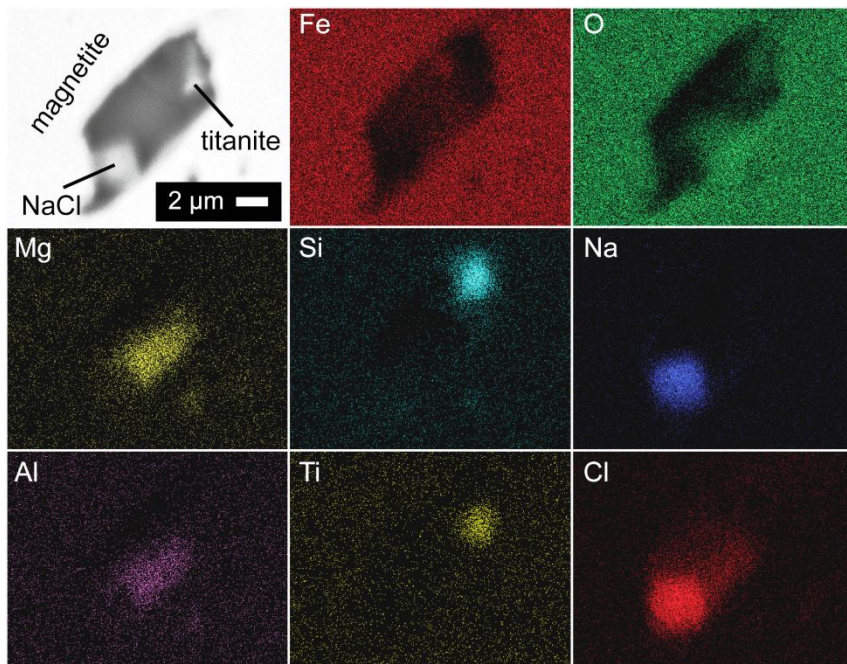
Figure 3.6: Example of an EDX elemental map of a small magnetite-hosted inclusion (<5 µm) trapped in the massive magnetite of the most Fe-rich bulk sample (LC-05-106). The inclusion is heterogeneous with distinct titanite and halite crystals implying a saline environment during magnetite crystallization.

They assumed this to be the temperature of a coexisting melt that was trapped in the apatites and pyroxenes during crystallization from an Fe-oxide melt. The inclusions observed in massive magnetite at Los Colorados may not be primary trapped melt inclusions during crystal growth, but represent phases that were entrapped during accumulation of several magnetite microlites (10s

to < 200 µm) (see Section 3.6.3), which may also explain the numerous amount of inclusions in the igneous cores of the massive magnetite. This observation is consistent with the experimental results of Matveev and Ballhaus (2002) who showed that chromite microlites coalesce and trap mineral, melt and fluid inclusions. To determine T_h of the melt that was surrounding the first liquidus phase (magnetite microlites) at Los Colorados, we attempted to re-homogenize magnetite-hosted inclusions from the sample with the highest bulk FeO content (LC-05-106) by using an Ar flushed heating-cooling-stage (Linkam TS1400XY). Due to the opacity of magnetite, re-homogenization was not observable *in-situ*. We therefore call the following procedure *blind re-homogenization*.

Magnetite grains were heated to temperatures between 750 °C and 1050 °C with 25 °C steps and quenched after 8 minutes at the target temperature. Afterwards, the grains were polished to expose inclusions. Fig. 3.7 shows different isolated inclusions quenched from four different temperatures. Notably, inclusions quenched from 750, 800 and 875 °C are still polycrystalline and contain Mg-rich clinopyroxene (Mg#: 0.84 ± 0.05) or actinolite (Mg#:0.85 ± 0.06), titanite, magnetite and an unspecified Mg-Al-Si phase mostly at the outer rim of the inclusions. Actinolite with Mg# > 0.8 was shown to be stable even at high temperatures (800-900 °C) at a pressure of 200 MPa (Lledo and Jenkins, 2008). Only inclusions heated to T ≥ 950 °C re-homogenized to one phase with up to 2400 ppm Cl. This phase has either a composition lacking Ca (25.8 ± 4.9 wt% MgO, 15.2 ± 3.8 wt% FeO, 15.5 ± 2.2 wt% Al_2O_3 and 33.9 ± 1.56 wt% SiO_2), or a Ca-bearing composition (20.4 ± 1.8 wt% MgO, 7.3 ± 2.2 wt% FeO, 2.1 ± 1.4 Al_2O_3, 54.7 ± 2.5 SiO_2 and 12.4 ± 0.5 CaO). The high temperatures are in agreement with T_h > 800 °C determined for the melt-like fluid inclusions in apatite and clinopyroxene from

the El Laco deposit, Chile (Broman et al., 1999). Notable are the similarities of the inclusions observed here with the polycrystalline inclusions in massive chromite from podiform chromite deposits (Melcher et al. 1997), which will be discussed later in Section 3.6.4.
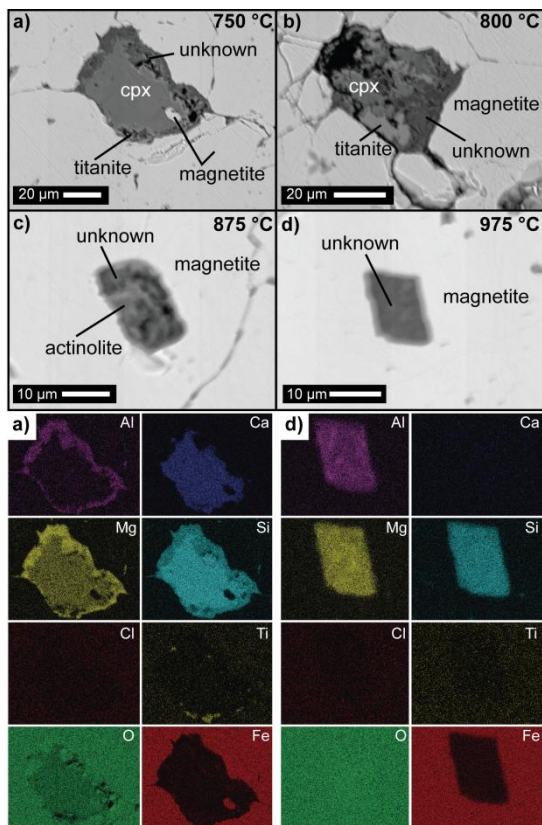
Figure 3.7: BSE images and EDX maps of heat-treated isolated magnetite-hosted inclusions (~10-50 μm) from sample LC-05-106. False-color EDX maps labeled panels a) and d) correspond to inclusions in BSE images in panels a) and d). Grains of this sample were heated to the indicated temperatures to re-homogenize inclusions. See text for detailed description of the procedure. Minerals in polycrystalline assemblage were identified by EMP analysis. a) Inclusion includes Mg-rich clinopyroxene, magnetite, titanite and an unknown Mg-Al-Si-phase at the outer rim (T = 750 °C) b) Polycrystalline inclusion includes Mg-rich clinopyroxene, titanite and an unknown Mg-Al-Si-phase (T=800 °C) c) After heating the magnetite up to 875 °C, inclusions still show inhomogeneity d) Homogeneous inclusion with a single Mg-Al-Si phase after heating to 975 °C.

44

3.6 DISCUSSION

3.6.1 Identification of the magnetites origin at Los Colorados

Recently, several studies have characterized the chemistry of magnetite grains from unique ore deposit types to create chemical discrimination diagrams for magnetite from porphyry, Kiruna, Fe-Ti-V, and IOCG deposits (Dupuis and Beaudoin, 2011; Nadoll et al., 2014a). Here, we use these discrimination diagrams to assess the magnetite chemistry (LA-ICP-MS and EPMA) of Los Colorados. Figure 3.8a is modified from Knipping et al. (2015) and presents the abundances of (Al + Mn) against (Ti + V) for all of the magnetite samples from the western magnetite dike (LC-05 and LC-04). As already described in Knipping et al. (2015) most of the samples and the average of all samples plot in the *Porphyry-box*, instead of the *Kiruna-box,* and some samples extend into the *Fe-Ti, V-box.* The Los Colorados data that overlap chemically with purely magmatic magnetite (*Fe-Ti, V-box*) are from the deepest samples in the center of the dike (LC-05-150), which are the most rich in V (6600-6800 ppm) and from the cores of individual magnetite grains (LC-05-129, Type 1), which are relatively rich Ti (3000-7500 ppm) and V (6000-6800 ppm). The majority of all data including magnetite from the transition zone (e.g., LC-05-129, Type 2) plot in the *Porphyry-box*, which comprises magnetite formed by magmatic-hydrothermal processes, while magnetite sampled more distal from the dike center (LC-04) or magnetite grain rims (LC-05-129, Type 3) plot at lower Al, Mn, Ti and V concentrations (*Kiruna-box*) consistent with a continually cooling fluid resulting in magnetite growth with lower concentrations of these elements. This observation is consistent with some magnetite from the El Laco deposit, Chile, which also plot in the *Porphyry-box* (Dupuis and Beaudoin, 2011). Analytical results of magnetite from Kiruna-type deposits such as the young (~2 Ma) El Laco deposit (Chile) and the unaltered Los Colorados deposit may provide more

45

reliable information about the formation of Kiruna-type deposits than IOA deposits from the Proterozoic (e.g., Pilot Knob and Pea Ridge, Missouri), which were included to define the *Kiruna-box* (Dupuis and Beaudoin, 2011). Thus, higher trace element contents can be expected in magnetite from young and/or unaltered Kiruna-type deposits, than previously thought.
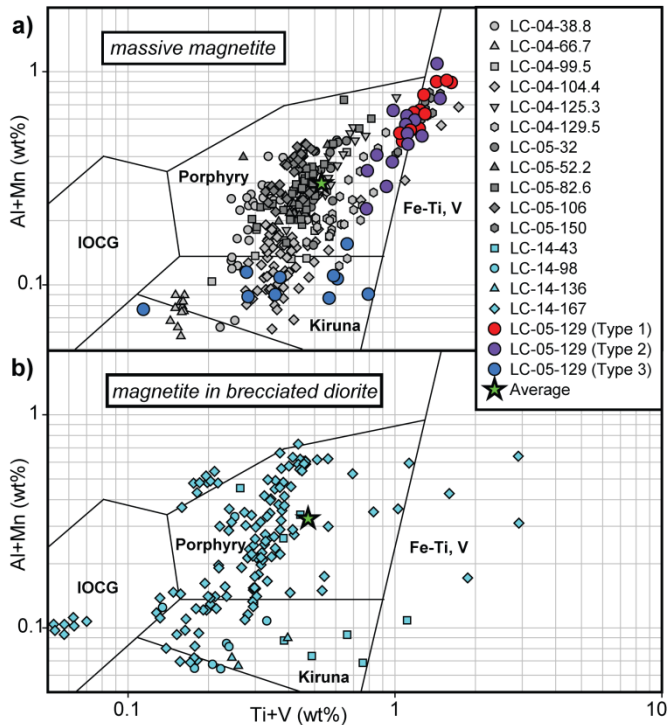
Figure 3.8: Chemical discrimination diagram for magnetite after Dupuis and Beaudoin (2011) modified by Nadoll et al (2014). Numbers in legend refer to the depth of the sample in the respective drill core. The green star represents the average composition of all samples in each panel. a) EPMA results from LC-04 and LC-05 (magnetite dike) plot mainly in the *Porphyry box*. Magnetite grain cores (Type 1 magnetite, red) have the highest trace element concentrations and overlap with magnetite formed in magmatic *Fe-Ti, V* deposits, whereas surrounding magnetite plot in the *Porphyry box* (Type 2 magnetite, purple) and magnetite rims in the *Kiruna box* (Type 3 magnetite, blue) b) EPMA results from magnetite sampled from LC-14 (brecciated diorite) show highly variable trace element concentrations even within individual samples (e.g., LC-14-167), but have a similar average composition as magnetite from the massive magnetite ore (green star).

The chemistry of magnetite from drill core LC-14, which is from the brecciated dioritic intrusion, shows in general a much larger elemental dispersion (Fig. 3.8b) not only for samples collected from different depths, but also within a single sample (LC-14-167). The average of all samples plots also in the middle of the *Porphyry-box*, but the data extend arbitrarily into the *Kiruna-*, *IOCG-* and *Fe-Ti, V-box*. This elemental dispersion may be caused by oscillatory zoning, which was observed in many magnetite of the brecciated diorite (Fig. 3.3c and 3.4b) and which is likely related to hydrothermal processes (Dare et al. 2014, 2015; Reich et al. 2013).

Nadoll et al. (2014a) classified different low temperature (BIF, Ag-Pb-Zn deposits), high temperature and igneous deposit types (Skarn, Climax and Porphyry deposits) using the Sn and Ga concentrations in magnetite from these deposits types. When comparing the ore magnetite data of the current study (Ga: 50-73 ppm, Sn: 0.8-3.4 ppm) to the data of Nadoll et al. (2014a), the chemistry of Los Colorados magnetite ranges between magnetite from porphyry type deposits (Ga: 50-90 ppm, Sn: 2-10 ppm) and igneous magnetite from the unmineralized Inner Zone Batholith, Japan (Ga: 15-150 ppm, Sn: below detection limit). In particular, high Ga contents are reported to be an indicator of high temperature magnetite crystallization and thus the high Ga concentrations (50-73 ppm) in magnetite from the dikes are consistent with higher formation temperatures than magnetite from the brecciated diorite intrusion that contains lower Ga concentrations (31-32 ppm); this is also consistent with the larger elemental dispersion and hydrothermal texture (oscillatory zoning) of magnetite from the brecciated diorite.

The high re-homogenization temperatures (>950 °C) of magnetite-hosted polycrystalline inclusions and elevated trace element contents (Ti, V,

47

Al, Mn, Ga) of the massive magnetite at Los Colorados are not consistent with magnetite crystallization at low temperatures from non-magmatic surface basinal brines (Barton and Johnson 1996, 2004; Haynes et al. 1995, 2000). Plausible hypotheses to explain the data include a magmatic origin either by purely magmatic processes, such as liquid immiscibility that is thought to have formed Fe-Ti-P/V deposits in layered intrusions such as the Bushveld Complex, South Africa (VanTongeren and Mathez, 2012) and Sept Iles layered intrusion, Canada (Charlier et al., 2011), or by magmatic-hydrothermal processes similar to those that form porphyry copper deposits (e.g., Baker, 2002; Candela and Piccoli, 2005; Pollard et al. 2006).

To test between these two fundamentally different hypotheses we used the multi-element diagram proposed by Dare et al. (2014), in which trace element concentrations in magnetites are normalized to the bulk continental crust (Fig. 3.9). The LA-ICP-MS results of the current study are compared to magmatic magnetite from Fe-Ti-P/V deposits (Fig. 3.9a, orange area), to low temperature (T) hydrothermal magnetite (Fig. 3.9b, blue area) and to high-T magmatic-hydrothermal magnetite (Fig. 3.9c, purple area) (see figure caption for detailed information about sample location and references). All of the ore magnetite data from Los Colorados overlap best with high-T magmatic-hydrothermal data from Dare et al. (2014) in agreement with the fingerprinting method of Dupuis and Beaudoin (2011) and Nadoll et al. (2014).   One exception (LC-04-104.4) has a distinct Zr and Hf enrichment that may arise from the accidental incorporation of some micro zircon inclusion which is more typical for a pure magmatic environment. In addition, the V and Cr concentrations from the Los Colorados dike magnetite (grey symbols) are throughout either higher or lower, respectively, than expected for high-T

magmatic hydrothermal deposits, such as porphyries, in contrast to the data from the brecciated diorite of Los Colorados (blue symbols).
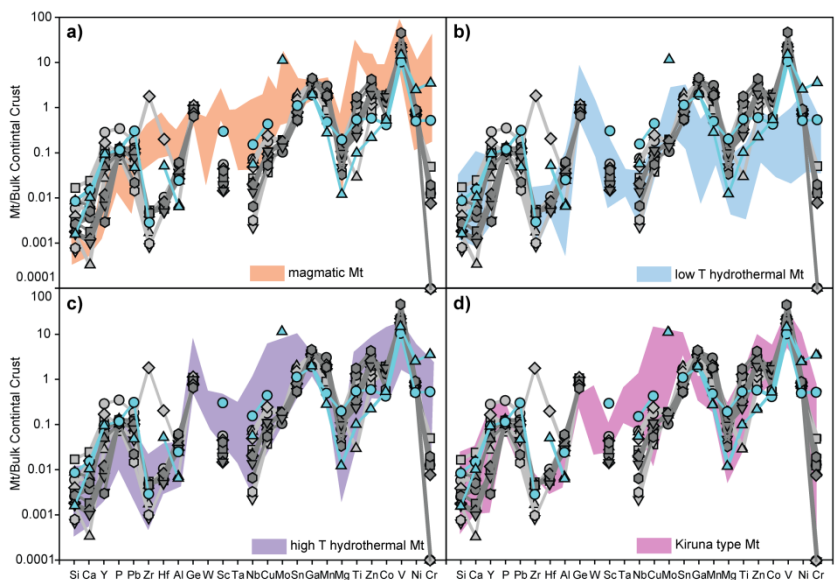
Figure 3.9: LA-ICP-MS results of magnetite (Mt) grains from all three drill cores of Los Colorados are normalized to bulk continental crust (Rudnick and Gao, 2003): magnetite dike (LC-04: bright gray symbols), LC-05: dark gray symbols))and brecciated diorite (LC-14: blue symbols). Symbols are the same as in Fig. 3.8. Small exsolutions and inclusions were included in the analysis following Dare et al. (2014), to achieve the original composition. Results of this study are compared to a) magmatic magnetites (orange), to b) high-T hydrothermal magnetite (purple) and to c) low-T hydrothermal magnetite (blue). These ranges are defined by Dare et al. (2014). The magmatic magnetite range includes analytical results of magnetites from fresh andesite of El Laco and Lascar (Chile) and from Fe-Ti-P/V deposits such as the Bushveld Complex in South Africa and Sept Iles layered intrusion in Canada. The high-T hydrothermal magnetites are defined by nine deposits including e.g. IOCG deposits such as Ernest Henry, Australia and Bafq, Iran and the porphyry deposit Morococha, Peru (Bonyadi et al., 2011; Nadoll et al., 2014; Boutroy, 2014; Dare et al., 2014). The low-T hydrothermal range includes results from Fe-skarns (Vegas Peledas, Argentina), Ag-Pb-Zn veins (Coeur d'Alene, USA), disseminated magnetite in carbonate veins in serpentinite (Thompson Ni-belt, Canada), and Banded Iron Formation (Thompson Ni-Belt, Canada; Dales Gorge, Australia) from data sets of Pecoits et al. (2009), Nadoll et al. (2014) and Dare et al. (2014). Additionally, the results of this study are compared to d) trace elements concentrations that are available in the literature for Kiruna type deposits (pink) such as the magnetite ores of El Laco and El Romeral, Chile and Kiruna, Sweden (Nystroem and Henriquez, 1994, Dupuis and Beaudoin, 2011; Dare et al. 2015).

Dare et al. (2014) hypothesized that low Cr concentrations and thus high Ni/Cr ratios are an indicator for hydrothermal magnetite. However, recent experimental data indicate that not just Cr^{6+} is highly mobile (James, 2003) but also Cr^{3+} is two to four orders of magnitude more soluble than Ni in aqueous fluid at high temperature (magmatic conditions) (Watenphul et al. 2012, 2013), which would result in low Ni/Cr ratios for magmatic hydrothermal magnetite. Although the discrimination by Ti vs. Ni/Cr (Dare et al., 2014) seems to work for many hydrothermal and magmatic magnetites, there are some exceptions such as the igneous magnetite from the unmineralized Inner Zone Batholith, Japan and from the igneous Climax-type Mo deposits, which were used by Nadoll et al. (2014a) as typical igneous magnetites. These magnetites have low Cr concentrations (Inner Zone Batholite: 32-198 ppm; Climax-type Mo deposits: below detection limit) and a relatively high median Ni/Cr ratio of 1.07 (Nadoll et al., 2014a) indicating that low Cr concentration (high Ni/Cr) in magnetite is not necessary an indicator of hydrothermal origin, especially when considering that higher Ni values are expected in magmatic magnetite than in hydrothermal magnetite (Fig. 3.9). Thus, the higher Ni concentrations detected in the cores of Los Colorados magnetite (Table 3.4) and the generally low Cr concentrations do not implicate a hydrothermal origin. In fact, a Cr-depletion and V-enrichment was also reported for other Kiruna-type deposits in Chile (El Romeral and El Laco) and in ore magnetite from Kiruna, Sweden (Nyström and Henriquez, 1994; Dupuis and Beaudoin, 2011; Dare et al. 2015). These data are illustrated in pink in Fig. 3.9d as well as concentrations for other trace elements that were available in the literature for Kiruna-type deposits (Nyström and Henriquez, 1994; Dupuis and Beaudoin, 2011; Dare et al. 2015) showing mostly,besides the elements Ge, Nb, Sn and Ga, a good agreement with our data. Since many elements (besides Si, Ca, Al, Cu, Mn, Mg, Ti, Zn, Co, V, Ni and Cr) are still based only on a few data of El Laco from Dare et al. (2015) a

larger data set is required to improve the identification of Kiruna-type deposits by this method.

In summary, trace elements concentrations in most magnetite from Kiruna-type deposits such as Los Colorados are similar to those observed in high-T hydrothermal systems, such as porphyry copper deposits (Fig. 3.8 and 3.9), in which magnetite is either of magmatic-hydrothermal origin (i.e., precipitated from aqueous fluid) or in the corresponding host rock of igneous origin (i.e., crystallization from silicate melt of intermediate to felsic composition). According to Nadoll et al. (2014a,b) these two contrasting magnetite formation scenarios can be distinguished by their trace element concentrations, since Al, Ti, V and Ga are higher on average in igneous magnetite. To discriminate igneous versus magmatic-hydrothermal magnetite in porphyry systems Nadoll et al. (2014b) proposed to compare Ti and V concentrations (Fig. 3.10), owing to the observation that igneous magnetite is ubiquitously enriched in these metals when compared to hydrothermally formed magnetite in porphyry deposits. The Los Colorados magnetite contains 1370-6430 ppm V (median: 2960 ppm V) (Table 3.3), which is consistent with the global range of igneous magnetite (< 70-6600 ppm V, Nadoll et al., 2014b), but only consistent with the highest values detected in hydrothermal magnetite (<15-3880 ppm V, Nadoll et al., 2014b). Titanium concentrations of Los Colorados magnetite vary between 125-7450 ppm (Table 3.3) overlapping completely with the global range of igneous magnetite (< 70-67100 ppm Ti; Nadoll et al., 2014b) and exceeding for six samples the range of hydrothermal magnetite (< 15-3560 ppm Ti; Nadoll et al., 2014b). Thus, the data presented here for Los Colorados magnetite are consistent with the novel magmatic-hydrothermal model by Knipping et al. (2015), which includes igneous magnetite (i.e., crystallization from silicate melt) in the ore forming process

51

and fully explains the generation of the massive iron ore at Los Colorados (see Section 3.6.3).
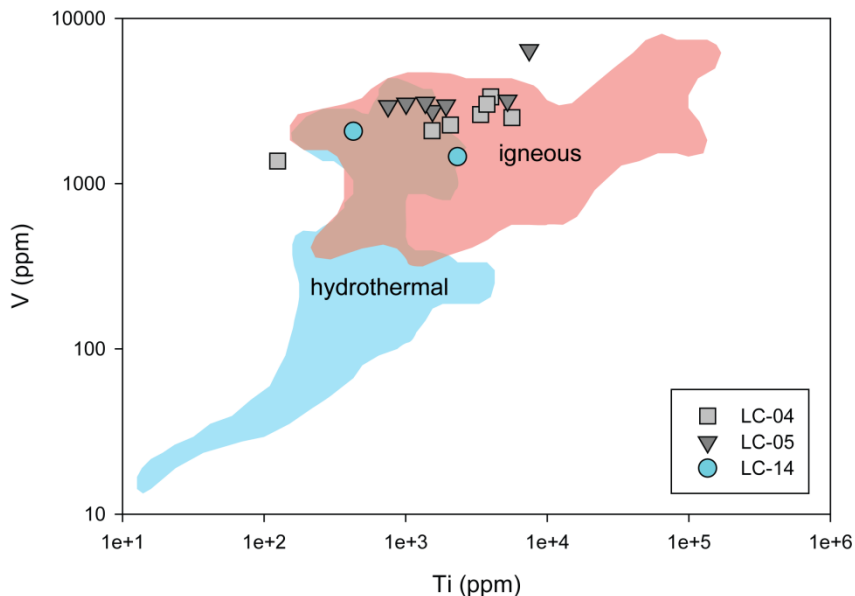
Figure 3.10: Concentration of Ti vs. V in magnetite. Red area includes igneous formed magnetite, while blue area is defined by hydrothermal magnetite based on the data set of Nadoll et al. 2014b. Data of Los Colorados plot mostly in the overlapping area with some samples tending to pure igneous magnetites.

3.6.2 A new identification diagram for magnetite-rich ore deposits based on Cr and V

Recent chemical discrimination diagrams (e.g., Fig. 3.8 and 3.9) are useful tools to distinguish between deposit types such as IOCG, porphyry, skarn, BIF and Fe-Ti-V/P-deposits, based on magnetite geochemistry (Dupuis and Beaudoin, 2011; Nadoll et al. 2014; Dare et al. 2014). However, the compositional range of magnetite from Kiruna-type deposits occurring in the Chilean Iron Belt, El Laco and the type locality of Kiruna seem to overlap mostly with high-T hydrothermal magnetite formed from environments such as porphyry type ore deposits and cannot be distinguished by using existing

52

discrimination diagrams. Thus, we present a new identification diagram to distinguish Kiruna-type from all other high temperature deposits, namely porphyry, IOCG and Fe-Ti-V/P deposits, owing to the relative high V and low Cr contents of Kiruna-type magnetite (Fig. 3.9b and 3.11), which was already observed by Nytröm and Henriquez (1994). We assign magnetite with Cr contents lower than ~100 ppm and simultaneous V contents higher than ~500 ppm to Kiruna-type deposits.
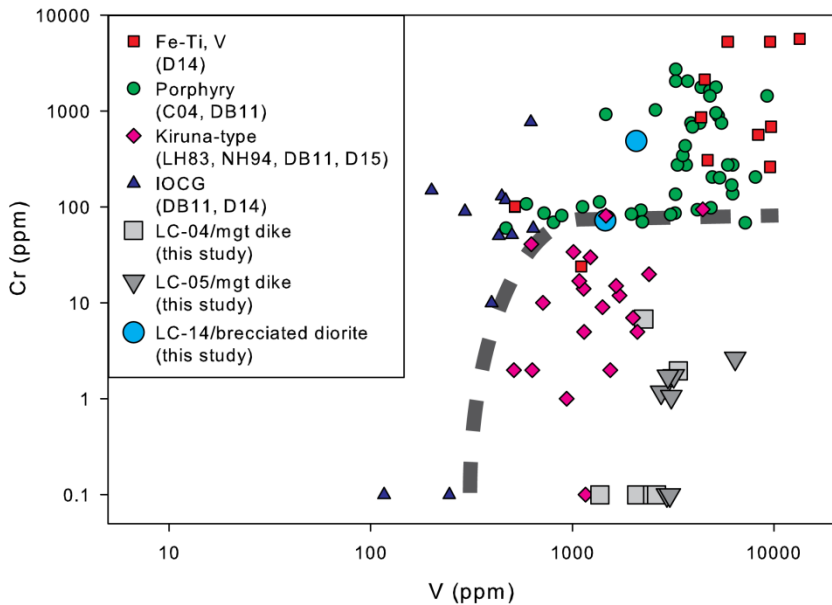
Figure 3.11: Kiruna-type deposits can be distinguished from other deposits such as magmatic Fe-Ti-V-, porphyry- and IOCG-type deposits by comparing V and Cr contents in the magnetite. Magnetites of Kiruna-type deposits have distinctly lower Cr, but higher V concentration than IOCG deposits. Higher V concentrations in magnetite indicate in general a more pronounced magmatic source. Literature data are LH83: Loberg and Horndahl (1983), NH94: Nyström and Henriquez (1994), C04: Core (2004), DB11: Dupuis and Beaudoin (2011), D14: Dare et al. (2014) and D15: Dare et al. 2015.

The elevated V concentrations are caused by magnetite crystallization at magmatic high temperatures in contrast to magnetite from IOCG deposits that are formed at relatively lower temperatures. Chromium may be depleted

in magnetite from Kiruna-type deposits, either due to fractionation of augite based on its high K_D value (partition coefficient between mineral/melt) for Cr or more likely due to the high mobility of Cr^{6+} (James, 2003) in fluids. These fluids could have potentially transported Cr out of the (oxidizing) iron oxide-ore forming system into the surrounding rock, where it partitions into hydrothermal magnetite due to a possible reduction from the incompatible and highly mobile Cr^{6+} (James, 2003) into the highly magnetite compatible Cr^{3+}, which is in agreement with the relatively high Cr concentration in magnetite from the brecciated diorite intrusion adjacent to the Los Colorados dikes (Fig. 3.11). This is consistent with the iron province in Missouri, where high V concentrations (>1000 ppm) and almost no Cr (~2 ppm) were detected in the magnetite of IOA deposits (Pea Ridge, Iron Mountain, Pilot Knob) in contrast to the brecciated IOCG deposit Boss Bixby in the same province (Cr: 26 ppm; V: 730 ppm), which possibly overlays a massive magnetite deposit (IOA) below (Kisvarsanyi and Proctor, 1967; Seeger, 2003; Nold et al. 2014).

3.6.3 A combined igneous and magmatic-hydrothermal model for Kiruna-type IOA deposits

The sum of all presented data agrees with the model of Knipping et al. (2015), which accounts for the following observations: 1) the chemistry of Los Colorados magnetite cores have trace element abundances most similar to igneous magnetite (Type 1; Fig. 3.4); i.e., crystallization from a silicate melt (Fig. 3.4 and 3.8); 2) magnetite grains ubiquitously have rims (Types 2 and 3; Fig. 3.4) that are chemically consistent with magnetite precipitated from, or in equilibrium with, a magmatic-hydrothermal fluid cooling from high to low temperature(Fig. 3.4 and 3.8); 3) halite-saturated inclusions trapped in magnetite (Fig. 3.6); and 4) massive magnetite ore bodies without associated

sodic and potassic alteration minerals (Table 3.2). Here, we briefly summarize the model of Knipping et al. (2015).

In hydrous, oxidized arc-magmas, magnetite is often the liquidus phase at 200 MPa (Martel et al., 1999). This magmatic magnetite is enriched in elements such as Ti, V, Mn, Al and Ga, consistent with Type 1 magnetite cores. Due to surface energy reduction, exsolving magmatic-hydrothermal fluid prefers to nucleate bubbles initially on mineral surfaces, and thus crystallizing magnetite promotes water supersaturation (Hurwitz and Navon, 1994). Owing to larger wetting angles (Ψ) between fluid and oxides (Ψ=45-50°) compared to fluid and silicate minerals (Ψ=5-25°) (Gualda and Ghiorso, 2007) the attachment of bubbles is energetically favored on magnetite microlites (Hurwitz et al. 1994; Gardner and Denis, 2004; Cluzel et al. 2008), which generates magnetite-bubble pairs (Fig. 3.12a). The total density of these pairs is less than the surrounding melt, consistent with experimental observations of sulfide melt ascending through less dense silicate melt owing to fluid bubble attachment (Mungall et al., 2015). This positive buoyancy allows magnetite-bubble pairs, as calculated by Knipping et al. (2015), to ascend through the magma chamber (Fig. 3.12b). During ascent, the magnetite-bubble pairs are able to "sweep up" other magnetite microlites becoming a rising suspension rich in primary magnetite (Fig. 3.12c), similar to explanations in Edmonds et al. (2014) who invoked magnetite flotation by fluid bubbles to explain magnetite-rich mafic enclaves in arc andesite. Since H_2O saturation is followed by significant partitioning of Cl into the fluid phase (Balcone-Boissard et al., 2008), the exsolving fluid will become Cl-rich consistent with the halite saturated inclusions in LC magnetite (Fig. 3.6), which in turn has the ability to scavenge from silicate melt up to several wt% Fe as $FeCl_2$ (Simon et al., 2004; Bell and Simon, 2011) (Fig. 3.12c). The originally

55

igneous magnetite can continue to grow by sourcing Fe from the magnetite-fluid suspension, and this magnetite is expected to have a chemical signature consistent with high-temperature magmatic-hydrothermal magnetite (Type 2 magnetite) similar to magnetite from porphyry fluids. In fact, the lack of potassic and sodic alteration that is common in magmatic-hydrothermal ore deposits (Barton, 2014) can also be explained at Los Colorados by magnetite growth from a highly saline brine in the silicate magma instead from a low salinity vapor. It has been shown experimentally that with decompression the solubilities of Na and K increase in the brine phase at 800 °C (145-140 MPa: Na = 5.9 ± 1.8 wt% 21 and K = 11.0 ± 1.0 wt%; 110 MPa: Na = 14.0 ± 0.8 wt% and K = 15.0 ± 1.6 wt%) while iron solubility slightly decreases (145 MPa: Fe = 7.2 ± 1.6 wt%; 110 MPa Fe = 6.4 ± 0.6 wt%) (Simon et al., 2004). Consequently, Fe precipitation from brine would be possible in the pressure range of the estimated paleo depth of Los Colorados (4-3 km ~ 145-110 MPa) without the formation of simultaneous K- and Na-rich minerals during adiabatic decompression, in contrast to low salinity vapor. The tectonic stress change in the back-arc setting, which was responsible for generating the Atacama Fault System (AFS) during the late Lower Cretaceous, may have created hydraulic fractures that served as conduits for the ascent of the less dense magnetite-bubble suspensions into the overlying crust (Hautman et al., 2013) compared to the remaining magma. The fast decompression explains the efficient transport and segregation of magnetite-bubble suspension from the magma as shown for chromite segregation by decompression experiments (Matveev and Ballhaus, 2002). Eventually massive magnetite is able to precipitate as dikes in the late Lower Cretaceous (Fig. 3.12d) instead of a less efficient segregation such as magnetite-rich enclaves observed in andesite of the Soufrière Hills Volcano (Edmonds et al., 2014). According to model calculations of Knipping et al. (2015) a magma chamber size with 50 km^3

would be sufficient to supply enough water and iron to create a deposit such as Los Colorados (~350 Mt Fe) even with a depositional efficiency of only, 50 % iron. This volume is in the range of typical arc volcano magma chambers (~4-60 km^3; Marsh, 1989) and similar to estimated caldera sizes of extrusive IOA deposits (~30 km^2; El Laco, Chile, Oyarzún and Frutos, 1984; Nyström and Henriquez, 1994).
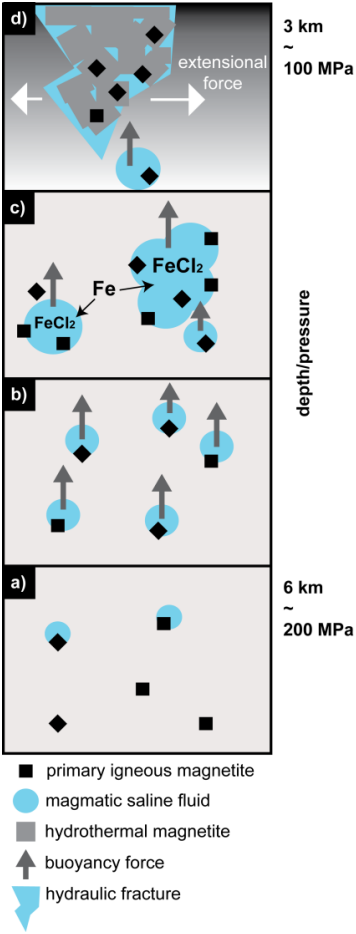
Figure 3.12: Novel magmatic-hydrothermal model modified after Knipping et al. (2015) including (a) magnetite saturation and preferred bubble nucleation on magnetite microlites,

57

(10s to < 200 μm) (b) ascension of bubble-magnetite pairs due to positive F[Buoyancy], (c) further ascent, growth, coalescence and accumulation of primary magnetite as well as scavenging of Fe from the surrounding melt due to the high salinity of the fluid, (d) formation of hydraulic fractures (due to tectonic stress changes) allowing fast efficient segregation of magnetite-rich fluid, and the eventual growth of hydrothermal magnetite (gray overgrowth on primary magnetite microlites) during progressive cooling. The color change in d implies increasing crystallinity.

3.6.4 Comparison to podiform chromite deposits

An oxide flotation and separation model based on experimental results was proposed by Matveev and Ballhaus (2002) for the origin of podiform chromite deposits. These authors demonstrated that decompression-induced volatile saturation results in the formation of a chromite-fluid suspension that allows for efficient segregation of chromite from a parental basaltic melt within a short time period (15 min). Owing to coalescence and fluid channelization, abundant chromite was able to be physically separated and concentrated in massive chromite cumulates that detached from the melt. Further, chromite-hosted inclusions from podiform chromite deposits are very similar to magnetite-hosted inclusions detected in the current study in terms of polycrystallinity, mineral assemblage (high Mg-actinolite, low Al-diopside, chlorite, Ca-Ti-silicates), as well as the additional presence of saline fluid inclusions (Melcher et al., 1997). These peculiar and complex inclusions were explained by reactions between anhydrous silicate minerals and volatile-rich melt that were simultaneously entrapped in oxide-hosted inclusions, which evolved as a closed system. Hence, in this study the presence or absence of clinopyroxene in the magnetite hosted phase could explain whether or not Ca can be found in the re-homogenized phase. Post-entrapment reactions resulted in mineral phases that are actually unstable at the formation temperature of the inclusions. Thus, chlorite can be formed at later stages in inclusions of magmatic oxides, which could also elucidate the presence of the unspecified Mg-Al-Si phase observed in inclusions of this study (Fig. 3.7). Further,

Matveev and Ballhaus (2002) described the polycrystalline silicate inclusions in chromite as recrystallized solute, while the saline fluid inclusions were interpreted as the solvent of a former magmatic fluid phase floating the oxides, consistent with our model.

3.6.5 Genetic link between Kiruna-type IOA and IOCG deposits?

The oscillatory zoning of magnetite in the brecciated diorite as well as the lower concentrations of magnetite-compatible elements (e.g., Ti, V, Ga), and the higher concentrations of magnetite-incompatible and fluid-mobile elements (e.g., Si, Ca, Y, Pb, Cu) (Fig. 3.9) indicate lower hydrothermal formation temperatures compared to the massive magnetite dikes. We suggest that after the formation of the IOA deposit, which is dominated by magnetite (>90 modal %), the fluid penetrates into the host rock, where it brecciate and alters also the adjacent diorite intrusion. These fluids maintain elevated concentrations of Cr (Fig. 3.11) and metals such as the REE, Fe, Cu and Au that it scavenged originallyfrom the silicate melt due to the magmatic temperatures and high salinity of the fluid (Reed et al., 2000; Simon et al., 2004, 2005, 2006; Zajacz et al., 2012; Frank et al., 2011; Migdisov et al., 2014; Hurtig and Williams-Jones, 2014). The high Cl content of the fluid facilitates metal-chloride complexes and allows it to transport these metals, some of which exhibit retrograde solubility, i.e. increasing solubility with decreasing temperature(Eugster and Chou, 1979; Migdisov et al., 2014; Hurtig and Williams-Jones, 2014), to cooler parts of the crust either laterally or vertically, where precipitation of oxides and sulfides can occur by either cooling alone (T<400 °C; Hezarkhani et al., 1999; Ulrich et al., 2001) or possibly by mixing with cooler meteoric fluid, as discussed in Barton (2014). This possible process would support the idea of IOA deposits being the deep Cu(-Au)-barren root of IOCG deposits (Naslund et al., 2002; Sillitoe, 2003; Barton, 2014; Nold et al.

2014). Magmatic saline fluids that retain certain elements after deposition of massive magnetite could also explain the only minor amount of apatite and the depleted REE pattern of the massive magnetite ore at Los Colorados (Fig. 3.2). The solubility of apatite and REE in the fluid is enhanced by the high Cl concentration (Antignano and Manning, 2008; Reed et al. 2000) and mixing with low temperature surface fluids would result in precipitation of REE-rich apatite at a later stage than magnetite deposition. Fluids transporting REE into the brecciated diorite are also consistent with the higher REE values (La, Ce, Sm and Yb) in the hydrothermal magnetite from the brecciated diorite when compared to the magnetite samples of the massive magnetite dike (Table 3.3), especially when considering that magnetite is usually highly incompatible in magnetite. This process could cause the parallel but elevated bulk REE pattern in the brecciated diorite compared to the magnetite dikes (Fig. 3.2) similar to observations of REE distribution in the hydrous altered host rock surrounding the massive magnetite ore at the Kiruna deposit (Sweden) (Jonsson et al., 2013).

3.7. CONCLUSION

We report magnetite trace element data from the unaltered Los Colorados (Chile) iron oxide-apatite (IOA) deposit to investigate the controversial origin of Kiruna-type IOA deposits in the Chilean Iron Belt (CIB). Bulk rock and high-resolution analyses by EPMA and LA-ICP-MS were conducted on magnetite from the massive magnetite dikes and from an adjacent brecciateddiorite intrusion. Magnetite grains from the magnetite ore have cores enriched in Ti, Al, Mn and Mg, typical for crystallization from a silicate melt, whereas rims are relatively depleted in these elements. Thus, the involvement of primary igneous magnetite is required for the initial stage of ore formation. Our data are consistent with the novel magmatic-hydrothermal

model proposed by Knipping et al. (2015) in which igneous magnetite is separated as fluid-magnetite aggregates from the silicate magma and become a rising suspension, based on its lower density relative to the surrounding magma. The coexisting fluid phase is likely a high salinity brine that is able to transport up to several wt% Fe in the fluid responsible for the later precipitation of massive magnetite with a magmatic-hydrothermal signature surrounding the igneous cores. The Fe-rich suspension efficiently ascends through hydraulic fractures during tectonic stress changes in the Cretaceous along the Atacama Fault System (AFS) resulting in dike shaped Fe-deposits at Los Colorados and probably also at other locations in the CIB that are associated to the AFS. Measurements of magnetite from the brecciated diorite intrusion reveal lower temperature hydrothermal processes consistent with IOCG deposits that are of purely hydrothermal origin and are often observed in close relationship to IOA deposits. Thus, an IOCG deposit lateral or stratigraphically above IOA systems is not excluded and estimations of Knipping et al. (2015) indicate that the underlying intrusion can provide sufficient Fe for both types of deposits. This study also provides a new geochemical diagram that discriminates magnetite of Kiruna-type deposits from porphyry, IOCG and Fe-Ti-V/P deposits. Magnetites from Kiruna-type deposits are expected to have low Cr (< 100 ppm) and high V (> 500 ppm) concentrations. However, more investigations and experimental studies are needed to understand the complex interplay of processes which lead to the formation of massive magnetite deposits in the Chilean Iron Belt and worldwide.

Table 3.1: Results for 70 elements of 15 bulk rock measurements from the magnetite dike (04-XX and 05-XX) and from the diorite intrusion (14-XX). Major elements were measured by ICP-OES and trace elements by ICP-MS.

Element	Unit	D.L.	04- 38.8	04- 66.7	04- 104.4	04- 125.3	04- 129.5	04- 143.1	05- 32	05- 52.2	05- 82.6	05- 106	05- 150	14- 43	14- 98	14- 148.5	14- 171.15
SiO_2	%	0.01	2.13	1.25	9.70	15.21	59.88	52.65	26.64	12.87	2.38	1.40	28.72	64.36	38.46	61.32	53.72
Al_2O_3	%	0.01	0.55	0.10	0.48	2.49	14.65	16.33	5.25	0.39	0.41	0.49	8.38	14.55	12.06	15.92	15.91
Fe_2O_3	%	0.01	97.62	97.55	81.85	73.74	6.54	9.79	51.68	83.78	95.83	98.97	44.40	2.99	26.19	4.17	7.60
MnO	%	0.001	0.082	0.085	0.202	0.228	0.272	0.145	0.297	0.197	0.233	0.220	0.513	0.100	0.185	0.157	0.374
MgO	%	0.01	0.95	0.82	3.83	4.92	4.04	7.31	4.31	1.72	1.30	0.92	5.99	3.48	12.77	4.43	6.87
CaO	%	0.01	0.86	0.79	2.68	3.06	4.39	3.38	7.67	1.65	1.33	0.63	6.71	3.65	1.62	3.78	5.58
Na_2O	%	0.01	0.02	0.02	0.09	0.17	7.52	2.91	1.22	0.06	0.03	0.02	0.86	8.02	0.63	7.37	4.72
K_2O	%	0.01	b.d.	b.d.	0.04	0.49	0.15	2.37	0.93	0.01	b.d.	b.d.	1.70	0.12	3.60	0.82	1.29
TiO_2	%	0.001	0.243	0.032	0.793	0.382	0.514	0.937	0.441	0.194	0.305	0.237	0.418	0.688	0.661	0.815	0.869
P_2O_5	%	0.01	0.02	0.30	b.d.	0.02	0.03	0.13	0.01	0.05	0.27	b.d.	b.d.	0.03	0.09	0.16	0.26
LOI	%		0.00	0.00	0.00	0.00	1.87	2.90	0.00	0.00	0.00	0.00	0.47	2.02	3.03	1.20	1.95
Total	%	0.01	100.60	98.18	98.77	99.56	99.84	98.86	98.10	99.07	99.55	99.96	98.16	100.00	99.28	100.10	99.13
Sc	ppm	1	2	b.d.	4	7	18	27	9	3	2	1	10	18	20	21	26
Be	ppm	1	b.d.	b.d.	b.d.	b.d.	1	1	b.d.	b.d.	b.d.	b.d.	b.d.	b.d.	b.d.	1	1
V	ppm	5	2441	1559	2034	2195	120	231	1603	2400	2924	3011	2590	80	371	148	196
Cr	ppm	20	b.d.	b.d.	b.d.	b.d.	b.d.	20	b.d.	b.d.	b.d.	b.d.	b.d.	b.d.	b.d.	b.d.	b.d.
Co	ppm	1	51	44	33	34	11	6	20	38	48	46	24	12	12	6	14
Ni	ppm	20	50	50	50	40	b.d.	b.d.	30	50	60	60	30	b.d.	30	10	b.d.
Cu	ppm	10	20	20	30	50	b.d.	50	b.d.	b.d.	b.d.	60	30	b.d.	b.d.	10	b.d.
Zn	ppm	30	b.d.	b.d.	140	100	40	70	130	100	130	120	120	b.d.	110	b.d.	70
Ga	ppm	1	63	46	50	46	20	20	35	51	66	58	36	18	24	17	16
Ge	ppm	0.5	2.0	2.0	3.4	2.7	2.2	1.9	2.6	2.4	2.1	1.7	2.9	1.6	2.2	1.8	1.8
As	ppm	5	8	6	7	b.d.	6	23	8	7	7	b.d.	8	7	17	7	11
Rb	ppm	1	b.d.	b.d.	2	8	2	85	24	b.d.	b.d.	b.d.	54	b.d.	144	23	47
Sr	ppm	2	5	4	7	7	60	198	69	3	4	2	80	18	108	75	205
Y	ppm	0.5	3.5	4.5	28.4	16.1	60.8	29.0	17.4	5.4	2.8	1.7	17.2	76.5	17.1	30.9	26.8
Zr	ppm	1	2	b.d.	9	50	152	104	86	6	3	3	118	150	55	212	97
Nb	ppm	0.2	1.9	1.3	1.7	1.6	3.6	4.4	1.4	2.7	2.4	1.9	1.9	6.6	3.1	5.9	4.3
Mo	ppm	2	b.d.	b.d.	2	b.d.	b.d.	b.d.	b.d.	b.d.	b.d.	b.d.	b.d.	b.d.	b.d.	b.d.	b.d.
Ag	ppm	0.5	1.3	0.8	1.1	2.0	3.2	2.9	0.9	2.8	1.8	1.3	3.2	2.9	1.8	3.0	1.4
Sn	ppm	1	2	2	3	2	2	3	b.d.	2	2	1	b.d.	3	2	2	2
Sb	ppm	0.2	1.7	1.0	1.4	1.4	2.2	2.3	1.5	2.8	1.5	1.1	2.1	2.8	2.3	1.6	1.8
Cs	ppm	0.1	b.d.	b.d.	0.2	0.1	b.d.	3.3	0.4	b.d.	b.d.	b.d.	2.6	b.d.	8.9	0.3	2.0
Ba	ppm	3	8	9	13	92	9	239	95	7	8	9	181	b.d.	310	91	166

Table continues

62

Element	Unit	D.L.	04-38.8	04-66.7	04-104.4	04-125.3	04-129.5	04-143.1	05-32	05-52.2	05-82.6	05-106	05-150	14-43	14-98	14-148.5	14-171.15
La	ppm	0.05	1.8	1.9	3.4	4.6	11.4	11.4	2.7	0.4	0.3	b.d.	1.9	16.3	4.3	13.4	12.5
Ce	ppm	0.05	3.8	5.9	7.6	9.8	32.3	25.3	7.9	1.6	1.1	0.2	3.4	64.7	11.4	39.1	26.4
Pr	ppm	0.01	0.44	0.85	1.23	1.53	5.45	3.74	1.26	0.30	0.19	0.04	0.49	11.40	1.79	5.37	3.28
Nd	ppm	0.05	1.8	3.9	6.3	7.6	26.6	17.3	6.5	1.6	1.0	0.3	2.6	52.9	9.1	22.1	14.3
Sm	ppm	0.01	0.41	0.86	2.43	2.14	7.42	4.46	2.02	0.48	0.25	0.12	1.03	12.70	2.34	5.07	3.49
Eu	ppm	0.005	0.029	0.034	0.207	0.397	1.140	1.090	0.267	0.062	0.030	0.012	0.117	1.920	0.367	1.500	0.842
Gd	ppm	0.01	0.46	0.85	3.34	2.66	8.28	4.79	2.37	0.73	0.34	0.19	1.61	12.90	2.64	5.17	3.77
Tb	ppm	0.01	0.09	0.13	0.66	0.46	1.56	0.87	0.45	0.14	0.06	0.04	0.34	2.21	0.47	0.89	0.68
Dy	ppm	0.01	0.57	0.76	4.26	2.76	9.91	5.15	2.85	0.82	0.39	0.28	2.39	13.30	2.88	5.63	4.21
Ho	ppm	0.01	0.12	0.15	0.93	0.58	2.12	1.01	0.60	0.18	0.08	0.06	0.56	2.71	0.62	1.17	0.89
Er	ppm	0.01	0.39	0.42	3.08	1.74	6.36	3.09	1.73	0.58	0.24	0.17	1.81	8.17	1.92	3.41	2.88
Tm	ppm	0.005	0.07	0.07	0.55	0.26	0.98	0.49	0.27	0.10	0.04	0.03	0.33	1.24	0.32	0.53	0.50
Yb	ppm	0.01	0.51	0.46	4.10	1.81	6.07	3.11	1.95	0.80	0.30	0.20	2.29	7.55	2.20	3.68	3.45
Lu	ppm	0.002	0.080	0.071	0.738	0.281	0.841	0.460	0.315	0.134	0.047	0.042	0.346	1.030	0.324	0.539	0.518
Hf	ppm	0.1	b.d.	b.d.	b.d.	1.4	4.1	2.9	1.9	0.1	b.d.	b.d.	3.2	4.2	1.5	5.1	2.3
Ta	ppm	0.01	0.25	0.14	0.20	0.16	0.52	0.34	0.02	0.18	0.20	0.19	0.17	0.56	0.24	0.50	0.46
W	ppm	0.5	3.1	2.0	2.6	2.4	4.7	13.8	1.0	3.5	3.1	2.2	3.0	2.8	2.5	2.1	1.3
Tl	ppm	0.05	b.d.	b.d.	b.d.	b.d.	b.d.	0.14	0.60	0.05	b.d.	b.d.	0.08	b.d.	0.24	b.d.	0.09
Bi	ppm	0.1	0.1	b.d.	b.d.	b.d.	0.1	0.14	0.1	b.d.	b.d.	b.d.	b.d.	b.d.	b.d.	b.d.	b.d.
Th	ppm	0.05	1.75	6.72	3.49	5.59	4.38	2.08	2.49	0.77	0.43	1.16	2.82	7.70	1.48	5.97	3.38
U	ppm	0.01	0.37	0.37	0.74	0.43	1.44	1.36	0.28	0.16	0.07	0.11	0.35	1.61	1.25	2.24	0.85
Cd	ppm	0.5	1.7	1.8	1.7	0.9	b.d.	b.d.	0.8	1.5	2.3	2.4	0.7	b.d.	0.5	b.d.	b.d.
Cu	ppm	1	11	12	23	51	1	55	6	8	8	7	4	2	3	13	9
Ni	ppm	1	48	47	38	36	8	14	29	44	50	54	24	9	26	9	21
Zn	ppm	1	37	35	125	82	38	70	106	92	114	108	100	18	88	30	69
S	%	0.001	0.158	0.014	0.024	0.029	0.054	0.023	0.027	0.007	0.012	0.005	0.100	0.109	0.029	0.045	0.143
Ag	ppm	0.3	0.6	0.8	0.5	0.4	b.d.	b.d.	0.3	1.2	0.6	1.0	b.d.	b.d.	b.d.	b.d.	b.d.
Pb	ppm	5	b.d.	6	b.d.	5	b.d.	b.d.	7	7	b.d.	b.d.	7	b.d.	b.d.	b.d.	b.d.
Au	ppb	2	b.d.	211	18	51	b.d.	48	34	730	24	446	14	b.d.	b.d.	45	b.d.
As	ppm	0.5	9.6	4.7	3.4	3.0	6.3	20.2	9.5	6.3	5.2	b.d.	5.7	6.3	14.2	5.2	11.0
Br	ppm	0.5	3.6	4.3	5.5	b.d.	b.d.	b.d.	b.d.	3.2	3.3	3.6	b.d.	b.d.	b.d.	b.d.	b.d.
Cr	ppm	5	12	18	b.d.	19	13	25	12	21	b.d.	6	13	b.d.	26	16	19
Sc	ppm	0.1	1.0	0.6	3.6	6.0	16.0	24.3	8.3	2.8	1.3	0.8	9.3	16.4	18.5	19.2	24.0
Sb	ppm	0.2	1.1	0.4	0.6	0.4	0.8	1.3	1.9	1.8	0.2	0.3	0.8	1.6	1.5	0.6	1.1

D.L. detection limit.

b.d. below detection limit.

Pb (D.L. 5ppm), In (D.L. 0.1 ppm), Ir (D.L. 5ppb) and Se (D.L. 3ppm) were always below detection limit.

Table 3.2: EPMA conditions at University of Michigan and University of Western Australia.

University of Michigan: Cameca SX-100
20 kV, 30 nA, focused

Element/Line	Crystal	Standard	Counting time (s)	MDL (wt%)
Mg/Kα	TAP	geikielite	100	0.01
Al/Kα	TAP	zoisite	100	0.01
Si/Kα	LTAP	wollastonite	100	0.01
Ca/Kα	PET	wollastonite	100	0.01
Ti /Kα	PET	ilmenite	120	0.01
V /Kα	LLIF	V_2O_5	120	0.01
Mn/Kα	LLIF	rhodondite	100	0.01
Fe/Kα	LLIF	magnetite	20	0.02

University of Western Australia: Jeol JXA8200
20 kV, 30 nA, focused

Element/Line	Crystal	Standard	Counting time (s)	MDL (wt%)
Mg/Kα	TAP	pyrope	60	0.01
Al/Kα	TAP	spessartine	60	0.01
Si/Kα	TAP	spessartine	60	0.01
Ca/Kα	PETJ	wollastonite	60	0.01
Ti /Kv	PETJ	rutile	60	0.01
V /Kα	LIFH	V-metal	60	0.01
Mn/Kα	LIFH	spessartine	60	0.01
Fe/Kα	LIF	magnetite	20	0.02

MDL mean detection limit based on counting statistics.

Table 3.3: Sector field LA-ICP-MS results averaged for 1-8 measured profiles (# of profiles) per magnetite sample.

sample	04-38.8	04-66.7	04-99.5b	04-104.4	04-125.3	04-129.5	05-32	05-52.2	05-82.6	05-106	05-126	05-129.1	05-150	14-98*	14-136**
# of profiles	8	3	2	4	3	5	4	4	6	4	3	3	2	4	1
unit	µg/g	µg/g	µg/g	µg/g	µg/g	µg/g	µg/g	µg/g	µg/g	µg/g	µg/g	µg/g	µg/g	µg/g	µg/g
Na	328 (286)	<18	269	324 (168)	108	<25	295 (255)	204 (142)	175 (90)	85 (59)	38	116 (125)	27	354 (313)	84
Mg	5819 (3012)	4308 (1354)	5738 (384)	4805 (727)	1384 (294)	937 (1007)	2294 (472)	3481 (955)	3934 (286)	3104 (979)	2770 (853)	3006 (432)	955 (424)	5615 (4857)	348
Al	3801 (1440)	603 (79)	2940 (182)	2306 (421)	3195 (485)	2604 (1670)	4836 (798)	2052 (618)	2436 (156)	2969 (351)	1902 (89)	2491 (352)	5238 (163)	2103 (218)	550
Si	7028 (2842)	3746 (1389)	7061 (2272)	5391 (681)	2441 (454)	2886 (923)	5668 (1428)	4827 (1827)	3362 (635)	3667 (784)	2906 (986)	2860 (651)	3091 (1335)	17487 (9952)	<2024
P	153 (260)	58 (16)	31	44 (11)	44	40	56 (4)	45 (11)	55 (22)	45 (9)	48	50 (11)	47 (8)	52	<63
K	424 (226)	103 (2)	549 (316)	296 (172)	105 (134)	34 (18)	481 (336)	194 (170)	200 (82)	172 (69)	52 (20)	110 (222)	50 (49)	1024 (565)	42
Ca	1508 (1062)	389 (334)	1176 (568)	479 (186)	<179	990	1265 (797)	565 (222)	394 (215)	419 (248)	281	211 (33)	228	816 (178)	<504
Sc	1.2 (0.5)	0.4 (0.1)	0.6 (0.1)	1.0 (1.1)	0.4 (0.1)	0.3	0.5 (0.1)	0.7 (0.1)	0.6 (0.2)	0.3 (0.0)	0.3 (0.1)	0.4 (0.1)	0.9 (0.2)	6.7 (2.1)	<1.9
Ti	1538 (254)	125 (15)	2070 (30)	5633 (623)	3383 (344)	3946 (858)	5241 (1337)	1549 (499)	1929 (317)	1275 (230)	752 (109)	992 (78)	7456 (84)	2329 (82)	428
V	2088 (254)	1368 (247)	2260 (21)	2509 (176)	2620 (93)	3287 (215)	3183 (19)	2755 (316)	2977 (164)	3068 (118)	2949 (85)	2995 (183)	6435 (926)	1455 (13)	2073
Cr	<13	<13	6.8 (1.4)	<13	<12	3.1 (1.7)	17	12	17	1.1	<13	<11	3	72 (129)	486
Mn	648 (159)	572 (226)	701 (18)	1352 (154)	1165 (105)	1201 (282)	2383 (282)	1482 (235)	1541 (113)	1676 (113)	1113 (31)	1217 (191)	1470 (382)	386 (25)	219
Co	44 (2)	51 (2)	40 (4)	40 (3)	39 (2)	34 (8)	37 (1)	48 (8)	52 (2)	47 (5)	46 (2)	47 (3)	16 (0)	11 (1)	14
Ni	46 (2)	50 (2)	32 (1)	43 (12)	48 (6)	47 (7)	47 (6)	45 (4)	50 (11)	51 (5)	40 (5)	48 (5)	54 (5)	30 (8)	152
Cu	4.9 (2.9)	6.9 (4.2)	1.0 (0.5)	6.7 (5.2)	1.1 (0.8)	1.1 (0.6)	2.0 (0.8)	2.5 (1.3)	2.9 (1.6)	2.3 (1.3)	1.4 (1.0)	2.0 (1.8)	1.5	12 (5)	b.d.
Zn	74 (21)	60 (40)	61 (14)	87 (12)	118 (20)	102 (45)	245 (32)	136 (46)	189 (28)	193 (37)	119 (12)	134 (31)	313 (106)	43 (24)	16
Ga	65 (8)	50 (4)	62 (0.5)	59 (4)	58 (2)	56 (11)	66 (5)	58 (4)	66 (1.8)	56 (2)	62 (3)	63 (3)	73 (1.3)	31 (2)	32
Ge	1.3 (0.2)	1.3 (0.1)	1.4 (0.3)	1.5 (0.1)	0.9 (0.0)	0.8 (0.2)	1.0 (0.1)	1.2 (0.3)	1.2 (0.2)	1.0 (0.1)	0.9 (0.2)	0.9 (0.4)	0.9 (0.2)	<1.5	<2.0
Rb	2.2 (1.3)	0.5 (0.1)	0.9 (0.1)	1.5 (0.9)	1.2 (1.4)	<0.3	1.9 (1.4)	1.2 (1.1)	1.6 (1.3)	1.0 (0.5)	0.6 (0.4)	0.9 (0.9)	0.3	6.3 (4.0)	0.2
Sr	4.7 (1.9)	1.4 (1.2)	2.6 (1.6)	2.7 (1.6)	1.3 (1.6)	0.5 (0.4)	5.5 (3.2)	2.5 (1.3)	3.2 (2.1)	2.3 (0.6)	1.5 (0.6)	1.2 (1.4)	0.4 (0.4)	5.0 (2.5)	0.6
Y	5.5 (4.3)	0.5 (0.4)	2.8 (2.0)	3.2 (2.4)	0.1 (0.0)	0.7 (1.0)	1.3 (0.9)	1.0 (0.4)	0.2 (0.1)	0.2 (0.1)	0.2 (0.2)	0.1 (0.1)	0.1	1.9 (1.4)	1.8
Zr	0.6 (0.2)	0.2 (0.1)	0.7 (0.4)	242 (484)	0.1 (0.0)	0.1	0.6 (0.5)	0.6 (0.3)	0.6 (0.1)	0.6 (0.2)	0.3 (0.2)	0.5 (0.3)	0.3 (0.2)	0.4 (0.0)	<0.3
Nb	0.6 (0.3)	0.6 (0.5)	0.2 (0.1)	0.4 (0.1)	0.1 (0.0)	0.0	0.2 (0.2)	0.2 (0.1)	0.2 (0.1)	0.2 (0.0)	0.1 (0.0)	0.1 (0.0)	0.1 (0.0)	1.2 (1.0)	0.5
Mo	0.1 (0.0)	0.1 (0.0)	0.2	0.1 (0.0)	<0.1	<0.2	0.1 (0.0)	0.1	0.1 (0.1)	0.1 (0.0)	0.2	0.1	<0.3	<0.6	9.2
Ag	<0.1	<0.1	<0.1	0.1	<0.1	<0.1	<0.2	<0.2	<0.2	<0.1	<0.1	<0.1	<0.2	<0.5	<0.9
Cd	0.01 (0.0)	<0.2	<0.2	0.1	<0.2	<0.3	0.1	0.1	0.1 (0.1)	0.1 (0.1)	<0.2	<0.1	<0.2	0.1	<2.2
Sn	3.0 (0.9)	3.4 (0.8)	2.3 (0.0)	2.6 (0.2)	1.6 (0.3)	1.6 (0.9)	0.9 (0.2)	1.5 (0.3)	1.3 (0.4)	1.4 (0.3)	0.8 (0.1)	1.0 (0.1)	0.9 (0.4)	1.9 (0.9)	<2.0
Sb	0.4 (0.2)	0.3 (0.0)	0.2 (0.0)	0.2 (0.1)	<0.12	0.2	0.6 (0.4)	0.3 (0.2)	0.4 (0.1)	0.4 (0.1)	<0.1	0.1 (0.0)	0.1 (0.0)	0.9 (0.2)	<1.1
Ba	15 (7)	2.4 (1.6)	8.2 (5.3)	8.4 (6.4)	3.8 (4.1)	1.7 (0.8)	13 (7)	6.9 (5.3)	7.2 (3.0)	7.4 (2.7)	2.8 (1.6)	4.2 (5.4)	1.1	26 (10)	1.2
La	3.6 (3.2)	0.3 (0.3)	1.2 (1.0)	0.9 (0.7)	0.1 (0.0)	0.1	0.6 (0.7)	0.5 (0.1)	0.3 (0.3)	0.2 (0.0)	0.2 (0.1)	0.2 (0.2)	0.04	3.0 (1.6)	10.3
Ce	11 (8)	0.9 (0.7)	3.5 (2.4)	2.6 (2.2)	0.1 (0.1)	0.1 (0.0)	1.5 (2.0)	1.2 (0.3)	0.5 (0.4)	0.4 (0.1)	0.5 (0.5)	0.2 (0.2)	0.1	7.6 (4.1)	22.9
Sm	1.4 (1.0)	0.1 (0.1)	0.5 (0.3)	0.4 (0.3)	<0.08	0.1	0.4 (0.3)	0.2 (0.1)	0.0 (0.0)	0.0 (0.0)	<0.09	<0.07	<0.06	0.9 (0.4)	1.8
Yb	0.5 (0.4)	0.1 (0.0)	0.4 (0.2)	0.7 (0.8)	0.02	0.2 (0.2)	0.2 (0.0)	0.2 (0.1)	0.1 (0.0)	0.1 (0.0)	0.1	0.01 (0.03)	0.03	0.7 (0.4)	<1.72
Hf	0.04 (0.02)	<0.04	<0.04	0.76 (1.05)	0.02 (0.00)	<0.05	0.03 (0.01)	0.03	0.02 (0.01)	0.03 (0.01)	0.02	0.02 (0.00)	<0.06	<0.43	0.2
Tl	0.03 (0.0)	0.01 (0.0)	0.03	0.03 (0.01)	0.01	0.01 (0.01)	0.03 (0.02)	0.02 (0.0)	0.02 (0.01)	0.02 (0.00)	0.01 (0.01)	0.03	0.0	0.01	0.3
Pb	2.0 (1.1)	0.7 (0.6)	0.6 (0.3)	1.4 (0.9)	0.5 (0.5)	0.2 (0.1)	1.4 (0.8)	0.9 (0.9)	1.3 (0.6)	1.1 (0.3)	0.4 (0.1)	0.6 (0.8)	0.2	3.4 (2.3)	0.5
Th	3.2 (3.6)	0.1 (0.0)	0.4 (0.2)	0.5 (0.3)	0.02 (0.02)	0.04 (0.03)	0.4 (0.2)	0.2 (0.1)	0.2 (0.1)	0.3 (0.1)	0.2 (0.2)	0.1 (0.4)	0.04 (0.02)	0.3 (0.2)	0.6
U	0.3 (0.1)	0.1 (0.1)	0.2 (0.2)	0.9 (1.4)	0.01 (0.0)	0.03 (0.01)	0.1 (0.0)	0.1 (0.0)	0.04 (0.01)	0.1 (0.0)	0.04 (0.04)	0.03 (0.03)	0.02	0.6 (0.3)	<0.23

* three of four measurements were point analysis using the quadrupole ICP-MS, due to sample size. ** based on spot analysis using the quadrupole ICP-MS, due to sample size. Standard deviations are given in parentheses. If no standard deviation is given, value is from one measured transect only (other were below detection limit).

Table 3.4: Variations of element concentration between core and rim for one representative transect per sample

sample		Mg µg/g	Al µg/g	P µg/g	Ti µg/g	V µg/g	Mn µg/g	Ga µg/g	Sr µg/g	Pb µg/g	Cr µg/g	Ni µg/g
04-38.8b	core	3746	2807	<25.78	1508	2623	553	61.2	2.54	0.60	<1.07	41.48
	rim	2672	2444	51.68	1249	2556	517	62.2	2.80	1.38	<1.90	39.67
04-66.7b	core	5862	693	46.63	111	1085	828	54.0	2.56	1.22	<1.56	49.12
	rim	2313	412	104.61	132	1105	671	43.3	0.78	0.12	<3.63	25.80
04-104.4c	core	5798	2773	30.76	6392	2684	1444	60.6	4.47	2.06	<1.04	43.74
	rim	2133	1745	<40.11	2592	2643	746	59.0	0.88	0.27	<1.66	39.21
04-129.3e	core	573	1789	<48.13	3571	3469	1303	58.9	0.12	0.05	<2.15	45.41
	rim	268	1589	<105.42	3030	3457	819	55.9	<0.31	<0.14	<4.99	37.90
05-32d	core	2020	4377	59.54	4494	3169	2452	62.3	2.71	1.44	<1.19	46.30
	rim	536	2183	92.65	2695	3121	1420	55.6	1.24	0.62	<1.92	39.56
05-52.2c	core	3489	2130	36.85	1811	2995	1548	59.6	2.31	0.82	<1.04	43.04
	rim	2065	1667	88.23	1548	2951	1503	57.5	1.74	1.03	3.14	37.44
05-82.6a	core	4266	2476	48.56	2019	3057	1636	68.0	6.76	1.91	<1.09	59.18
	rim	393	1315	60.35	568	3031	1297	59.0	1.00	0.25	<1.84	46.92
05-106d	core	3061	3012	33.74	1274	3146	1732	57.3	2.50	0.90	1.05	53.63
	rim	1021	2389	<47.57	679	3132	1275	51.5	0.87	0.18	<1.99	48.30
05-129.1d	core	3243	2957	60.77	1091	3193	1383	66.3	2.40	0.91	<1.00	48.17
	rim	1917	2186	98.62	1038	3171	1219	63.3	1.37	0.40	<1.75	47.93
05-150d	core	1254	5123	52.05	7396	7089	1740	72.5	0.66	0.24	2.65	57.81
	rim	618	4934	71.64	6325	6987	1681	73.1	0.24	0.09	2.12	50.84

Chapter 4: *In-situ* iron isotope analyses reveal igneous and magmatic-hydrothermal growth of magnetite at the Los Colorados Kiruna-type iron oxide - apatite deposit, Chile.

Jaayke L. Knipping[1, 2, 3], Adrian Fiege[1], Adam C. Simon[3], Martin Oeser[2], Martin Reich[4], Laura D. Bilenker[5]

[1]Department of Earth and Planetary Sciences, American Museum of Natural History, Central Park West at 79th Street, New York, NY 10024-5192 (Present Address)

[2]Institut für Mineralogie, Leibniz Universität Hannover, Callinstraße 3, 30167 Hannover, Germany

[3]Department of Earth and Environmental Sciences, University of Michigan, 1100 North University Ave Ann Arbor, MI 48109-1005, USA.

[4]Department of Geology and Andean Geothermal Center of Excellence (CEGA), FCFM, Universidad de Chile, Plaza Ercilla 803, Santiago, Chile

[5]Pacific Centre for Isotopic and Geochemical Research, Department Earth, Ocean, & Atmospheric Sciences, University of British Columbia, 2020 – 2207 Main Mall, Vancouver, BC Canada V6T 1Z4

ABSTRACT

Iron-oxide apatite (IOA) deposits are mined for iron (Fe) and can also contain economically exploitable amounts of Cu, P, U, Ag, Co and rare earth elements (REE). Recently, it has been proposed based on trace element zonation in magnetite grains from the Los Colorados Kiruna-type IOA deposit, Chile, that ore formation is directly linked to a magmatic source. The model begins with the crystallization of magnetite microlites within an oxidized volatile-rich (H_2O+Cl) andesitic magma reservoir, followed by decompression, nucleation of fluid bubbles on magnetite microlite surfaces, segregation of a

Fe-Cl-rich fluid-magnetite suspension within the magma reservoir, and subsequent ascent of the suspension from the magma chamber via pre-existing structurally enhanced dilatant zones that act as conduits. Emplacement and precipitation of the suspension results in the formation of magnetite grains with core-to-rim features that record a transition from purely igneous to magmatic-hydrothermal conditions within IOA deposits. Here we test this model by using *in situ* femtosecond laser–ablation MC-ICP-MS measurements of Fe isotopes to determine grain-to-grain and intra-grain Fe isotope variations in magnetite grains from the Los Colorados IOA deposit. All *in situ* δ^{56}Fe values (^{56}Fe/^{54}Fe relative to IRMM-14) plot within the magmatic range (0.06 to 0.50 ‰), in agreement with previously published bulk Fe isotope analyses in magnetite from the Los Colorados IOA deposit. Different trace element signatures of these magnetite grains indicate an igneous or magmatic-hydrothermal origin, respectively. Although data partly overlap, the assigned igneous magnetites yield on average higher δ^{56}Fe values (0.24 ± 0.07 ‰; n=33), when compared to magmatic-hydrothermal magnetites (0.15 ± 0.05 ‰; n=26). Some magnetite grains exhibit a distinct core-to-rim trend from higher towards lower δ^{56}Fe signatures. Further, the δ^{56}Fe of the igneous magnetites correlate negatively with trace elements contents typical for igneous formation (Ti, Al, Ga, V, Mn, Zn); igneous magnetites become isotopically heavier with decreasing concentrations of these elements, indicating a trend towards higher δ^{56}Fe in the magnetite with magma evolution. Model calculations of the δ^{56}Fe evolution in melt, magnetite, and fluid further constrain the magmatic-hydrothermal origin of Kiruna-type IOA deposits.

Keywords: Los Colorados, Chilean Iron Belt, Kiruna-type deposits, iron oxide-apatite deposits, iron isotopes, magnetite flotation.

4.1 INTRODUCTION

68

The Los Colorados iron oxide-apatite (IOA) mineral deposit is one of about fifty Kiruna-type IOA and iron oxide-copper-gold (IOCG) mineral deposits in the Chilean Iron Belt. The Chilean Iron Belt is directly linked to the crustal-scale transcurrent Atacama Fault System (Fig. 1a), which was created by the tectonic change from transtensional to transpressional stress along the South American subduction zone during the late Lower Cretaceous (Uyeda and Kanamori, 1979). The Los Colorados IOA deposit consists of two sub-parallel massive magnetite ore bodies, referred to as dikes by the mining company geologists, (Fig. 4.1b) and both are hosted within andesite of the Punta del Cobre Formation (Pincheira et al., 1990) along with several plutonic units (Fig. 4.1a). Los Colorados has proven resources of up to 986 Mt iron ore with an average grade of 34.8% (CAP-summary, 2013).
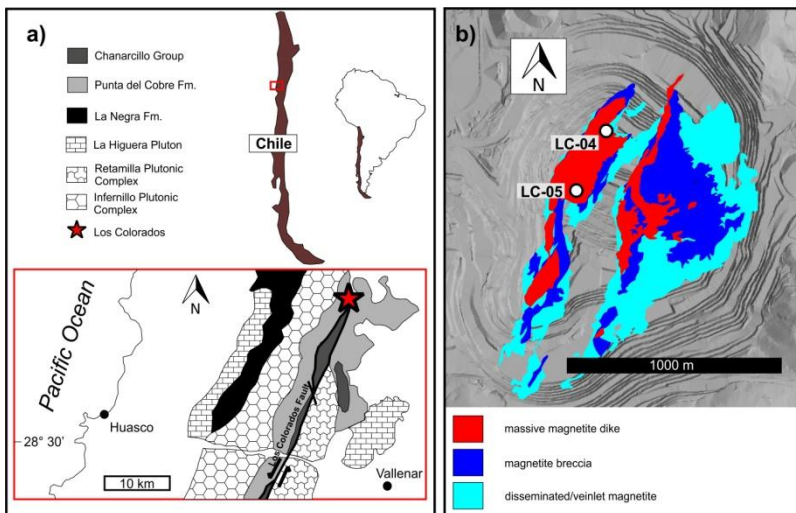
Figure 4.1: Maps of Los Colorados. a) Location of the Los Colorados IOA deposit in Chile. Geological map shows the close relationship between Los Colorados and different plutons (modified after Arévalo et al. 2003) associated with the Los Colorados Fault, which is the central branch of the Atacama Fault System at this latitude. b) Plan view of Los Colorados IOA deposit and locations of drill cores (LC-04 and LC-05).

The genesis of Kiruna-type IOA deposits remains controversial, with several models proposed to explain mineralization, ranging from (non-) magmatic-hydrothermal (Menard, 1995; Rhodes and Oreskes, 1995, 1999; Barton and Johnson, 1996, 2004; Haynes et al., 1995; Rhodes et al., 1999; Haynes, 2000; Sillitoe and Burrows, 2002 and Pollard, 2006) to purely igneous processes such as liquid immiscibility between iron-rich and silicate-rich melts (e.g., Nyström and Henriquez, 1994; Travisany et al., 1995; Naslund et al., 2002; Henriquez et al., 2003; Chen et al., 2010, Hou et al. 2017, 2018). A recently proposed genetic model for Los Colorados and other Kiruna-type IOA deposits in the Chilean Iron Belt involves a synergistic combination of igneous and magmatic-hydrothermal processes to explain the complex geochemistry and textures of magnetite from the Los Colorados ore bodies (Knipping et al., 2015a, b; Rojas et al., 2018a, b).

In general, elevated concentrations of compatible and/or immobile trace elements such as Ti, V, Al, and Mn in magnetite were previously interpreted to indicate a magmatic origin (i.e., crystallization from a silicate melt), whereas relatively low concentrations of these elements in magnetite were interpreted to indicate a magmatic-hydrothermal origin (i.e., precipitation from a cooling aqueous fluid) (Nielsen et al., 1994; Toplis and Carrol, 1995; Dupuis and Beaudoin, 2011; Dare et al., 2012; Nadoll et al. 2014). However, at Los Colorados, some magnetite samples are characterized by trace element concentrations indicating crystallization from a melt, while other magnetite samples indicate precipitation from a hydrothermal fluid (Fig. 4.2). In addition, many magnetite samples from Los Colorados reveal systematic intra-grain trace element zoning of trace elements such as Ti, V, Al, Mn, with enriched magnetite cores and depleted magnetite rims, hinting at a direct transition from purely magmatic to magmatic-hydrothermal processes (Fig. 4.2).

70
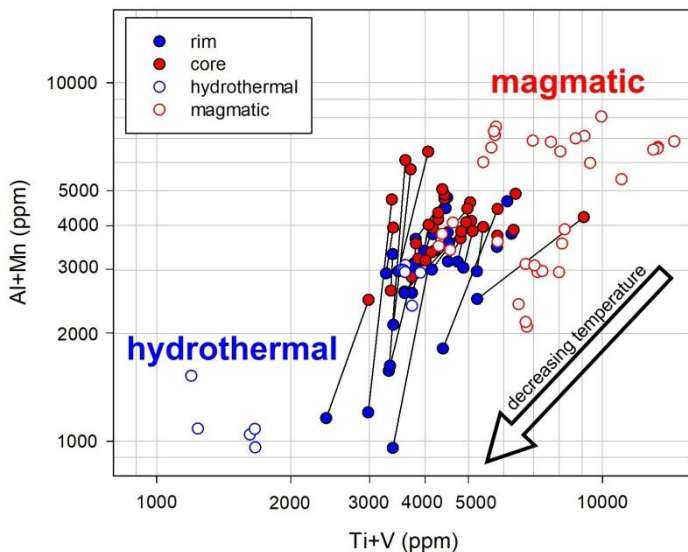
Figure 4.2: Trace element data for magnetite grains from Los Colorados (Knipping et al. 2015b). The data indicate a transition from high concentrations of [Ti+V] vs. [Al+Mn] (open red circles) typical for a high temperature magmatic (igneous) origin, towards lower trace element concentrations (open blue circles) consistent with precipitation from a cooling (magmatic-) hydrothermal fluid. Many samples are characterized by a distinct, intra-grain core-to-rim trace element zoning (filled red and blue circles connected by tie lines).

In order to explain this contradictory geochemistry Knipping et al. (2015a,b) proposed a magnetite flotation model, which consists of four steps: **i)** igneous magnetite crystallization from silicate melt in an andesitic magma reservoir followed by decompression-induced exsolution of volatile phase bubbles that nucleate on magnetite microlite surfaces (Fig. 4.3a); **ii)** further decompression-induced degassing and buoyancy-driven bubble-magnetite pair ascent (Fig. 4.3b); **iii)** growth and Fe enrichment of the saline bubble-magnetite suspension during continued ascent of the suspension (Fig. 4.3c); and **iv)** fast and efficient segregation of the magnetite suspension facilitated by hydraulic fracturing in an extensional tectonic regime (Fig. 4.3d). Cooling of the magnetite-fluid suspension at the final emplacement depth results in the precipitation of

magmatic-hydrothermal magnetite as rims surrounding igneous magnetite grains and interstitially as matrix of the ore body (Fig. 4.3e). Importantly, the preferential nucleation and growth of fluid bubbles on crystal faces of oxides such as magnetite has been documented in studies of natural system, and in experiments (Hurwitz and Navon, 1994; Gardner and Denis, 2004; Gualda and Ghiorso, 2007; Edmonds et al. 2014).
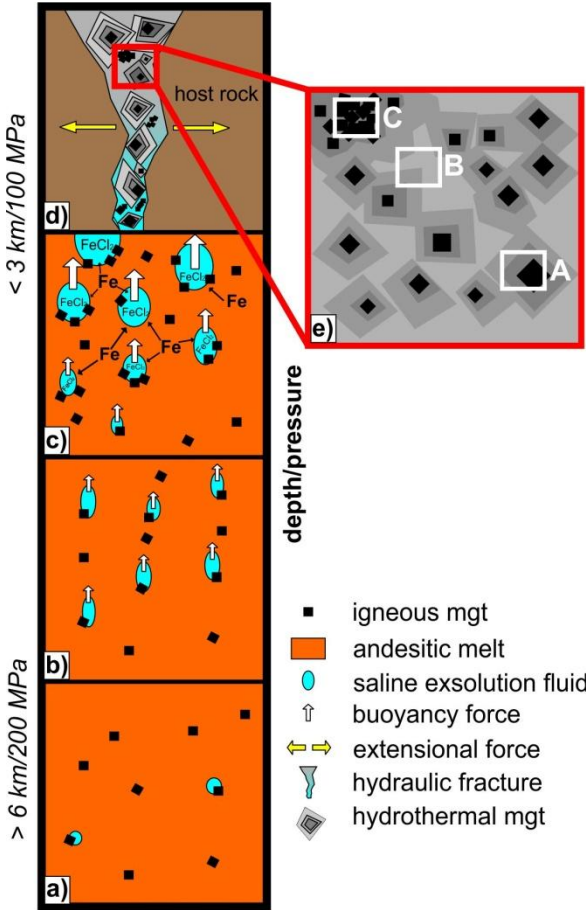
Figure 4.3: Illustration of the flotation model modified from Knipping et al. (2015a,b): a) igneous magnetite crystallization and initial fluid bubble nucleation; b) further decompression-induced degassing and buoyancy-driven bubble-magnetite pair ascent; c) Fe

enrichment of the saline bubble-magnetite suspension during continued ascent; and, d) efficient segregation of the magnetite suspension by hydraulic fracturing and precipitation of dissolved Fe. e) Schematic sketch of massive magnetite from Los Colorados, including igneous magnetite "cores" (black) with magmatic-hydrothermal magnetite "rims" (dark grey) and/or within a magmatic-hydrothermal magnetite "matrix" (light grey). Areas A, B and C are examples for possible sampling regions for the analyses of this study: (A) sampling typical igneous magnetite core with magmatic-hydrothermal rim, (B) sampling pure magmatic-hydrothermal magnetite matrix, (C) sampling an agglomerate of pure igneous magnetite crystals.

In addition to systematic core-to-rim variability of trace element concentrations, the flotation model also relies on the bulk Fe isotope signature of the Los Colorados magnetite (Knipping et al., 2015a; Bilenker et al., 2016), which plots in the "magmatic range" (δ^{56}Fe = +0.06 to +0.50 ‰; Heimann et al., 2008; Weis, 2013). Thus, bulk magnetite from Los Colorados is consistent with magnetite that grew from silicate melt and/or high-temperature magmatic-hydrothermal fluid in contrast to magnetite from hydrothermal iron oxide deposits (-1.6 to ~ 0.0 ‰) (Severmann and Anbar, 2008) such as iron skarns that reveal significantly lower δ^{56}Fe values (- 0.36 to + 0.01 ‰) (Weis, 2013). Despite the unambiguously magmatic/magmatic-hydrothermal Fe isotope signal recorded in magnetite from Los Colorados, the intra-grain and grain-to-grain variation in Fe isotope composition remains unconstrained. However, it is expected from the magnetite flotation model that δ^{56}Fe values would differentiate, consistent with trace-element variability, between magnetite cores (i.e. igneous magnetite enriched in, e.g., Ti, V, Al, Mn) and respective rims (i.e. magmatic-hydrothermal magnetite depleted in, e.g., Ti, V, Al, Mn) due to Fe isotope fractionation between melt-magnetite and magnetite-fluid.

The current study was motivated by recent improvements in using femtosecond laser-ablation multi-collector inductively-coupled plasma mass spectrometry (LA-MC-ICP-MS) for high-precision, high-spatial resolution Fe isotope measurements (Oeser et al., 2014). We test the Knipping *et al.* flotation model by using *in situ* LA-MC-ICP-MS Fe isotope data collected from Los

Colorados magnetite grains. Notably, the measurements were performed on the same grains previously analyzed by Knipping et al. (2015a, b) for their major and trace element compositions. Our new *in situ* Fe isotope data reveal core-to-rim variations in δ^{56}Fe values that are consistent with Fe isotope fractionation processes occurring during the continuum from purely igneous to magmatic-hydrothermal conditions. We further explore the Fe isotope variations within igneous magnetite (cores) by using model calculations of the δ^{56}Fe evolution of melt, magnetite, and fluid, providing constrains for the magmatic-hydrothermal evolution of Kiruna-type IOA systems.

4.2 SAMPLES AND ANALYTICAL PROCEDURE

We analyzed 15 magnetite separate grains with *in situ* Fe isotope LA-MC-ICP-MS, wherein ten magnetite grains originate from drill core LC-04 and five from drill core LC-05 (Fig. 1b). Both drill holes crosscut the western (main) magnetite ore body of the Los Colorados deposit (Table 1). Magnetite samples from drill core LC-04 were taken at depths of 38.8, 66.7, 99.5, 104.4, 125.3 and 129.3 m from the northernmost part of the western ore body, while magnetite samples from drill core LC-05 were extracted at 20.7, 82.6, 106.0, 126.0 and 150.0 m, in the center of the western ore body. Each magnetite grain was analyzed with two to eight raster spots (~ 100 x 100μm) for a total of 69 analyses. When possible, raster spots were taken as close as possible to previous LA-ICP-MS line transects for trace element analysis measured by Knipping et al. (2015a, b); however, sample surface and inclusions sometimes inhibited measurements in the immediate vicinity.

The Fe isotope measurements were performed at the Leibniz Universität Hannover (Germany) by using a high mass resolution MC-ICP-MS (Thermo-Finnigan Neptune Plus) connected to a Spectra-Physics Solstice femtosecond laser ablation system. The laser ablation system is equipped with

a 100 femtosecond Ti-sapphire regenerative amplifier, operating at a fundamental wavelength of 775 nm, which was frequency-quadrupled, resulting in a wavelength of 194 nm. The output energy was about 3.2 mJ/pulse at a fundamental wavelength of 775 nm. Pumping with 500 Hz resulted in a pulse energy of 70 µJ at a wavelength of 194 nm. We used the ablation cell and stage/visualization system (modified New Wave LUV 266) as described in Horn et al. (2006) and Horn and von Blanckenburg (2007). The femtosecond LA-MC-ICP-MS Fe isotope measurements were performed at high mass resolution (M/ΔM $\approx$ 9000, 5–95% peak side width definition) to resolve molecular interferences of argon nitrides and argon oxides on Fe isotopes (and also potentially sample-induced interferences of CaO and CaN; see Weyer and Schwieters 2003). Employment of an H-type skimmer cone for the *in situ* Fe isotope determinations resulted in normal intensities of interfering argon oxides and argon nitrides, i.e., < 1V. All analyses were performed by using a raster technique in which areas of ~ 100 µm x 100 µm were ablated by using a 50-60 µm spot size.

The Fe isotope compositions are reported using delta notation, and δ^{56}Fe values are given as variation in parts per million (‰) from the composition of IRMM-14 (Institute of Reference Materials and Measurements standard 014).

$$\delta^{56}\text{Fe} = [((^{56}\text{Fe}/^{54}\text{Fe})_{\text{sample}}/(^{56}\text{Fe}/^{54}\text{Fe})_{\text{IRMM-14}})\text{-}1]\times 1000$$

equation 1

The IRMM-14 standard was measured after every 1-2 sample analyses for drift monitoring. Horn et al. (2006) demonstrated that this procedure yields absolute values with a high accuracy of $\leq$ 0.1 ‰ for δ^{56}Fe in oxides, hydroxides, carbonates metals and sulfides (see their Fig. 9). The high

accuracy was confirmed by session-to-session and in-session monitoring of an internal secondary pure Fe reference material ("puratronic", Johnson Matthey, lot No. FE495007IF2, 99.995% Fe) for which we reproduced the absolute δ^{56}Fe within ± 0.05 ‰. Importantly, during our *in situ* Fe isotope analyses a Ni reference solution (NIST SRM 986, 5 ppm Ni in 0.5 M HNO$_3$ solution) was added via a quartz glass spray chamber and introduced into the plasma along with the ablation aerosol in order to (a) use the measured Ni isotope ratios as an external mass bias monitor (Oeser et al., 2014), and (b) maintain "wet" plasma conditions. As demonstrated by Zheng et al. (2018), potential matrix effects during *in situ* Fe isotope analyses by fs-LA-MC-ICP-MS are drastically reduced under such "wet" plasma conditions, enabling us to perform accurate and precise Fe isotope measurements without matrix-matching of sample (magnetite) and standard (metal).
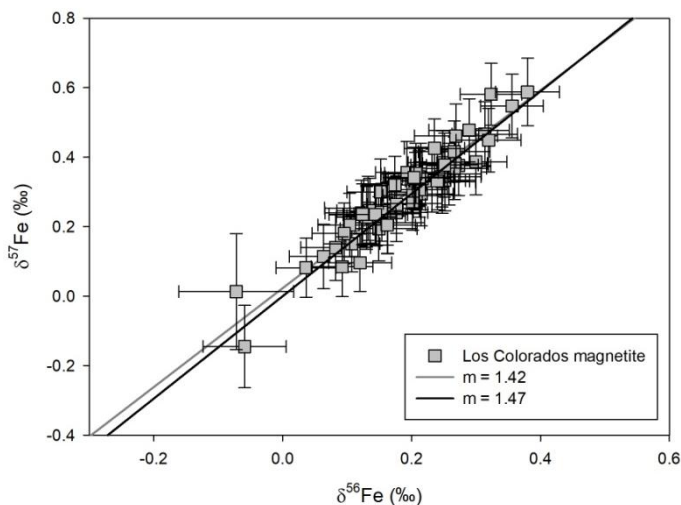
Figure 4.4: δ^{57}Fe plotted against δ^{56}Fe. The measured δ^{56}Fe and δ^{57}Fe values plot on a near-ideal trend (gray line; m = 1.42, R^2 = 0.9) for mass dependent isotope fractionation (black line; m = 1.47) allowing the comparability of our results with published δ^{57}Fe values.

Each analytical spot analysis was measured for ^{54}Fe, ^{56}Fe and ^{57}Fe, and the calculated ratios of ^{56}Fe/^{54}Fe and ^{57}Fe/^{54}Fe and the resulting δ^{56}Fe and δ^{57}Fe values are plotted against each other in Fig. 4.4, revealing a slope of 1.42 (R^2=0.9) , which is in good agreement with the mass dependent fractionation ratio of 1.47 that is based on the natural abundances of Fe isotopes; ^{54}Fe = 5.85% ; ^{56}Fe = 91.75; ^{57}Fe = 2.12% (e.g., Dauphas and Rouxel, 2006), as we do not expect any mass-independent fractionation during measurements (Horn et al., 2006). Thus, fractionation factors from the literature given in δ^{57}Fe-notation can be simply recalculated into δ^{56}Fe-notation, or vice versa, when comparing them with our data. Further details about the method are provided in Horn et al. (2006) and Oeser et al. (2014).

4.3 RESULTS

The *in situ* δ^{56}Fe values for magnetite from Los Colorados range from 0.04 to 0.38 ‰ (n=69; Table 1), wherein samples from drill core LC-05 have a more narrow range (0.06 to 0.27 ‰) when compared to samples from drill core LC-04. Some magnetite grains are zoned from heavier δ^{56}Fe values in magnetite cores to lower values in magnetite rims (e.g., sample LC-05-82.6: 0.24 ± 0.02 ‰ in the core versus 0.16 ± 0.04 ‰ in the rim). Other samples show constant low δ^{56}Fe values (e.g., sample LC-05-126: 0.11 ± 0.02‰), or constant high δ^{56}Fe values (e.g., sample LC-04-38.8d: 0.33 ± 0.06‰) without obvious zoning (Table 1). One exception is sample LC-05-20.7, which shows zoning from lighter δ^{56}Fe values in the core (0.07 ± 0.01‰) towards relatively heavier δ^{56}Fe values in its rim (0.13 ± 0.02‰). In order to interpret these Fe isotope signatures, we will use the textural appearance and sample depths information of magnetite grains combined with trace element data published by Knipping et al. (2015b) to assign the results of this study to magmatic-hydrothermal and igneous origin.

4.4 DISCUSSION

4.4.1 Igneous vs. magmatic-hydrothermal magnetite

Almost all of the δ^{56}Fe values measured in this study plot in the magmatic range (0.06-0.50 ‰) (Table 1) defined by Heimann et al. (2008), and are consistent with previous bulk δ^{56}Fe data of entire magnetite grains from the same samples analyzed by traditional solution MC-ICP-MS (Knipping et al., 2015a; Bilenker et al., 2016). In these samples, Knipping et al. (2015a,b) discovered systematic variation in trace element abundances of, e.g., Ti, Al, Mn, between magnetite cores and rims, interpreted by those authors as evidence for the crystallization of magnetite cores from a silicate melt (i.e., igneous magnetite) followed by the precipitation of magnetite rims and matrix magnetite (i.e., interstitial magnetite) from a fluid phase derived from the same magma reservoir (i.e., magmatic-hydrothermal magnetite). In order to determine whether the new Fe isotope data indicate an igneous and/or magmatic-hydrothermal origin for magnetite, trace element transects collected using LA-ICP-MS by Knipping et al. (2015b) and sample depths information were used to initially distinguish (see supplementary material).

Magnetite has an inverse spinel structure in which ferrous Fe can be substituted by divalent (Mg, Ni, Mn, Co and Zn) and ferric Fe by trivalent cations (Al, Cr, V, Mn and Ga) as well as by Ti^{4+} in combination with a divalent cation (Lindsley, 1976; Wechsler et al. 1984; Ghiorso and Evans, 2008). A higher concentration of these compatible elements, especially elements that are immobile in fluids, e.g., Ti and Al (Van Baalen, 1993; Verlaguet et al. 2006), are robust indicators of an igneous formation. According to many studies, Ti and Al are the best trace elements to discriminate between igneous and hydrothermal magnetite because they are mainly detected in high temperature igneous magnetite (Nielsen et al., 1994;

Toplis and Carrol, 1995; Dupuis and Beaudoin, 2011; Dare et al., 2012; Nadoll et al. 2014).

Thus, we used Ti and Al concentrations in Los Colorados magnetite as a proxy for discrimination between igneous (core) and hydrothermal (rim) magnetite. Fig. 4.5 shows an example of a previous LA-ICP-MS trace element transect (Knipping et al. 2015b) in proximity to the *in situ* Fe isotope measurements.
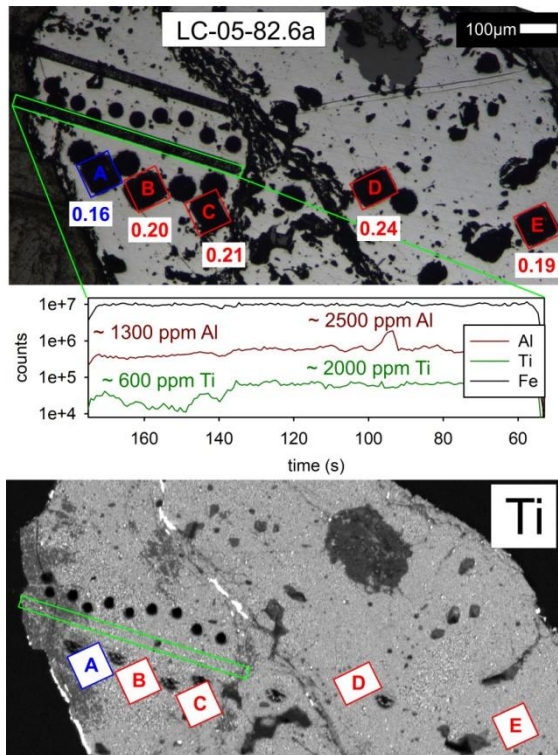
Figure 4.5: Reflected light image of sample LC-05-82.6a and trace element transect. The green box highlights the previous measured trace element transect by LA-ICP-MS (Knipping et al. 2015b). Red and blue values represent δ⁵⁶Fe data (in ‰) of raster areas collected by *in-situ* Fe-isotope LA-MC-ICP-MS. LA-ICP-MS elemental profiles are shown for Fe (black), Al (dark red) and Ti (dark green) indicating a sudden decrease in trace elements towards the grain rim that is also visible in EPMA trace element map for Ti.

A sudden decrease in Ti and Al concentration was detected when measuring from core to rim. Hence, the raster spot A (δ^{56}Fe = 0.16 ± 0.04 ‰) is assigned as magmatic-hydrothermal magnetite "rim", whereas the remaining raster spots B-F (δ^{56}Fe = 0.19-0.24 ± 0.05 ‰) are interpreted as igneous magnetite "core". Also other measured grains show this kind of zoning where isotopically heavier Fe is concentrated with a high concentration of compatible and/or immobile elements (e.g., Ti and Al) in the center of the grains, and isotopically lighter Fe and lower concentrations of these elements exist in the rims of the grains (Table 1). In contrast, samples LC-04-66.7b, LC-04-129.3c, and LC-05-126 have constantly low concentrations of Ti (~ 110, ~ 3800 and ~ 650 ppm) and Al (400-700, ~1800 and ~ 1900 ppm), and were assigned as magnetite formed solely under magmatic-hydrothermal conditions, whereas samples LC-04-129.3d and LC-05-150b show constantly higher concentrations of trace elements typical for an igneous origin (Ti = 4800-5400 and ~7400 ppm; Al = 5000-5500 ppm and ~ 5100 ppm) (see supplementary material). The samples analyzed from Los Colorados were fragments of massive magnetite that sometimes show distinct magnetite cores with magmatic-hydrothermal rims or within a massive magmatic-hydrothermal magnetite matrix (Fig. 4.3e, area A). However, some areas may reflect completely magmatic-hydrothermal matrix magnetite, which precipitated in void spaces after cooling (Fig. 4.3e, area B), while other locations likely reveal aggregates of several accumulated igneous magnetite crystals (Fig. 4.3e, area C).

Simultaneously, the magnetite samples without trace element zoning, i.e., with constant low or constant high trace element concentration (e.g., Ti and Al), also have relatively constant Fe isotope ratios without any obvious zoning (LC-04-66.7b: 0.15 - 0.22 ‰, LC-04-129.3c: 0.04 - 0.11 ‰, LC-05-126: 0.09 - 0.13 ‰, LC-04-129.3d: 0.18 - 0.24 ‰, LC-05-150b: 0.14 – 0.20 ‰). The anomalous sample LC-05-20.7, which yielded lighter Fe isotope values in its

core (0.07 ± 0.05 ‰) versus relatively heavier Fe isotope values in its rim (0.14 ± 0.06 ‰), contains high Ti (2400-2600 ppm) and Al concentrations (4400-4800 ppm) throughout the grain indicating an exclusively igneous formation.

After assigning all *in situ* Fe isotope values to their probable origin (i.e., igneous vs. magmatic-hydrothermal, Table 1 and supplementary material) based on textural and trace element chemical data and plotted versus sample depth for each drill core, a systematic pattern is revealed (Fig. 4.6), where δ^{56}Fe decreases from relatively heavy values (δ^{56}Fe= 0.24 ± 0.07 ‰; 2SD with n=33) in primary igneous magnetite to relatively lower values (δ^{56}Fe= 0.15 ± 0.05 ‰; 2SD with n=26) in magmatic-hydrothermal magnetite.
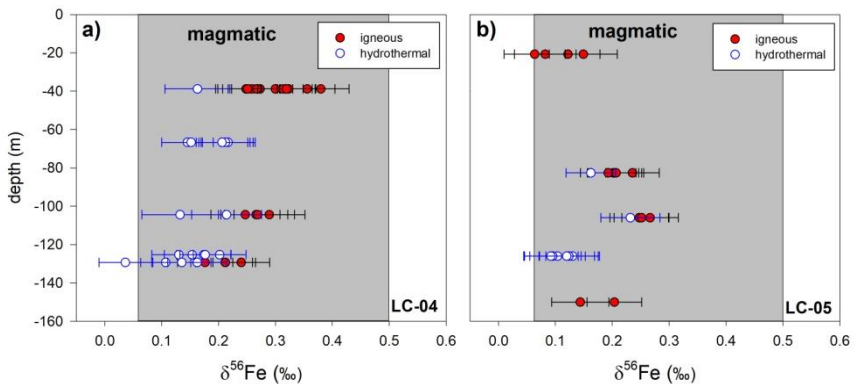
Figure 4.6: δ^{56}Fe vs. depth of sampled magnetite grains. (a) Results of drill core LC-04 and (b) results of drill core LC-05. Grey bands represent the magmatic range defined by Heimann et al. (2008), which include both pure igneous and magmatic-hydrothermal magnetite. Red symbols indicate igneous magnetite and blue data represent magmatic-hydrothermal magnetite rims/matrix from Los Colorados.

However, there is an additional trend within the purely igneous realm (i.e., red data in Fig. 4.7) indicating increasing δ^{56}Fe with decreasing compatible and/or immobile trace elements (e.g., Ti, Al, V, Ga, Zn and Mn) in magnetite, which provide new insights on the transition between the igneous phase of magnetite crystallization to the subsequent magmatic-hydrothermal stage.

81
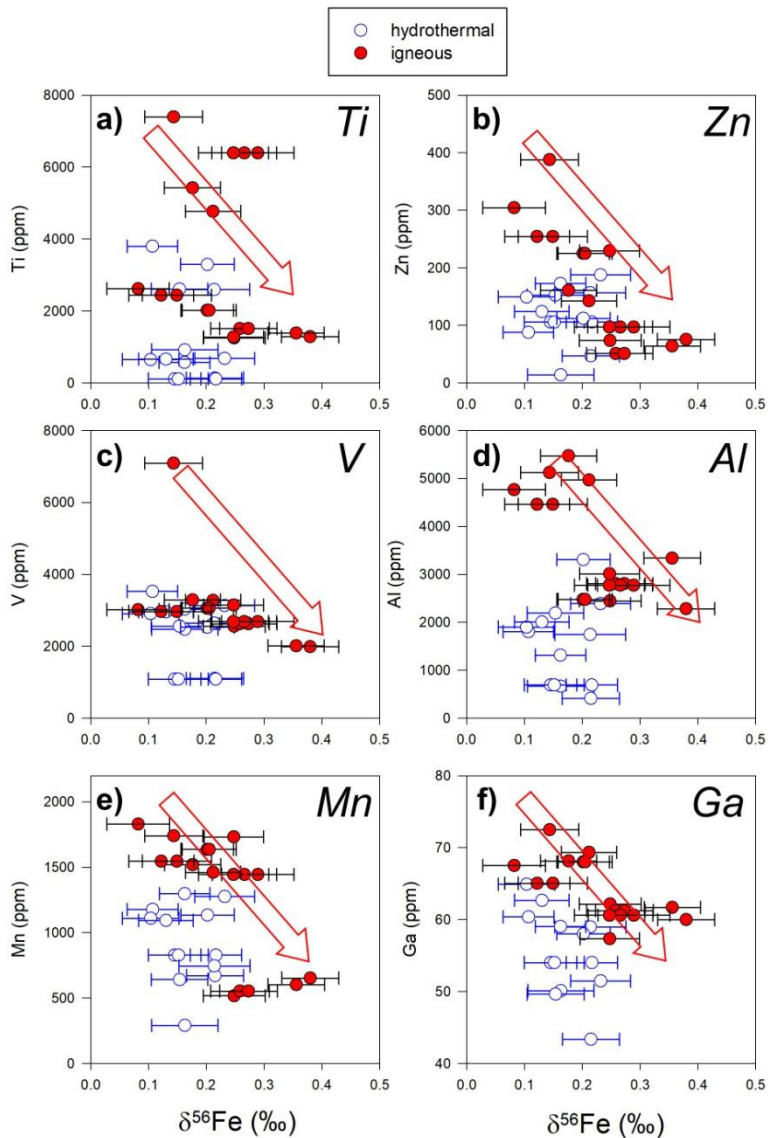
Figure 4.7: Compatible trace element concentrations in magnetite vs. δ^{56}Fe indicate the compositional evolution of igneous magnetite with ongoing fluid exsolution shown by red arrow. Here, only those δ^{56}Fe data are plotted where previous LA-ICP-MS trace element analyses were collected in direct proximity.

4.4.2 Igneous magnetite crystallization

Observations from empirical and experimental studies indicate that elements such as Al, Mn, Ti, V, Ga and Zn are typically enriched in magmatic magnetite, and that the concentrations of trace elements in magnetite increase systematically with increasing temperature (Nadoll et al., 2014; Toplis and Carroll, 1995). This is in agreement with the observed enrichment of Ti and Al in magnetite from more primitive silicate melts when compared to more evolved systems (Dare et al., 2012; Grigsby, 1990; Lindsley, 1991). Thus, higher concentrations of Al, Mn, Ti, V, Ga and Zn are expected in magnetite that nucleates and grows during early magmatic stages, while relatively lower concentrations of trace elements in igneous magnetite may indicate growth during a later magmatic stage (indicated by red arrow in Fig. 4.7). Hence, the magnetite sample with highest concentration of Al, Mn, Ti, V, Ga and Zn (LC-05-150) is interpreted here as the most primitive magnetite composition, which simultaneously reveals among the lowest $\delta^{56}Fe_{mgt}$ values (0.14 to 0.20 ‰) of igneous magnetite (red data in Fig. 4.6) measured at Los Colorados. A potential parental melt can be calculated for these $\delta^{56}Fe_{mgt}$ data by using equation 2, which was determined by Sossi et al. (2012) based on tholeiitic samples of the Red Hill intrusion.

$$\Delta^{56}Fe_{mgt\text{-}melt} = \delta^{56}Fe_{mgt} - \delta^{56}Fe_{melt} = \Delta^{56}Fe_{mgt\text{-}melt} * 1.47 = +0.20 \text{ ‰} * 10^6/T^2$$

$$\text{equation 2}$$

The derived $\delta^{56}Fe_{melt}$ values (0.07 to 0.13 ‰ at 1125 °C; i.e., the temperature of first crystallizing magnetite) are in agreement with the average bulk Fe isotope composition ($\delta^{56}Fe_{bulk} = 0.11 \pm 0.05$‰) of silicate rocks ranging between 55-70 wt% SiO_2 determined by various studies (Table 2; e.g., Poitrasson and Freydier, 2005; Schoenberg and von Blanckenburg, 2006;

Heimann et al. 2008; Teng et al. 2008; Schüssler et al., 2009; Sossi et al., 2012; Telus et al., 2012; Zambardi et al., 2014), which is in agreement with the local and regional geology around Los Colorados (andesitic host rock and dioritic plutons) (Fig. 4.1).

However, the igneous magnetite at Los Colorados with lower concentrations of Ti, V, Al, Mn, Ga and Zn (Fig. 4.7) reveal a heavier Fe isotope composition ($\delta^{56}Fe_{mgt}$ up to 0.38 ‰), consistent with magnetite that would have need to be crystallized from a melt with a significantly higher $\delta^{56}Fe_{melt}$ (up to 0.30 ‰ at T = 1050 °C). Such heavy Fe isotope compositions are often measured in silicate rocks with more evolved compositions ($SiO_2 >$ 70 wt%) when compared to andesite.

Initially, this observation was explained by the exsolution of deuteric fluids during late differentiation stages (Poitrasson and Freydier, 2005; Heimann et al. 2008; Telus et al., 2012). Exsolved magmatic-hydrothermal fluids were supposed to preferentially leach ferrous Fe and, thus, relatively light $\delta^{56}Fe$ from the silicate melt (Poitrasson and Freydier, 2005; Heimann et al. 2008; Telus et al., 2012; Bilenker et al., 2012); e.g., $\delta^{56}Fe_{fluid} =$ -0.05 to -0.39 ‰ at 500 and 700 °C (Heimann et al., 2008).

Although the fractionation effect by deuteric fluids at late differentiation stages was recently determined to be of minor importance in order to explain the increasing $\delta^{56}Fe_{bulk}$ of rocks with SiO_2 >70 wt% (Dauphas et al. 2017), it may still play a significant role for early fractionation melt-dominant magmas that exsolve fluids during degassing processes caused by magma ascent or overlaying pluton formation.

Thus, a degassing melt would become enriched in heavy $\delta^{56}Fe$ resulting in crystallizing igneous magnetite that would consequently incorporate also increasingly heavier Fe isotopes as a function of degassing ($\delta^{56}Fe_{mgt} > 0.18$ ‰.), correlating negatively with trace element concentrations

in magnetite, such as Ti, V, Ga, Mn, Zn and Al (Fig. 4.7). This is because Ti, V, Ga, Mn, and Zn are compatible in magnetite relative to silicate melts (Nielsen, 1992; Okamoto, 1979; La Tourette et al., 1991; Ewart and Griffin, 1994) and ongoing decompression-induced crystallization of magnetite itself would lower their concentrations in the residual melt. In addition, decompression-induced degassing of a (sulfur-poor) system may increase oxygen fugacity of the system (Mathez, 1984; Burgisser and Scaillet, 2007; Bell and Simon, 2011) and, thus, may affect the oxidation state of V and Mn, limiting the substitution into magnetite's structure. In contrast the partitioning of Sn into magnetite may increase with increasing oxygen fugacity (Carew, 2004) which is consistent with correlating higher Sn values and heavier Fe isotope signatures that are caused during degassing of the melt (Fig. 4.8).
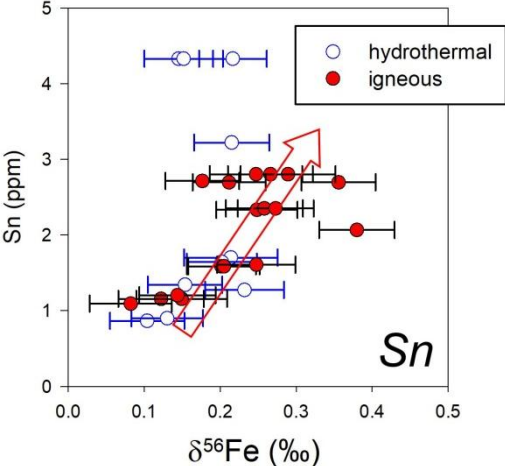
Figure 4.8: δ^{56}Fe vs. Sn in Los Colorados magnetite. Tin is more compatible in magnetite at more oxidizing conditions (Carew, 2004) suggesting oxidation during decompression-induced crystallization (Mathez, 1984; Burgisser and Scaillet, 2007; Bell and Simon, 2011). Here, only those δ^{56}Fe data are plotted where previous LA-ICP-MS trace element analyses were collected in direct proximity.

Manganese and Zn are compatible in magmatic-hydrothermal fluid (Zajacz et al., 2008) and degassing would therefore decrease the concentration of these

85

elements in magnetite even more significantly. In contrast, Al is a major element in silicate melts and incompatible in magnetite ($D^{mgt/melt}_{Al}$=0.117; La Tourette et al., 1991), and is often considered as an immobile element in magmatic-hydrothermal fluid (e.g., Carmichael, 1969). However, this characterization is mainly based on the low solubility of aluminum hydroxides and aluminum silicates in aqueous fluids. Indeed, more recent experimental studies (e.g., Verlaguet et al., 2006) have shown that Al can be mobile despite its low solubility in aqueous fluid. This mobility is especially pronounced during disequilibrium processes such as fluctuations in pressure, temperature, and fluid composition. Thus, a kinetic degassing process may be capable of leaching Al from the melt into the fluid phase, resulting in a decreasing Al content in magnetite with continued degassing, while $\delta^{56}Fe_{mgt}$ increases (Fig. 4.7).

4.4.3 Magmatic-hydrothermal magnetite precipitation

The extensional tectonic stress in the Atacama Fault System promotes ongoing decompression and allows an efficient separation of the fluid-magnetite suspension from the parental magma reservoir and its rapid transport via hydraulic fractures in crustal fault systems. The dissolved $FeCl_2$ in the fluid-magnetite suspension will precipitate magmatic-hydrothermal magnetite due to the decreasing solubility of $FeCl_2$ at hydrothermal temperatures (~ 450-620 °C) that is more effective with the degree of decompression, i.e. rapid decompression may lead to the formation of larger ore bodies (Simon et al., 2004; Rojas et al. 2018). The magmatic-hydrothermal magnetite will precipitate as rims and as matrix surrounding the igneous magnetite grains or accumulation of igneous grains (Fig. 4.3e) (Knipping et al., 2015a,b). Accordingly, the hydrothermally precipitated magnetite contains relatively high concentrations of compatible and mobile elements like Mn and Zn that are

almost as high as in the igneous magnetite (Fig. 4.7), when compared to immobile elements that are more depleted in the hydrothermally precipitated magnetite. However, a clear trend towards isotopically heavy or light Fe isotope composition with trace element variation, as observed for the igneous magnetite domains, is not detectable for the magmatic-hydrothermal magnetite (Fig. 4.7 and 4.8). The constant value of $\delta^{56}Fe = 0.15 \pm 0.05$ ‰ for the magmatic-hydrothermal magnetite probably indicates one fast depositional event at a certain pressure and temperature (Rojas et al. 2018). When applying equation 3 (Heimann et al., 2008) for the calculation of magnetite-fluid Fe isotope fractionation, the Fe isotope composition of a hypothetical parental magmatic-hydrothermal fluid ranges from -0.15 to -0.32 ‰ for temperatures between 700 and 500 °C; this range is consistent with Fe isotope compositions of magmatic-hydrothermal fluids ($\delta^{56}Fe_{fluid}$ = -0.05 to -0.39 ‰) estimated by Heimann et al. (2008).

$\Delta^{56}Fe_{mgt\text{-}fluid}= \delta^{56}Fe_{mgt} - \delta^{56}Fe_{fluid} = +0.28$ ‰ * $10^6/T^2$; T in K

equation 3

Equation 3 predicts a $\Delta^{56}Fe_{mgt\text{-}fluid}$ value of +0.25 ‰ at 800 °C, which, we highlight, is fairly consistent with the results of recent magnetite-fluid Fe isotope fractionation experiments in the presence of a 2 M $FeCl_2 \cdot 4H_2O$ solution that yielded fractionation factors of $\Delta^{56}Fe_{mgt\text{-}fluid}$ of +0.35 ‰ (based on measured $^{56}Fe/^{54}Fe$ in experimental fluids) or +0.30 ‰ (re-calculated from $\Delta^{57}Fe_{mgt\text{-}fluid}$) at 800 °C (Sossi and O'Neill, 2017).

4.5 IRON ISOTOPE FRACTIONATION MODEL

To explain the observed variation in Fe isotope composition among magnetite grains, we developed an holistic Fe isotope fractionation model for the formation of the Los Colorados magnetite. These calculations take into

account the *magnetite-flotation model* for Kiruna-type IOA deposits developed by Knipping et al. (2015a,b) and serves as a first order verification of this model.

During the four steps of the magnetite-flotation model, three stages of Fe fractionation can be distinguished: crystallization of magnetite from the melt in a parent magma chamber (i.e., δ^{56}Fe fractionation between magnetite-melt; **Stage 1**), decompression-induced crystallization of igneous magnetite from a degassing melt during magma ascent (i.e., δ^{56}Fe fractionation between melt-fluid and magnetite-melt; **Stage 2**), and precipitation of magnetite from a segregated magmatic-hydrothermal fluid (i.e., δ^{56}Fe fractionation between magnetite-fluid; **Stage 3**). Here, the current ("snapshot") Fe isotope compositions of magnetite grown during Stage 2-3 are predicted to estimate the maximum variability in δ^{56}Fe$_{mgt}$ in the system presuming negligible re-equilibration after crystallization/precipitation during fast open system degassing. This procedure allows us to compare the modeled range of δ^{56}Fe to the measured *in situ* range.

4.5.1 Stage 1: Initial magnetite crystallization

Stage 1 of the model simulates cooling of a magma reservoir after emplacement from T$_{liquidus}$ to a reasonable pre-eruptive storage T of 1050 °C, resulting in initial crystallization of magnetite from silicate melt (*initial igneous mgt*) (Fig. 4.9a).
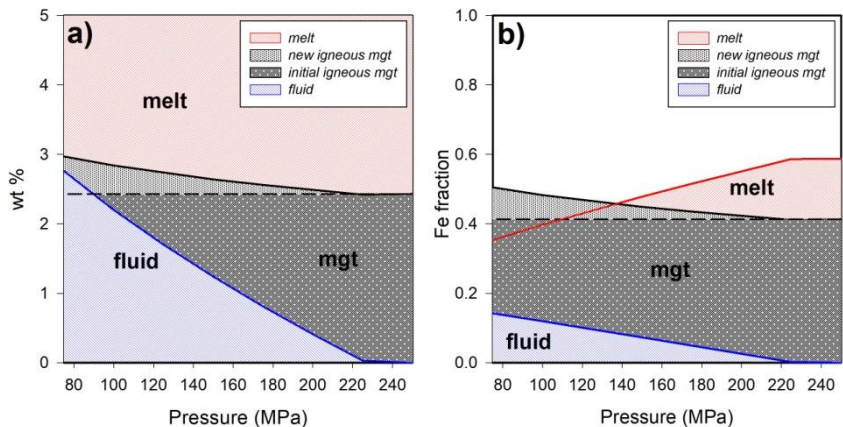
Figure 4.9: MELTS models using the P1D andesite composition (Martel et al. 1999), 1050 °C, NNO+3 and 6 wt% H₂O. (a) wt% of the existing phases (melt, mgt and fluid) and (b) Fe fraction between existing phases during decompression from 250 to 75 MPa. 35 wt% NaClₑq was assumed for the fluid (according to Knipping et al. 2015b) and thus a partition coefficient of $D^{f/m}_{Fe}$=8.5 (Zajacz et al., 2008) was used to calculate the Fe concentration in the fluid. *Initial igneous mgt* **indicates the amount of mgt crystallized prior to decompression and** *new igneous mgt* **indicates the amount of mgt crystallized during/after decompression.**

The Los Colorados Kiruna-type IOA deposit is located within the andesitic Punta del Cobre formation, which is a formation typical for arc settings and, thus, andesite (i.e., P1D andesite from Martel et al., 1999) is used as the source magma composition for the following predictions. Arc magmas are typically hydrous (2-8 wt% H₂O) and oxidized (NNO+0 to NNO+4; in log units oxygen fugacity (fO₂) relative to the Ni-NiO oxygen buffer) (Carmichael, 1991), while crustal thinning in back-arc settings allows for the storage of relatively hot magma (> 1000 °C) at intermediate depths (3-10 km ~ 100-400 MPa). We used the software package MELTS (cf. Ghiorso and Sack, 1995) to predict cooling- and decompression-induced magma evolution; i.e., magnetite, melt, and fluid fractions, and residual melt composition (see Fig. 4.9). We assume an initial bulk water content of 6 wt%, an fO₂ of NNO+3, and an initial pressure of 250 MPa (depth ~7 km). For these parameters, MELTS predicts magnetite as the liquidus phase with a liquidus temperature (T$_{liquidus}$) of 1125

°C, in agreement with experiments by Martel et al. (1999), where magnetite was the liquidus phase in andesite at T > 1040 °C, 200 MPa and NNO+2 to NNO+3.

The bulk Fe isotope composition of the andesitic magma reservoir was set at $\delta^{56}Fe_{melt}$ = 0.11 ‰ (see Section 4.4.2; red star in Fig. 4.10). When applying equation 2 for the calculation of Fe isotope fractionation between magnetite-melt, the first magnetite grains to crystallize from the andesitic melt have a $\delta^{56}Fe_{mgt}$ of 0.18 ‰. Cooling of the andesitic magma reservoir results in continued crystallization of magnetite, which preferentially incorporates heavy Fe isotopes due to its elevated ferric/ferrous Fe composition (Bigeleisen and Mayer, 1947; Polyakov et al., 2007; Schauble, 2004; Schauble et al., 2009). Thus, the $\delta^{56}Fe$ of the model parental melt ($\delta^{56}Fe_{melt}$) decreases during magnetite crystallization and equilibration as long as only magnetite is crystallizing. Here, magnetite-melt Fe isotope equilibrium fractionation is likely, considering that cooling rates in magma reservoirs are typically low (often <200 °C/Ma; e.g., Hess et al., 1993).

For instance, the crystallization of a total of 2.43 wt% magnetite (calculated with MELTS for 1050 °C) (Fig. 4.9a) would decrease the $\delta^{56}Fe_{melt}$ from 0.11 ‰ (bulk) to 0.08 ‰, calculated by using equation 4 (Fig. 4.10; Stage 1)

$$\delta^{56}Fe_{melt} = \delta^{56}Fe_{bulk} - f * \Delta^{56}Fe_{mgt\text{-}melt}$$

equation 4

where $\delta^{56}Fe_{bulk}$ is the bulk Fe isotopic composition of the system, f is the Fe fraction used from melt (here by only magnetite crystallization) and $\Delta^{56}Fe_{mgt\text{-}melt}$ is the temperature dependent fractionation factor between magnetite and melt (equation 2). The coexisting magmatic magnetite (i.e., *initial igneous mgt*)

90

has a predicted $\delta^{56}Fe_{mgt}$ of 0.16 ‰ (Fig. 4.10), presuming equilibrium fractionation at 1050 °C, which is 0.02 ‰ lighter than the first crystallizing magnetite grains (Fig. 4.10).
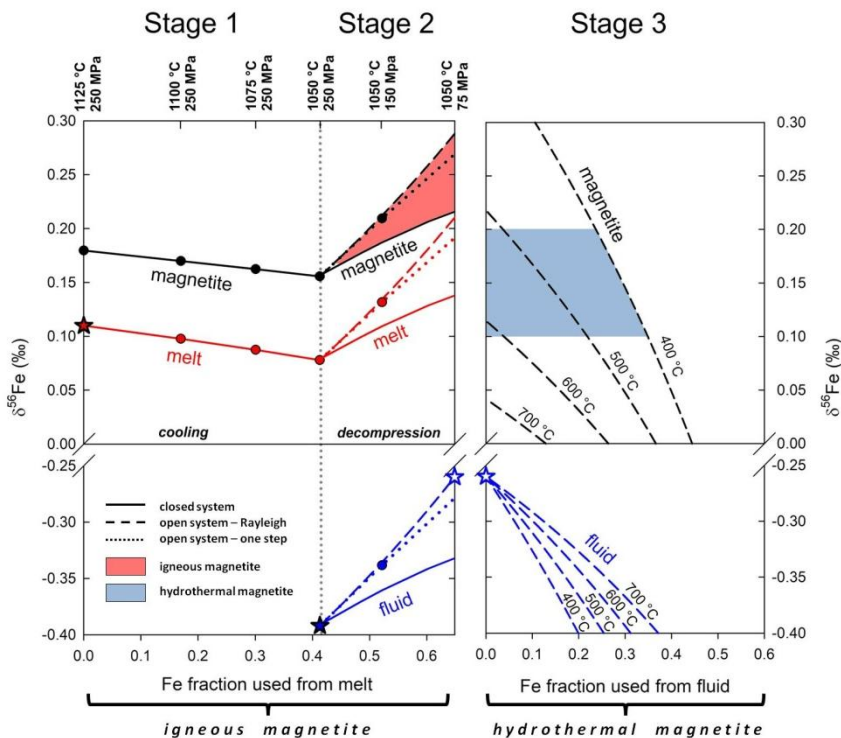
Figure 4.10: Predicted Fe isotope evolution of co-existing melt, fluid and magnetite. The $\delta^{56}Fe$ values for melt and fluid represent the bulk remaining Fe isotope composition at a given fraction. In contrast, the $\delta^{56}Fe$ values displayed for magnetite represent the "snapshot" Fe isotope composition at a given *f*. This allows direct comparison of the $\delta^{56}Fe$ values for magnetite to the measured values, presuming grain-to-grain and within grain diffusive re-equilibration is negligible (unless for closed-system scenario). *Stage 1:* Cooling-induced crystallization of *initial igneous mgt* in the magma reservoir. *Stage 2*: Decompression-induced degassing and crystallization of *new igneous mgt* in the magma reservoir. At the end of Stage 2 a fluid-magnetite suspension is separated from the magma reservoir. *Stage 3*: Cooling-induced precipitation of magmatic-hydrothermal magnetite from a separated fluid at shallow depth.
Assumed conditions contain an andesitic melt with a $\delta^{56}Fe_{bulk}$ = 0.11 ‰ (red star) at 250 MPa with 6 wt% dissolved H_2O. Decompression is assumed down to 75 MPa with the exsolution of ~2.8 wt% H_2O with a molality of 5.9 m Cl (= 35 wt% $NaCl_{eq}$). The red and blue areas

highlight the average δ⁵⁶Fe (± 2σ) of the measured and assigned igneous (0.24 ± 0.07 ‰) and magmatic-hydrothermal magnetite grains (0.15 ± 0.05 ‰), respectively.
Comparison to Fig. 4.3: Fig. 4.3a represents end of Stage 1 and beginning of Stage 2; Fig. 4.3b-c represents Stage 2; Fig. 4.3d represents Stage 3.

4.5.2 Stage 2: Igneous magnetite crystallization during magma decompression

Stage 2 represents magma ascent from intermediate depths (~7 km) to shallow depths (~2 km), resulting in decompression-induced volatile saturation of the silicate melt and leading to additional igneous magnetite crystallization in the presence of a fluid phase owing to an increase of $T_{liquidus}$.

Decompression of the volatile-rich magma, e.g., through overlaying pluton formation common in this region (Fig. 1) or magma ascent, would lead to the exsolution of volatiles and crystallization of *new igneous mgt* (Fig. 4.9a). In order to estimate the Fe isotope fractionation between all three phases (i.e., melt-fluid, magnetite-melt), the Fe fraction among these phases must be quantified. The Fe concentration in the fluid is dependent on the Cl concentration of the fluid (Simon et al. 2004). Here, a Cl concentration of 35 wt% $NaCl_{eq}$ is estimated for the exsolved fluid (molality, m=5.9 mol/kg) based on observations of euhedral halite crystals in magnetite hosted fluid inclusions (Knipping et al. 2015b). This allows the application of a partition coefficient of $D^{f/m}_{Fe}$=8.5 between fluid and melt according to the experimentally derived relationship: $D^{f/m}_{Fe}$=1.44*m (Zajacz et al., 2008). Thus, the exsolved fluid at a low P of 75 MPa accounts for 14 % of the total Fe, while the *initial igneous mgt* scavenges 41 % Fe and the *new igneous mgt* (magnetite crystallized between 250 and 75 MPa at 1050 °C) scavenges only 9 % Fe, leaving 35% Fe for the remaining melt (Fig. 4.9b). There are no published experimentally determined Fe isotope fractionation factors for melts and aqueous fluids. Thus, we estimate a fractionation factor based on an assumed initial light Fe isotope composition for the exsolving magmatic fluid of $\delta^{56}Fe_{fluid}$ = -0.39 ‰ (c.f.,

Heimann et al., 2008) at the beginning of the degassing (filled blue star in Fig. 4.10). This implies that $\Delta^{56}Fe_{melt-fluid} = 0.47$ at 1050 °C (equation 5), when using the final value of $\delta^{56}Fe_{melt}$ of Stage 1.

$$\Delta^{56}Fe_{melt-fluid} = \delta^{56}Fe_{melt} - \delta^{56}Fe_{fluid}$$

equation 5

In this model scenario, the exsolution of fluid would have a stronger effect on Fe isotope fractionation than decompression-induced magnetite crystallization. Thus, when assuming closed system equilibrium fractionation, the continuous exsolution of a saline fluid phase would increase $\delta^{56}Fe_{fluid}$ from -0.39 ‰ at 250 MPa to -0.33 ‰ at 75 MPa (equation 6) and consequently, $\delta^{56}Fe_{melt}$ would increase from 0.08 to 0.13 ‰ (equation 7), resulting in all magnetite being as heavy as 0.22 ‰ at 75 MPa (equation 8).

$$\delta^{56}Fe_{fluid} = x\Delta^{56}Fe_{mgt-melt} + x\Delta^{56}Fe_{melt-fluid} - \delta^{56}Fe_{bulk} + y\Delta^{56}Fe_{melt-fluid}$$

equation 6

$$\delta^{56}Fe_{melt} = \delta^{56}Fe_{fluid} + \Delta^{56}Fe_{melt-fluid}$$

equation 7

$$\delta^{56}Fe_{mgt} = (\delta^{56}Fe_{bulk} - y\delta^{56}Fe_{melt} - z\delta^{56}Fe_{fluid}) / x$$

equation 8

In equation 8, x is the Fe fraction used by all igneous magnetite (*initial igneous mgt + new igneous mgt*), y is the Fe fraction used by the melt, and z is the Fe fraction used by the fluid, i.e., $x + z = 1 - y = f$, which is the Fe fraction used from melt.

An open system Rayleigh style fractionation would further increase $\delta^{56}Fe_{melt}$, from 0.08 to 0.21 ‰ (equation 9) and $\delta^{56}Fe_{fluid}$ from -0.39 to -0.26 ‰

93

(equation 10), resulting in a maximum $\delta^{56}Fe_{mgt}$ of 0.29 ‰ (equation 2) (Fig. 4.10 - Stage 2).

$$\delta^{56}Fe_{melt} = ((1000 + \delta^{56}Fe_{initial-M2}) * f^{(1-\alpha)}) - 1000$$

<div align="right">equation 9</div>

$$\delta^{56}Fe_{fluid} = (1000 + \delta^{56}Fe_{melt}) / \alpha - 1000$$

<div align="right">equation 10</div>

In equation 9, f equals the sum of *new igneous mgt* (magnetite growing during degassing) and fluid fraction ($x_{new}+z$), $\delta^{56}Fe_{initial-M2}$ is the Fe isotopy of the melt at the beginning of *Stage 2* ($\delta^{56}Fe_{initial-M2} = 0.08$ ‰) and $\Delta^{56}Fe^{melt-fluid} \approx 1000 \ln(\alpha)$.

Considering that both fractionation styles are end member scenarios, we also calculated an intermediate scenario in which magnetite (*new igneous mgt*) and aqueous fluid are extracted only once from the system during degassing at an intermediate pressure step of 150 MPa; this is referred to as "open system - one step" fractionation in Fig. 4.10. This scenario would increase $\delta^{56}Fe_{fluid}$ from -0.39 to -0.28 ‰ (equation 11), $\delta^{56}Fe_{melt}$ from 0.08 to 0.19 ‰ (equation 12) and result in a maximum $\delta^{56}Fe_{mgt}$ value as heavy as 0.27 ‰ (equation 13).

$$\delta^{56}Fe_{fluid} = x\Delta^{56}Fe_{mgt-melt} + x\Delta^{56}Fe_{melt-fluid} - \delta^{56}Fe_{one-step} + y\Delta^{56}Fe_{melt-fluid}$$

<div align="right">equation 11</div>

$$\delta^{56}Fe_{melt} = \delta^{56}Fe_{fluid} + \Delta^{56}Fe_{melt-fluid}$$

<div align="right">equation 12</div>

$\delta^{56}Fe_{mgt} = (\delta^{56}Fe_{one\text{-}step} - y\delta^{56}Fe_{melt} - z\delta^{56}Fe_{fluid}) / x$

equation 13

Here, $\delta^{56}Fe_{one\text{-}step}$ is the Fe isotopic composition of the melt calculated for the desired step (e.g., 150 MPa) using equations 6 and 7, but excluding the *initial mgt* from the Fe fractions between melt, aqueous fluid and *new igneous mgt*.

Consequently, degassing of a saline fluid with an initial $\delta^{56}Fe_{fluid}$ as light as -0.39 ‰ (Heimann et al., 2008) would increase $\delta^{56}Fe_{mgt}$ of the *new igneous mgt* (i.e., magnetite that crystallizes during decompression) to be as isotopically heavy as the measured natural igneous magnetite samples from Los Colorados (Table 1), shown as a red field in Fig. 4.10. Importantly, this is consistent with the measured increasing $\delta^{56}Fe_{mgt}$ values in igneous magnetite with decreasing concentrations of trace elements such as Ti, Al, Mn, V, Ga and Zn (Fig. 4.7).

4.5.3 Stage 3: Magmatic-hydrothermal magnetite precipitation during fluid cooling

Stage 3 of the model simulates magnetite precipitation from an aqueous fluid as a result of cooling. This fluid was separated from the source magma at the end of Stage 2, together with significant amounts of igneous magnetite (i.e., a fluid-magnetite suspension).

The evolution of $\delta^{56}Fe_{mgt}$ for magnetite that precipitates from the magmatic-hydrothermal fluid can be predicted as a function of decreasing temperature (e.g., from 800 to 400 °C) by using equation 3. As a first order assumption, we suggest that the Fe isotope composition of this magmatic-hydrothermal magnetite is best approximated by (open system) Rayleigh crystallization (equation 14).

95

$\delta^{56}Fe_{fluid}{}^f = (1000 + \delta^{56}Fe_{initial\text{-}F3}) * f^{(\alpha-1)} - 1000$

equation 14

The "snapshot" $\delta^{56}Fe_{mgt}{}^f$ at a given fraction f can then be determined by equation 15:

$\delta^{56}Fe_{mgt}{}^f = \Delta^{56}Fe_{mgt\text{-}fluid} + \delta^{56}Fe_{fluid}{}^f$

equation 15

where $\Delta^{56}Fe_{mgt\text{-}fluid} \approx 1000\ \ln(\alpha)$. We assume an initial Fe isotope composition of the fluid of $\delta^{56}Fe_{initial\text{-}F3} = -0.26$ ‰, which is the heaviest predicted $\delta^{56}Fe$ value at the end of *Stage 2* (white star in Fig. 4.10). Thus, the predicted Fe isotope composition of the magmatic-hydrothermal magnetite represents the maximum possible value (i.e., isotopically heaviest).

Model calculations for *Stage 3* indicate that the measured $\delta^{56}Fe_{mgt}$ value of the magmatic-hydrothermal magnetite, shown as a blue field in the Fig. 4.10, is reproduced by the proposed model scenario (i.e., Rayleigh fractionation), if precipitation occurs during cooling from 600 to 400 °C. However, the slightly elevated $\Delta^{56}Fe_{mgt\text{-}fluid}$ values determined experimentally by Sossi and O'Neill (2017) at 800 °C, when compared to the model values predicted by equation 3, indicate that precipitation temperatures may have exceeded 600 °C. These temperatures are consistent with fluid inclusion studies of IOA/IOCG deposits in Chile and Peru, where homogenization temperatures range from 150 to 550 °C, with some >800 °C (Bromann et al, 1999; Chen 2010; Kreiner 2011; Velasco and Tornos 2009; Barton, 2014). Notably, the estimated pressures (50-150 MPa) and fluid salinities (6-50 wt% NaCl$_{eq}$) in these studies are consistent with the predicted conditions of our model (i.e., P$_{final}$< 75 MPa, magmatic-hydrothermal fluid composition of 35

wt% NaCl$_{eq}$). The remaining iron in the hydrothermal fluid (>60 %) can further ascend and eventually precipitate at lower temperatures and pressures forming potentially IOCG deposits stratigraphically above IOA deposits (Knipping et al. 2015 a and b).

4.6 IMPLICATIONS

New *in situ* Fe isotope data, used in conjunction with trace element compositions (e.g., Ti, Al), textural observations and sample depth information, can help to distinguish igneous magnetite cores from magmatic-hydrothermal magnetite rims in the Los Colorados Kiruna-type IOA deposit, Chile. The model presented explains the measured δ^{56}Fe variability within magnetite grains, where hydrothermal parts are lighter than igneous parts. When trace elemental compositions and sample depths information are taken into account for those magnetite grains that show no zoning in order to discriminate between igneous and hydrothermal magnetite, most of the interpreted purely magmatic-hydrothermal magnetites have on average lower δ^{56}Fe when compared to purely igneous magnetites. The sum of all results reveal a systematic pattern at Los Colorados where δ^{56}Fe is on average higher in igneous magnetite (mean δ^{56}Fe= 0.24 ± 0.07 ‰; n=33) when compared to magmatic-hydrothermal magnetite (mean δ^{56}Fe= 0.15 ± 0.05 ‰; n=26).

Using magnetite-melt, melt-fluid, and magnetite-fluid Fe isotope fractionation factors, we predict the evolution of δ^{56}Fe$_{mgt}$ in purely igneous magnetite formed during crystallization from a cooling (Stage 1) and decompression-induced degassing silicate melt (Stage 2), and precipitation of magmatic-hydrothermal magnetite from a cooling exsolved saline magmatic-hydrothermal fluid (Stage 3). These stages, and their pressure-temperature evolution, are modeled in accordance with the *magnetite-flotation model* proposed by Knipping et al. (2015a, b) for the formation of Los Colorados. The

predicted variations in $\delta^{56}Fe_{mgt}$ cover the ranges measured in the igneous and magmatic-hydrothermal magnetite from Los Colorados, respectively. We conclude that *in situ* Fe isotope analyses together with trace element composition of magnetite grains (1) can provide important insights about the source and evolution of magnetite-rich ore deposits, and (2) confirm the magnetite-flotation model as a plausible scenario for the formation of Kiruna-type IOA deposits.

Chapter 5: Accumulation of magnetite by flotation on bubbles during decompression of silicate magma

Jaayke L. Knipping[1,2], James D. Webster[2], Adam C. Simon[3] and François Holtz[1]

[1]*Institut für Mineralogie, Leibniz Universität Hannover, Callinstraße 3, 30167 Hannover, Germany*

[2]*Department of Earth and Planetary Science, American Museum of Natural History, Central Park West at 79th Street, New York, NY 10024-5192*

[3]*Department of Earth and Environmental Sciences, University of Michigan, 1100 North University Ave, Ann Arbor, Michigan 48109-1005, USA*

ABSTRACT

Magnetite (Fe_3O_4) is an iron ore mineral that is globally mined especially for steel production. It is denser (5.15 g/cm^3) than Earth`s crust (~2.7 g/cm^3) and is expected to accumulate at the bottom of melt-rich magma reservoirs. However, recent studies revealed heterogeneous fluid bubble nucleation on oxide minerals such as magnetite during fluid degassing in volcanic systems. To test if the attachment on fluid bubbles is strong enough to efficiently float magnetite in silicate magma, decompression experiments were conducted at geologically relevant magmatic conditions with subsequent annealing to simulate re-equilibration after decompression. The results demonstrate that magnetite-bubble pairs do ascend in silicate melt, accumulating in an upper layer that grows during re-equilibration. This outcome contradicts the paradigm that magnetite must settle gravitationally in silicate melt.

5.1 INTRODUCTION

Fractional crystallization in transcrustal magmatic systems is a fundamental control on magma differentiation, wherein gravitational settling and flotation of minerals based on density contrasts causes compositional evolution of magmas and, in turn, the evolution of Earth's crust (Bowen, 1956). Accordingly, minerals with a density less than Earth`s crust (~2.7 g/cm^3), such as plagioclase (2.6-2.7 g/cm^3), are separated by mineral flotation (Bottinga and Weill, 1970), while dense ore phases such as sulfide melt droplets and oxide minerals (e.g., magnetite: 5.15 g/cm^3, chromite: ~4.5 g/cm^3) are separated by gravitational settling. However, flotation of dense ore phases must be re-evaluated when fluid bubbles exsolve during decompression; i.e., magma ascent (Matveev and Ballhaus, 2002; Mungall et al. 2015). Fluid bubbles preferably nucleate heterogeneously on existing surfaces of sulfide melt droplets and oxide minerals such as magnetite and chromite (Matveev and Ballhaus, 2002; Mungall et al. 2015; Hurwitz and navon, 1994; Gardner and denis, 2004; Gualda and Ghiorso, 2007; Edmonds et al. 2014) owing to larger wetting angles ($\Psi = 45\text{-}50°$) when compared to silicate minerals ($\Psi = 5\text{-}25°$) (Gualda and Ghiorso, 2007) (Fig. 5.1b). Actually, more than 100 years ago the mining industry took advantage of this phenomenon and shifted mineral processing methods from classical gravity separation to more efficient froth flotation wherein dense ore minerals are wetted by pine oil and injected air bubbles. The resulting mineral-bubble pairs float upwards relative to unwetted silicate minerals that sink in the reagent solutions (Fuerstenau et al. 2007). Despite this well-demonstrated beneficiation process, the flotation of ore minerals in magma reservoirs has rarely been considered as a natural process leading to the concentration of ore minerals. Only a few studies attempted to explain ore formation by the wetting affinity between exsolved fluids and ore phases. Examples include chromite pods in podiform chromite deposits

(Matveev and Ballhaus, 2002), Cu-Au-rich sulfide melts in porphyry ore deposits (Mungall et al. 2015) as well as magnetite in Kiruna-type iron oxide-apatite deposits (Knipping et al. 2015a) (hereafter, referred to as IOA deposit).
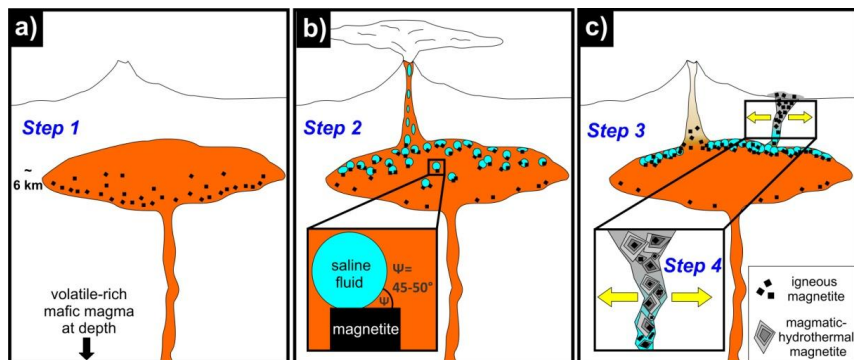
Figure 5.1: Schematic illustration of the magnetite-flotation model for Kiruna-type iron oxide-apatite deposits (Knipping et al. 2015a). (a) Primary igneous magnetite crystallizes from silicate melt in a magma reservoir and should gravitationally settle owing to its higher density relative to melt. However, (b) if saline fluid exsolves during decompression and bubbles nucleate on magnetite crystals owing to favorable wetting properties, then (c) magnetite-bubble pairs form and buoyantly ascend, coalesce and separate as a magnetite-fluid suspension within the magma, and can escape the magma if extensional tectonic stress opens crustal fractures wherein secondary magmatic-hydrothermal magnetite can precipitate, at lower pressures and temperatures, and surround primary igneous magnetite crystals.

Genetic models proposed to explain the formation of IOA deposits are fiercely debated. IOA deposits occur worldwide and are economically important not just because of their high concentration of Fe, but also their enrichment in rare earth elements (REE) crucial for modern technologies. Classical hypotheses invoke (magmatic-) hydrothermal (Barton and Johnson, 2000; Sillitoes and Burrows, 2002; Westhues et al. 2017) versus purely magmatic processes such as liquid immiscibility between Si-rich melt and Fe-rich melt (Nyström and Henriquez, 1994; Naslund et al. 2002; Tornos et al. 2016; Hou et al. 2018). In the case of the numerous IOA deposits along the Chilean Iron Belt, none of these classical models fully explain the complex textures and chemical

composition of magnetite. Thus, based on observations at the world-class Los Colorados IOA deposit (~ 350 Mt Fe, magnetite ≤ 90 % modal) within the Chilean Iron Belt, a novel formation model was proposed that combines the contrasting textural/geochemical observations (Knipping et al. 2015a), i.e., silicate inclusion-rich magnetite cores with an igneous signature (high Ti, V, Al, Mn) surrounded by pristine magnetite with a (magmatic-) hydrothermal signature (low Ti, V, Al, Mn), into one coherent process. In this model, primary igneous magnetite crystals are proposed to form as a liquidus phase in an oxidized, hydrous andesitic magma reservoir, which are ubiquitous in arc magma systems (Fig. 5.1a). Upon magma ascent and decompression, saline fluids exsolve from the silicate melt and, owing to enhanced heterogeneous nucleation of fluid bubbles on magnetite surfaces, magnetite and fluid attach to each other to form a suspension that is proposed, although not demonstrated experimentally, to have a lower average density than the surrounding melt (Knipping et al. 2015a) (Fig. 5.1b and c). Importantly, depending on the Cl concentration of the exsolved volatile phase, the magnetite-fluid suspension will contain a significant fraction of Fe dissolved as $FeCl_2$ in the fluid (Simon et al. 2004). The solubility of $FeCl_2$ in fluid decreases during cooling (600-400 °C), resulting in precipitation of secondary magmatic-hydrothermal magnetite, a process that is even more effective at large decompression rates (Rojas et al. 2018). Thus, changing tectonic stress in the late Lower Cretaceous within the Atacama Fault System - host to the Chilean Iron Belt – allowed the ascent of the magnetite-fluid suspension into shallow crustal hydraulic fractures with concomitant precipitation of magmatic-hydrothermal magnetite surrounding primary igneous magnetite (Fig. 5.1c). This model explains the apparently contrasting geochemistry within and among magnetite grains at Los Colorados (Knipping et al. 2015a) and other Chilean IOA deposits (Rojas et al. 2018; Simon et al. 2018; Ovalle et al. 2018). However, it was unclear if the

attachment force between degassing bubbles and magnetite would be strong enough to segregate magnetite from silicate melt, and how much degassing is necessary for efficient separation of magnetite.

In this study, we performed high-temperature decompression experiments to test the hypothesis that magnetite flotation in a silicate melt is physically possible, and if decompression and simultaneous volatile saturation of silicate melt can lead to the formation of a magnetite-bubble suspension that has a density low enough to separate from, and ascend within, silicate melt. We assumed that the parental mantle-derived basalts in subduction zones are water-rich and lead to the emplacement of hydrous andesitic magmas in the upper crust (3-10 km) (Annen et al. 2005). Arc-derived andesitic magmas are generally more oxidized (NNO to NNO+4) (Carmichael, 1991), more hydrous (5-7 wt% H_2O, sometimes up to 16 wt%) (Annen et al. 2005; Carmichael, 2002) and enriched in halogens such as Cl (Wallace, 2005) when compared to magmas in other geologic settings. These and other parameters (see Supplementary Material S5.1) influence the exact depth range for possible magnetite flotation. Since Knipping et al. (2015a) proposed these arc-magmatic conditions as prerequisite for the magnetite-flotation model, we equilibrated an andesitic melt with 6 wt% H_2O ± 1wt% Cl at near-liquidus, fluid-undersaturated, oxidized conditions (250 MPa ≈ 6 km, 1050 °C, ~NNO+3). The starting melt composition (andesite P1D; Martel et al. 1999) crystallizes magnetite as the sole liquidus phase at these conditions. All experiments were initially equilibrated for 72 hours prior to isobaric quenching or isothermal decompression wherein pressure was decreased to 150 MPa before any other phase begins to crystallize (see Supplementry Material: Fig. S5.1). A continuous rate of ~0.025 MPa/s was chosen, which is equal to magma ascent rate of ~0.5 m/s. The decompression experiments were either

quenched immediately after decompression (t_a=0h) or they were held at elevated temperature after decompression and annealed for different time scales (t_a=3h or 72h) to allow the ascent of magnetite-fluid bubble assemblages. After the experiments, capsules were mounted in epoxy to maintain their spatial orientation at run conditions, and the vertical walls of the capsule were removed by double-sided polishing to allow analysis of the quenched experimental magma perpendicular to the bubble ascent direction.

5.2 RESULTS

Image analysis of the isobaric, fluid-undersaturated runs (i.e., without decompression) reveals accumulation of magnetite crystals that settled to the bottom of the melt for both the H_2O-bearing (Fig. 5.2a) and the H_2O+Cl-bearing experiments. The measured thermal gradient across the charge was always $\leq$ 5 °C; thus, gravitational force is the only explanation for spatial heterogeneity of magnetite crystals. However, after decompression and subsequent annealing, magnetite accumulated in the upper part of the melt (Fig. 5.2b).
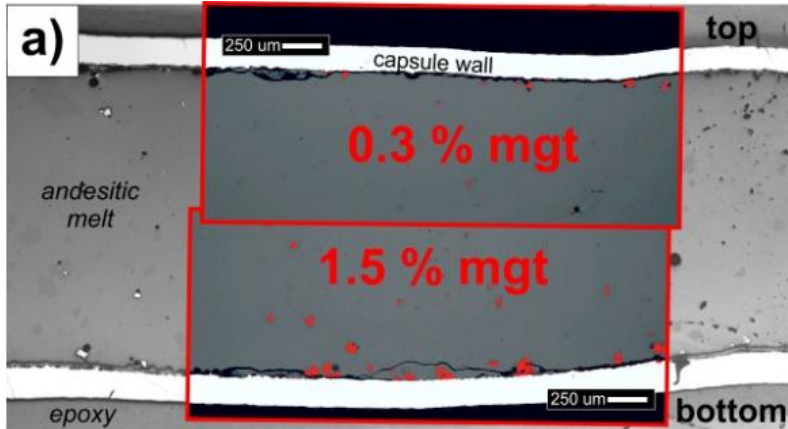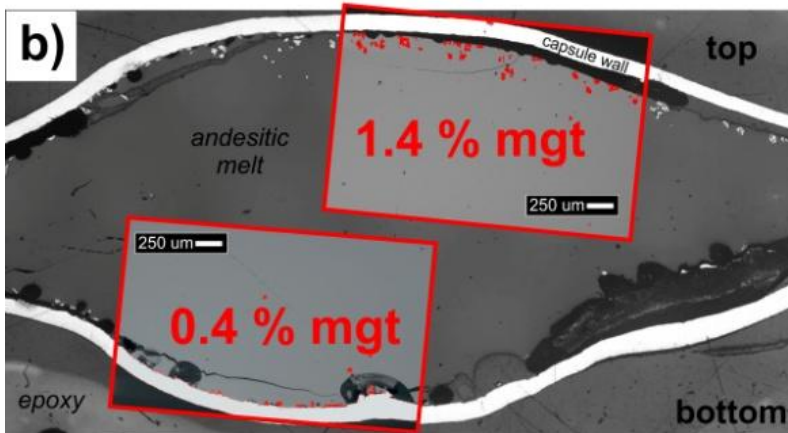
Figure 5.2: Reflected light images with backscattered-electron (BSE) image insets of H$_2$O-only experiments showing andesitic glass (quenched melt), magnetite (mgt) crystals, and vesicles containing fluid bubbles: (a) Prior to decompression and (b) after decompression and 72h annealing (t$_a$=72h). The phase proportion of magnetite crystals, highlighted in red, was determined quantitatively by using the software *imageJ*. Prior to decompression, the abundance of magnetite is larger at the bottom of the experimental setup (owing to gravitational crystal settling), but after decompression (and annealing) a larger concentration of magnetite is observed in the upper part of the capsule (due to magnetite-bubble ascent).

For both fluid compositions, images of almost all decompression experiments reveal a magnetite layer that accumulated efficiently at the top of the melt and becomes thicker and denser with increasing annealing time (Fig. 5.3). The only distinct difference caused by the fluid compositions is magnetite crystal size, which is always smaller in H_2O+Cl-bearing decompression experiments.
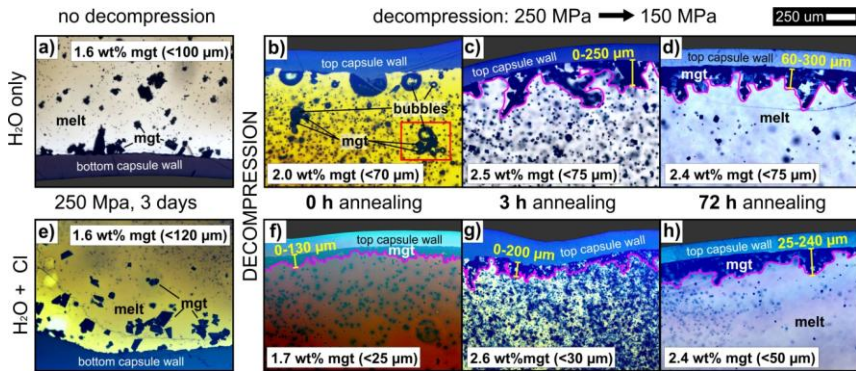
Figure 5.3: Transmitted light images of andesitic glass, magnetite crystals, and vesicles of all experiments. (a) to (d) represent H_2O-only and (e) to (h) H_2O+Cl experiments. (a) and (e) show the gravitational settling of large magnetite crystals at the bottom of the capsules prior to decompression (250 MPa). (b) and (f) reveal the beginning of magnetite-bubble ascent and first upper accumulation of magnetite immediately after decompression (250 $\rightarrow$ 150 Mpa, t_a=0h). (c) and (g) show the upper accumulation after t_a=3h and (d) and (h) after t_a=72 h implying a growth of up to 300 μm of the upper magnetite-rich layer with increasing t_a.

A smaller crystal size allows faster ascent (Gualda and Ghiorso, 2007), and thus, greater upward accumulation of magnetite crystals occurs immediately after decompression to form a magnetite layer up to 130 μm thick in the H_2O+Cl-bearing run (Fig. 5.3f). In contrast, larger magnetite crystals in the H_2O-bearing experiments appear to have ascended more slowly (Fig. 5.3b and 5.4a). The magnetite size limit for a positive buoyancy of bubble-magnetite pairs held together by surfaces forces ranges between 500-1000 μm (Gualda and Ghiorso, 2007). Therefore, even the large crystals of the H_2O-only bearing experiments (~75 μm) are comfortably within the range of possible flotation, as long as similar sized bubbles are present. Such large bubbles are easily

produced by diffusive coarsening; i.e., Ostwald ripening within days to months (Lautze et al. 2011). At t_a=3h, for both fluid compositions, magnetite layers of ~200 μm thickness form (Fig. 5.3 c,g) and grow to ~300 μm at t_a=72h (Fig. 5.3 d,h). Owing to the smaller crystal size in the H_2O+Cl-bearing experiments, the upper magnetite-enriched layers appear to be less thick, but more dense. Larger magnetite crystals in the H_2O-bearing experiments clearly indicate the formation of individual ascending magnetite-fluid bubble pairs in silicate magma (Fig. 5.3b and 5.4a).
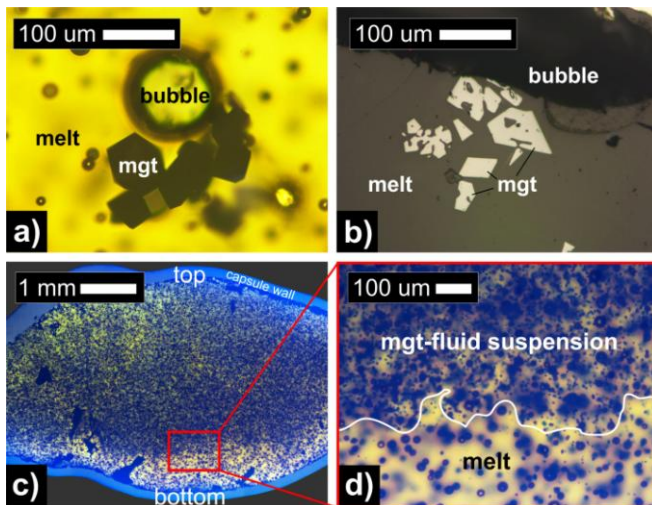
Figure 5.4: Microscopy images of andesitic glass, magnetite crystals, and vesicles in decompression experiments. (a) represents the inset (red rectangular) in Fig. 5.3b showing the microscopic process of magnetite flotation due to preferential attachment of magnetite onto an upward ascending exsolved fluid bubble (additional images in the Supplementary Material: Fig. S5.5). (b) is a reflected light image of the H_2O-only experiment after t_a=72h exhibiting rapid magnetite (white) growth from dendritic into euhedral crystals (hopper growth) entrapping several melt (gray) inclusions. (c) and (d) are transmitted light images from the H_2O+Cl experiment after t_a=3h that reveal the macroscopic ascent and buoyant separation of a magnetite–fluid bubble-suspension from the residual melt after decompression (see also BSE images in Supplementary Material S5.3: Fig. S5.4).

The abundance of smaller magnetite crystals in the H_2O+Cl-bearing experiments reveals that a large-scale process by which innumerable magnetite-fluid bubble pairs separate buoyantly as a magnetite-fluid suspension within silicate melt may be realistic (Fig. 5.4c and d). At t_a=72h, all exsolved fluid bubbles accumulated into a single mass located between the capsule wall and the melt. Thus, no further growth of the upper layer is expected at t_a>72h and a minimum velocity of 42 μm/h of the floating suspension is estimated. Therefore, a magnetite layer of ~ 30 m is theoretically able to accumulate through flotation after ~ 2700 years on a magma reservoir scale of 1000 m (see Supplementary Material S5.2). The decompression experiments agree with a static run at 150 MPa, where small magnetite crystals accumulated along with exsolved fluid bubbles at the top of the melt column, in contrast to the static fluid-absent experiment at 250 MPa (see Supplementary Material: Fig. S5.6).

The crystal textures of magnetite also provide information on the magmatic processes involved. We observed the ubiquitous growth of magnetite crystals that appear as dendritic magnetite transitioning into euhedral crystals; i.e., hopper crystals (Fig. 5.4b).

5.3 DISCUSSION

Supersaturation caused by fast decompression rates lead to rapid, diffusion-limited crystal growth, such as hopper crystals (Brugger and Hammer, 2010), which entrap melt inclusions within eventual large (up to ~100 μm), euhedral crystals (Wallace, 2005). Skeletal crystal growth reflects rapid, diffusion-limited crystallization that can lead to the entrapment of silicate melt inclusions within eventual large (up to ~100 μm), euhedral magnetite crystals (Wallace, 2005). Such melt inclusions are consistent with polycrystalline silicate inclusions observed in magnetite "cores" from IOA deposits and in chromite

from podiform chromite deposits that are interpreted as igneous artifacts (Melcher et al. 1997; Nold et al. 2014; Knipping et al. 2015a; Rojas et al. 2018; Ovalle et al. 2018). Our experimental results provide clear evidence that polycrystalline silicate inclusions in oxides can be primary igneous features resulting from rapid oxide crystallization from silicate melt. Abundant diffusion-limited grown dendritic magnetite grains are also observed in feeder dikes of the enigmatic El Laco IOA deposit as well as in the roof-zone of the Skaergaard layered intrusion (Henriquez and Martin, 1978; Naslund, 1984). In both distinctly different localities, the magnetite habit was interpreted to result from degassing-induced supersaturation (Henriquez and Martin, 1978; Naslund, 1984), which is consistent with our experimental results.

In the case of IOA deposits, tectonic stress changes in arc/back-arc settings may cause either crustal scale venting fractures (Chilean Iron Belt; Kiruna and Grängesberg, Sweden) or caldera collapses (El Laco, Chile; St. Francois Mountains, Missouri, USA), where the opened fractures would have filled with the magnetite-fluid-suspension to form massive magnetite deposits with both igneous and hydrothermal features (Fig. 5.1c) (Ovalle et al., 2018). In contrast, undisturbed magnetite layers are found in economically important Fe-, Ti-, V-, Cr-, and platinum group element- (PGE) mineralized layered mafic intrusions. These are intact, ancient, sill-like magma reservoirs that did not experience significant tectonic disturbance during their evolution. Layered intrusions such as the Bushveld complex and Skaergaard contain ubiquitous oxide monomineralic layers of magnetite (5.15 g/cm^3), ilmenite (4.7 g/cm^3) and/or chromite (4.5 g/cm^3) that sometimes overlie less dense cumulates of plagioclase (2.6-2.7 g/cm^3) and thus cannot be explained by typical gravitational settling (Reynolds, 1985). Our experiments demonstrate that already a moderate amount of fluid exsolution ($\leq$ 0.90 wt% H_2O, Table S5.2) is

sufficient for oxide flotation. Thus, even if only minor vapor saturation occurs in the melt-rich magma that overlays the crystal pile in layered intrusions, possibly enriched in H_2O by dehydration of underlying country rocks (Boudreau, 2016), mineral-bubble flotation should be considered a plausible process, possibly acting jointly with others, to form monomineralic oxide layers in mafic layered intrusions.

5.4 METHODS
5.4.1 Experiments

All experiments were conducted in an internally heated pressure vessel (IHPV) at the American Museum of Natural History (AMNH). For this, powdered synthetic glass representative of the andesite P1D composition (Martel et al., 1999) was loaded with 5.75 ± 0.01 wt% doubly distilled water ± 1.02 wt% Cl as $FeCl_3$ solution into AuPd capsules (3 mm or 5 mm in diameter) and compacted by using a piston. The capsules were welded shut and tested for leakage at T > 100 °C prior to experiments. Each experiment was loaded with two capsules, one water-only and one water+Cl-bearing capsule. All experiments were equilibrated for three days at slightly subliquidus (magnetite-bearing) water-undersaturated conditions of 1050 °C and 250 MPa and intrinsic redox conditions that are approximately NNO+3 (Webster et al. 1996). The temperature of the charge was constantly monitored by using two K-type thermocouples at different positions of the capsule (upper left and lower right) and the measured thermal gradient was always < 5 °C. Therefore, the heterogeneous spatial distribution of crystals cannot be explained by a thermal gradient. One experiment (*09-H2O* and *09-Cl*) was run at constant pressure and quenched after equilibration without decompression, while all others were decompressed isothermally after equilibration with a continuous decompression rate of ~ 0.025 MPa/s down to 150 MPa, which is equal to

magma ascent rate of ~0.5 m/s. At this rate, water diffusion into bubbles is fast enough to maintain melt-fluid equilibrium (Rutherford et al. 2000). These experiments were either quenched immediately after reaching final pressure (t_a=0h: *16-H₂O* and *14-Cl*) or annealed after decompression for different durations: t_a=3h (*28-H₂O* and *28-Cl*) and t_a=72h (*01-H₂O* and *01-Cl*). After quenching, the capsules were carefully extracted from the vessel and mounted in epoxy while maintaining their original experimental orientation (top vs. bottom). In order to allow analyses perpendicular to the apparent bubble ascent direction, all capsules were mounted in epoxy, polished on both sides, and prepared as a thick section through the middle of the capsule body. For a first estimate of the magnetite distribution, reflected and transmitted light microscopy were conducted on each sample and 40-60 5x-magnified pictures were stitched together by using the software *Microsoft ICE* (e.g., Fig. 5.3c).

5.4.2 BSE image analysis

To quantify magnetite distribution within the capsules, backscattered-electron (BSE) images were taken of the top and the bottom of each capsule using a *ZEISS EVO60 VP SEM* at the AMNH. The contrast of the images was adjusted to allow easy discrimination of magnetite from glass, capsule material and epoxy. The BSE images were afterwards analyzed by using the image analysis software *imageJ* that allowed the calculation of the phase proportion of magnetite within the glass (excluding the capsule material and epoxy). The quantification of each top and bottom area is visualized in Fig. S5.3 in the Supplementary Material.

5.4.3 Electron probe microanalysis

All experimental glasses were analyzed quantitatively by using a *Cameca SX-100* electron microprobe at the AMNH. Fifteen data points were collected per sample to measure the concentration of all major and minor elements other

than H_2O (Na, K, Mg, Ca, Al, Si, Ti, Fe and Cl) in the glass. An accelerating voltage of 15 kV was applied using a 10-μm beam size, beam currents of 5 nA (Na, K), 10 nA (Mg, Ca, Al, Si, Ti) and 40 nA (Cl) and counting times of 5s (Na), 10 s (K), 20 s (Mg, Ca, Al, Si, Ti) and 120 s (Cl). Prior to each analytical session, the microprobe was calibrated by using the standards diopside (Si, Ca, Mg), jadeite (Na), orthoclase (K and Al), rutile (Ti), fayalite (Fe) and scapolite (Cl). The standardization process was checked by measuring three internal standards (basalt, andesite and rhyolite) prior and after each session. The results of the experimental glass analyses were normalized to 100% and are listed in Table S5.1 in the Supplementary Material. Since magnetite was the only mineral phase in all samples, and Fe loss to the AuPd capsule is negligible at wet and oxidizing conditions (Kawamoto et al. 1994), the wt% concentration of magnetite (Fe_3O_4) was easily calculated from the FeO concentration in the residual glass by difference to the fully glassy starting composition P1D.

5.4.4 IR-spectroscopy

In order to measure the water concentration and distribution within the samples, IR-profiles were measured perpendicular to bubble ascent direction (bottom to top) by using a *Nicolet Nexus 670 Fourier Transform Infra Red (FTIR) spectrometry system* with an attached IR Plan microscope (micro-FTIR system) at the AMNH. The spectral resolution was set to 4 cm^{-1} and five measurements were taken per sample using 200 scans. The background was analyzed after each sample. The Lambert-Beer law was applied to calculate the concentration of dissolved OH- (4500 cm^{-1}) and molecular H_2O (5200 cm^{-1}) in the glass. Therefore, doubly polished glass chips (~ 100 μm) were prepared for the analyses and measured exactly using a micrometer (88-100 μm). The density of the glasses was estimated using the known glass composition in a density calculation model (Ochs and Lange, 1999). The absorption coefficients

1.27 ± 0.07 L/mol cm for molecular water and 0.84 ± 0.07 L/mol cm for hydroxyl groups in andesitic melt composition were applied (Fiege et al. 2014). The results for the total water concentrations are listed in Table S5.2 in the Supplementary Material. Water distribution is homogeneous and no systematic variation was detected in either direction for the samples.

6. Conclusion

During this PhD study magnetite samples from the Los Colorados IOA deposit in the Chilean Iron Belt were investigated extensively with several perological and geochemical methods in order to unravel the controversial discussed formation of these ore deposit types.

The analytical results of trace element analyses on magnetite (*Chapter 2 + 3*) revealed zoning from core to rim. Especially those elements, which are commonly used for discrimination between different iron ore deposit types (Ti, V, Al and Mn) are more enriched in the center, while they are relatively depleted in the magnetite rims or surrounding magnetite matrix. The concentrations measured in the cores are compareable to magnetite from nelsonites (Al+Mn > 0.4 wt%; Ti+V > 1 wt%), i.e. indicate an igneous formation such as crystallization from a melt, while the concentrations in the rims are more similar to magnetite precipitated from a hydrothermal fluid (Al+Mn < 0.2 wt%; Ti+V < 0.8 wt%). Intermediate concentrations imply a transitioning phase in which magnetite precipitated from a magmatic-hydrothermal phase such as in porphyry deposits.

Additionally, *in-situ* Fe-isotope measurements were conducted on the same samples (*Chapter 4)* in which also changing isotope signatures were discovered between the assigned igneous and (magmatic-) hydrothermal magnetites. The analytical results revealed, that magmatic-hydrothermal magnetite is on average lighter in their $\delta^{56}Fe$ values (0.15 ± 0.05 ‰; n=26) when compared to igneous magnetite (0.24 ± 0.07 ‰; n=33). Further, the $\delta^{56}Fe$ of the igneous magnetite correlate negatively with trace elements concentration typical for an igneous formation (Ti, Al, Ga, V, Mn, Zn) (Nadoll et al. 2014); igneous magnetite becomes isotopically heavier with decreasing concentrations

of these elements, indicating a trend towards higher δ^{56}Fe in the magnetite with magma evolution. This observation was unexpected as igneous magnetite is known to capture heavy δ^{56}Fe due to its high ferric component (Bigeleisen and Mayer, 1947; Polyakov et al., 2007; Schauble, 2004; Schauble et al., 2009) that would usually deplete the remaining magma in heavy δ^{56}Fe and in turn would result in magnetite with a lighter δ^{56}Fe with ongoing magma evolution (i.e. magnetite crystallization). However, an assumed simultaneous exsolving magmatic hydrothermal fluid could uptake mainly ferrous Fe and thus light δ^{56}Fe (Poitrasson and Freydier, 2005; Heimann et al. 2008; Telus et al., 2012; Bilenker et al., 2012) enriching the remaining magma in heavy δ^{56}Fe and thus could lead to crystallization of magnetite with heavier δ^{56}Fe at later igneous stages (lower concentration of Ti, Al, Ga, V, Mn and Zn).

The findings of *Chapter 2*, *3* and *4* did not fit any of the formation models existing to that date, since none of the models involved true igneous magnetite crystallization from a melt directlty coupled to hydrothermal precipitation of magnetite. Therefore, we proposed a completely new formation model for Kiruna-type IOA deposits.

In our new formation model magnetite initially crystallizes from a hydrous, oxidized silicate melt with an andesitic composition (not an immiscible Fe-rich melt) common for arc-magmatism (Fig. 6.1a). As magma ascends, e.g. during a volcanic eruption, these magnetite crystals serve as nucleation sites for exsolving fluid bubbles, in order to reduce surface tensions (Hurwitz and Navon, 1994). The wetting properties between fluid bubbles and oxide minerals such as magnetite are more pronounced than between fluid bubbles and silicate minerals such as plagioclase (Hurwitz and Navon, 1994; Gardner and Denis, 2004; Cluzel et al. 2008) due to larger wetting angles on oxides (Ψ=45-50°) than on silicate minerals (Ψ=5-25°) (Gualda and Ghiorso,

2007). This feature allows for the flotation of magnetite, which is a mineral that is actually significantly denser (5.15 g/cm^3) than common silicate magma (~2.7 g/cm^3).
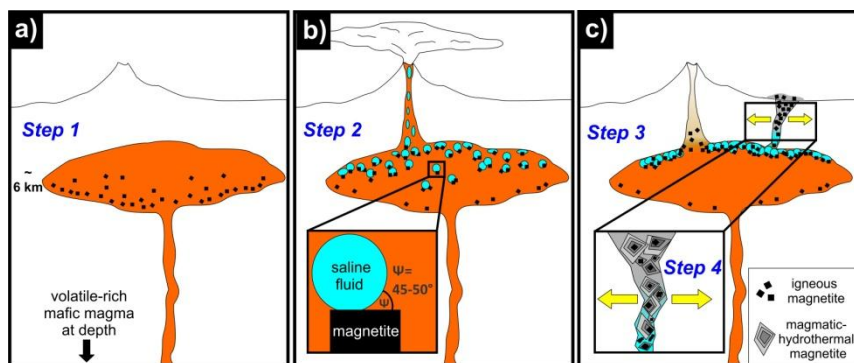
Figure 6.1: Schematic illustration of the magnetite-flotation model for Kiruna-type iron oxide-apatite deposits. (a) Primary igneous magnetite crystallizes from silicate melt in a magma chamber and should gravitationally settle owing to its higher density relative to melt. However, (b) if saline fluid exsolves during decompression and bubbles nucleate on magnetite crystals due to favorable wetting properties, then (c) magnetite-bubble pairs form and buoyantly ascend, coalesce and separate as a magnetite-fluid suspension within the magma, and can escape the magma if extensional tectonic stress opens crustal fractures wherein secondary magmatic-hydrothermal magnetite can precipitate, at lower pressures and temperatures, and surround primary igneous magnetite crystals (from Knipping et al. 2019).

The magnetite-fluid bubble pairs with a lower density than the surrounding magma would ascend within the magma and possibly collect further magnetite and fluid bubbles resulting in a rising magnetite-rich suspension (Fig. 6.1b). This process was described and used by Edmonds et al. (2014) to explain the formation of magnetite-rich mafic enclaves in arc-andesites. Simultaneously, high chlorine concentration in the parental magma of Los Colorados caused by recycling of the subducted oceanic crust (Philippot et al. 1998), led to an additional Fe enrichment via dissolved iron chloride complexes in the fluid (Simon et al., 2004; Bell and Simon, 2011). Changing tectonic conditions in the Atacama Fault System during the late Lower Cretaceous (~110 Ma) may have caused a sudden destabilization of the magma chamber. Resulting

hydraulic fractures in the overlaying crystalline crust could have enhanced a further, even faster and more efficient ascent of the iron rich suspension into more shallow levels. Due to the sudden change in temperature and pressure, the dissolved iron ($FeCl_2$) precipitates as massive magmatic-hydrothermal magnetite surrounding the igneous magnetite crystals (cores) (Fig. 6.1c). This process is able to explain the coeval existence of pure igneous magnetite cores and magmatic-hydrothermal magnetite within one deposit. Model calculations of the δ^{56}Fe evolution in melt, magnetite, and fluid in *Chapter 4* support this flotation model as feasible formation process for Los Colorados and likely other Kiruna-type IOA deposits.

In fact, more than 100 years ago the mining industry utilized the preferred wetting on ore minerals and changed mineral processing methods from classical gravity separation to more efficient froth flotation wherein dense ore minerals are wetted by pine oil and injected air bubbles. The resulting mineral-bubble pairs float upwards relative to non-wetted silicate minerals that sink in the reagent solutions. Despite this well-demonstrated concentration process, the flotation of ore minerals in magma chambers, has to date rarely been considered as a natural process leading to the formation of ore deposits.

To change these original views, we conducted in *Chapter 5* decompression experiments at magmatic reasonable conditions in internally heated pressure vessels (IHPV). We wanted to test, if magnetite flotation on exsolved fluid bubbles is really possible in a silicate melt and if the density of a magnetite-fluid suspension would be low enough to efficiently segregate and accumulate magnetite at the top of residual silicate magma. All experimental parameters (pressure, temperature, oxygen fugacity, magma and fluid composition, decompression rate) were set to suit those of arc-magmatic conditions expected within the Chilean Iron Belt. Image analysis of the fluid

absent isobaric experiments (without decompression) revealed an expected accumulation of magnetite at the bottom of the experimental capsules, whereas the samples from fluid present (decompression + annealing) experiments revealed an efficient accumulation of the dense minerals magnetite at the top of the experimental capsules overlaying less dense silicate melt. This observation is not just experimental evidence for our new formation model, but may also change classical views on fractional crystallization, which is a basic concept in understanding magma evolution. Dense minerals are expected to settle gravitationally within silicate magma fractionating the residual magma toward a more felsic composition (Bowen, 1956). However, when exsolved fluids are present, our experimental results contradict the paradigm, that magnetite and probably other dense phases such as chromite (Matveev and Ballhaus, 2002) or sulphide melt droplets (Mungall et al. 2015) must settle gravitationally. In fact, our observations may also solve parts of the ongoing debate about mafic layered intrusions, such as Bushveld complex and Skaergaard, in which oxide monomineralic layers of magnetite, ilmenite and/or chromite sometimes overlie less dense cumulates of plagioclase (anorthosite).

References

Allen, R. L., Lundstrom, I, Ripa, M., & Christofferson, H. (1996). Facies analysis of a 1.9 Ga, continental margin, back-arc, felsic caldera province with diverse Zn-Pb-Ag-(Cu-Au) sulfide and Fe oxide deposits, Bergslagen region, Sweden. *Econ. Geol.* **91**(6), 979-1008.

Annen, C., Blundy, J.D. & Sparks, R.S.J. (2005) The genesis of intermediate and silicic magmas in deep crustal hot zones. *J. Petrol.*, **47**(3), 505-539.

Antignano, A. and Manning C.E. (2008) Fluorapatite solubility in H_2O and H_2O–NaCl at 700 to 900 °C and 0.7 to 2.0 GPa. *Chem. Geol.* **251**, 112-119.

Arévalo, C., Grocott, J. and Welkner, D. (2003) The Atacama Fault System in the Huasco province, southern Atacama Desert, Chile. In Proceedings of the 10th Congreso Geológico Chileno, p 1-5.

Asimow, P.D., Ghiorso, M.S. (1998) Algorithmic Modifications Extending MELTS to Calculate Subsolidus Phase Relations. *Am. Min.*, **83**, 1127-1131

Baker, T. (2002) Emplacement depth and carbon dioxide-rich fluid inclusions in intrusion-related gold deposits. *Econ. Geol.* **97**, 1111–1117.

Balcone-Boissard, H., Villemant, B. and Boudon, G. (2010) Behavior of halogens during the degassing of felsic magmas. *Geochem. Geophys. Geosys.* **11**, 1-22.

Barton, M.D. (2014) Iron oxide(–Cu–Au–REE–P–Ag–U–Co) systems. In *Treatise of Geochemistry* (eds. Holland, H. and Turekian, K.) v. 13, pp. 515-536.

Barton, M.D., and Johnson, D.A. (1996) Evaporitic-source model for igneous-related Fe-oxide (REE-Cu-Au-U) mineralization. *Geology* **24**, 259-262.

Barton, M.D. and Johnson, D.A. (2004) Footprints of Fe-oxide(-Cu-Au) systems. SEG 2004: Predictive Mineral Discovery Under Cover. Centre for Global Metallogeny. *The University of Western Australia*, Spec. Pub. **33**, 112-116.

Bell, A. and Simon, A.C. (2011) Evidence for the alteration of the $Fe^{3+}/\Sigma Fe$ of silicate melt caused by the degassing of chlorine-bearing aqueous volatiles. *Geology* **39**, 499-502.

Bigeleisen, J., & Mayer, M. G. (1947) Calculation of equilibrium constants for isotopic exchange reactions. *J. Chem. Physics* **15** (5), 261-267.

Bilenker, L.D., Simon, A., Lundstrom, C.C. and Gajos, N. (2012) Iron isotope fractionation among magnetite, pyrrhotite, chalcopyrite, rhyolite melt and aqueous fluid at magmatic-hydrothermal conditions. AGU Fall Meeting, ID: V11A-2734, San Francisco, CA, USA.

Bilenker, L.D., Simon, A.C., Reich, M., Lundstrom, C.C., Gajos, N., Bindeman, I., Barra, F. and Munizaga, R. (2016) Fe-O stable isotope pairs elucidate a high-temperature origin of Chilean iron oxide-apatite deposits. *Geochim.Cosmochim. Acta* **177**, 94-104.

Bodnar R.J. and Vityk M.O (1994) Interpretation of microthermometric data of H_2O-NaCl fluid inclusions. In *Fluid inclusions in minerals, Methods and Application*, Virginia Tech, Blackburg, p. 117-130.

Bonyadi, Z., Davidson, G.J., Mehrabi, B., Meffre, S. and Ghazban, F. (2011) Significance of apatite REE depletion and monazite inclusions in the brecciated Se–Chahun iron oxide–apatite deposit, Bafq

district, Iran: insights from paragenesis and geochemistry. *Chem. Geol.* **281**, 253–269.

Bottinga, Y. & Weill, D (1970) Densities of liquid silicate systems calculated from partial molar volumes of oxide components. *AJS*, **269**(2), 169-182.

Boudreau, A. (2016) Bubble migration in a compacting crystal-liquid mush. *Contrib. Mineral. Petrol.*, **171**(4), 32.

Bowen, N.L., *The evolution of the igneous rocks*. (Dover Publications, 1956).

Broman, C., Nyström, J.O., Henríquez, F. and Elfman, M. (1999) Fluid inclusions in magnetite-apatite ore from a cooling magmatic system at El Laco, Chile. *GFF* **121**, 253–267.

Brugger, C. R., & Hammer, J. E. (2010) Crystallization kinetics in continuous decompression experiments: implications for interpreting natural magma ascent processes. *J. Petrol.*, **51**(9), 1941-1965.

Burgisser, A. and Scaillet, B. (2007). Redox evolution of a degassing magma rising to the surface. *Nature* **445** (7124), 194.

Candela, P.A. and Piccoli, P.M. (2005) Magmatic Processes in the Development of Porphyry-type Ore Systems. In: *Econ. Geol. 100th Anniversary Volume* (eds. Hedenquist, J.W., Thompson, J.F.H., Goldfarb, R.J., Richards, J.P.). pp. 25–38.

CAP-presentation NEVASA September, 2013, http://www.cap.cl/wp/content/uploads/2013/09/cap_presentacion_nevasa_septiembre_2013.pdf

Carew, M. J. (2004) Controls on Cu-Au mineralisation and Fe oxide metasomatism in the Eastern Fold Belt, P.h.D thesis, James Cook University, NW Queensland, Australia.

Carmichael, D. M. (1969). On the mechanism of prograde metamorphic reactions in quartz-bearing pelitic rocks. *Contrib. Mineral. Petrol.* **20** (3), 244-267.

Carmichael, I. S. (1991) The redox states of basic and silicic magmas: a reflection of their source regions? *Contrib. Mineral. Petrol.* **106** (2), 129-141.

Charlier, B., Namur, O., Toplis, M.J., Schiano, P., Cluzel, N., Higgins, M.D., and Vander Auwera, J. (2011) Large-scale silicate liquid immiscibility during differentiation of tholeiitic basalt to granite and the origin of the Daly gap. *Geology* **39**, 907–910.

Charlier, B. and Grove, T.L. (2012) Experiments on liquid immiscibility along tholeiitic liquid lines of descent. Contrib. Mineral. Petrol. 164, 27-44.

Chen, H., Clark, A.H. and Kyser, T.K. (2010) The Marcona Magnetite Deposit, Ica, South-Central Peru: A Product of Hydrous, Iron Oxide-Rich Melts? *Econ. Geol.* **105**, 1441–1456.

Chen, H., Cooke, D. R., & Baker, M. J. (2013). Mesozoic iron oxide copper-gold mineralization in the central Andes and the Gondwana Supercontinent breakup. *Econ. Geol.*, **108**(1), 37-44.

Chen, W.T., Zhou, M.-F., and Zhao, T.-P. (2013) Differentiation of nelsonitic magmas in the formation of the ~1.74 Ga Damiao Fe–Ti–P ore deposit, North China. *Contrib. Mineral. Petrol.* **165**, 1341–1362.

Chiaradia, M., Banks, D., Cliff, R., Marschik, R., and De Haller, A. (2006) Origin of fluids in iron oxide–copper–gold deposits: constraints from δ ^{37}Cl, ^{87}Sr/^{86}Sr$_i$ and Cl/Br. *Mineral. Deposita* **41**, 565-573.

Cluzel, N., Laporte , D. and Provost, A. (2008) Kinetics of heterogeneous bubble

nucleation in rhyolitic melts: implications for the number density of bubbles in volcanic conduits and for pumice textures. *Contrib. Mineral. Petrol.* **156**, 745–763.

Core, D.P. (2004) PhD thesis, Univ. of Michigan (Ann Arbor)

Dare, S. A., Barnes, S. J., & Beaudoin, G. (2015). Did the massive magnetite "lava flows" of El Laco (Chile) form by magmatic or hydrothermal processes? New constraints from magnetite composition by LA-ICP-MS. *Mineral. Deposita*, **50**(5), 607-617.

Dare, S.A.S., Barnes, S.-J., Beaudoin, G., Méric,, J., Boutroy, E. and Potvin-Doucet, C. (2014) Trace elements in magnetite as petrogenetic indicators. *Mineral. Deposita.* **49**, 785-796.Dare, S.A.S., Barnes, S.-J. and Beaudoin, G. (2015) Did the massive magnetite "lava flows" of El Laco (Chile) form by magmatic or hydrothermal processes? New constraints from magnetite composition by LA-ICP-MS. *Mineral. Deposita.***50**, 607-617.

Dauphas, N. and Rouxel, O. (2006) Mass spectrometry and natural variations of iron isotopes. *Mass Spec. Rev.* **25** (4), 515-550.

Dauphas, N., John, S. G. and Rouxel, O. (2017) Iron isotope systematics. *Rev. Mineral. Geochem.* **82** (1), 415-510.

Driesner, T. (2007). The system H2O–NaCl. Part II: Correlations for molar volume, enthalpy, and isobaric heat capacity from 0 to 1000 C, 1 to 5000 bar, and 0 to 1 XNaCl. *Geochim. Cosmochim. Acta*, **71**(20), 4902-4919.

Dupuis, C. and Beaudoin, G. (2011) Discriminant diagrams for iron oxide trace element fingerprinting of mineral deposit types. *Mineral.Deposita.* **46**, 319–335.

Edmonds, M., Brett, A., Herd, R.A., Humphreys, M.C.S. and Woods A. (2014)

Magnetite-bubble aggregates at mixing interfaces in andesite magma bodies. *Geological Society, London.* Spec. Pub. **410,** DOI 10.1144/SP410.7.

Eugster, H.P. and Chou, I.-M. (1979) A Model for the Deposition of Cornwall-type Magnetite Deposits. *Econ. Geol.* **74**, 763-774.

Ewart, A. and Griffin, W. L. (1994) Application of proton-microprobe data to trace-element partitioning in volcanic rocks. *Chem. Geol.* **117** (1-4), 251-284.

Fiege, A., Behrens, H., Holtz, F. & Adams, F. (2014) Kinetic vs. thermodynamic control of degassing of H2O–S±Cl-bearing andesitic melts. *Geochim. Cosmochim. Acta*, **125**, 241-264.

Fischer, L. A., Wang, M., Charlier, B., Namur, O., Roberts, R. J., Veksler, I. V., ... & Holtz, F. (2016). Immiscible iron-and silica-rich liquids in the Upper Zone of the Bushveld Complex. *Earth Planet. Sci. Lett*, **443**, 108-117.

Foose, M.P., and McLelland, J.M. (1995) Proterozoic low-Ti iron-oxide deposits in New York and New Jersey; relation to Fe oxide (Cu-U-Au-rare earth element) deposits and tectonic implications. *Geology* **23**, 665–668.

Frank, M.R., Simon, A., Pettke, T., Candela, P., Piccoli, P. (2011) Gold and copper partitioning in magmatic-hydrothermal systems at 800°C and 100 MPa. *Geochim. Cosmochim Acta* **75(9)**, 2470-2482

Fuerstenau, M.C., Jameson, G.J. Yoon, R.H. (Eds.), *Froth Flotation: A Century of innovation*. SME (2007).

Gardner, J. E. and Denis, M.-H. (2004) Heterogeneous bubble nucleation on Fe-Ti oxide crystals in high-silica rhyolite melts. *Geochim. Cosmochim Acta* **68**, 3587-3597.

Geijer, P. (1931) The iron ores of Kiruna-type. Geographical distribution, geological characters and origin. *Sver. Geol. Unders. Ser. C.* **367**, 39pp.

Ghiorso, M.S. and Sack, R.O. (1995) Chemical Mass Transfer in Magmatic Processes IV. A revised and internally consistent thermodynamic model for the interpolation and extrapolation of liquidsolid equilibria in magmatic systems at elevated temperatures and pressures. *Contrib. Mineral. Petrol.* **119**, 197–212.

Ghiorso, M. S. and Evans, B. W. (2008). Thermodynamics of rhombohedral oxide solid solutions and a revision of the Fe-Ti two-oxide geothermometer and oxygen-barometer. *Amer. J. Sci.* **308** (9), 957-1039.

Giordano, D., Russell, J. K., & Dingwell, D. B. (2008) Viscosity of magmatic liquids: a model. *Earth. Planet. Sci. Lett.*, **271**(1-4), 123-134.

Gualda, G.A.R and Ghiorso, M.S. (2007) Magnetite scavenging and the buoyancy of bubbles in magmas. Part 2: Energetics of crystal-bubble attachment in magmas. *Contrib. Min. Petrol.* **154**, 479–490.

Guillong M., Meier D. M., Allan M. M., Heinrich C. A. and Yardley B. (2008) SILLS: A MATLAB-Based Program for the Reduction of Laser Ablation ICP–MS Data of Homogeneous Materials and Inclusions: Mineralogical Association of Canada Short Course 40, Vancouver, B.C., pp. 328–333.

Hautmann, S., Witham, F., Christopher, T., Cole, P., Linde, A.T., Sacks, S. and Sparks, S.J. (2013) Strain field analysis on Montserrat (W.I.) as tool for assessing permeable flow paths in the magmatic system of Soufriere Hills Volcano. *Geochem. Geophys. Geosys.* **15**, 676-690.

Haynes DW, Cross KC, Bills RT, Reed MH (1995) Olympic Dam ore genesis: a fluid-mixing model. *Econ. Geol.* **90**, 281–307.

Haynes, D.W. (2000) Iron oxide–copper(–gold) deposits: their position in the ore deposit spectrum and modes of origin. In: *Hydrothermal iron oxide–copper–gold and related deposits—a global perspective* (ed. Porter, T.M.), 1. PGC Publishing, Adelaide, Australia. pp. 71–90.

Heimann, A., Beard, B. L., & Johnson, C. M. (2008). The role of volatile exsolution and sub-solidus fluid/rock interactions in producing high 56Fe/54Fe ratios in siliceous igneous rocks. *Geochim. Cosmochim. Acta*, **72**(17), 4379-4396.

Henriquez, F. & Martin, R.F. (1978) Crystal-growth textures in magnetite flows and feeder dykes, El Laco, Chile. *Can. Mineral.*, **16**(4), 581-589.

Henríquez, F., Naslund, H.R., Nyström, J.O., Vivallo, W., Aguirre, R., Dobbs, F.M., and Lledo, H. (2003) New Field Evidence Bearing on the Origin of the El Laco Magnetite Deposit, Northern Chile - A Discussion. *Econ. Geol.* **98**, 1497-1500.

Hersum, T., Hilpert, M., & Marsh, B. (2005). Permeability and melt flow in simulated and natural partially molten basaltic magmas. *Earth Planet. Sci.Lett.*, **237**(3-4), 798-814.

Hess, J. C., Lippolt, H. J., Gurbanov, A. G. and Michalski, I. (1993) The cooling history of the late Pliocene Eldzhurtinskiy granite (Caucasus, Russia) and the thermochronological potential of grain-size/age relationships. *Earth Planet. Sci Lett.* **117** (3-4), 393-406.

Hezarkhani, A., Williams-Jones, A. E. and Gammons, C. H. (1999) Factors controlling copper solubility and chalcopyrite deposition in the Sungun porphyry copper

deposit, Iran. *Mineral. Deposita.* **34**, 770-783.

Horn, I., von Blanckenburg, F., Schoenberg, R., Steinhoefel, G. and Markl, G. (2006) In situ iron isotope ratio determination using UV-femtosecond laser ablation with application to hydrothermal ore formation processes. *Geochim. Cosmochim. Acta* **70** (14), 3677-3688.

Horn, I. and von Blanckenburg, F. (2007) Investigation on elemental and isotopic fractionation during 196 nm femtosecond laser ablation multiple collector inductively coupled plasma mass spectrometry. *Spectrochimica Acta* Part B: Atomic Spectroscopy **62** (4), 410-422.

Hou, T., Charlier, B., Namur, O., Schütte, P., Schwarz-Schampera, U., Zhang, Z. and Holtz, F. (2017) Experimental study of liquid immiscibility in the Kiruna-type Vergenoeg iron–fluorine deposit, South Africa. *Geochim. Cosmochim. Acta* **203**, 303-322.

Hou, T., Charlier, B., Holtz, F., Veksler, I., Zhang, Z., Thomas, R., & Namur, O. (2018). Immiscible hydrous Fe–Ca–P melt and the origin of iron oxide-apatite ore deposits. *Nat. comm.*, **9**(1), 1415.

Hurtig, N.C. and Williams-Jones, A.E. (2014) An experimental study of the transport of gold through hydration of AuCl in aqueous vapour and vapour-like fluids. *Geochim. Cosmochim. Acta* **127**, 305-325.

Hurwitz, S. and Navon, O. (1994) Bubble nucleation in rhyolitic melts: Experiments at high pressure, temperature, and water content. *Earth Planet. Sci. Lett.* **122**, 267-280.

James, B.R. (2003) Chromium. In: *Encyclopedia of water science* (eds. Stewart, B.A., Howell, T.A.), Marcel Dekker Inc, pp. 77–82.

Jonsson, E., Troll, V.R., Hoegdahl, K., Harris, C., Weis, F., Nilsson, K.P., and Skelton, A. (2013) Magmatic origin of giant `Kiruna-type` apatite-iron-oxide ores in Central Sweden. *Sci. Rep.* **3**, 1644-1652.

Kawamoto, T. and Hirose, K. (1994) Au-Pd sample containers for melting experiments on iron and water bearing systems. *European Journal of Mineralogy-Ohne Beihefte*, **6(3)**, 381-386.

Kisvarsanyi, G., and Proctor, P. (1967) Trace element content of magnetites and hematites, southeast Missouri iron metallogenic province, USA. *Econ. Geol.* **62**, 449–470.

Klein-BenDavid, O., Pettke, T. and Kessel, R. (2011) Chromium mobility in hydrous fluids at upper mantle conditions. *Lithos* **125**, 122-130.

Knipping, J.L., Bilenker, L.D., Simon, A.C., Reich, M., Barra, F., Deditius, A.P., Lundstrom, C., Bindeman, I. and Munizaga, R. (20XX) Giant Kiruna-type deposits form by efficient flotation of magmatic magnetite suspensions. *Geology* (in press), DOI 10.1130/G36650.1.

Knipping, J. L., Bilenker, L. D., Simon, A. C., Reich, M., Barra, F., Deditius, A. P., Wälle, M., Heinrich, C.A., Holtz, F.and Munizaga, R. (2015b) Trace elements in magnetite from massive iron oxide-apatite deposits indicate a combined formation by igneous and magmatic-hydrothermal processes. *Geochim. Cosmochim. Acta* **171**, 15-38.

Kreiner DC (2011) Epithermal Style Iron Oxide(–Cu–Au) (=IOCG) Vein Systems and Related Alteration, 659p. Ph.D. thesis, University of Arizona.

La Tourrette, T. Z., Burnett, D. S. and Bacon, C. R. (1991) Uranium and minor-element partitioning in Fe-Ti oxides and zircon from partially melted granodiorite,

Crater Lake, Oregon. *Geochim. Cosmochim. Acta* **55** (2), 457-469.

Lautze, N. C., Sisson, T. W., Mangan, M. T., & Grove, T. L. (2011) Segregating gas from melt: an experimental study of the Ostwald ripening of vapor bubbles in magmas. *Contrib. Mineral. Petrol.*, **161**(2), 331-347.

Lindsley, D.H. (1976) The crystal chemistry and structure of oxide minerals as exemplified by the Fe–Ti oxides. In D. Rumble III, Ed., Oxide Minerals, p. L1–L60. *Rev. Mineral. Geochem.* Mineralogical Society of America.

Lindsley, D. H. (1991) Oxide minerals: petrologic and magnetic significance. *Rev. in Mineral*. **25**, 509.

Lledo, H.L. and Jenkins, D.M. (2008) Experimental investigation of the upper thermal stability of Mg-rich actinolite; Implications for Kiruna-type iron deposits. *J. Petrol.* **49**, 225-238.

Loberg, E.H, and Horndahl, A.-K. (1983) Ferride geochemistry of Swedish Precambrian iron ores. *Mineral. Deposita* **18**, 487-504.

Marsh, B.D. (1989) Magma chambers. *An. Rev. Earth Planet. Sci.* **17**, 439-474.

Martel, C., Pichavent, M., Holtz, F. and Scaillet, B. (1999) Effects of fO_2 and H_2O on andesite phase relations between 2 and 4 kbar. *J. Geophys. Res.* **104**, 29453-29470.

Mathez, E. A. (1984) Influence of degassing on oxidation states of basaltic magmas. *Nature* **310** (5976), 371.

Matveev, S. and Ballhaus, C. (2002) Role of water in the origin of podiform chromitite deposits. *Earth Planet. Sci. Lett.* **203**, 235-243.

Melcher, F., Grum, W. Simon, G., Thalhammer, T.V. and Stumpfl, E.F. (1997) Petrogenesis of the Ophiolitic Giant Chromite Deposits of Kempirsai, Kazakhstan: a Study of Solid and Fluid Inclusions in Chromite. *J. Petrol.* **38**, 1419–1458.

Menard, J. J. (1995) Relationship between altered pyroxene diorite and the magnetite mineralization in the Chilean Iron Belt, with emphasis on the El Algarrobo iron deposits (Atacama region, Chile). *Mineral. Deposita* **30** (3-4), 268-274.

Migdisov, A.A., Bychkov, A.Y., Williams-Jones, A.E. and van Hinsberg, V.J. (2014) A predictive model for the transport of copper by HCl-bearing water vapour in ore-forming magmatic-hydrothermal systems: Implications for copper porphyry ore formation. *Geochim. Cosmochim. Acta* **129**, 33-53.

Millet, M. A., Baker, J. A., & Payne, C. E. (2012). Ultra-precise stable Fe isotope measurements by high resolution multiple-collector inductively coupled plasma mass spectrometry with a 57Fe–58Fe double spike. *Chem. Geol.*, **304**, 18-25

Mumin, A.H., Corriveau, L. Somarin, A.K. and Ootes, L. (2007) Iron oxide copper-gold-type polymetallic mineralization in the Contact Lake Belt, Great Bear Magmatic Zone, Northwest Territories, Canada. *Explor. Min. Geol.* **16**, 187-208.

Mungall, J.E., Brenan, J.M., Godel, B. Barnes, S.J. and Gaillard, F. (2015) Transport of metals and sulphur in magmas by flotation of sulphide melt on vapour bubbles. *Nat. Geosci.* DOI: 10.1038/NGEO2373

Nadoll, P. and Koenig, A.E. (2011) LA-ICP-MS of magnetite: methods and reference materials. *J. Anal. At. Spectrom.* **26,** 1872-1877.

Nadoll, P, Angerer, T., Mauk, J.L., French, D. and Walshe, J. (2014) The chemistry of hydrothermal magnetite: A review. *Ore Geol. Rev.* **61**, 1–32.

Nadoll, P., Mauk, J.L., Leveille, R.A. and Koenig, A.E. (2014b) Geochemistry of magnetite from porphyry Cu and skarn deposits in the southwestern United States. *Mineral. Deposita.*, DOI 10.1007/s00126-014-0539-y.

Naslund, H.R. (1983) The effect of oxygen fugacity on liquid immiscibility in iron-bearing silicate melts, *Am. J. Sci.* **283**, 1034-1059.

Naslund, H.R. (1984) Supersaturation and crystal growth in the roof-zone of the Skaergaard magma chamber. *Contrib. Mineral. Petrol.*, **86**(1), 89-93.

Naslund, H.R., Aguirre, R., Dobbs, F.M., Henriquez, F.J., and Nystrom, J.O. (2000) The Origin, emplacement, and eruption of ore magmas. *IX Congreso Geologico Chileno Actas* **2**,135-139.

Naslund, H.R., Henriquez, F., Nyström, J.O., Vivallo, W., and Dobbs, F.M. (2002) Magmatic iron ores and associated mineralisation: examples from the Chilean high Andes and coastal Cordillera. In: *Hydrothermal iron oxide copper-gold & related deposits - a global perspectiv*e (ed. Porter, T.M.) 2. PGC Publishing, Adelaide, Australia. pp. 207-226.

Nielsen, R. L. (1992) BIGD. FOR: a FORTRAN program to calculate trace-element partition coefficients for natural mafic and intermediate composition magmas. *Comput. Geosci.* **18** (7), 773-788.

Nielsen, R. L., Forsythe, L. M., Gallahan, W. E. and Fisk, M. R. (1994) Major-and trace-element magnetite-melt equilibria. *Chem. Geol.* **117**(1-4), 167-191.

Nold, J.L., Dudley, M.A. and Davidson, P. (2014) The Southeast Missouri (USA) Proterozoic iron metallogenic province—Types of deposits and genetic relationships to magnetite–apatite and iron oxide–copper–gold deposits. *Ore Geol. Rev.* **57**, 154-171.

Nyström, J.O., and Henríquez, F. (1994) Magmatic features of iron ores of the Kiruna-type in Chile and Sweden: Ore textures and magnetite geochemistry. *Econ. Geol.* **89**, 820-839.

Ochs, F. A., & Lange, R. A. (1999). The density of hydrous magmatic liquids. *Science*, **283**(5406), 1314-1317.

Oeser, M., Weyer, S., Horn, I. and Schuth, S. (2014) High-Precision Fe and Mg Isotope Ratios of Silicate Reference Glasses Determined In Situ by Femtosecond LA-MC-ICP-MS and by Solution Nebulisation MC-ICP-MS. *Geostand. Geoanal. Res.* **38** (3), 311-328.

Okamoto, K. (1979) Geochemical study on magmatic differentiation of Asama Volcano, central Japan. *J. Geol. Soc. Japan* **85**, 525–535.

Ovalle, J.T. et al. (2018) Formation of massive iron deposits linked to explosive volcanic eruptions. *Sci. Rep* **8**(1), 14855.

Oyarzún, J. and Frutos, J. (1984) Tectonic and petrological frame of the Cretaceous iron deposits of north Chile. *Min. Geol.* **34**, 21-31.

Park, C. F. (1961). A magnetite" flow" in northern Chile. *Econ. Geol.* **56**(2), 431-436.

Pecoits, E., Gingras, M., Barley, M., Kappler, A., Posth, N. and Konhauser, K. (2009) Petrography and geochemistry of the Dales Gorge banded iron formation: paragenetic sequence, source and

implications for palaeo-ocean chemistry. *Precambrian Res.* **172**, 163–187.

Pettke, T., Oberli, F., Audetat, A., Guillong, M., Simon, A.C., Hanley, J.J., Klemm, L.M. (2012) Recent developments in element concentration and isotope ratio analysis of individual fluid inclusions by laser ablation single and multiple collector ICP-MS. *Ore Geol. Rev.* **44**, 10–38.

Philippot, P., Agrinier, P., & Scambelluri, M. (1998). Chlorine cycling during subduction of altered oceanic crust. *Earth Planet. Sci. Lett.*, **161**(1-4), 33-44.

Philpotts, A.R. (1967) Origin of certain iron-titanium oxide and apatite rocks, *Econ. Geol.* **62**, 303-315.

Pichon, R. (1981) Ph.D. thesis, Univ. Paris Xl (Orsay)

Pincheira, M., Thiele, R., and Fontbote, L. (1990) Tectonic Transpression along the Southern Segment of the Atacam Fault-Zone, Chile. In *Colloques et Seminaires: Symposium International Geodynamique Andine*, Grenoble,133-136.

Pitzer, K. S., & Sterner, S. M. (1995). Equations of state valid continuously from zero to extreme pressures with H 2 O and CO 2 as examples. *Intern. J. Thermophysics*, **16**(2), 511-518.

Poitrasson, F. and Freydier, R. (2005) Heavy iron isotope composition of granites determined by high resolution MC-ICP-MS. *Chem. Geol.* **222** (1-2), 132-147.

Pollard, P.J. (2006) An intrusion-related origin for Cu-Au mineralization in iron oxide-copper-gold (IOCG) provinces. *Mineral. Deposita.* **41**, 179–187.

Polyakov, V. B., Clayton, R. N., Horita, J. and Mineev, S. D. (2007) Equilibrium iron isotope fractionation factors of minerals: reevaluation from the data of nuclear

inelastic resonant X-ray scattering and Mössbauer spectroscopy. *Geochim. Cosmochim. Acta* **71** (15), 3833-3846.

Reed, M.J., Candela, P.A. and Piccoli, P.M. (2000) The distribution of rare earth elements between monzogranitic melt and the aqueous volatile phase in experimental investigations at 800 °C and 200 MPa. *Contrib. Mineral. Petrol.* **140**, 251-262.

Reich, M., Deditius, A., Chryssoulis, S., Li, J.-W., Ma, C-Q., Parada, M.A., Barra, F. and Mittermayr, F. (2013) Pyrite as a record of hydrothermal fluid evolution in a porphyry copper system: A SIMS/EMPA trace element study. *Geochim. Cosmochim. Acta* **104**, 42-62.

Reynolds, I. M. (1985) The nature and origin of titaniferous magnetite-rich layers in the upper zone of the Bushveld Complex; a review and synthesis. *Econ. Geol.*, **80**(4), 1089-1108.

Rhodes, A.L., & Oreskes, N. (1995) Magnetite deposition at El Laco, Chile: Implications for Fe-oxide formation in magmatic-hydrothermal systems, In: *Giant ore deposits II: Controls on the scale of orogenic magmatic-hydrothermal mineralization* (ed. Clark, A.H.), Proceedings of the second giant ore deposits workshop, Kingston, Ontario,pp. 582-622.

Rhodes, A.L., and Oreskes, N. (1999) Oxygen isotope composition of magnetite deposits at El Laco, Chile: Evidence of formation from isotopically heavy fluids, In: *Geology and ore deposits of the Central Andes, Society of Economic Geologists* (ed. Skinner, B.J.), Special Publication 7, p. 333-351.

Rhodes, A.L., Oreskes, N., and Sheets, S. (1999) Geology and rare earth element geochemistry of magnetite deposits at El Laco, Chile, In: *Geology and ore deposits of the Central Andes, Society of Economic*

Geologists (ed. Skinner, B.J.), Special Publication 7, p. 299-332.

Rojas, P. A., Barra, F., Reich, M., Deditius, A., Simon, A., Uribe, F., Romero, R. and Rojo, M. (2018) A genetic link between magnetite mineralization and diorite intrusion at the El Romeral iron oxide-apatite deposit, northern Chile. *Mineral. Deposita* 1-20.

Rudnick, R.L. and Gao, S. (2003) Composition of the continental crust. In: *The Crust* (ed. Rudnick, R.L.) Vol. 3, Treatise on Geochemistry (eds. H.D. Holland and K.K. Turekian), Elsevier, Oxford.

Rutherford, M.J., Gardner, J.E. & Sigurdsson, H. (2000) "Rates of magma ascent" in *Encyclopedia of Volcanoes* p. 207-217.

Schauble E. A. (2004) Applying stable isotope fractionation theory to new systems. In C. M. Johnson, B. L. Beard and F. Albarede, Eds., Geochemistry of Non-Traditional Stable Isotopes, p. 65-111. *Rev. Mineral. Geochem.*, Mineralogical Society of America, Washington, DC, USA.

Schauble, E. A., Méheut, M. and Hill, P. S. (2009) Combining metal stable isotope fractionation theory with experiments. *Elements* **5** (6), 369-374.

Schoenberg, R., and von Blanckenburg, F. (2006) Modes of planetary-scale Fe isotope fractionation. *Earth Planet. Sci. Lett.* **252** (3-4), 342-359

Schuessler, J. A., Schoenberg, R., and Sigmarsson, O. (2009) Iron and lithium isotope systematics of the Hekla volcano, Iceland—evidence for Fe isotope fractionation during magma differentiation. *Chem. Geol.* **258** (1), 78-91.

Seeger, C.M. (2003) Ph.D. thesis, Univ. of Missouri (Rolla)

Severmann, S. and Anbar, A. D. (2009) Reconstructing paleoredox conditions through a multitracer approach: the key to the past is the present. *Elements* **5** (6), 359-364.

Sillitoe, R.H., and Burrows, D.R. (2002) New field evidence bearing on the origin of the El Laco magnetite deposit, northern Chile. *Econ. Geol.* **97**, 1101–1109.

Sillitoe, R.H. (2003) Iron oxide-copper-gold deposits: an Andean view. *Mineral. Deposita.* **38**, 787–812.

Simon, A.C., Pettke, T., Candela, P.A., Piccoli, P.M. and Heinrich, A.H. (2004) Magnetite solubility and iron transport in magmatic-hydrothermal environments. *Geochim. Cosmochim. Acta* **68**, 4905–4914.

Simon, A., Pettke, T., Candela, P.A., Piccoli, P.M. and Heinrich, C.A. (2005) Gold partitioning in melt vapor-brine systems. *Geochim. Cosmochim. Acta* **69**, 3321-3335.

Simon, A., Pettke, T., Candela, P.A., Piccoli, P.M., Heinrich, C. (2006) Copper partitioning in melt-vapor-brine-magnetite-pyrrhotite assemblage. *Geochim. Cosmochim. Acta* **70**, 5583-5600.

Simon, A.C. et al. (2018) Kiruna type iron oxide - apatite (IOA) and iron oxide - copper - gold (IOCG) form by a combination of igneous and magmatic-hydrothermal processes: Evidence from the Chilean Iron Belt. SEG Spec. Pub., **21**, 89-114.

Sossi, P. A., Foden, J. D. and Halverson, G. P. (2012) Redox-controlled iron isotope fractionation during magmatic differentiation: an example from the Red Hill intrusion, S. Tasmania. *Contrib. Mineral. Petrol.* **164** (5), 757-772.

Sossi, P. A. and O'Neill, H. S. C. (2017) The effect of bonding environment on iron isotope fractionation between minerals at high temperature. *Geochim. Cosmochim. Acta* **196**, 121-143.

Sun, S.-S. and McDonough, W.F. (1989) Chemical and isotopic systematics of oceanic basalts: Implications for mantle composition and processes. In: *Magmatism in the ocean basins* (eds. Saunders, A.D., and Norry, M.J.), Geological Society, Special Publication **42**, p. 313–345, London.

Taylor Jr, H. P. (1967). Oxygen isotope studies of hydrothermal mineral deposits. *In* Barnes, H.L., ed., Geochemistry of Hydrothermal Ore Deposits: New York, Holt, Rinehart and Winston, p. 109-142.

Tegner, C, Cawthorn, R.G. and Kruger, F.J. (2006) Cyclicity in the Main and Upper Zones of the Bushveld Complex, South Africa: crystallization from a zoned magma sheet. *J. Petrol.* **47**, 2257-2279.

Telus, M., Dauphas, N., Moynier, F., Tissot, F. L., Teng, F. Z., Nabelek, P. I., Craddock, P.R. and Groat, L. A. (2012) Iron, zinc, magnesium and uranium isotopic fractionation during continental crust differentiation: The tale from migmatites, granitoids, and pegmatites. *Geochim. Cosmochim. Acta* **97**, 247-265.

Teng, F. Z., Dauphas, N. and Helz, R. T. (2008) Iron isotope fractionation during magmatic differentiation in Kilauea Iki lava lake. *Science* **320** (5883), 1620-1622.

Tollari, N. Barnes, S.-J., Cox, R.A. and Nabil, H. (2008) Trace element concentrations in apatites from the Sept-Îles Intrusive Suite, Canada — Implications for the genesis of nelsonites. *Chem. Geol.* **252**, 180-190.

Toplis, M. J. and Carroll, M. R. (1995) An experimental study of the influence of oxygen fugacity on Fe-Ti oxide stability, phase relations, and mineral—melt equilibria in ferro-basaltic systems. *J. Petrol.* **36** (5), 1137-1170.

Tornos, F., Velasco, F., & Hanchar, J. M. (2016). Iron-rich melts, magmatic magnetite, and superheated hydrothermal systems: The El Laco deposit, Chile. *Geology*, **44**(6), 427-430.

Travisany, V., Henriquez, F. and Nyström, J.O. (1995) Magnetite lava flows in the Pleito-Melon District of the Chilean Iron Belt. *Econ. Geol.* **90**, 438-444.

Ulrich, T., Günther, D. and Heinrich, C.A. (2001) The evolution of a porphyry Cu–Au deposit, based on LA-ICP-MS analysis of fluid inclusions: Bajo de la Alumbrera, Argentina. *Econ. Geol.* **96**, 1743–1774.

Uyeda, S. and Kanamori, H. (1979) Back-arc opening and the mode of subduction. *J. Geophys. Res.* **84**,1049-1061.

Valley, P. M., Hanchar, J. M., & Whitehouse, M. J. (2011). New insights on the evolution of the Lyon Mountain Granite and associated Kiruna-type magnetite-apatite deposits, Adirondack Mountains, New York State. *Geosphere*, **7**(2), 357-389.

Van Baalen, M. R. (1993) Titanium mobility in metamorphic systems: a review. *Chem. Geol.* **110** (1-3), 233-249.

VanTongeren, J.A., and Mathez, E.A. (2012) Large-scale liquid immiscibility at the top of the Bushveld Complex, South Africa. *Geology* **40**, 491-494.

Velasco, F. and Tornos, F. (2009) Pegmatite-like magnetite–apatite deposits of northern Chile: A place in the evolution of immiscible iron oxide melts? In T. Bleninsop and M. Gettings, Eds.,

Proceedings of the 10th Biennial SGA Meeting, p. 665–667. Society for Geology Applied to Ore Deposits, Townsville, Australia.

Verlaguet, A., Brunet, F., Goffé, B. and Murphy, W. M. (2006) Experimental study and modeling of fluid reaction paths in the quartz–kyanite±muscovite–water system at 0.7 GPa in the 350–550 C range: Implications for Al selective transfer during metamorphism. *Geochim. Cosmochim. Acta* **70** (7), 1772-1788.

Wallace, P.J. (2005) Volatiles in subduction zone magmas: concentrations and fluxes based on melt inclusion and volcanic gas data. *J. Volcanol. Geotherm. Res.*, **140**(1-3), 217-240.

Watenphul, A.,Schmidt, C. and Scholten, L. (2012) First insights into Cr^{3+} solubility in aqueous fluids at elevated P and T by μ-XRF, *1st European Mineralogical Conference – EMC*. Frankfurt, Germany #544 (abstr.).

Watenphul, A., Scholten, L, Kavner, A., Alraun, P., Falkenberg, G., Newville, M., Lanzirotti, A. and Schmidt C. (2013) Cu and Ni solubility in high-temperature aqueous fluids. *American geophysical Union – AGU, Fall meeting*. San Francisco, CA, USA #MR33A-2311 (abstr.).

Webster, J.D., Kinzler, R.J. & Mathez, E.A. (1996) Chloride and water solubility in basalt and andesite melts and implications for magmatic degassing. *Geochim. Cosmochim. Acta*, **63**(5), 729-738.

Wechsler, B. A., Lindsley, D. H. and Prewitt, C. T. (1984) Crystal structure and cation distribution in titanomagnetites ($Fe_{3-x}Ti_xO_4$). *Am. Mineral.* **69** (7-8), 754-770.

Weis, F., (2013), Oxygen and iron isotope systematics of the Grängesberg mining district (GMD), Central Sweden (Ph.D. thesis): Uppsala, Sweden, Uppsala University, 83p.

Westhues, A., Hanchar, J. M., LeMessurier, M. J., & Whitehouse, M. J. (2017). Evidence for hydrothermal alteration and source regions for the Kiruna iron oxide–apatite ore (northern Sweden) from zircon Hf and O isotopes. *Geology*, **45**(6), 571-574.

Weyer, S. and Schwieters, J. B. (2003) High precision Fe isotope measurements with high mass resolution MC-ICPMS. *Internat. J. Mass Spectr.* **226** (3), 355-368.

Williams, P.J., Barton, M.D., Johnson, D.A., Fontboté, L., de Haller, A., Mark, G., Oliver, N.H.S., and Marschik, R. (2005) Iron oxide copper-gold deposits: Geology, Space-time distribution, and possible modes of origin. *Econ. Geol.*, 100th Anniversary Volume, (eds. Hedenquist, J.W., Thompson, J.F.H., Goldfarb, R.J., Richards, J.P.). pp. 371–405.

Williams-Jones, A. E., & Migdisov, A. A. (2014). Experimental constraints on the transport and deposition of metals in ore-forming hydrothermal systems. *Soc. Econ. Geol.* **18**, 77-96.

Zajacz, Z., Candela, P.A., Piccoli, P.M., Wälle, M., Sanchez-Valle, C. (2012). Gold and copper in volatile saturated mafic to intermediate magmas: Solubilities, partitioning, and implications for ore deposit formation. *Geochim. Cosmochim. Acta* **91**, 140-159.

Zambardi, T., Lundstrom, C., Li, X. and McCurry, M. (2014) Fe and Si isotope variations at Cedar Butte volcano; insight into magmatic differentiation. *Earth Planet. Sci. Lett.* **405**, 169-179.

Zheng, X.-Y., Beard, B.L. and Johnson, C.M. (2018) Assessment of matrix effects associated with Fe isotope analysis using 266 nm femtosecond and 193 nm nanosecond laser ablation multi-collector inductively coupled plasma mass

spectrometry. *J. Anal. Atomic Spectr.* **33**, 68–8

Supplementary Material

Supplementary Information for Chapter 2: "Giant Kiruna-type deposits form by efficient flotation of magmatic magnetite suspensions"

Jaayke L. Knipping, Laura D. Bilenker, Adam C. Simon, Martin Reich, Fernando Barra, Artur P. Deditius, Craig Lundstrom, Ilya Bindeman, Rodrigo Munizaga

Supplementary Data: Fe and O Isotope Data

Stable isotope data are reported in the conventional delta notation, following the equations:

$\delta^{56}Fe_{sample}$ (‰) = [$(^{56}Fe/^{54}Fe)_{measured}$ / $(^{56}Fe/^{54}Fe)_{IRMM-14}$ − 1] * 1000   (equation 1)

$\delta^{18}O_{sample}$ (‰) = [$(^{18}O/^{16}O)_{measured}$ / $(^{18}O/^{16}O)_{SMOW}$ − 1] * 1000   (equation 2)

Iron isotope values were obtained by using a Multi-Collector Inductively Coupled Plasma Mass Spectrometer (MC-ICP-MS) at the University of Illinois, Urbana-Champaign by following the double-spike method of Millet et al. (2012) by using dry plasma and pseudo high resolution analysis. Oxygen isotope values were measured by using a laser fluorination line and Thermo-Finnigan MAT 253 gas isotope ratio mass spectrometer in dual inlet mode at the University of Oregon. For all measurements, only magnetite separates were analyzed. Since LC magnetite grains contain inclusions, sample would respond to exposure of the laser by "jumping" out of the sample well. Therefore, we employed a careful approach during the laser fluorination process in which the laser power was increased percentage-wise once the entire sample was exposed evenly to the current strength. Smaller grain size fractions were optimal for this method to insure homogeneous and quicker heating of individual grains.

The data reported in Table S2.1 below include stable Fe and O isotope pairs for thirteen LC samples, as well as two additional deposits for comparison: one from the Fe oxide deposit at Mineville, NY, USA, and one from the Paleoproterozoic Kiruna deposit, Sweden. The deposit at Mineville is speculated to have formed by secondary hydrothermal processes (Valley et al. 2012), which explains its significantly lighter signature in both Fe and O stable isotopes. By contrast, the Kiruna deposits are believed to be of an origin similar to that of Los Colorados and the CIB IOAs, as reflected by their similar isotopic signature although the lighter δ^{18}O-values of Kiruna ore may be due to the fact that Kiruna is much older, with reported isotopic age constraints ranging from ~1882 to ~1887 Ma (Westhues et al., 2014). Thus, Kiruna has likely suffered greater post-formation alteration.

Table S2.1: δ^{56}Fe- and δ^{18}O-values with twice standard deviation for each indicated sample from drill core LC-05 and LC-04. Standard deviations were calculated based on the entire population of analyses, which ranged from 2-4 data points for each sample. The following numbers refer to sample depth (m) in each drill core.

Location	Sample	δ^{56}Fe (‰)	2sd (‰)	δ^{18}O (‰)	2sd (‰)
Los Colorados, Core LC-05	05-3.30	0.22	0.02	2.41	0.02
	05-20.7	0.09	0.06	3.04	0.05
	05-32	0.22	0.01	2.75	0.04
	05-52.2	0.14	0.08	3.17	0.03
	05-72.9	0.13	0.05	2.36	0.04
	05-90	0.21	0.07	2.99	0.01
	05-106	0.12	0.02	2.78	0.03
	05-126.15	0.10	0.06	2.48	0.03
Los Colorados, Core LC-04	04-38.8	0.18	0.01	2.04	0.04
	04-66.7	0.18	0.07	1.92	0.03
	04-129.3	0.22	0.02	2.62	0.04
	04-104.4	0.24	0.08	2.43	0.04
Mineville, NY	Mineville	-0.92	0.01	-0.79	0.03
Kiruna, Sweden	K-2	0.16	0.07	0.89	0.04

Supplementary Data: Methodology for EPMA Analyses of Magnetite

The EMP analysis of the magnetite was a combined study using the Cameca SX-100 (EMAL) at the University of Michigan and the JEOL 8530F (Centre of Microscopy) at the University of Western Australia to resolve zonation from high-Ti magnetite to the surrounding magnetite matrix (Fig. S2.1). In both cases, operating conditions employed an accelerating voltage of 20 kV and a focused beam to avoid measuring inclusions or exsolutions in the magnetite. The beam current was set to 30 nA at the University of Michigan and to 50 nA at the University of Western Australia. The standards and analytical conditions used are summarized for each institution in Table S3.2.
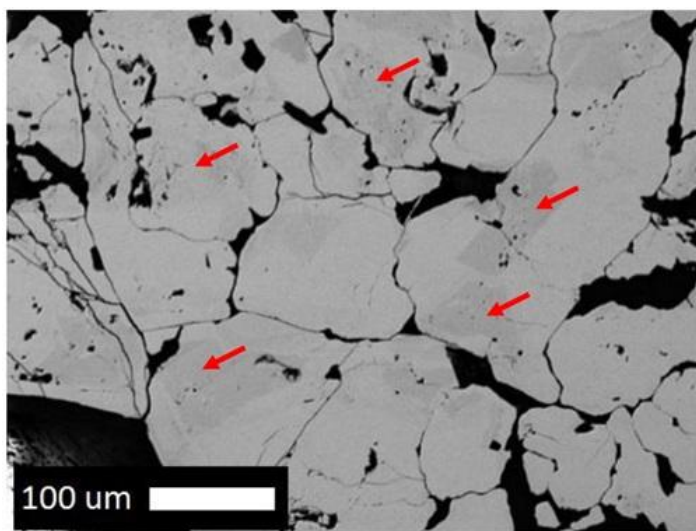
Figure S2.1: BSE image showing massive magnetite with high-Ti (dark grey) magnetite microlites (~100 μm) surrounded by massive low-Ti magnetite (bright grey). Red arrows point to some microlites (Sample LC-05-129). As discussed in the text, the chemical signature of the high-Ti zones is consistent with magnetite that grows from a silicate melt and the chemical signature of the low-Ti zones is consistent with magnetite that grows from a magmatic-hydrothermal aqueous fluid.

A total of 551 spot electron probe microanalyses (EPMA) were conducted on magnetite from two different drill cores including 10 samples from drill core LC-05 with 1-3 grains per sample (10-40 analyses per grain) and 7 samples from drill core LC-04 with 1-3 grains per sample (11-40 analyses per grain). Energy dispersive X-ray (EDX) maps were generated using the Hitachi S-3200N scanning electron microscope (SEM) at the University of Michigan, while wavelength dispersive X-ray (WDX) maps were collected at the University of Western Australia using an accelerating voltage of 20 kV, a beam current of 150 nA and a counting time of 20-40 ms/step.

Table S3.3 below includes all results of every single measurement of magnetite from drill core LC-14. Relative errors are on average 4% (Ti+V) and 8% (Al+Mn). The samples in each drill core are listed from shallow to deep levels and the results from each grain (indicated with lowercase letters) are listed from core to rim. Oxygen values are calculated based on the assumption that all Fe is present as Fe_3O_4 with a stoichiometric magnetite composition. Thus, large deviations from 100 % total may indicate non-stoichiometric compositions. Figures S1a and S1b include elemental maps of additional grains showing core (magmatic) to rim (magmatic-hydrothermal) zonation.

Table S2.2: Probe conditions of wavelength dispersive (WDS) X-ray spectrometers for each institute. MDL: mean detection limit

<u>University of Michigan: Cameca SX-100</u>

20 kV, 30 nA, focused

Element/Line	Crystal	Standard	Counting time [s]	MDL [wt%]
Mg/Kα	TAP	geikielite	100	0.0121
Al/Kα	TAP	zoisite	100	0.0084
Si/Kα	LTAP	wollastonite	100	0.0033
Ca/Kα	PET	wollastonite	100	0.0085
Ti /Kα	PET	ilmenite	120	0.0094
V /Kα	LLIF	V_2O_5	120	0.0064
Mn/Kα	LLIF	rhodondite	100	0.0088
Fe/Kα	LLIF	magnetite	20	0.0241

<u>Murdoch University: Jeol JXA8200</u>

20 kV, 30 nA, focused

Element/Line	Crystal	Standard	Counting time [s]	MDL [wt%]
Mg/Kα	TAP	pyrope	60	0.0060
Al/Kα	TAP	spessartine	60	0.0048
Si/Kα	TAP	spessartine	60	0.0045
Ca/Kα	PETJ	wollastonite	60	0.0038
Ti /Kv	PETJ	rutile	60	0.0047
V /Kα	LIFH	V-metal	60	0.0044
Mn/Kα	LIFH	spessartine	60	0.0057
Fe/Kα	LIF	magnetite	20	0.0161
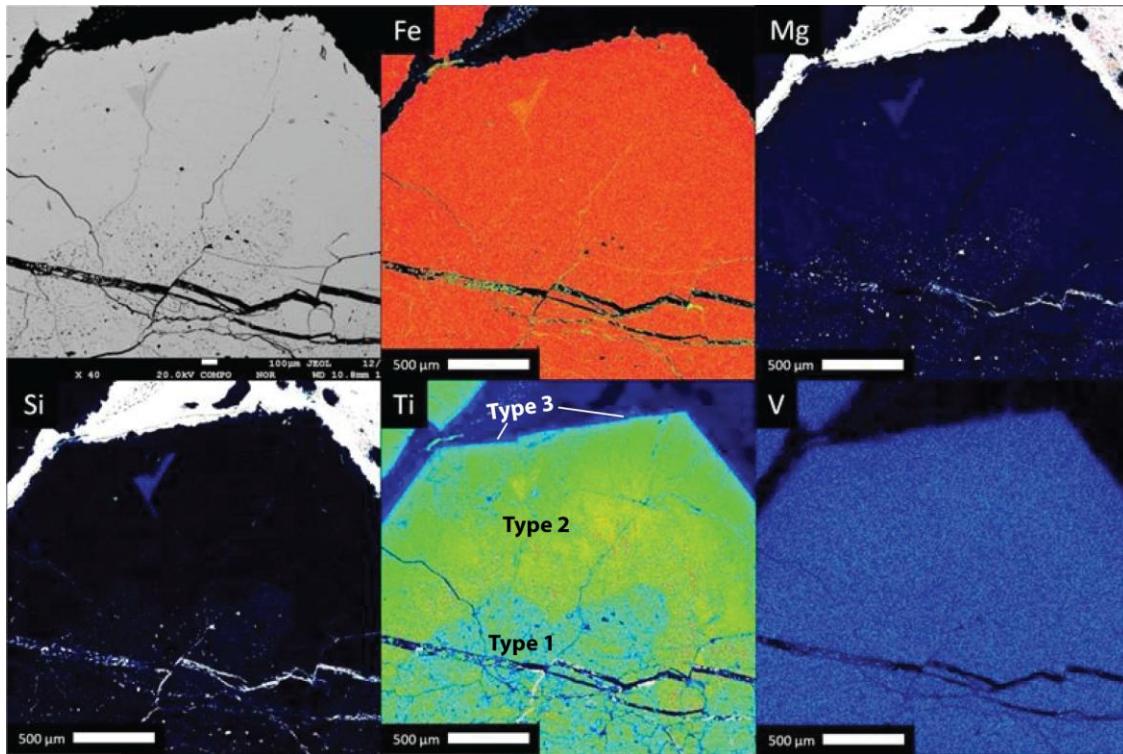
Figure S2.2a: caption below
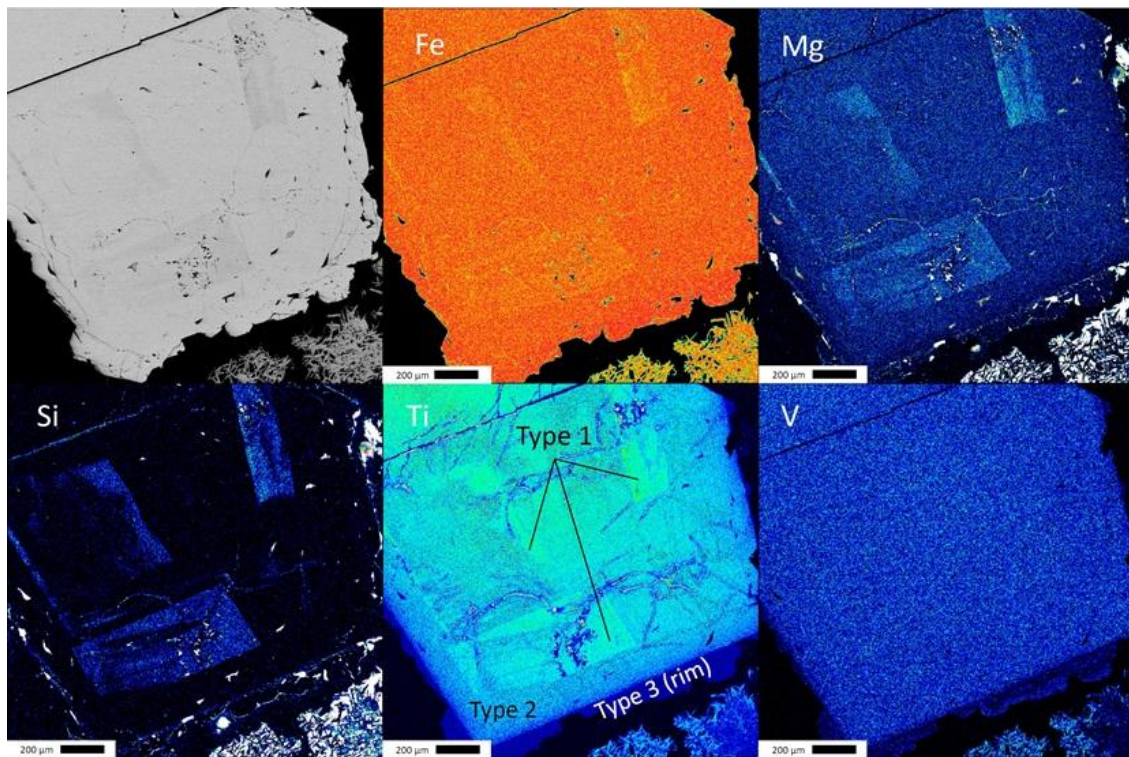
Figure S2.2a and b: WDX maps of two different grains of magnetite from sample LC-05-129. Upper left: BSE image, followed by Fe, Mg, Si, Ti and V individual WDX maps. Strong zonation is observed, and the three magnetite types (1, 2 and 3) are labeled in Fig. S2.2a and b. Scale bar in top left panel of Figure S2.2a is 100 microns. Scale bar in all other panels of Figure S2a are 500 microns.

Table S2.3: All EMP analysis ordered by depth within drill cores LC-05 and LC-04. Lowercase letters indicate different grains from the same sample depth. Analyses are ordered from core to rim in grains, which were analyzed at UMich. Empty boxes indicated that the concentration was below the limit of detection for the element.

sample	Mg	Al	Si	Ca	Ti	V	Mn	Fe	O	Total	Point#	Ti+V	Al+Mn	Institute
	[wt%]	[wt%]	[wt%]	[wt%]	[wt%]	[wt%]	[wt%]	[wt%]	[wt%]	[wt%]		[wt%]	[wt%]	
LC-05-32d	0.072	0.360	0.016		0.298	0.307	0.117	70.944	27.874	99.987	1	0.605	0.477	UMIch
LC-05-32d	0.100	0.345	0.017		0.304	0.308	0.122	71.140	27.960	100.294	2	0.611	0.467	UMIch
LC-05-32d	0.098	0.319	0.016	0.013	0.199	0.305	0.104	71.403	27.966	100.423	3	0.504	0.423	UMIch
LC-05-32d	0.065	0.319	0.016		0.264	0.311	0.135	71.366	27.979	100.454	4	0.575	0.453	UMIch
LC-05-32d	0.057	0.305	0.017		0.280	0.305	0.148	71.301	27.951	100.365	5	0.586	0.454	UMIch
LC-05-32d	0.028	0.309	0.024		0.349	0.309	0.164	71.522	28.080	100.784	6	0.658	0.473	UMIch
LC-05-32d	0.012	0.195	0.024	0.016	0.267	0.307	0.157	71.616	27.949	100.542	7	0.574	0.352	UMIch
LC-05-32d	0.012	0.100	0.021	0.022	0.283	0.301	0.148	71.875	27.969	100.731	8	0.585	0.247	UMIch
LC-05-32d	0.639	0.880	0.469	0.010	0.779	0.303	0.424	68.897	28.858	101.259	9	1.083	1.303	UMIch
LC-05-32d	0.000	0.168	0.015		0.222	0.305	0.178	71.976	28.015	100.880	10	0.528	0.346	UMIch
LC-05-32d	0.205	0.646	0.178	0.028	1.459	0.319	0.181	68.090	28.120	99.226	11	1.779	0.827	UMIch
LC-05-32d	0.006	0.082	0.014		0.180	0.305	0.150	72.251	28.011	100.999	12	0.485	0.232	UMIch
LC-05-32d	0.020	0.239	0.017		0.263	0.309	0.180	71.773	28.046	100.846	13	0.572	0.419	UMIch
LC-05-32d	0.014	0.193	0.057	0.019	0.192	0.306	0.154	71.275	27.809	100.020	14	0.498	0.347	UMIch
LC-05-32d	0.029	0.146	0.084	0.076	0.196	0.299	0.104	71.340	27.840	100.114	15	0.495	0.250	UMIch
LC-05-32d	0.072	0.066	0.181	0.088	0.206	0.289	0.088	69.280	27.120	97.390	16	0.495	0.153	UMIch
LC-05-51b	0.041	0.168	0.011	0.007	0.204	0.298	0.206	70.597	27.497	99.036	1b	0.502	0.373	UWAustralia
LC-05-51b	0.032	0.111	0.011	0.005	0.084	0.297	0.154	70.791	27.419	98.912	2b	0.381	0.264	UWAustralia
LC-05-51b	0.032	0.123	0.027		0.044	0.298	0.118	71.017	27.501	99.184	3b	0.342	0.241	UWAustralia
LC-05-51b	0.274	0.075	0.006		0.170	0.297	0.189	70.334	27.442	98.822	4b	0.467	0.264	UWAustralia

139

LC-05-51b	0.188	0.192	0.009		0.198	0.305	0.250	70.290	27.515	98.981	5b	0.503	0.441	UWAustralia
LC-05-51b	0.259	0.174	0.008		0.159	0.296	0.197	70.367	27.529	99.026	7b	0.455	0.371	UWAustralia
LC-05-51b	0.356	0.210	0.008		0.185	0.302	0.210	70.258	27.601	99.152	8b	0.487	0.420	UWAustralia
LC-05-51b	0.403	0.217	0.008		0.244	0.299	0.253	69.839	27.526	98.795	9b	0.544	0.470	UWAustralia
LC-05-51b	0.143	0.142	0.120	0.014	0.130	0.299	0.210	69.919	27.364	98.356	10b	0.428	0.352	UWAustralia
LC-05-51b	0.271	0.155	0.008		0.113	0.300	0.173	70.496	27.528	99.067	11b	0.414	0.327	UWAustralia
LC-05-51b	0.223	0.107	0.007		0.054	0.304	0.099	70.641	27.445	98.886	12b	0.358	0.206	UWAustralia
LC-05-51b	0.061	0.144	0.012		0.358	0.294	0.440	70.219	27.514	99.054	13b	0.651	0.583	UWAustralia
LC-05-51b	0.041	0.110	0.006		0.055	0.294	0.130	71.214	27.551	99.410	14b	0.349	0.240	UWAustralia
LC-05-51b	0.110	0.170	0.010		0.034	0.301	0.104	70.641	27.422	98.815	15b	0.335	0.274	UWAustralia
LC-05-51b	0.226	0.154	0.012	0.025	0.153	0.300	0.142	70.090	27.383	98.530	16b	0.453	0.295	UWAustralia
LC-05-51b	0.134	0.124	0.007		0.033	0.306	0.085	71.014	27.537	99.278	17b	0.339	0.210	UWAustralia
LC-05-51b	0.284	0.230	0.005		0.068	0.305	0.091	70.749	27.647	99.411	18b	0.373	0.321	UWAustralia
LC-05-51b	0.156	0.159	0.008	0.004	0.044	0.298	0.114	70.762	27.496	99.065	19b	0.342	0.274	UWAustralia
LC-05-51b	0.233	0.170	0.008		0.071	0.308	0.093	70.988	27.655	99.542	20b	0.379	0.263	UWAustralia
LC-05-51b	0.263	0.195	0.010	0.007	0.075	0.310	0.065	70.892	27.658	99.483	21b	0.385	0.260	UWAustralia
LC-05-51b	0.274	0.160	0.007	0.015	0.060	0.307	0.068	70.913	27.636	99.461	22b	0.367	0.228	UWAustralia
LC-05-51b	0.295	0.215	0.011	0.006	0.038	0.303	0.059	71.007	27.715	99.667	23b	0.341	0.274	UWAustralia
LC-05-51b	0.310	0.196	0.011	0.008	0.080	0.307	0.087	70.775	27.658	99.447	24b	0.387	0.283	UWAustralia
LC-05-51b	0.224	0.139	0.011	0.010	0.063	0.308	0.082	70.744	27.524	99.109	25b	0.370	0.221	UWAustralia
LC-05-51b	0.103	0.069	0.013	0.025	0.052	0.297	0.099	69.901	27.063	97.636	26b	0.349	0.169	UWAustralia
LC-05-51b	0.401	0.288	0.008	0.005	0.148	0.303	0.169	70.771	27.860	99.967	27b	0.451	0.457	UWAustralia
LC-05-51b	0.260	0.167	0.007	0.008	0.042	0.301	0.079	70.974	27.639	99.487	28b	0.343	0.247	UWAustralia
LC-05-51b	0.300	0.180	0.012	0.007	0.078	0.304	0.085	71.024	27.727	99.723	29b	0.383	0.265	UWAustralia
LC-05-51b	0.299	0.171	0.007	0.006	0.079	0.307	0.090	70.829	27.643	99.444	30b	0.386	0.260	UWAustralia

LC-05-51b	0.079	0.176	0.009		0.131	0.305	0.194	71.477	27.826	100.246	31b	0.436	0.370	UWAustralia
LC-05-51b	0.468	0.155	0.160		0.133	0.313	0.159	71.000	28.038	100.443	32b	0.446	0.314	UWAustralia
LC-05-51b	0.341	0.133	0.010		0.065	0.315	0.119	71.067	27.732	99.795	33b	0.380	0.252	UWAustralia
LC-05-51b	0.420	0.176	0.115	0.006	0.153	0.314	0.193	70.456	27.790	99.634	34b	0.468	0.369	UWAustralia
LC-05-51b	0.365	0.189	0.024		0.123	0.309	0.154	70.901	27.800	99.890	35b	0.432	0.343	UWAustralia
LC-05-51b	0.917	0.086	0.006	0.098	0.214	0.318	0.262	68.001	27.108	97.191	36b	0.532	0.348	UWAustralia
LC-05-51b	0.372	0.138	0.038		0.089	0.317	0.141	70.826	27.717	99.641	37b	0.406	0.279	UWAustralia
LC-05-51b	0.371	0.168	0.017		0.160	0.310	0.184	70.716	27.733	99.659	38b	0.469	0.352	UWAustralia
LC-05-51b	0.370	0.134	0.011		0.148	0.315	0.212	71.162	27.881	100.275	39b	0.463	0.346	UWAustralia
LC-05-51b	0.029	0.077	0.017	0.007	0.055	0.309	0.138	71.722	27.741	100.129	40b	0.364	0.215	UWAustralia
LC-05-51d	0.248	0.171	0.008	0.005	0.155	0.309	0.208	70.709	27.648	99.468	21d	0.464	0.379	UWAustralia
LC-05-51d	0.374	0.180	0.013		0.135	0.310	0.171	70.610	27.685	99.492	22d	0.445	0.351	UWAustralia
LC-05-51d	0.124	0.131	0.014		0.097	0.310	0.168	71.186	27.673	99.725	23d	0.407	0.299	UWAustralia
LC-05-51d	0.752	0.155	0.352	0.009	0.125	0.304	0.153	69.521	27.873	99.266	24d	0.429	0.308	UWAustralia
LC-05-51d	0.238	0.160	0.008		0.127	0.309	0.175	70.854	27.669	99.586	25d	0.437	0.335	UWAustralia
LC-05-51d	0.414	0.157	0.111	0.008	0.154	0.309	0.208	70.459	27.771	99.612	26d	0.464	0.365	UWAustralia
LC-05-51d	0.313	0.102	0.046	0.013	0.193	0.310	0.251	70.363	27.590	99.208	27d	0.503	0.353	UWAustralia
LC-05-51d	0.404	0.164	0.084	0.009	0.205	0.308	0.222	70.401	27.757	99.575	28d	0.513	0.386	UWAustralia
LC-05-51d	0.179	0.160	0.007		0.144	0.304	0.211	70.688	27.576	99.286	29d	0.448	0.371	UWAustralia
LC-05-51d	0.395	0.159	0.100	0.005	0.167	0.304	0.187	70.480	27.754	99.563	30d	0.471	0.346	UWAustralia
LC-05-52c	0.173	0.124	0.023	0.000	0.172	0.283	0.144	72.017	28.059	100.994	17	0.455	0.268	UMich
LC-05-52c	0.402	0.163	0.244	0.040	0.167	0.281	0.147	71.563	28.339	101.345	18	0.448	0.310	UMich
LC-05-52c	0.154	0.118	0.014		0.177	0.287	0.099	72.102	28.058	101.009	19	0.464	0.217	UMich
LC-05-52c	0.382	0.156	0.225	0.023	0.179	0.281	0.120	71.357	28.210	100.934	20	0.460	0.276	UMich
LC-05-52c	0.269	0.160	0.113		0.279	0.279	0.293	71.524	28.186	101.102	21	0.559	0.453	UMich

LC-05-52c	0.175	0.104	0.078	0.016	0.145	0.289	0.141	72.021	28.098	101.066	22	0.433	0.245	UMich
LC-05-52c	0.174	0.101	0.116	0.040	0.101	0.285	0.124	71.884	28.059	100.883	23	0.386	0.225	UMich
LC-05-52c	0.110	0.080	0.015		0.162	0.288	0.135	72.064	27.982	100.835	24	0.450	0.215	UMich
LC-05-52c	0.280	0.126	0.220	0.053	0.190	0.284	0.174	71.458	28.186	100.971	25	0.475	0.300	UMich
LC-05-52c	0.219	0.148	0.109	0.058	0.181	0.291	0.130	71.428	28.014	100.577	26	0.472	0.277	UMich
LC-05-52c	0.122	0.089	0.081	0.019	0.140	0.280	0.128	70.675	27.529	99.060	27	0.420	0.217	UMich
LC-05-52c	1.482	0.288	1.723	0.286	0.065	0.206	0.109	56.837	25.200	86.195	28	0.270	0.397	UMich
LC-05-52e	0.189	0.082	0.015	0.000	0.160	0.278	0.130	72.250	28.099	101.203	29	0.438	0.212	UMich
LC-05-52e	0.328	0.116	0.163	0.024	0.167	0.274	0.132	71.697	28.192	101.092	30	0.441	0.248	UMich
LC-05-52e	0.230	0.061	0.117	0.026	0.185	0.275	0.155	72.151	28.220	101.418	31	0.460	0.216	UMich
LC-05-52e	0.196	0.137	0.015		0.139	0.274	0.105	72.262	28.133	101.260	32	0.413	0.242	UMich
LC-05-52e	0.238	0.140	0.066	0.013	0.137	0.271	0.100	71.939	28.099	101.003	33	0.408	0.240	UMich
LC-05-52e	0.468	0.161	0.257	0.026	0.146	0.273	0.126	71.627	28.386	101.468	34	0.419	0.286	UMich
LC-05-52e	0.400	0.187	0.191	0.019	0.184	0.275	0.170	71.657	28.338	101.422	35	0.460	0.357	UMich
LC-05-52e	1.419	0.157	1.173	0.039	0.119	0.270	0.104	70.381	29.558	103.220	36	0.389	0.261	UMich
LC-05-52e	0.167	0.096	0.063	0.009	0.095	0.271	0.102	70.630	27.481	98.915	37	0.367	0.198	UMich
LC-05-52e	0.222	0.098	0.088	0.009	0.128	0.275	0.120	72.462	28.277	101.678	38	0.403	0.218	UMich
LC-05-52e	0.402	0.124	0.645	0.039	0.154	0.264	0.116	70.035	28.150	99.929	39	0.418	0.241	UMich
LC-05-63a	0.424	0.269	0.151	0.047	0.367	0.305	0.189	69.433	27.685	98.888	51a	0.672	0.458	UWAustralia
LC-05-63a	0.538	0.276	0.275	0.046	0.368	0.302	0.179	69.607	27.976	99.600	52a	0.670	0.455	UWAustralia
LC-05-63a	0.441	0.288	0.220	0.071	0.369	0.305	0.190	69.207	27.724	98.856	53a	0.674	0.478	UWAustralia
LC-05-63a	0.372	0.275	0.074	0.025	0.410	0.306	0.212	69.408	27.588	98.708	54a	0.716	0.487	UWAustralia
LC-05-63a	0.537	0.290	0.307	0.047	0.403	0.307	0.215	69.359	27.978	99.517	55a	0.710	0.505	UWAustralia
LC-05-63a	0.543	0.275	0.356	0.115	0.395	0.305	0.211	68.852	27.856	98.989	56a	0.700	0.487	UWAustralia
LC-05-63a	0.352	0.233	0.124	0.066	0.298	0.306	0.158	69.706	27.644	98.949	57a	0.604	0.391	UWAustralia

LC-05-63a	0.454	0.267	0.248	0.078	0.392	0.301	0.218	69.447	27.866	99.323	58a	0.693	0.484	UWAustralia
LC-05-63a	0.399	0.277	0.168	0.056	0.378	0.303	0.202	69.540	27.754	99.109	59a	0.681	0.479	UWAustralia
LC-05-63a	0.406	0.232	0.247	0.050	0.308	0.304	0.184	69.427	27.709	98.885	60a	0.612	0.416	UWAustralia
LC-05-63a	0.261	0.204			0.394	0.306	0.232	70.060	27.603	99.110	61a	0.700	0.436	UWAustralia
LC-05-63a	0.177	0.129		0.010	0.260	0.299	0.166	70.432	27.514	99.028	62a	0.559	0.295	UWAustralia
LC-05-63a	0.156	0.162		0.006	0.209	0.307	0.093	70.344	27.440	98.744	63a	0.516	0.256	UWAustralia
LC-05-63a	0.194	0.149		0.024	0.294	0.304	0.174	69.730	27.316	98.271	64a	0.598	0.324	UWAustralia
LC-05-63a	0.280	0.244	0.005	0.007	0.346	0.303	0.188	69.591	27.436	98.462	65a	0.649	0.432	UWAustralia
LC-05-63a	0.286	0.255			0.406	0.300	0.204	69.975	27.629	99.102	66a	0.706	0.459	UWAustralia
LC-05-63a	0.206	0.193	0.013	0.004	0.319	0.309	0.243	69.955	27.492	98.796	67a	0.627	0.436	UWAustralia
LC-05-63a	0.207	0.210			0.243	0.305	0.153	70.357	27.559	99.070	68a	0.548	0.363	UWAustralia
LC-05-63a	0.196	0.198			0.243	0.305	0.131	70.317	27.524	98.969	69a	0.548	0.329	UWAustralia
LC-05-63a	0.320	0.212	0.014	0.017	0.259	0.305	0.130	69.799	27.455	98.568	70a	0.564	0.342	UWAustralia
LC-05-63a	0.210	0.223			0.145	0.303	0.047	70.492	27.529	98.991	71a	0.448	0.270	UWAustralia
LC-05-63a	0.307	0.279			0.389	0.305	0.176	69.635	27.511	98.625	72a	0.695	0.455	UWAustralia
LC-05-63a	0.298	0.271			0.403	0.304	0.183	70.000	27.646	99.123	73a	0.706	0.454	UWAustralia
LC-05-63a	0.134	0.238			0.327	0.305	0.365	70.249	27.617	99.284	74a	0.632	0.604	UWAustralia
LC-05-63a	0.263	0.237			0.150	0.304	0.075	70.378	27.534	98.949	75a	0.454	0.312	UWAustralia
LC-05-63a	0.133	0.233			0.222	0.300	0.236	70.129	27.457	98.754	76a	0.522	0.469	UWAustralia
LC-05-63a	0.231	0.285			0.477	0.306	0.307	69.463	27.501	98.603	77a	0.783	0.592	UWAustralia
LC-05-63a	0.000	0.221			0.240	0.311	0.289	70.059	27.356	98.499	78a	0.551	0.510	UWAustralia
LC-05-63a	0.010	0.087	0.008	0.005	0.079	0.291	0.165	69.166	26.761	96.593	79a	0.369	0.252	UWAustralia
LC-05-63a	0.215	0.000			0.301	0.305	0.171	70.208	27.358	98.570	80a	0.606	0.171	UWAustralia
LC-05-63a	0.120	0.167			0.305	0.263	0.299	70.307	27.503	98.980	81a	0.568	0.466	UWAustralia
LC-05-63a	0.170	0.211			0.335	0.307	0.233	70.057	27.501	98.832	82a	0.642	0.443	UWAustralia

LC-05-63a	0.575	0.357	0.246	0.093	0.282	0.303	0.066	69.204	27.808	98.943	83a	0.585	0.423	UWAustralia
LC-05-63a	0.136	0.220		0.006	0.347	0.308	0.136	69.851	27.401	98.462	84a	0.655	0.356	UWAustralia
LC-05-63a	0.237	0.196			0.300	0.300	0.157	70.149	27.520	98.883	85a	0.600	0.354	UWAustralia
LC-05-63a	0.085	0.234			0.166	0.304	0.103	70.692	27.561	99.176	86a	0.470	0.337	UWAustralia
LC-05-82.6a	0.343	0.099	0.021		0.089	0.294	0.125	71.924	28.056	100.951	40	0.382	0.224	Umich
LC-05-82.6a	0.375	0.169	0.018	0.000	0.056	0.291	0.069	71.789	28.042	100.808	41	0.347	0.238	Umich
LC-05-82.6a	0.416	0.133	0.126	0.061	0.198	0.295	0.182	71.528	28.216	101.154	42	0.493	0.315	Umich
LC-05-82.6a	0.371	0.174	0.014		0.129	0.288	0.103	71.895	28.141	101.113	43	0.417	0.276	Umich
LC-05-82.6a	0.411	0.185	0.014	0.000	0.166	0.293	0.130	71.498	28.060	100.757	44	0.459	0.316	Umich
LC-05-82.6a	0.269	0.187	0.020	0.000	0.294	0.293	0.272	71.352	28.047	100.734	45	0.587	0.459	Umich
LC-05-82.6a	1.811	0.193	1.251	0.050	0.149	0.280	0.151	68.024	29.079	100.987	46	0.429	0.344	Umich
LC-05-82.6a	0.641	0.535	0.022		0.349	0.295	0.203	70.892	28.443	101.380	47	0.644	0.738	Umich
LC-05-82.6a	0.303	0.128	0.016		0.168	0.291	0.179	71.905	28.111	101.100	48	0.459	0.307	Umich
LC-05-82.6a	0.395	0.205	0.016		0.201	0.288	0.153	71.875	28.240	101.373	49	0.489	0.358	Umich
LC-05-82.6a	0.457	0.307	0.016		0.441	0.294	0.235	70.855	28.168	100.772	50	0.735	0.542	Umich
LC-05-82.6a	0.500	0.265	0.018	0.000	0.525	0.290	0.338	71.122	28.349	101.407	51	0.816	0.603	Umich
LC-05-82.6a	0.323	0.141	0.017		0.186	0.289	0.185	71.915	28.152	101.208	52	0.476	0.326	Umich
LC-05-82.6a	0.303	0.175	0.022		0.133	0.293	0.121	72.050	28.175	101.271	53	0.426	0.296	Umich
LC-05-82.6a	0.070	0.151	0.016		0.023	0.291	0.081	72.506	28.081	101.219	54	0.314	0.232	Umich
LC-05-82.6a	0.053	0.150	0.020		0.046	0.286	0.085	72.461	28.072	101.174	55	0.332	0.235	Umich
LC-05-82.6a	0.010	0.098	0.028		0.016	0.288	0.089	72.394	27.963	100.886	56	0.304	0.187	Umich
LC-05-82.6a	0.015	0.116	0.024		0.059	0.288	0.124	72.272	27.970	100.868	57	0.347	0.240	Umich
LC-05-82.6a	0.058	0.182	0.034		0.168	0.285	0.230	71.709	27.957	100.623	58	0.453	0.412	Umich
LC-05-82.6a	0.151	0.183	0.768	0.066	0.075	0.211	0.133	62.364	25.183	89.135	59	0.286	0.316	Umich
LC-05-82.6a	0.028	0.116	0.078		0.021	0.271	0.088	71.267	27.613	99.481	60	0.291	0.204	Umich

LC-05-82.6d	0.273	0.154	0.014		0.253	0.290	0.214	69.671	27.327	98.196	61	0.543	0.368	Umich
LC-05-82.6d	0.304	0.167	0.023		0.201	0.292	0.165	71.503	28.019	100.674	62	0.494	0.331	Umich
LC-05-82.6d	0.319	0.206	0.015		0.168	0.298	0.146	71.618	28.072	100.842	63	0.466	0.351	Umich
LC-05-82.6d	0.263	0.144	0.013		0.203	0.287	0.152	71.517	27.962	100.541	64	0.490	0.296	Umich
LC-05-82.6d	0.288	0.165	0.015		0.156	0.293	0.119	71.330	27.891	100.256	65	0.448	0.284	Umich
LC-05-82.6d	0.693	0.182	0.302	0.025	0.216	0.283	0.092	69.748	27.931	99.472	66	0.499	0.274	Umich
LC-05-82.6d	0.301	0.116	0.022		0.177	0.289	0.110	71.545	27.956	100.516	67	0.466	0.226	Umich
LC-05-82.6d	0.315	0.173	0.025	0.009	0.128	0.284	0.095	71.374	27.914	100.316	68	0.412	0.268	Umich
LC-05-82.6d	0.224	0.071	0.011		0.122	0.270	0.087	71.826	27.905	100.516	69	0.392	0.158	Umich
LC-05-82.6d	0.288	0.118	0.017		0.213	0.290	0.143	71.523	27.969	100.561	70	0.503	0.262	Umich
LC-05-82.6d	0.286	0.166	0.016		0.198	0.287	0.137	70.886	27.749	99.725	71	0.486	0.303	Umich
LC-05-82.6d	0.182	0.071	0.023		0.154	0.294	0.121	71.842	27.940	100.626	72	0.448	0.191	Umich
LC-05-82.6d	0.220	0.086	0.032	0.011	0.156	0.283	0.152	71.783	27.975	100.697	73	0.438	0.238	Umich
LC-05-82.6d	0.221	0.102	0.059	0.028	0.126	0.279	0.100	71.569	27.908	100.392	74	0.405	0.202	Umich
LC-05-82.6d	0.397	0.132	0.145	0.016	0.179	0.286	0.111	71.548	28.178	100.991	75	0.465	0.243	Umich
LC-05-82.6d	0.202	0.118	0.047	0.023	0.213	0.279	0.181	70.879	27.713	99.656	76	0.492	0.300	Umich
LC-05-82.6d	0.151	0.072	0.040	0.031	0.162	0.283	0.131	71.409	27.789	100.067	77	0.445	0.203	Umich
LC-05-90.1b	0.081	0.168	0.031		0.229	0.257	0.283	71.004	27.724	99.795	41b	0.486	0.451	UWAustralia
LC-05-90.1b	0.222	0.380	0.036	0.007	0.309	0.259	0.263	71.330	28.184	100.998	42b	0.568	0.643	UWAustralia
LC-05-90.1b	0.024	0.105	0.028		0.355	0.255	0.495	70.708	27.657	99.647	43b	0.610	0.600	UWAustralia
LC-05-90.1b	0.175	0.205	0.011	0.028	0.310	0.258	0.258	71.075	27.885	100.247	44b	0.567	0.464	UWAustralia
LC-05-90.1b	0.147	0.290	0.012		0.169	0.261	0.125	70.817	27.699	99.542	45b	0.430	0.415	UWAustralia
LC-05-90.1b	0.395	0.397	0.298	0.032	0.271	0.256	0.184	70.429	28.234	100.529	46b	0.527	0.581	UWAustralia
LC-05-90.1b	0.320	0.346	0.253	0.042	0.242	0.261	0.165	70.177	27.968	99.786	47b	0.503	0.511	UWAustralia
LC-05-90.1b	1.198	0.396	1.057	0.032	0.254	0.260	0.199	69.295	29.186	101.903	48b	0.514	0.595	UWAustralia

LC-05-90.1b	0.197	0.337	0.022		0.255	0.263	0.182	70.911	27.891	100.067	49b	0.518	0.519	UWAustralia
LC-05-90.1b	0.145	0.280	0.008		0.116	0.258	0.093	70.929	27.677	99.511	50b	0.374	0.373	UWAustralia
LC-05-90.1b	0.054	0.250	0.013		0.141	0.255	0.234	71.525	27.889	100.396	51b	0.396	0.484	UWAustralia
LC-05-90.1b	0.095	0.337	0.007		0.254	0.262	0.216	71.263	27.959	100.430	52b	0.516	0.554	UWAustralia
LC-05-90.1b	0.105	0.404	0.007		0.197	0.261	0.174	70.794	27.798	99.789	53b	0.458	0.578	UWAustralia
LC-05-90.1b	0.084	0.285	0.013		0.238	0.256	0.215	70.789	27.717	99.630	54b	0.494	0.500	UWAustralia
LC-05-90.1b	0.118	0.432	0.015		0.223	0.252	0.256	71.202	28.037	100.589	55b	0.475	0.688	UWAustralia
LC-05-90.1b	0.080	0.264	0.012		0.181	0.264	0.199	71.079	27.761	99.859	56b	0.445	0.463	UWAustralia
LC-05-90.1b	0.051	0.164	0.015		0.198	0.258	0.208	70.915	27.606	99.432	57b	0.456	0.372	UWAustralia
LC-05-90.1b	0.061	0.252	0.008		0.165	0.259	0.181	71.028	27.695	99.665	58b	0.424	0.433	UWAustralia
LC-05-90.1b	0.106	0.360	0.009		0.282	0.257	0.271	70.814	27.847	99.969	59b	0.539	0.631	UWAustralia
LC-05-90.1b	0.112	0.327	0.026		0.236	0.263	0.223	70.775	27.785	99.776	60b	0.499	0.550	UWAustralia
LC-05-90.1b	0.106	0.266	0.009		0.219	0.261	0.167	70.669	27.637	99.353	61b	0.480	0.433	UWAustralia
LC-05-90.1b	0.120	0.275	0.009		0.208	0.262	0.166	70.937	27.751	99.755	62b	0.471	0.441	UWAustralia
LC-05-90.1b	0.240	0.204	0.116		0.212	0.266	0.242	70.794	27.871	100.007	63b	0.477	0.445	UWAustralia
LC-05-90.1b	0.929	0.570	1.553		0.291	0.264	0.197	67.800	29.452	101.855	64b	0.555	0.768	UWAustralia
LC-05-90.1b	0.161	0.337	0.013		0.252	0.260	0.188	70.767	27.801	99.788	65b	0.512	0.524	UWAustralia
LC-05-90.1b	0.212	0.383	0.012		0.297	0.263	0.220	70.794	27.926	100.119	66b	0.560	0.603	UWAustralia
LC-05-90.1b	0.162	0.369	0.015		0.284	0.257	0.362	70.632	27.851	99.936	67b	0.542	0.731	UWAustralia
LC-05-90.1b	0.172	0.256	0.014		0.225	0.264	0.156	70.703	27.690	99.495	68b	0.489	0.412	UWAustralia
LC-05-90.1b	0.314	0.536	0.013		0.334	0.260	0.341	70.638	28.132	100.586	69b	0.594	0.877	UWAustralia
LC-05-90.1b	0.233	0.420	0.154	0.020	0.252	0.262	0.205	70.272	27.936	99.900	70b	0.514	0.624	UWAustralia
LC-05-90.1b	0.040	0.112	0.037	0.004	0.413	0.260	0.538	70.335	27.598	99.354	31d	0.673	0.650	UWAustralia
LC-05-90.1b	0.107	0.355	0.012		0.242	0.257	0.241	70.631	27.738	99.601	32d	0.499	0.596	UWAustralia
LC-05-90.1b	0.097	0.347	0.018	0.019	0.269	0.253	0.195	70.876	27.840	99.937	33d	0.522	0.543	UWAustralia

LC-05-90.1b	0.109	0.317	0.014		0.229	0.253	0.159	70.729	27.718	99.561	34d	0.482	0.477	UWAustralia
LC-05-90.1b	0.120	0.395	0.015		0.278	0.259	0.194	70.494	27.750	99.535	35d	0.538	0.589	UWAustralia
LC-05-90.1b	0.114	0.292	0.021	0.018	0.314	0.256	0.234	70.149	27.573	99.011	36d	0.571	0.526	UWAustralia
LC-05-90.1b	0.152	0.368	0.015		0.268	0.256	0.199	70.811	27.861	99.967	37d	0.523	0.567	UWAustralia
LC-05-90.1b	0.048	0.235	0.021		0.244	0.253	0.338	71.184	27.846	100.206	38d	0.497	0.573	UWAustralia
LC-05-90.1b	0.153	0.409	0.012		0.312	0.259	0.231	70.500	27.815	99.726	39d	0.571	0.640	UWAustralia
LC-05-90.1b	0.147	0.390	0.012		0.281	0.256	0.198	70.462	27.742	99.498	40d	0.537	0.588	UWAustralia
LC-05-106c	0.200	0.104	0.016		0.166	0.312	0.166	71.501	27.872	100.336	78	0.478	0.270	UMich
LC-05-106c	0.075	0.121	0.053		0.057	0.301	0.100	71.796	27.863	100.365	79	0.357	0.220	UMich
LC-05-106c	0.219	0.214	0.015		0.138	0.297	0.132	71.492	27.942	100.449	80	0.435	0.346	UMich
LC-05-106c	0.029	0.165	0.027		0.036	0.299	0.079	72.017	27.902	100.553	81	0.335	0.243	UMich
LC-05-106c	0.057	0.142	0.022		0.086	0.308	0.110	71.787	27.855	100.366	82	0.394	0.252	UMich
LC-05-106c	0.352	0.244	0.265	0.052	0.154	0.299	0.158	70.168	27.876	99.568	83	0.453	0.402	UMich
LC-05-106c	0.148	0.256	0.021		0.121	0.299	0.120	71.500	27.929	100.392	84	0.420	0.375	UMich
LC-05-106c	0.048	0.190	0.027		0.043	0.302	0.100	71.760	27.852	100.322	85	0.346	0.290	UMich
LC-05-106c	0.241	0.279	0.015		0.079	0.307	0.089	71.486	27.965	100.460	86	0.386	0.368	UMich
LC-05-106c	0.153	0.258	0.017		0.115	0.300	0.136	71.538	27.945	100.463	87	0.415	0.395	UMich
LC-05-106c	0.077	0.191	0.019		0.063	0.308	0.081	71.735	27.864	100.337	88	0.371	0.272	UMich
LC-05-106c	0.079	0.184	0.018		0.066	0.304	0.111	71.842	27.906	100.510	89	0.370	0.295	UMich
LC-05-106c	0.398	0.263	0.026	0.026	0.135	0.301	0.109	70.847	27.871	99.977	90	0.436	0.372	UMich
LC-05-106c	0.190	0.061	0.109		0.116	0.280	0.128	68.789	26.840	96.513	91	0.396	0.189	UMich
LC-05-106c	0.191	0.060	0.043	0.000	0.167	0.285	0.191	71.274	27.768	99.979	92	0.452	0.251	UMich
LC-05-106d	0.346	0.231	0.082	0.027	0.124	0.296	0.164	71.282	28.047	100.598	93	0.419	0.395	UMich
LC-05-106d	0.069	0.189	0.028		0.136	0.295	0.199	71.660	27.916	100.492	94	0.431	0.388	UMich
LC-05-106d	0.160	0.212	0.028		0.115	0.299	0.178	71.610	27.960	100.562	95	0.414	0.390	UMich

LC-05-106d	0.067	0.155	0.084		0.202	0.295	0.270	71.389	27.913	100.374	96	0.497	0.425	UMich
LC-05-106d	0.309	0.283	0.014		0.128	0.302	0.162	71.362	28.018	100.578	97	0.430	0.445	UMich
LC-05-106d	0.296	0.254	0.015		0.123	0.300	0.147	71.274	27.942	100.350	98	0.422	0.401	UMich
LC-05-106d	0.320	0.276	0.017		0.163	0.299	0.183	71.359	28.046	100.663	99	0.461	0.459	UMich
LC-05-106d	0.110	0.204	0.026		0.184	0.300	0.231	71.424	27.911	100.390	100	0.484	0.435	UMich
LC-05-106d	0.272	0.237	0.024		0.168	0.297	0.220	71.233	27.951	100.400	101	0.465	0.456	UMich
LC-05-106d	0.345	0.225	0.117	0.036	0.145	0.299	0.175	71.258	28.097	100.699	102	0.444	0.400	UMich
LC-05-106d	0.302	0.244	0.023		0.144	0.302	0.167	70.913	27.829	99.925	103	0.446	0.411	UMich
LC-05-106d	0.319	0.182	0.097	0.014	0.149	0.299	0.190	71.052	27.935	100.236	104	0.447	0.372	UMich
LC-05-106d	0.275	0.200	0.020		0.134	0.299	0.186	71.579	28.022	100.714	105	0.433	0.385	UMich
LC-05-106d	0.296	0.219	0.031		0.116	0.300	0.148	71.211	27.899	100.219	106	0.416	0.367	UMich
LC-05-106d	0.122	0.192	0.084		0.030	0.298	0.082	71.715	27.935	100.457	107	0.327	0.274	UMich
LC-05-106d	0.053	0.161	0.103	0.011	0.051	0.301	0.116	72.014	28.029	100.837	108	0.352	0.277	UMich
LC-05-106d	0.095	0.205	0.100		0.099	0.295	0.159	71.342	27.874	100.169	109	0.394	0.364	UMich
LC-05-106d	0.307	0.162	0.124	0.028	0.123	0.296	0.176	71.031	27.916	100.162	110	0.419	0.338	UMich
LC-05-106e	0.427	0.352	0.020	0.020	0.136	0.300	0.161	70.399	27.807	99.621	1	0.435	0.513	UMich
LC-05-106e	0.085	0.114	0.054		0.132	0.304	0.164	71.437	27.796	100.086	2	0.436	0.278	UMich
LC-05-106e	0.334	0.257	0.019		0.247	0.303	0.264	70.594	27.834	99.851	3	0.550	0.521	UMich
LC-05-106e	0.253	0.184	0.015		0.065	0.303	0.131	71.308	27.822	100.080	4	0.368	0.315	UMich
LC-05-106e	0.193	0.216	0.025		0.135	0.301	0.166	71.117	27.804	99.955	5	0.436	0.381	UMich
LC-05-106e	0.090	0.114	0.022		0.158	0.302	0.209	71.229	27.713	99.836	6	0.460	0.323	UMich
LC-05-106e	0.018	0.110	0.024		0.135	0.294	0.194	71.571	27.770	100.115	7	0.429	0.304	UMich
LC-05-106e	0.410	0.355	0.062	0.027	0.183	0.298	0.189	70.381	27.880	99.784	8	0.481	0.543	UMich
LC-05-106e	0.343	0.251	0.071		0.151	0.300	0.175	70.759	27.862	99.910	9	0.450	0.425	UMich
LC-05-106e	0.205	0.218	0.026		0.156	0.303	0.179	71.316	27.910	100.312	10	0.459	0.397	UMich

148

LC-05-106e	0.125	0.114	0.021		0.100	0.302	0.158	71.215	27.677	99.712	11	0.401	0.272	UMich
LC-05-106e	0.084	0.167	0.029		0.132	0.296	0.175	71.336	27.777	99.995	12	0.428	0.342	UMich
LC-05-106e	0.052	0.191	0.020		0.046	0.302	0.099	71.297	27.678	99.685	13	0.348	0.290	UMich
LC-05-106e	0.011	0.092	0.023		0.042	0.300	0.090	71.570	27.663	99.791	14	0.342	0.182	UMich
LC-05-106e	0.712	0.185	0.445		0.118	0.295	0.176	70.173	28.228	100.331	15	0.412	0.361	UMich
LC-05-106e	0.208	0.180	0.023		0.077	0.297	0.124	71.325	27.806	100.038	16	0.374	0.304	UMich
LC-05-106e	0.238	0.195	0.044	0.010	0.112	0.294	0.158	70.950	27.755	99.755	17	0.406	0.353	UMich
LC-05-129.1c	0.173	0.221	0.016		0.085	0.314	0.113	70.349	27.452	98.724	1	0.399	0.335	UMich
LC-05-129.1c	0.172	0.249	0.019		0.090	0.311	0.124	70.664	27.599	99.229	2	0.401	0.374	UMich
LC-05-129.1c	0.190	0.211	0.042	0.017	0.104	0.310	0.138	70.329	27.498	98.840	3	0.414	0.350	UMich
LC-05-129.1c	0.134	0.151	0.016		0.103	0.307	0.126	70.645	27.487	98.968	4	0.410	0.277	UMich
LC-05-129.1c	0.118	0.129	0.017		0.061	0.310	0.116	70.876	27.517	99.143	5	0.370	0.245	UMich
LC-05-129.1c	0.477	0.240	0.386		0.104	0.305	0.142	69.794	27.895	99.341	6	0.408	0.382	UMich
LC-05-129.1c	0.236	0.269	0.128	0.027	0.128	0.305	0.129	69.955	27.550	98.726	7	0.433	0.398	UMich
LC-05-129.1c	0.159	0.185	0.017		0.087	0.306	0.126	70.784	27.576	99.238	8	0.393	0.310	UMich
LC-05-129.1c	0.132	0.181	0.018		0.056	0.312	0.118	70.683	27.498	98.998	9	0.368	0.299	UMich
LC-05-129.1c	0.100	0.137	0.031	0.010	0.090	0.308	0.168	70.567	27.446	98.855	10	0.398	0.305	UMich
LC-05-129.1c	0.128	0.181	0.016		0.030	0.308	0.098	70.744	27.487	98.992	11	0.338	0.278	UMich
LC-05-129.1c	0.156	0.220	0.019		0.097	0.311	0.115	70.387	27.464	98.769	12	0.408	0.335	UMich
LC-05-129.1c	0.115	0.166	0.017		0.103	0.308	0.153	70.453	27.423	98.739	13	0.411	0.319	UMich
LC-05-129.1c	0.205	0.139	0.023	0.026	0.136	0.306	0.138	70.072	27.347	98.392	14	0.441	0.277	UMich
LC-05-129.1c	0.085	0.095	0.017		0.065	0.305	0.149	70.827	27.457	99.000	15	0.370	0.245	UMich
LC-05-129.1c	0.099	0.045	0.031		0.095	0.301	0.127	70.876	27.468	99.042	16	0.396	0.172	UMich
LC-05-129.1c	0.075	0.035	0.026		0.055	0.307	0.117	70.781	27.374	98.771	17	0.362	0.152	UMich
LC-05-129.1c	0.061	0.025	0.029		0.244	0.302	0.110	70.593	27.413	98.776	18	0.546	0.135	UMich

149

LC-05-129.1c	0.136	0.179	0.020		0.092	0.303	0.145	70.252	27.361	98.487	19	0.395	0.324	UMich
LC-05-129.1d	0.209	0.191	0.023		0.080	0.305	0.111	70.635	27.554	99.108	20	0.385	0.302	UMich
LC-05-129.1d	0.215	0.190	0.017		0.081	0.309	0.099	70.620	27.546	99.076	21	0.390	0.289	UMich
LC-05-129.1d	0.199	0.173	0.017		0.094	0.312	0.118	70.732	27.578	99.223	22	0.406	0.292	UMich
LC-05-129.1d	0.200	0.125	0.018		0.069	0.308	0.101	70.795	27.534	99.150	23	0.377	0.226	UMich
LC-05-129.1d	0.154	0.094	0.014		0.123	0.309	0.143	70.918	27.570	99.324	24	0.432	0.237	UMich
LC-05-129.1d	0.391	0.158	0.273	0.084	0.071	0.306	0.110	70.046	27.733	99.171	25	0.377	0.268	UMich
LC-05-129.1d	0.207	0.180	0.018		0.133	0.309	0.120	70.644	27.582	99.193	26	0.443	0.300	UMich
LC-05-129.1d	0.250	0.218	0.019		0.161	0.305	0.189	70.527	27.637	99.306	27	0.467	0.407	UMich
LC-05-129.1d	0.220	0.157	0.017		0.078	0.312	0.106	70.725	27.561	99.176	28	0.389	0.263	UMich
LC-05-129.1d	0.232	0.177	0.018		0.134	0.305	0.141	70.674	27.614	99.295	29	0.439	0.318	UMich
LC-05-129.1d	0.206	0.181	0.020		0.055	0.308	0.085	71.029	27.668	99.552	30	0.363	0.266	UMich
LC-05-129.1d	0.199	0.181	0.020		0.094	0.304	0.112	70.759	27.590	99.258	31	0.398	0.293	UMich
LC-05-129.1d	0.169	0.093	0.023		0.052	0.301	0.086	70.825	27.485	99.033	32	0.353	0.179	UMich
LC-05-129.1d	0.251	0.074	0.083		0.029	0.266	0.090	67.762	26.395	94.950	33	0.296	0.164	UMich
LC-05-129.1d	0.164	0.077	0.027		0.070	0.305	0.091	70.768	27.468	98.969	34	0.375	0.168	UMich
LC-05-129.1d	0.176	0.136	0.147		0.066	0.282	0.092	68.321	26.716	95.936	35	0.348	0.228	UMich
LC-05-129a	0.451	0.461	0.239	0.069	0.378	0.597	0.117	67.515	27.412	97.390	1a	0.975	0.578	UWAustralia
LC-05-129a	0.783	0.673	0.658	0.298	0.302	0.623	0.138	65.899	27.774	97.381	2a	0.925	0.812	UWAustralia
LC-05-129a	0.641	0.617	0.504	0.239	0.568	0.621	0.133	66.161	27.688	97.358	3a	1.189	0.750	UWAustralia
LC-05-129a	0.636	0.585	0.526	0.255	0.529	0.602	0.145	65.855	27.545	96.881	4a	1.131	0.729	UWAustralia
LC-05-129a	0.765	0.659	0.597	0.293	0.755	0.609	0.160	65.233	27.722	97.019	5a	1.363	0.820	UWAustralia
LC-05-129a	0.672	0.648	0.428	0.168	0.552	0.621	0.147	65.778	27.467	96.672	26a	1.173	0.795	UWAustralia
LC-05-129a	0.689	0.625	0.445	0.143	0.416	0.629	0.147	66.430	27.636	97.382	27a	1.045	0.773	UWAustralia
LC-05-129a	0.754	0.703	0.496	0.170	0.518	0.624	0.134	65.648	27.583	96.860	28a	1.141	0.837	UWAustralia

LC-05-129a	0.278	0.310			0.312	0.641	0.064	68.454	27.139	97.210	29a	0.953	0.375	UWAustralia
LC-05-129a	0.701	0.598	0.464	0.233	0.486	0.634	0.228	65.679	27.458	96.669	30a	1.120	0.826	UWAustralia
LC-05-129a	0.536	0.475	0.334	0.158	0.456	0.638	0.133	66.881	27.462	97.220	31a	1.094	0.608	UWAustralia
LC-05-129a	0.349	0.352	0.054	0.013	0.349	0.625	0.151	67.977	27.161	97.075	32a	0.974	0.503	UWAustralia
LC-05-129a	0.345	0.345	0.057	0.033	0.348	0.625	0.168	67.974	27.174	97.136	33a	0.973	0.513	UWAustralia
LC-05-129a	0.324	0.391	0.064	0.021	0.372	0.612	0.085	67.755	27.115	96.839	34a	0.983	0.476	UWAustralia
LC-05-129a	0.396	0.416	0.134	0.062	0.456	0.610	0.136	67.509	27.246	97.022	35a	1.065	0.552	UWAustralia
LC-05-129a	0.251	0.220			0.294	0.683	0.110	69.123	27.320	98.019	6a	0.978	0.329	UWAustralia
LC-05-129a	0.348	0.428			0.399	0.678	0.122	68.529	27.417	97.954	7a	1.077	0.550	UWAustralia
LC-05-129a	0.298	0.296			0.392	0.679	0.148	68.833	27.384	98.053	8a	1.072	0.444	UWAustralia
LC-05-129a	0.319	0.368			0.402	0.674	0.108	68.630	27.378	97.909	9a	1.075	0.475	UWAustralia
LC-05-129a	0.343	0.395			0.400	0.669	0.144	68.562	27.401	97.951	10a	1.069	0.539	UWAustralia
LC-05-129a	0.309	0.358			0.409	0.638	0.139	68.492	27.304	97.665	11a	1.047	0.498	UWAustralia
LC-05-129a	0.294	0.345			0.341	0.600	0.114	68.632	27.265	97.606	12a	0.941	0.459	UWAustralia
LC-05-129a	0.305	0.371			0.402	0.592	0.112	68.503	27.282	97.581	13a	0.994	0.482	UWAustralia
LC-05-129a	0.239	0.237			0.301	0.580	0.121	68.903	27.207	97.605	14a	0.881	0.358	UWAustralia
LC-05-129a	0.192		0.068	0.034	0.010	0.053	0.092	70.067	27.051	97.596	15a	0.064	0.092	UWAustralia
LC-05-129a	0.231	0.056	0.087	0.046	0.029	0.118	0.102	69.515	26.994	97.223	37a	0.147	0.158	UWAustralia
LC-05-129a	0.129	0.009			0.014	0.201	0.090	70.107	27.016	97.603	38a	0.215	0.099	UWAustralia
LC-05-129a	0.182	0.123			0.312	0.488	0.194	68.315	26.824	96.454	39a	0.800	0.316	UWAustralia
LC-05-129a	0.134		0.011	0.021	0.010	0.111	0.093	69.968	26.932	97.311	41a	0.122	0.093	UWAustralia
LC-05-129a	0.130			0.009	0.005	0.090	0.084	69.833	26.834	96.986	42a	0.095	0.084	UWAustralia
LC-05-129a	0.116			0.012	0.007	0.334	0.097	69.736	26.916	97.241	43a	0.341	0.097	UWAustralia
LC-05-129a	0.124			0.008	0.007	0.170	0.090	70.112	26.978	97.494	44a	0.177	0.090	UWAustralia
LC-05-129a	0.104			0.013	0.008	0.297	0.101	69.923	26.959	97.414	45a	0.305	0.101	UWAustralia

LC-05-129a	0.132			0.012	0.009	0.127	0.085	69.969	26.921	97.284	46a	0.136	0.085	UWAustralia
LC-05-129a	0.115	0.020		0.009	0.018	0.357	0.100	69.810	26.979	97.429	47a	0.375	0.120	UWAustralia
LC-05-129a	0.087	0.046		0.009	0.275	0.480	0.102	68.893	26.865	96.773	48a	0.754	0.148	UWAustralia
LC-05-129a	0.130	0.055		0.012	0.037	0.403	0.105	69.569	26.967	97.298	49a	0.440	0.160	UWAustralia
LC-05-129a	0.132	0.008		0.007	0.013	0.345	0.098	69.632	26.896	97.135	50a	0.359	0.105	UWAustralia
LC-05-150d	0.056	0.473	0.021		0.527	0.673	0.164	68.952	27.553	98.419	36	1.201	0.637	UMich
LC-05-150d	0.048	0.467	0.018		0.451	0.671	0.098	68.790	27.406	97.948	37	1.122	0.564	UMich
LC-05-150d	0.137	0.546	0.407	0.204	0.640	0.662	0.124	67.369	27.646	97.734	38	1.302	0.669	UMich
LC-05-150d	0.048	0.381	0.021		0.462	0.674	0.137	69.016	27.440	98.178	39	1.136	0.518	UMich
LC-05-150d	0.320	0.668	0.497	0.166	0.677	0.669	0.131	66.892	27.810	97.830	40	1.346	0.799	UMich
LC-05-150d	0.076	0.470	0.017		0.707	0.676	0.171	68.315	27.439	97.869	41	1.383	0.640	UMich
LC-05-150d	0.089	0.489	0.037		0.649	0.673	0.132	68.737	27.597	98.403	42	1.322	0.620	UMich
LC-05-150d	0.158	0.619	0.053		0.811	0.668	0.172	68.225	27.695	98.400	43	1.479	0.791	UMich
LC-05-150d	0.094	0.537	0.020		0.630	0.678	0.088	68.732	27.600	98.378	44	1.308	0.625	UMich
LC-05-150d	0.117	0.563	0.019		0.689	0.675	0.190	68.196	27.499	97.947	45	1.363	0.753	UMich
LC-05-150d	0.064	0.500	0.016		0.567	0.683	0.121	68.957	27.597	98.504	46	1.250	0.621	UMich
LC-05-150d	0.077	0.452	0.022		0.577	0.676	0.145	68.875	27.547	98.370	47	1.253	0.596	UMich
LC-05-150d	0.070	0.547	0.022		0.623	0.673	0.177	68.472	27.513	98.096	48	1.296	0.723	UMich
LC-05-150d	0.050	0.364	0.018		0.520	0.676	0.163	68.803	27.387	97.981	49	1.196	0.527	UMich
LC-05-150d	0.038	0.320	0.027		0.337	0.668	0.089	69.454	27.454	98.387	50	1.005	0.410	UMich
LC-05-150d	0.018	0.253	0.016	0.009	0.365	0.661	0.167	69.197	27.311	97.996	51	1.026	0.420	UMich
LC-04-38.8d	0.117	0.194	0.013		0.113	0.170	0.041	70.654	27.432	98.734	69	0.283	0.235	UMich
LC-04-38.8d	0.137	0.201	0.018		0.117	0.176	0.043	70.698	27.478	98.869	70	0.294	0.245	UMich
LC-04-38.8d	0.144	0.221	0.015		0.116	0.173	0.044	70.957	27.595	99.266	71	0.289	0.266	UMich
LC-04-38.8d	0.150	0.211	0.021		0.106	0.173	0.045	70.958	27.592	99.256	72	0.279	0.256	UMich

LC-04-38.8d	0.127	0.176	0.018		0.099	0.163	0.048	70.675	27.424	98.730	73	0.263	0.224	UMich
LC-04-38.8d	0.109	0.091	0.029	0.013	0.077	0.167	0.039	70.924	27.432	98.881	74	0.244	0.130	UMich
LC-04-38.8d	0.082	0.076	0.015		0.091	0.167	0.047	71.491	27.607	99.576	75	0.258	0.123	UMich
LC-04-38.8d	0.309	0.077	0.311	0.019	0.108	0.164	0.040	69.652	27.408	98.086	76	0.272	0.117	UMich
LC-04-38.8d	6.955	1.816	4.178	0.044	0.079	0.143	0.026	53.200	31.427	97.869	77	0.223	1.842	UMich
LC-04-38.8d	0.054	0.032	0.022	0.001	0.059	0.163	0.031	71.118	27.390	98.869	78	0.221	0.063	UMich
LC-04-38.8d	0.299	0.088	0.407	0.194	0.090	0.156	0.047	70.080	27.740	99.099	79	0.245	0.135	UMich
LC-04-38.8d	0.240	0.077	0.259	0.058	0.089	0.156	0.042	70.656	27.688	99.265	80	0.245	0.119	UMich
LC-04-38.8d	0.831	0.211	0.472	0.031	0.169	0.152	0.046	67.825	27.401	97.137	81	0.321	0.256	UMich
LC-04-38.8d	0.535	0.209	0.281	0.035	0.089	0.155	0.045	69.595	27.609	98.551	82	0.244	0.253	UMich
LC-04-38.8e	2.506	0.808	0.968	0.041	0.080	0.165	0.038	64.432	28.250	97.287	83	0.245	0.846	UMich
LC-04-38.8e	0.451	0.138	0.592	0.222	0.114	0.167	0.044	69.474	27.896	99.098	84	0.281	0.181	UMich
LC-04-38.8e	0.086	0.127	0.018		0.086	0.170	0.037	70.999	27.468	98.992	85	0.257	0.165	UMich
LC-04-38.8e	0.062	0.039	0.016		0.070	0.182	0.029	71.307	27.482	99.187	86	0.251	0.068	UMich
LC-04-38.8e	1.212	0.348	1.070	0.184	0.153	0.182	0.053	67.567	28.421	99.189	87	0.335	0.401	UMich
LC-04-38.8e	0.140	0.187	0.015		0.103	0.196	0.048	70.974	27.567	99.229	88	0.299	0.235	UMich
LC-04-38.8e	0.209	0.253	0.017		0.112	0.206	0.041	70.794	27.617	99.250	89	0.318	0.294	UMich
LC-04-38.8e	0.222	0.245	0.022		0.121	0.215	0.044	70.736	27.613	99.216	90	0.335	0.290	UMich
LC-04-38.8e	0.202	0.201	0.019		0.118	0.224	0.052	70.779	27.580	99.175	91	0.342	0.253	UMich
LC-04-38.8e	0.191	0.205	0.019		0.123	0.229	0.044	70.866	27.611	99.287	92	0.352	0.249	UMich
LC-04-38.8e	0.175	0.120	0.047		0.057	0.227	0.042	70.887	27.520	99.074	93	0.284	0.162	UMich
LC-04-38.8e	0.265	0.198	0.305	0.015	0.149	0.223	0.052	68.413	27.065	96.684	94	0.372	0.250	UMich
LC-04-38.8e	0.648	0.340	0.286	0.071	0.161	0.220	0.055	69.332	27.803	98.915	95	0.381	0.395	UMich
LC-04-66.7c	0.315	0.047	0.014		0.013	0.148	0.032	71.235	27.571	99.374	96	0.160	0.079	UMich
LC-04-66.7c	0.323	0.036	0.012		0.012	0.150	0.040	71.100	27.516	99.188	97	0.162	0.075	UMich

LC-04-66.7c	0.309	0.022	0.011		0.009	0.148	0.036	71.178	27.515	99.227	98	0.158	0.057	UMich
LC-04-66.7c	0.493	0.058	0.028		0.015	0.148	0.032	70.820	27.556	99.149	99	0.163	0.089	UMich
LC-04-66.7c	0.302	0.034	0.015		0.008	0.145	0.029	71.315	27.574	99.422	100	0.154	0.063	UMich
LC-04-66.7c	0.315	0.042	0.014		0.015	0.144	0.033	71.134	27.530	99.226	101	0.159	0.075	UMich
LC-04-66.7c	0.308	0.036	0.013		0.006	0.138	0.032	71.295	27.569	99.397	102	0.144	0.068	UMich
LC-04-66.7c	0.334	0.041	0.049		0.007	0.143	0.037	71.177	27.589	99.377	103	0.150	0.078	UMich
LC-04-66.7c	0.369	0.043	0.056		0.015	0.143	0.040	71.344	27.694	99.702	104	0.157	0.083	UMich
LC-04-66.7c	0.475	0.048	0.218	0.017	0.014	0.136	0.041	70.528	27.645	99.123	105	0.151	0.090	UMich
LC-04-66.7c	0.375	0.043	0.068		0.013	0.148	0.041	71.195	27.655	99.537	106	0.161	0.084	UMich
LC-04-99.5b	0.352	0.149	0.017		0.108	0.237	0.059	71.324	27.836	100.081	25	0.345	0.207	UMich
LC-04-99.5b	0.398	0.236	0.031		0.204	0.243	0.065	70.966	27.896	100.037	26	0.446	0.300	UMich
LC-04-99.5b	0.322	0.120	0.020		0.082	0.235	0.069	71.252	27.753	99.853	27	0.317	0.189	UMich
LC-04-99.5b	0.310	0.075	0.037		0.121	0.245	0.062	71.414	27.818	100.081	28	0.365	0.137	UMich
LC-04-99.5b	0.334	0.126	0.026		0.113	0.241	0.073	71.193	27.776	99.882	29	0.354	0.199	UMich
LC-04-99.5b	0.334	0.126	0.021		0.086	0.245	0.064	71.641	27.924	100.441	30	0.331	0.191	UMich
LC-04-99.5b	0.343	0.155	0.022		0.198	0.245	0.065	71.165	27.849	100.041	31	0.443	0.219	UMich
LC-04-99.5b	0.344	0.141	0.023		0.105	0.243	0.070	71.420	27.872	100.217	32	0.348	0.211	UMich
LC-04-99.5b	0.312	0.123	0.019		0.091	0.245	0.066	71.339	27.794	99.988	33	0.336	0.189	UMich
LC-04-99.5b	0.402	0.158	0.137	0.045	0.147	0.237	0.076	70.893	27.902	99.998	34	0.384	0.234	UMich
LC-04-99.5b	0.542	0.232	0.348	0.092	0.206	0.240	0.084	69.689	27.904	99.337	35	0.446	0.316	UMich
LC-04-99.5b	0.581	0.250	0.375	0.114	0.159	0.241	0.069	70.016	28.073	99.880	36	0.400	0.319	UMich
LC-04-99.5b	0.518	0.214	0.299	0.098	0.149	0.242	0.077	70.178	27.964	99.737	37	0.390	0.290	UMich
LC-04-99.5b	0.521	0.201	0.333	0.113	0.172	0.242	0.072	70.110	27.988	99.753	38	0.414	0.273	UMich
LC-04-99.5b	0.416	0.151	0.293	0.095	0.176	0.243	0.075	70.175	27.850	99.474	39	0.419	0.226	UMich
LC-04-99.5b	1.050	0.410	1.018	0.341	0.277	0.246	0.092	67.552	28.491	99.477	40	0.523	0.502	UMich

LC-04-99.5b	0.751	0.284	0.744	0.258	0.144	0.246	0.077	68.765	28.209	99.478	41	0.390	0.360	UMich
LC-04-99.5b	0.673	0.308	0.591	0.136	0.185	0.249	0.063	69.146	28.125	99.474	42	0.434	0.370	UMich
LC-04-99.5b	0.597	0.287	0.692	0.150	0.131	0.244	0.079	69.604	28.320	100.103	43	0.375	0.366	UMich
LC-04-99.5b	0.564	0.331	0.826	0.229	0.159	0.238	0.058	66.855	27.480	96.741	44	0.398	0.389	UMich
LC-04-99.5b	0.667	0.301	0.863	0.325	0.173	0.247	0.053	68.752	28.340	99.720	45	0.420	0.353	UMich
LC-04-99.5b	0.532	0.224	0.583	0.189	0.170	0.249	0.047	69.372	28.042	99.408	46	0.419	0.271	UMich
LC-04-99.5b	0.523	0.195	0.584	0.174	0.204	0.255	0.061	69.382	28.039	99.416	47	0.459	0.256	UMich
LC-04-99.5b	2.668	0.936	1.447	0.056	0.294	0.267	0.046	65.813	29.744	101.271	48	0.561	0.983	UMich
LC-04-99.5b	0.540	0.236	0.461	0.081	0.207	0.251	0.058	69.924	28.117	99.876	49	0.459	0.294	UMich
LC-04-99.5b	0.778	0.266	0.797	0.229	0.278	0.254	0.057	68.801	28.360	99.819	50	0.532	0.323	UMich
LC-04-99.5b	0.655	0.230	0.788	0.274	0.491	0.254	0.066	68.352	28.230	99.340	51	0.745	0.296	UMich
LC-04-99.5b	0.648	0.224	0.681	0.213	0.117	0.258	0.061	69.399	28.223	99.824	52	0.375	0.285	UMich
LC-04-99.5b	0.564	0.218	0.659	0.235	0.142	0.257	0.065	69.302	28.127	99.568	53	0.399	0.282	UMich
LC-04-99.5b	0.419	0.179	0.438	0.163	0.132	0.247	0.049	69.428	27.750	98.805	54	0.379	0.228	UMich
LC-04-99.5b	0.988	0.397	0.837	0.199	0.159	0.239	0.093	68.477	28.450	99.840	55	0.398	0.491	UMich
LC-04-99.5b	1.444	0.606	0.671	0.031	0.039	0.235	0.054	68.970	28.776	100.827	56	0.275	0.661	UMich
LC-04-99.5b	0.810	0.321	0.589	0.081	0.113	0.241	0.088	69.218	28.187	99.647	57	0.354	0.409	UMich
LC-04-99.5b	2.291	0.847	1.217	0.172	0.476	0.254	0.075	66.013	29.401	100.745	58	0.730	0.922	UMich
LC-04-99.5b	0.276	0.044	0.025		0.118	0.235	0.052	71.487	27.773	100.010	59	0.352	0.096	UMich
LC-04-99.5b	1.627	0.718	1.340	0.125	0.077	0.218	0.060	64.622	28.153	96.939	60	0.295	0.778	UMich
LC-04-99.5b	0.756	0.275	0.770	0.246	0.098	0.235	0.070	69.212	28.360	100.021	61	0.332	0.344	UMich
LC-04-99.5b	0.719	0.301	0.566	0.222	0.218	0.234	0.046	68.861	28.057	99.224	62	0.452	0.347	UMich
LC-04-99.5b	0.515	0.258	0.649	0.213	0.244	0.231	0.072	69.092	28.086	99.360	63	0.475	0.330	UMich
LC-04-99.5b	0.276	0.149	0.023		0.142	0.284	0.072	71.464	27.897	100.305	64	0.426	0.220	UMich
LC-04-99.5c	0.270	0.142	0.062		0.162	0.279	0.072	71.294	27.878	100.159	65	0.441	0.214	UMich

LC-04-99.5c	0.264	0.101	0.022		0.230	0.271	0.078	71.244	27.818	100.028	66	0.501	0.179	UMich
LC-04-99.5c	0.551	0.129	0.453	0.244	0.166	0.271	0.073	70.469	28.278	100.632	67	0.436	0.202	UMich
LC-04-99.5c	0.262	0.110	0.027		0.141	0.266	0.106	71.446	27.852	100.211	68	0.407	0.217	UMich
LC-04-99.5c	0.228	0.097	0.019		0.112	0.271	0.065	71.554	27.819	100.164	69	0.382	0.162	UMich
LC-04-99.5c	0.513	0.184	0.318	0.084	0.219	0.267	0.062	70.762	28.229	100.639	70	0.485	0.246	UMich
LC-04-99.5c	0.138	0.100	0.053		0.200	0.267	0.033	71.653	27.892	100.336	71	0.466	0.133	UMich
LC-04-99.5c	0.127	0.118	0.032		0.300	0.267	0.050	71.500	27.890	100.283	72	0.567	0.168	UMich
LC-04-99.5c	0.986	0.342	0.707	0.119	0.388	0.272	0.078	69.206	28.662	100.759	73	0.660	0.419	UMich
LC-04-99.5c	0.620	0.251	0.529	0.151	0.188	0.263	0.073	69.773	28.229	100.078	74	0.451	0.324	UMich
LC-04-99.5c	0.183	0.086	0.053	0.007	0.144	0.265	0.046	71.469	27.804	100.058	75	0.409	0.132	UMich
LC-04-99.5c	0.436	0.112	0.771	0.228	0.064	0.239	0.069	70.021	28.288	100.229	76	0.303	0.182	UMich
LC-04-99.5c	0.470	0.073	0.802	0.211	0.071	0.228	0.064	69.981	28.288	100.187	77	0.299	0.137	UMich
LC-04-99.5c	1.489	0.052	2.060	0.648	0.017	0.189	0.052	66.634	29.210	100.350	78	0.206	0.104	UMich
LC-04-104.4c	0.141	0.107	0.027		0.265	0.252	0.076	71.218	27.750	99.834	79	0.517	0.183	UMich
LC-04-104.4c	0.127	0.071	0.018		0.121	0.254	0.037	71.776	27.809	100.213	80	0.375	0.108	UMich
LC-04-104.4c	0.169	0.066	0.015	0.009	0.138	0.250	0.051	71.826	27.861	100.384	81	0.388	0.116	UMich
LC-04-104.4c	0.124	0.036	0.013		0.095	0.251	0.026	71.838	27.772	100.154	82	0.346	0.062	UMich
LC-04-104.4c	0.165	0.041	0.040	0.011	0.102	0.253	0.039	71.444	27.695	99.790	83	0.355	0.080	UMich
LC-04-104.4c	0.200	0.071	0.033		0.215	0.261	0.037	71.596	27.869	100.282	84	0.476	0.108	UMich
LC-04-104.4c	0.177	0.075	0.024	0.016	0.256	0.248	0.084	71.369	27.801	100.049	85	0.504	0.159	UMich
LC-04-104.4c	0.154	0.098	0.018		0.214	0.257	0.055	71.647	27.867	100.309	86	0.471	0.153	UMich
LC-04-104.4c	0.285	0.134	0.164	0.084	0.097	0.259	0.046	70.992	27.855	99.917	87	0.356	0.180	UMich
LC-04-104.4c	0.647	0.125	0.342	0.038	0.244	0.256	0.081	70.699	28.265	100.697	88	0.500	0.206	UMich
LC-04-104.4c	0.988	0.115	0.072	0.018	4.071	0.252	0.834	64.364	28.518	99.232	89	4.323	0.948	UMich
LC-04-104.4c	0.331	0.098	0.390	0.173	0.160	0.255	0.052	70.826	28.124	100.408	90	0.415	0.149	UMich

LC-04-104.4c	0.517	0.135	0.351	0.200	0.842	0.247	0.174	69.336	28.166	99.969	91	1.090	0.309	UMich
LC-04-104.4c	4.948	1.580	1.979	0.228	8.979	0.226	2.227	43.844	30.516	94.527	92	9.205	3.806	UMich
LC-04-104.4c	0.560	0.110	0.075		1.478	0.253	0.573	68.665	28.068	99.782	93	1.731	0.683	UMich
LC-04-104.4c	0.235	0.094	0.130		0.068	0.247	0.030	71.523	27.888	100.216	94	0.316	0.124	UMich
LC-04-104.4c	0.083	0.066	0.020		0.117	0.247	0.035	71.737	27.753	100.057	95	0.364	0.101	UMich
LC-04-104.4c	0.109	0.106	0.014		0.173	0.254	0.044	71.708	27.830	100.238	96	0.427	0.150	UMich
LC-04-104.4c	0.128	0.046	0.013		0.133	0.249	0.041	71.605	27.720	99.935	97	0.382	0.086	UMich
LC-04-104.4c	0.167	0.053	0.025		0.106	0.257	0.037	71.606	27.751	100.002	98	0.363	0.090	UMich
LC-04-104.4c	0.458	0.119	0.467	0.060	0.091	0.245	0.045	70.455	28.075	100.015	99	0.336	0.164	UMIch
LC-04-104.4c	0.120	0.090	0.012		0.080	0.252	0.044	71.861	27.819	100.278	100	0.333	0.134	UMIch
LC-04-104.4c	0.136	0.116	0.016		0.155	0.256	0.051	71.520	27.781	100.032	101	0.412	0.167	UMIch
LC-04-104.4c	0.119	0.092	0.012		0.313	0.251	0.054	71.416	27.805	100.060	102	0.564	0.145	UMIch
LC-04-104.4c	0.136	0.092	0.016		0.077	0.255	0.050	71.748	27.792	100.166	103	0.332	0.142	UMIch
LC-04-104.4c	0.254	0.105	0.020	0.011	1.241	0.249	0.455	69.936	28.091	100.363	104	1.490	0.560	UMIch
LC-04-104.4c	0.152	0.046	0.016		0.101	0.249	0.042	71.697	27.754	100.056	105	0.350	0.088	UMIch
LC-04-104.4c	0.179	0.081	0.033		0.100	0.253	0.041	71.423	27.720	99.830	106	0.352	0.122	UMIch
LC-04-104.4c	2.027	0.921	3.766	3.645	4.643	0.237	0.126	47.381	29.257	92.003	107	4.881	1.047	UMIch
LC-04-104.4c	0.201	0.126	0.061	0.021	0.112	0.249	0.044	71.165	27.721	99.699	108	0.361	0.170	UMIch
LC-04-104.4c	0.148	0.072	0.018	0.051	0.148	0.253	0.043	71.548	27.773	100.053	109	0.401	0.115	UMIch
LC-04-104.4c	0.189	0.097	0.029	0.053	0.122	0.251	0.043	71.675	27.866	100.324	110	0.372	0.140	UMIch
LC-04-104.4c	0.157	0.064	0.021	0.057	0.142	0.254	0.046	71.521	27.764	100.026	111	0.396	0.111	UMIch
LC-04-104.4c	0.680	0.211	0.069	0.033	0.255	0.257	0.050	70.852	28.108	100.515	112	0.511	0.261	UMIch
LC-04-104.4c	0.149	0.059	0.026	0.033	0.126	0.251	0.046	71.627	27.779	100.096	113	0.377	0.105	UMIch
LC-04-104.4c	0.158	0.079	0.023	0.018	0.178	0.247	0.042	71.583	27.809	100.137	114	0.425	0.121	UMIch
LC-04-104.4c	0.184	0.104	0.047	0.019	0.159	0.251	0.040	71.437	27.808	100.049	115	0.410	0.144	UMIch

LC-04-104.4d	0.195	0.118	0.014		0.133	0.234	0.053	71.925	27.944	100.616	116	0.368	0.171	UMIch
LC-04-104.4d	0.183	0.108	0.015		0.107	0.242	0.042	71.794	27.864	100.355	117	0.348	0.150	UMIch
LC-04-104.4d	0.195	0.130	0.010		0.505	0.240	0.120	71.261	27.970	100.431	118	0.746	0.250	UMIch
LC-04-104.4d	0.166	0.103	0.012	0.012	0.137	0.239	0.050	71.880	27.907	100.507	119	0.376	0.154	UMIch
LC-04-104.4d	0.168	0.140	0.012	0.012	0.107	0.241	0.046	71.953	27.947	100.626	120	0.349	0.186	UMIch
LC-04-104.4d	0.153	0.122	0.015	0.012	0.126	0.236	0.046	71.865	27.903	100.478	121	0.362	0.167	UMIch
LC-04-104.4d	0.064	0.041	0.016		0.142	0.240	0.056	72.064	27.859	100.482	122	0.382	0.097	UMIch
LC-04-104.4d	0.084	0.044	0.043	0.015	0.128	0.234	0.032	71.773	27.782	100.136	123	0.362	0.076	UMIch
LC-04-104.4d	0.147	0.104	0.010		0.097	0.236	0.057	71.869	27.854	100.373	124	0.332	0.161	UMIch
LC-04-104.4d	0.204	0.175	0.019		0.158	0.242	0.053	71.734	27.957	100.540	125	0.400	0.228	UMIch
LC-04-104.4d	0.180	0.106	0.016	0.014	0.102	0.235	0.052	71.749	27.848	100.303	126	0.337	0.158	UMIch
LC-04-104.4d	0.165	0.086	0.017		0.153	0.240	0.048	71.762	27.857	100.329	127	0.394	0.134	UMIch
LC-04-104.4d	0.131	0.058	0.011		0.096	0.233	0.037	71.763	27.756	100.084	128	0.329	0.095	UMIch
LC-04-104.4d	0.139	0.046	0.021		0.045	0.231	0.048	72.099	27.860	100.487	129	0.276	0.094	UMIch
LC-04-104.4d	0.103	0.054	0.012		0.099	0.240	0.041	71.864	27.778	100.190	130	0.338	0.095	UMIch
LC-04-104.4d	0.100	0.052	0.106	0.114	0.104	0.238	0.044	71.523	27.805	100.086	131	0.343	0.096	UMIch
LC-04-104.4d	0.049	0.059	0.012		0.038	0.240	0.021	72.115	27.801	100.336	132	0.278	0.081	UMIch
LC-04-104.4d	0.065	0.072	0.017		0.257	0.241	0.056	71.935	27.915	100.557	133	0.498	0.128	UMIch
LC-04-104.4e	0.296	0.112	0.122	0.023	0.130	0.254	0.041	71.069	27.818	99.865	134	0.384	0.153	UMIch
LC-04-104.4e	0.483	0.141	0.640	0.103	0.083	0.245	0.050	69.495	27.955	99.195	135	0.328	0.191	UMIch
LC-04-104.4e	0.195	0.074	0.016		0.070	0.253	0.034	71.712	27.792	100.145	136	0.323	0.108	UMIch
LC-04-104.4e	0.263	0.145	0.136	0.048	0.099	0.243	0.038	71.070	27.825	99.867	137	0.342	0.183	UMIch
LC-04-104.4e	0.201	0.132	0.016		0.086	0.253	0.040	71.482	27.775	99.986	138	0.340	0.172	UMIch
LC-04-104.4e	0.259	0.142	0.073		0.094	0.252	0.040	71.411	27.864	100.136	139	0.346	0.182	UMIch
LC-04-104.4e	0.214	0.102	0.016		0.175	0.243	0.056	71.617	27.862	100.285	140	0.418	0.158	UMIch

LC-04-104.4e	0.147	0.076	0.020		0.079	0.253	0.034	71.849	27.823	100.280	141	0.332	0.110	UMIch
LC-04-104.4e	0.121	0.081	0.017		0.105	0.246	0.034	72.057	27.900	100.560	142	0.350	0.115	UMIch
LC-04-104.4e	0.087	0.046	0.022		0.038	0.255	0.040	71.693	27.676	99.856	143	0.293	0.086	UMIch
LC-04-104.4e	0.085	0.097	0.018		0.087	0.238	0.052	71.756	27.769	100.102	144	0.325	0.149	UMIch
LC-04-104.4e	0.090	0.079	0.012		0.039	0.243	0.048	71.915	27.778	100.204	145	0.282	0.127	UMIch
LC-04-104.4e	0.103	0.057	0.016	0.011	0.057	0.248	0.037	71.878	27.773	100.179	146	0.305	0.094	UMIch
LC-04-104.4e	0.124	0.061	0.024		0.187	0.249	0.035	71.721	27.823	100.225	147	0.436	0.096	UMIch
LC-04-104.4e	0.071	0.028	0.026		0.173	0.245	0.040	71.880	27.818	100.280	148	0.418	0.069	UMIch
LC-04-125.3e	0.084	0.190	0.018		0.269	0.280	0.074	71.322	27.831	100.067	149	0.549	0.264	UMIch
LC-04-125.3e	0.083	0.228	0.016		0.283	0.280	0.089	71.521	27.953	100.454	150	0.563	0.317	UMIch
LC-04-125.3e	0.082	0.197	0.021		0.229	0.279	0.093	71.487	27.884	100.272	151	0.508	0.290	UMIch
LC-04-125.3e	0.088	0.254	0.018		0.224	0.277	0.074	71.645	27.982	100.562	152	0.501	0.328	UMIch
LC-04-125.3e	0.091	0.254	0.022		0.370	0.270	0.156	71.156	27.919	100.238	153	0.640	0.410	UMIch
LC-04-125.3e	0.087	0.295	0.021		0.433	0.276	0.180	71.087	27.980	100.360	154	0.709	0.476	UMIch
LC-04-125.3e	0.111	0.355	0.019		0.399	0.280	0.160	70.971	27.972	100.266	155	0.679	0.514	UMIch
LC-04-125.3e	0.067	0.296	0.019		0.288	0.277	0.105	71.576	28.034	100.663	156	0.565	0.401	UMIch
LC-04-125.3e	0.046	0.165	0.014		0.120	0.277	0.061	71.819	27.865	100.368	157	0.397	0.227	UMIch
LC-04-125.3e	0.115	0.414	0.021		0.419	0.278	0.134	71.037	28.063	100.481	158	0.697	0.549	UMIch
LC-04-125.3e	0.081	0.252	0.022		0.302	0.275	0.112	71.486	27.982	100.512	159	0.578	0.364	UMIch
LC-04-125.3e	0.052	0.189	0.017		0.295	0.280	0.106	71.585	27.935	100.459	160	0.575	0.295	UMIch
LC-04-125.3e	0.068	0.357	0.021		0.495	0.282	0.144	71.072	28.050	100.488	161	0.776	0.501	UMIch
LC-04-125.3e	0.074	0.274	0.018		0.329	0.279	0.090	71.454	27.992	100.508	162	0.608	0.363	UMIch
LC-04-125.3e	0.103	0.404	0.024		0.734	0.277	0.356	70.402	28.082	100.381	163	1.012	0.759	UMIch
LC-04-125.3e	0.044	0.213	0.020		0.232	0.280	0.053	71.744	27.957	100.543	164	0.512	0.266	UMIch
LC-04-125.3e	0.036	0.215	0.015		0.183	0.278	0.051	71.879	27.966	100.622	165	0.461	0.266	UMIch

Sample														
LC-04-125.3e	0.029	0.171	0.019		0.160	0.279	0.053	71.942	27.936	100.588	166	0.438	0.224	UMIch
LC-04-125.3e	0.021	0.141	0.021		0.112	0.280	0.040	72.068	27.920	100.603	167	0.392	0.181	UMIch
LC-04-125.3e	0.034	0.209	0.020		0.152	0.281	0.055	71.718	27.885	100.354	168	0.433	0.263	UMIch
LC-04-129.3a	0.034	0.115	0.025		0.143	0.327	0.087	71.975	27.932	100.637	169	0.470	0.202	UMIch
LC-04-129.3a	0.035	0.115	0.021		0.174	0.332	0.082	72.057	27.984	100.801	170	0.506	0.197	UMIch
LC-04-129.3a	0.036	0.128	0.028		0.251	0.331	0.087	71.938	28.012	100.811	171	0.582	0.215	UMIch
LC-04-129.3a	0.046	0.145	0.024		0.375	0.324	0.080	71.520	27.945	100.460	172	0.700	0.225	UMIch
LC-04-129.3a	0.026	0.108	0.024		0.134	0.332	0.051	72.021	27.922	100.618	173	0.466	0.159	UMIch
LC-04-129.3a	0.034	0.166	0.019		0.343	0.327	0.145	71.572	27.965	100.571	174	0.670	0.311	UMIch
LC-04-129.3a	0.040	0.147	0.018		0.254	0.329	0.057	71.842	27.971	100.658	175	0.583	0.203	UMIch
LC-04-129.3a	0.057	0.161	0.023		0.599	0.325	0.357	70.838	27.931	100.291	176	0.924	0.518	UMIch
LC-04-129.3a	0.052	0.267	0.020		0.434	0.329	0.132	71.475	28.089	100.798	177	0.763	0.399	UMIch
LC-04-129.3a	0.035	0.135	0.017		0.259	0.320	0.046	71.752	27.919	100.483	178	0.579	0.181	UMIch
LC-04-129.3a	0.025	0.133	0.021		0.294	0.327	0.127	71.678	27.937	100.541	179	0.621	0.259	UMIch
LC-04-129.3a	0.034	0.193	0.030		0.373	0.319	0.057	71.215	27.861	100.082	180	0.692	0.250	UMIch
LC-04-129.5a	0.016	0.126	0.015		0.190	0.315	0.079	71.824	27.884	100.450	181	0.506	0.206	UMIch
LC-04-129.5a	0.020	0.187	0.021		0.234	0.322	0.085	71.621	27.907	100.398	182	0.556	0.273	UMIch
LC-04-129.5a	0.029	0.190	0.027		0.436	0.318	0.045	71.327	27.931	100.302	183	0.754	0.235	UMIch
LC-04-129.5a	0.021	0.128	0.028		0.425	0.318	0.073	71.418	27.905	100.316	184	0.743	0.201	UMIch
LC-04-129.5a	0.015	0.151	0.030		0.310	0.319	0.041	71.529	27.882	100.276	185	0.628	0.192	UMIch
LC-04-129.5a	0.000	0.098	0.022	0.009	0.350	0.312	0.035	71.473	27.825	100.124	186	0.662	0.133	UMIch
LC-04-129.5a	0.014	0.088	0.034	0.022	0.527	0.305	0.183	71.145	27.871	100.188	187	0.831	0.271	UMIch
LC-04-129.5a	0.011	0.078	0.026	0.030	0.315	0.303	0.045	71.568	27.832	100.207	188	0.618	0.123	UMIch
LC-04-129.5a	0.006	0.132	0.017		0.241	0.315	0.072	71.695	27.866	100.344	189	0.556	0.205	UMIch
LC-04-129.5a	0.017	0.114	0.020		0.192	0.319	0.073	71.723	27.844	100.302	190	0.511	0.187	UMIch

LC-04-129.5a	0.022	0.128	0.019		0.327	0.318	0.064	71.479	27.853	100.210	191	0.645	0.192	UMIch
LC-04-129.5a	0.019	0.143	0.015		0.250	0.320	0.058	71.685	27.883	100.372	192	0.569	0.200	UMIch
LC-04-129.5a	0.020	0.231	0.020		0.421	0.319	0.109	71.176	27.905	100.200	193	0.740	0.341	UMIch
LC-04-129.5a	0.019	0.124	0.017	0.003	0.255	0.320	0.050	71.636	27.856	100.281	194	0.575	0.174	UMIch
LC-04-129.5a	0.000	0.094	0.023	0.028	0.547	0.317	0.343	70.603	27.723	99.678	195	0.864	0.437	UMIch
LC-04-129.5a	0.036	0.096	0.205	0.073	0.273	0.294	0.073	69.699	27.347	98.095	196	0.567	0.169	UMIch

Supplementary Data: Model calculation
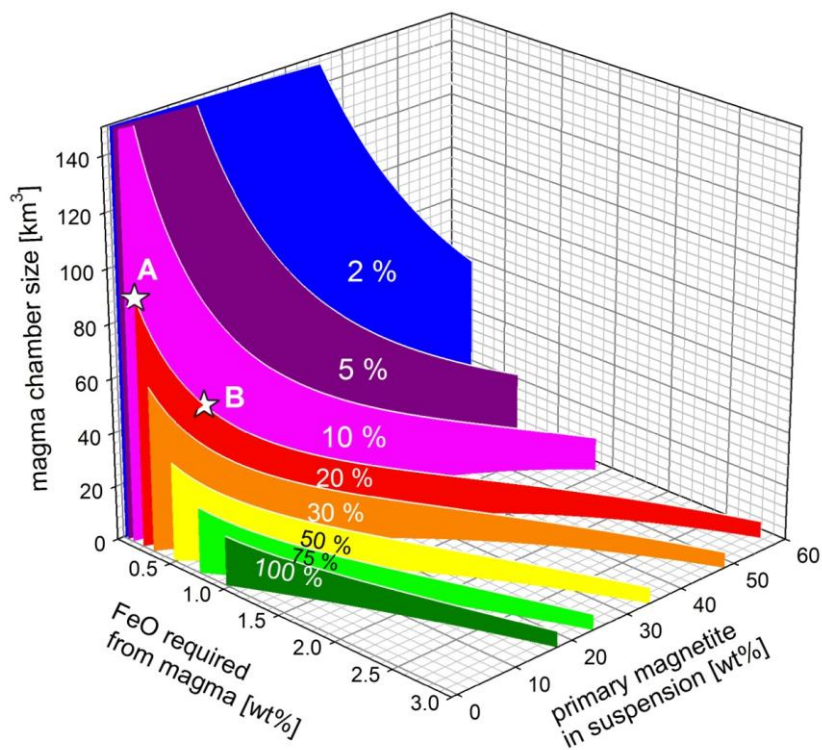
Figure S2.3: Portion of primary magnetite in aqueous fluid suspension vs. FeO leached from magma vs. magma chamber size. The percentages indicate degassing portions of a hydrous andesitic magma (6 wt% H_2O) with a density of 2.27 g/cm^3 (calculated by using the model of Ochs & Lange (1999) for 1000 °C and 2 kbar). A magnetite-bubble-suspension will not ascend when primary magnetite makes up > 65 wt% (> 37 vol%) of the suspension ($F^{Buoyancy} < 0$). The deposition of 343 Mt Fe at Los Colorados exclusively from conventional orthomagmatic fluids would require a large degassing proportion or a large magma chamber size to exsolve sufficient fluid (white star, A=92 km^3, when assuming 20% degassing). In contrast, the addition of 8 wt% primary (type 1) magnetite microlites to this suspension would decrease the required magma chamber significantly to magma chamber sizes reasonable (white star, B=50 km^3) for the caldera sizes measured at the extrusive IOA deposit of El Laco (~6 km caldera diameter), assuming a similar magma chamber size as for Crater Lake (6.5 km caldera diameter, 55 km^3 total erupted volume, Bacon, 1983; Lipmann, 1997). In this case, the total amount of FeO leached from the parental magma chamber to deposit 343 Mt Fe (including magmatic and magmatic-hydrothermal magnetite) would be 0.4 wt% FeO.
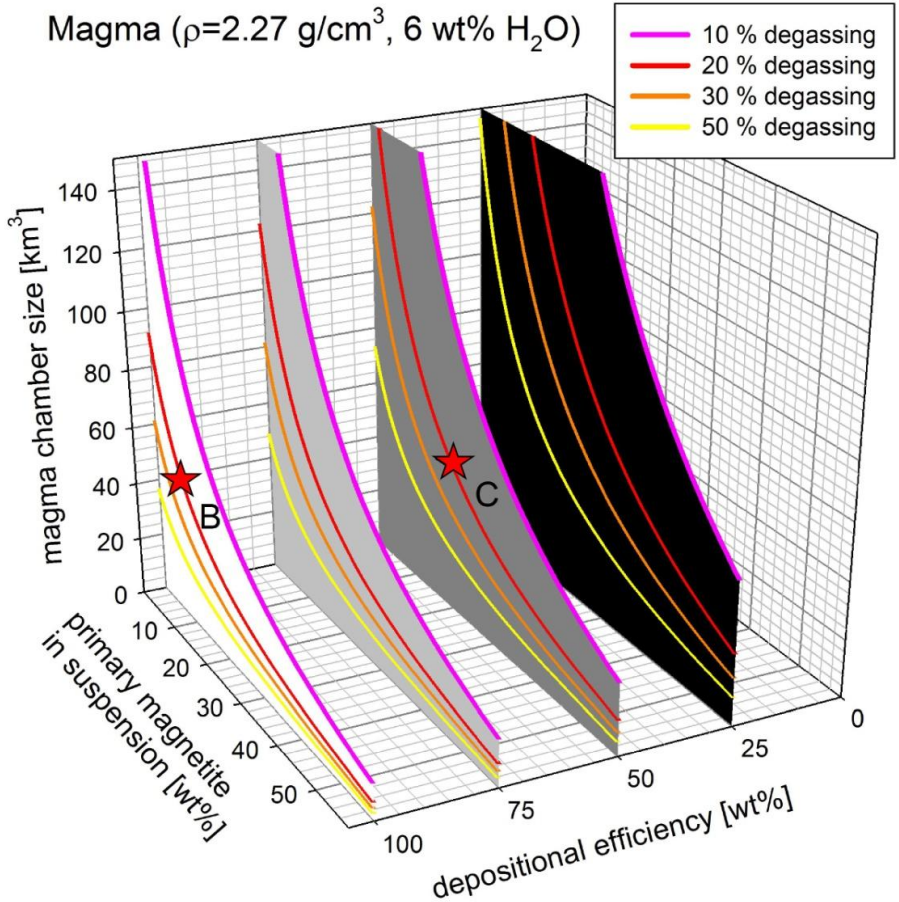
Figure S2.4: Portion of primary magnetite in aqueous fluid suspension vs. depositional efficiency of Fe precipitation from fluid vs. magma chamber size. While the previous figure (Fig. S2.3) shows the dependence on the magma chamber size assuming an Fe depositional efficiency of 100% from the fluid phase, this figure presents different scenarios of 100, 75, 50 and 25% depositional efficiencies of Fe and variable degassing portions at 10, 20, 30 and 50%. For instance, a more realistically smaller depositional efficiency of 50% based on the thermally retrograde solubility behavior of Fe would increase the required amount of primary magnetite microlites in the suspension (when keeping the same magma chamber size of 50 km^3) from 8 wt% (B) to 20 wt% (C), which is still comfortably within the window of an ascending bubble-magnetite-suspension.

Additional References

Bacon, C.R., 1983, Eruptive history of mount Mazama and Crater Lake caldera, Cascade Range, U.S.A.: Journal of Volcanology and Geothermal Research, vol. 18, p. 57–115.

Lipman, P.W., 1997, Subsidence of ash-flow calderas: relation to caldera size and magma-chamber geometry: Bulletin of Volcanology, v. 59, p. 198–218.

Westhues, A., Hanchar, J.M. & Whitehouse, M.J., 2014, The Kiruna apatite iron oxide deposits, Sweden-new ages and isotopic constraints, Goldschmidt Conference, 24th, Sacramento, Abstracts # 2691.

Supplementary Information for Chapter 3: "Trace elements in magnetite from massive iron oxide-apatite deposits indicate a combined formation by igneous and magmatic-hydrothermal processes"

Jaayke L. Knipping, Laura Bilenker, Adam C. Simon, Martin Reich, Fernando Barra, Artur Deditius, Markus Wälle, Christoph A. Heinrich, François Holtz and Rodrigo Munizaga
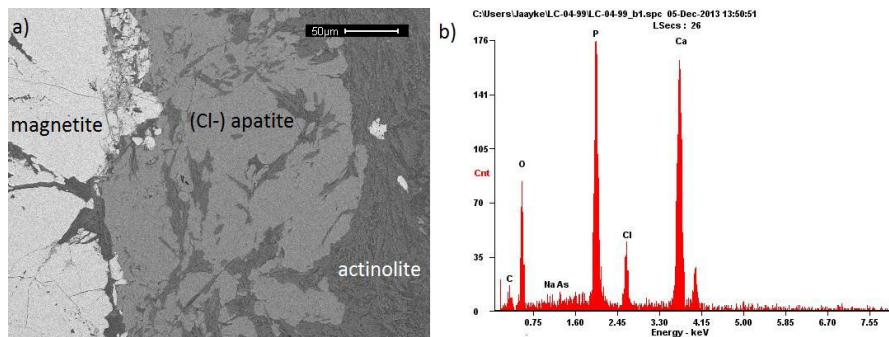
Fig S3.1: a) BSE image of sample LC-04-99 showing a (Cl-) apatite vein in contact with actinolite. b) Semi-quantitative EDX spectrum of (Cl-) apatite.

Table S3.1: Quality control of bulk rock measurements (70 elements) provided by Actlabs

Analyte Symbol	SiO2	Al2O3	Fe2O3(T)	MnO	MgO	CaO	Na2O	K2O	TiO2	P2O5	LOI	Total
Unit Symbol	%	%	%	%	%	%	%	%	%	%	%	%
Detection Limit	0.01	0.01	0.01	0.001	0.01	0.01	0.01	0.01	0.001	0.01		0.01
Analysis Method	FUS-ICP	FUS-ICP	FUS-ICP	FUS-ICP	FUS-ICP	FUS-ICP	FUS-ICP	FUS-ICP	FUS-ICP	FUS-ICP	FUS-ICP	FUS-ICP
NIST 694 Meas	11.45	1.9	0.75	0.013	0.34	42.89	0.87	0.54	0.117	30.22		
NIST 694 Cert	11.2	1.8	0.79	0.0116	0.33	43.6	0.86	0.51	0.11	30.2		
DNC-1 Meas	47.12	18.35	9.65	0.147	10.05	11.41	1.9	0.22	0.481	0.06		
DNC-1 Cert	47.15	18.34	9.97	0.15	10.13	11.49	1.89	0.234	0.48	0.07		
GBW 07113 Meas	69.36	12.79	3.19	0.142	0.14	0.6	2.48	5.41	0.28	0.04		
GBW 07113 Cert	72.8	13	3.21	0.14	0.16	0.59	2.57	5.43	0.3	0.05		
W-2a Meas	53.07	15.63	10.64	0.167	6.29	11.13	2.24	0.63	1.076	0.13		
W-2a Cert	52.4	15.4	10.7	0.163	6.37	10.9	2.14	0.626	1.06	0.13		
SY-4 Meas	49.81	19.94	6.17	0.107	0.5	8.06	6.91	1.65	0.284	0.12		
SY-4 Cert	49.9	20.69	6.21	0.108	0.54	8.05	7.1	1.66	0.287	0.131		
BIR-1a Meas	48	15.69	11.25	0.17	9.55	13.46	1.81	0.02	0.973	0.02		
BIR-1a Cert	47.96	15.5	11.3	0.175	9.7	13.3	1.82	0.03	0.96	0.021		
LC-14-148.5 Orig	61.02	15.87	4.15	0.157	4.41	3.76	7.36	0.82	0.817	0.15	1.2	99.72
LC-14-148.5 Dup	61.63	15.98	4.19	0.157	4.45	3.8	7.38	0.82	0.812	0.16	1.2	100.6

Analyte Symbol	Sc	Be	V	Cr	Co	Ni	Cu	Zn	Ga	Ge	As	Rb	Sr
Unit Symbol	ppm	ppm	ppm	ppm	ppm	ppm	ppm	ppm	ppm	ppm	ppm	ppm	ppm
Detection Limit	1	1	5	20	1	20	10	30	1	0.5	5	1	2
Analysis Method	FUS-ICP	FUS-ICP	FUS-ICP	FUS-MS	FUS-MS	FUS-MS	FUS-MS	FUS-MS	FUS-MS	FUS-MS	FUS-MS	FUS-MS	FUS-ICP
NIST 694 Meas			1654										
NIST 694 Cert			1740										
DNC-1 Meas	31		161	270	58	260	100	70					144
DNC-1 Cert	31		148	270	57	247	100	70					144
GBW 07113 Meas	5	4	8										41
Analyte Symbol	Sc	Be	V	Cr	Co	Ni	Cu	Zn	Ga	Ge	As	Rb	Sr

166

Unit Symbol	ppm	ppm	ppm	ppm	ppm	ppm	ppm	ppm	ppm	ppm	ppm	ppm	ppm
Detection Limit	1	1	5	20	1	20	10	30	1	0.5	5	1	2
Analysis Method	FUS-ICP	FUS-ICP	FUS-ICP	FUS-MS	FUS-MS	FUS-MS	FUS-MS	FUS-MS	FUS-MS	FUS-MS	FUS-MS	FUS-MS	FUS-ICP
GBW 07113 Cert	5	4	5										43
LKSD-3 Meas							30	50	40		72		
LKSD-3 Cert							30	47	35		78		
W-2a Meas	35	< 1	280	90	44	70	110	80	17	1.9		19	200
W-2a Cert	36	1.3	262	92	43	70	110	80	17	1		21	190
SY-4 Meas	1	3	12										1196
SY-4 Cert	1.1	2.6	8										1191
CTA-AC-1 Meas							60	30					
CTA-AC-1 Cert							54	38					
BIR-1a Meas	44	< 1	341	380	53	170			15				109
BIR-1a Cert	44	0.58	310	370	52	170			16				110
NCS DC86312 Meas													
NCS DC70014 Meas					25	70	2580	7400	25				
NCS DC70014 Cert					26	70	2600	7400	25.2				
NCS DC70009 (GBW07241) Meas							1010	110	16	11.2	73	505	
NCS DC70009 (GBW07241) Cert							960	100	16.5	11.2	69.9	500	
OREAS 100a (Fusion) Meas					17		170						
OREAS 100a (Fusion) Cert					18.1		169						
OREAS 101a (Fusion) Meas					48		430						
OREAS 101a (Fusion) Cert					48.8		434						
JR-1 Meas					< 1	< 20		< 30	17		15	247	
JR-1 Cert					0.83	1.67		30.6	16.1		16.3	257	
LC-14-148.5 Orig	21	1	147	< 20	6	< 20	10	< 30	17	1.8	7	23	75
LC-14-148.5 Dup	21	1	148	< 20	6	< 20	10	< 30	17	1.8	7	23	75
Method Blank				< 20	< 1	< 20	< 10	< 30	< 1	< 0.5	< 5	< 1	
Analyte Symbol	Y	Zr	Nb	Mo	Ag	In	Sn	Sb	Cs	Ba	La	Ce	Pr

Unit Symbol	ppm	ppm	ppm	ppm	ppm	ppm	ppm	ppm	ppm	ppm	ppm	ppm	ppm
Detection Limit	0.5	1	0.2	2	0.5	0.1	1	0.2	0.1	3	0.05	0.05	0.01
Analysis Method	FUS-MS	FUS-ICP	FUS-MS	FUS-MS	FUS-MS	FUS-MS	FUS-MS	FUS-MS	FUS-MS	FUS-ICP	FUS-MS	FUS-MS	FUS-MS
DNC-1 Meas	16.7	34								105	3.52		
DNC-1 Cert	18	38								118	3.6		
GBW 07113 Meas		389								497			
GBW 07113 Cert		403								506			
LKSD-3 Meas	27.6			< 2					2.3		47.7	88.5	
LKSD-3 Cert	30			2					2.3		52	90	
W-2a Meas	21.4	85		< 2	< 0.5					176	10.7	23.2	
W-2a Cert	24	94		0.6	0.046					182	10	23	
SY-4 Meas		541								344			
SY-4 Cert		517								340			
CTA-AC-1 Meas											> 2000	> 3000	
CTA-AC-1 Cert											2176	3326	
BIR-1a Meas	16.3	15								7			
BIR-1a Cert	16	18								6			
NCS DC86312 Meas	966										> 2000	178	
NCS DC86312 Cert	976										2360	190	
NCS DC70014 Meas	31.6			> 100	16.5		180				45	87.7	10.1
NCS DC70014 Cert	32.1			270	16.7		180				45.3	87	10.8
NCS DC70009 (GBW07241) Meas	138					1.3	> 1000		43.9		24.8	61.5	8.03
NCS DC70009 (GBW07241) Cert	128					1.3	1701		41		23.7	60.3	7.9
OREAS 100a (Fusion) Meas	133		23								256	455	44.4
OREAS 100a (Fusion) Cert	142		24.1								260	463	47.1
OREAS 101a (Fusion) Meas	172										793	1340	127
OREAS 101a (Fusion) Cert	183										816	1396	134
JR-1 Meas	41.1		14	3	< 0.5	< 0.1	3		20.9		20.1	47	5.85
JR-1 Cert	45.1		15.2	3.25	0.031	0.028	2.86		20.8		19.7	47.2	5.58
LC-14-148.5 Orig	30.9	209	6	< 2	3.1	< 0.1	2	1.5	0.3	91	13.4	38.8	5.32
LC-14-148.5 Dup	30.9	216	5.9	< 2	2.9	< 0.1	2	1.7	0.3	91	13.5	39.5	5.41
Analyte Symbol	Y	Zr	Nb	Mo	Ag	In	Sn	Sb	Cs	Ba	La	Ce	Pr
Unit Symbol	ppm	ppm	ppm	ppm	ppm	ppm	ppm	ppm	ppm	ppm	ppm	ppm	ppm

Detection Limit	0.5	1	0.2	2	0.5	0.1	1	0.2	0.1	3	0.05	0.05	0.01
Analysis Method	FUS-MS	FUS-ICP	FUS-MS	FUS-MS	FUS-MS	FUS-MS	FUS-MS	FUS-MS	FUS-MS	FUS-ICP	FUS-MS	FUS-MS	FUS-MS
Method Blank	< 0.5		< 0.2	< 2	< 0.5	< 0.1	< 1	< 0.2	< 0.1		< 0.05	< 0.05	< 0.01

Analyte Symbol	Nd	Sm	Eu	Gd	Tb	Dy	Ho	Er	Tm	Yb	Lu	Hf	Ta
Unit Symbol	ppm	ppm	ppm	ppm	ppm	ppm	ppm	ppm	ppm	ppm	ppm	ppm	ppm
Detection Limit	0.05	0.01	0.005	0.01	0.01	0.01	0.01	0.01	0.005	0.01	0.002	0.1	0.01
Analysis Method	FUS-MS	FUS-MS	FUS-MS	FUS-MS	FUS-MS	FUS-MS	FUS-MS	FUS-MS	FUS-MS	FUS-MS	FUS-MS	FUS-MS	FUS-MS
DNC-1 Meas	4.75		0.563							1.95			
DNC-1 Cert	5.2		0.59							2			
LKSD-3 Meas	41.5	7.64	1.36			4.62				2.68	0.384	4	0.65
LKSD-3 Cert	44	8	1.5			4.9				2.7	0.4	4.8	0.7
W-2a Meas	12.6	3.26	1.05		0.65	3.9	0.81		0.342	2.21	0.303		
W-2a Cert	13	3.3	1		0.63	3.6	0.76		0.38	2.1	0.33		
CTA-AC-1 Meas	1170	170	46.6	125						11.4	1.17	1.7	2.44
CTA-AC-1 Cert	1087	162	46.7	124						11.4	1.08	1.13	2.65
BIR-1a Meas			0.569	2.06						1.81	0.273	0.6	
BIR-1a Cert			0.55	2						1.7	0.3	0.6	
NCS DC86312 Meas	1550			227	34	183	35.6	96.3	14.4	87.4	12		
NCS DC86312 Cert	1600			225	34.6	183	36	96.2	15.1	87.79	11.96		
NCS DC70014 Meas	38	7.92	1.65	7.18	1.2	6.61	1.3	3.56	0.557	3.52	0.498		
NCS DC70014 Cert	39.9	8	1.8	7.4	1.1	6.7	1.3	3.5	0.57	3.3	0.5		
NCS DC70009 (GBW07241) Meas	32.1	12.8		14.5	3.29	20.6	4.31	12.7	2.26	15.9	2.25		
NCS DC70009 (GBW07241) Cert	32.9	12.5		14.8	3.3	20.7	4.5	13.4	2.2	14.9	2.4		
OREAS 100a (Fusion) Meas	142	23.2	3.49		3.61	22	4.75	13.9	2.25	14.9	2.09		
OREAS 100a (Fusion) Cert	152	23.6	3.71		3.8	23.2	4.81	14.9	2.31	14.9	2.26		
OREAS 101a (Fusion) Meas	381	49	7.78		5.42	31.2	6.42	18.7	2.88	18	2.49		
Analyte Symbol	Nd	Sm	Eu	Gd	Tb	Dy	Ho	Er	Tm	Yb	Lu	Hf	Ta
Unit Symbol	ppm	ppm	ppm	ppm	ppm	ppm	ppm	ppm	ppm	ppm	ppm	ppm	ppm

Detection Limit	0.05	0.01	0.005	0.01	0.01	0.01	0.01	0.01	0.005	0.01	0.002	0.1	0.01
Analysis Method	FUS-MS	FUS-MS	FUS-MS	FUS-MS	FUS-MS	FUS-MS	FUS-MS	FUS-MS	FUS-MS	FUS-MS	FUS-MS	FUS-MS	FUS-MS
OREAS 101a (Fusion) Cert	403	48.8	8.06		5.92	33.3	6.46	19.5	2.9	17.5	2.66		
JR-1 Meas	22.6	5.8	0.277	5.38	1.04	6.17		3.93	0.703	4.67	0.696	4.4	
JR-1 Cert	23.3	6.03	0.3	5.06	1.01	5.69		3.61	0.67	4.55	0.71	4.51	
LC-14-148.5 Orig	22	4.98	1.51	5.1	0.88	5.6	1.19	3.39	0.529	3.72	0.527	5	0.5
LC-14-148.5 Dup	22.1	5.15	1.49	5.23	0.91	5.65	1.15	3.43	0.54	3.65	0.551	5.1	0.51
Method Blank	< 0.05	< 0.01	< 0.005	< 0.01	< 0.01	< 0.01	< 0.01	< 0.01	< 0.005	< 0.01	< 0.002	< 0.1	< 0.01

Analyte Symbol	W	Tl	Pb	Bi	Th	U	Cd	Cu	Ni	Zn	S	Ag	Pb
Unit Symbol	ppm	ppm	ppm	ppm	ppm	ppm	ppm	ppm	ppm	ppm	%	ppm	ppm
Detection Limit	0.5	0.05	5	0.1	0.05	0.01	0.5	1	1	1	0.001	0.3	5
Analysis Method	FUS-MS	FUS-MS	FUS-MS	FUS-MS	FUS-MS	FUS-MS	TD-ICP	TD-ICP	TD-ICP	TD-ICP	TD-ICP	TD-ICP	TD-ICP
GXR-1 Meas							3.5	1160	40	749	0.246	30.8	705
GXR-1 Cert							3.3	1110	41	760	0.257	31	730
GXR-4 Meas							< 0.5	6470	53	82	1.76	3.3	52
GXR-4 Cert							0.86	6520	42	73	1.77	4	52
SDC-1 Meas							< 0.5	31	36	100	0.071	< 0.3	22
SDC-1 Cert							0.08	30	38	103	0.065	0.041	25
GXR-6 Meas							< 0.5	70	26	130	0.016	0.6	91
GXR-6 Cert							1	66	27	118	0.016	1.3	101
LKSD-3 Meas					11.1	4.3							
LKSD-3 Cert					11.4	4.6							
W-2a Meas	< 0.5	< 0.05	8	< 0.1	2.47	0.52							
W-2a Cert	0.3	0.2	9.3	0.03	2.4	0.53							
CTA-AC-1 Meas					23.9	4.19							
CTA-AC-1 Cert					21.8	4.4							
BIR-1a Meas			< 5										
Analyte Symbol	W	Tl	Pb	Bi	Th	U	Cd	Cu	Ni	Zn	S	Ag	Pb
Unit Symbol	ppm	ppm	ppm	ppm	ppm	ppm	ppm	ppm	ppm	ppm	%	ppm	ppm

Detection Limit	0.5	0.05	5	0.1	0.05	0.01	0.5	1	1	1	0.001	0.3	5
Analysis Method	FUS-MS	FUS-MS	FUS-MS	FUS-MS	FUS-MS	FUS-MS	TD-ICP	TD-ICP	TD-ICP	TD-ICP	TD-ICP	TD-ICP	TD-ICP
BIR-1a Cert			3										
NCS DC86312 Meas					25.8								
NCS DC86312 Cert					23.6								
NCS DC70014 Meas			> 10000	80.3									
NCS DC70014 Cert			27200	80.3									
NCS DC70009 (GBW07241) Meas	2200				30.9								
NCS DC70009 (GBW07241) Cert	2200				28.3								
OREAS 100a (Fusion) Meas					51.6	135							
OREAS 100a (Fusion) Cert					51.6	135							
OREAS 101a (Fusion) Meas					36.6	422							
OREAS 101a (Fusion) Cert					36.6	422							
JR-1 Meas	2	1.59	21		27.2	9.05							
JR-1 Cert	1.59	1.56	19.3		26.7	8.88							
DNC-1a Meas								101	236	57			
DNC-1a Cert								100	247	70			
SBC-1 Meas							0.6	34	88	185			30
SBC-1 Cert							0.4	31	82.8	186			35
LC-14-148.5 Orig	2	0.08	< 5	< 0.1	5.91	2.26							
LC-14-148.5 Dup	2.1	< 0.05	< 5	< 0.1	6.03	2.22							
LC-14-171.15 Orig							< 0.5	9	19	69	0.141	< 0.3	< 5
LC-14-171.15 Dup							< 0.5	9	23	70	0.145	< 0.3	< 5
Method Blank	< 0.5	< 0.05	< 5	< 0.1	< 0.05	< 0.01							
Method Blank							< 0.5	< 1	< 1	< 1	0.002	< 0.3	< 5
Method Blank							< 0.5	< 1	< 1	< 1	0.007	< 0.3	< 5

Analyte Symbol	Au	As	Br	Cr	Sc	Se	Sb
Unit Symbol	ppb	ppm	ppm	ppm	ppm	ppm	ppm
Detection Limit	2	0.5	0.5	5	0.1	3	0.2

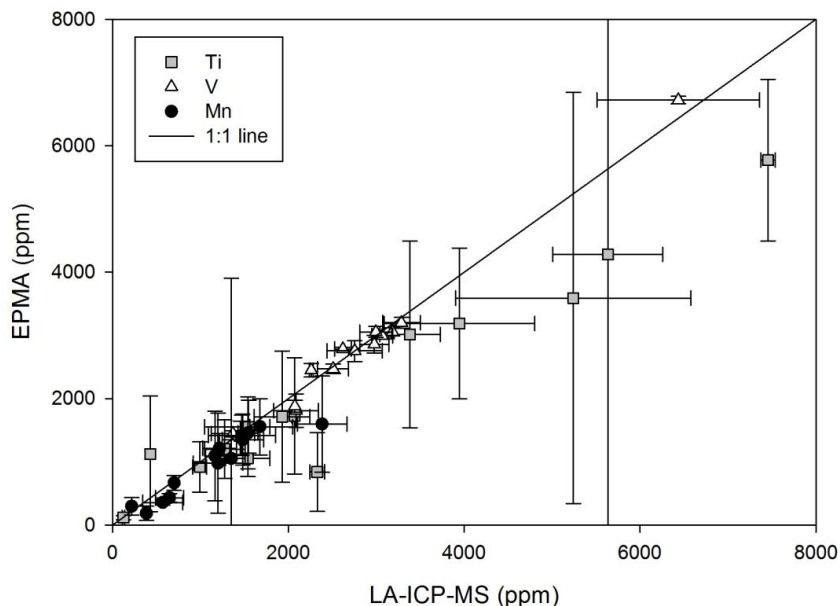| Analysis Method	INAA	INAA	INAA	INAA	INAA	INAA	INAA
GXR-1 Meas	3380	426	< 0.5		1.5	17	116
GXR-1 Cert	3300	427	0.5		1.58	16.6	122
CDN-CGS-11 Meas	720						
CDN-CGS-11 Cert	730						
DMMAS 116 Meas	1600	1560		74	5.9		6.7
DMMAS 116 Cert	1610	1560		77	6.3		6.8

Fig. S3.2: Analytical results of LA-ICP-MS measurements using NIST 610 as a standard versus results of EPMA measurements. Within the error of each method the analytical results show a relatively good agreement especially for the element V, which is not affected by inclusions/exsolutions like it is the case for Ti. When high Ti concentrations are detected, its concentrations may be overestimated by LA-ICP-MS, because of the larger beam size, which made it impossible to avoid micro/nano-exsolutions. The large errors for some EPMA measurements may arise from the accidental incorporation of nano-inclusions, which had a larger impact on the standard deviation of each averaged sample composition since individual points were analyzed instead of a continuous signal like for LA-ICP-MS.

Table S3.2: All EPMA analysis ordered from shallow to deep levels in drill core LC-14. See Table S2.3 for LC-04 and LC-05.

sample	Mg	Al	Si	Ca	Ti	V	Mn	Fe	O	Total	Point#	Ti+V	Al+Mn	Institute
	[wt%]	[wt%]	[wt%]	[wt%]	[wt%]	[wt%]	[wt%]	[wt%]	[wt%]	[wt%]		[wt%]	[wt%]	
LC-14-43a	0.03	0.08	0.12	0.01	0.30	0.37	0.01	69.00	27.00	96.92	67	0.66	0.09	UMIch
LC-14-43a	0.03	0.08	0.05		0.05	0.33	0.01	69.11	26.76	96.42	68	0.38	0.09	UMIch
LC-14-43b	0.03	0.05	0.03	0.02	0.14	0.61	0.02	71.49	27.84	100.24	69	0.76	0.07	UMIch
LC-14-43b	0.02	0.01	0.03	0.08	31.50	0.44	0.56	33.05	34.15	99.85	70	31.94	0.57	UMIch
LC-14-43c	0.03	0.06	0.04		0.17	0.32	0.01	72.00	27.92	100.55	71	0.49	0.07	UMIch
LC-14-43c	0.05	0.09	0.17	0.03	0.80	0.31	0.02	70.64	28.02	100.14	72	1.11	0.11	UMIch
LC-14-43d	0.07	0.24	0.30	0.03	0.07	0.31	0.03	68.14	26.86	96.06	73	0.38	0.26	UMIch
LC-14-43d	0.18	0.10	0.24	0.01	0.02	0.27	0.04	68.79	26.93	96.58	74	0.30	0.13	UMIch
LC-14-43e	0.15	0.39	1.07	0.05	0.03	0.23	0.06	66.37	27.20	95.56	75	0.26	0.45	UMIch
LC-14-43e	0.18	0.26	0.72	0.10	0.17	0.27	0.08	67.82	27.41	97.01	76	0.44	0.34	UMIch
LC-14-98a	0.04	0.06	0.05	0.01	0.04	0.17	0.01	72.31	27.90	100.58	31	0.21	0.07	UMIch
LC-14-98a	0.02	0.05	0.04	0.01	0.06	0.16	0.01	69.56	26.83	96.74	32	0.22	0.06	UMIch
LC-14-98a	0.04	0.07	0.18	0.02	0.22	0.11	0.04	71.71	27.94	100.34	33	0.33	0.11	UMIch
LC-14.98b	0.04	0.05	0.08	0.01	0.13	0.10	0.04	71.05	27.58	99.08	36	0.23	0.08	UMIch
LC-14.98c	0.35	0.11	0.60	0.03	0.03	0.10	0.02	69.74	27.74	98.72	38	0.13	0.12	UMIch
LC-14.98d	0.01	0.07	0.03	0.01	0.08	0.16	0.01	69.63	26.84	96.85	39	0.24	0.08	UMIch
LC-14.98d	0.03	0.06	0.04		0.03	0.15	0.01	72.13	27.77	100.21	40	0.18	0.06	UMich
LC-14.98d	0.06	0.11	0.15	0.05	0.06	0.14	0.01	69.69	27.07	97.34	41	0.20	0.12	UMich
LC-14.98d	0.17	0.31	0.42	0.12	0.10	0.15	0.02	70.73	28.09	100.12	42	0.25	0.33	UMich
14-136.5a	0.02	0.04	0.02	0.01	0.06	0.20	0.02	72.31	27.88	100.56	57	0.26	0.07	UMich
14-136.5a	0.03	0.05	0.03	0.02	0.06	0.19	0.02	71.83	27.71	99.94	59	0.24	0.07	UMich

14-136.5b	0.00	0.04	0.06	0.08	0.22	0.18	0.05	71.81	27.83	100.28	61	0.40	0.09	UMich
LC-14-167c	0.09	0.21	0.15	0.04	0.09	0.25	0.05	71.06	27.78	99.77	46c	0.33	0.26	UWAustralia
LC-14-167c	0.05	0.19	0.07	0.02	0.08	0.24	0.06	71.44	27.79	100.04	47c	0.32	0.25	UWAustralia
LC-14-167c	0.25	0.33	0.55	0.23	0.12	0.25	0.05	69.54	27.98	99.42	48c	0.37	0.38	UWAustralia
LC-14-167c	0.06	0.16	0.07	0.01	0.07	0.24	0.04	71.63	27.81	100.13	49c	0.31	0.20	UWAustralia
LC-14-167c	0.06	0.16	0.03	0.01	0.07	0.24	0.05	71.50	27.72	99.85	50c	0.32	0.21	UWAustralia
LC-14-167c	0.23	0.24	0.26	0.03	0.13	0.25	0.05	70.73	27.93	99.92	51c	0.37	0.29	UWAustralia
LC-14-167c	0.12	0.22	0.16	0.05	0.10	0.25	0.04	70.84	27.75	99.58	52c	0.35	0.27	UWAustralia
LC-14-167c	0.11	0.22	0.15	0.04	0.08	0.24	0.05	71.01	27.78	99.74	53c	0.33	0.27	UWAustralia
LC-14-167c	0.16	0.30	0.28	0.06	0.10	0.24	0.05	70.46	27.86	99.64	54c	0.34	0.35	UWAustralia
LC-14-167c	0.07	0.18	0.06	0.01	0.08	0.24	0.05	71.47	27.78	99.98	55c	0.32	0.23	UWAustralia
LC-14-167c	0.08	0.18	0.08	0.01	0.06	0.24	0.04	71.50	27.80	100.03	56c	0.31	0.21	UWAustralia
LC-14-167c	0.12	0.22	0.16	0.03	0.17	0.25	0.06	71.10	27.89	100.06	57c	0.42	0.27	UWAustralia
LC-14-167c	0.27	0.51	0.52	0.12	0.12	0.26	0.05	69.88	28.26	100.27	58c	0.38	0.56	UWAustralia
LC-14-167c	0.39	0.68	0.80	0.20	0.18	0.26	0.05	68.53	28.38	99.88	59c	0.43	0.73	UWAustralia
LC-14-167c	0.05	0.13	0.05	0.01	0.09	0.24	0.04	71.80	27.82	100.25	60c	0.33	0.17	UWAustralia
LC-14-167b	0.29	0.55	0.71	0.26	0.18	0.26	0.06	68.50	28.10	99.21	76b	0.44	0.60	UWAustralia
LC-14-167b	0.34	0.53	0.82	0.29	0.21	0.25	0.05	68.78	28.36	99.93	77b	0.46	0.59	UWAustralia
LC-14-167b	0.43	0.55	0.99	0.40	0.21	0.25	0.06	68.25	28.49	99.99	78b	0.46	0.61	UWAustralia
LC-14-167b	0.36	0.56	0.84	0.29	0.26	0.25	0.05	68.63	28.41	99.96	79b	0.51	0.62	UWAustralia
LC-14-167b	0.43	0.55	0.91	0.29	0.20	0.26	0.05	68.66	28.51	100.20	80b	0.45	0.60	UWAustralia
LC-14-167c	0.38	0.55	0.91	0.37	0.19	0.26	0.05	68.50	28.43	99.98	41c	0.45	0.60	UWAustralia
LC-14-167c	0.36	0.56	0.86	0.32	0.19	0.25	0.06	68.43	28.34	99.74	42c	0.44	0.62	UWAustralia
LC-14-167c	0.37	0.55	0.87	0.33	0.21	0.25	0.05	68.33	28.32	99.63	43c	0.46	0.60	UWAustralia
LC-14-167c	0.40	0.57	0.83	0.26	0.31	0.25	0.05	68.47	28.40	99.89	44c	0.56	0.62	UWAustralia

LC-14-167c	0.34	0.53	0.91	0.39	0.19	0.25	0.06	68.32	28.33	99.64	45c	0.43	0.59	UWAustralia
LC-14-167b	0.68	0.54	1.37	0.51	0.88	0.25	0.06	66.74	29.05	100.60	81b	1.13	0.59	UWAustralia
LC-14-167b	0.29	0.54	0.66	0.21	0.20	0.26	0.05	69.24	28.31	100.13	82b	0.46	0.59	UWAustralia
LC-14-167b	0.25	0.50	0.62	0.24	0.19	0.25	0.05	69.11	28.15	99.70	83b	0.44	0.55	UWAustralia
LC-14-167b	0.23	0.50	0.59	0.21	0.19	0.26	0.05	69.28	28.15	99.79	84b	0.45	0.55	UWAustralia
LC-14-167b	0.28	0.48	0.81	0.35	0.45	0.24	0.04	67.89	28.13	99.05	85b	0.69	0.53	UWAustralia
LC-14-167b	0.15	0.28	0.31	0.11	0.12	0.26	0.04	70.51	27.92	99.81	71b	0.37	0.32	UWAustralia
LC-14-167b	0.22	0.31	0.40	0.14	0.13	0.25	0.05	70.43	28.09	100.19	72b	0.38	0.36	UWAustralia
LC-14-167b	0.19	0.32	0.42	0.14	0.14	0.25	0.05	70.36	28.08	100.11	73b	0.39	0.37	UWAustralia
LC-14-167b	0.28	0.41	0.56	0.14	0.15	0.25	0.05	69.97	28.28	100.41	74b	0.41	0.46	UWAustralia
LC-14-167b	0.25	0.36	0.47	0.16	0.13	0.25	0.05	69.72	28.02	99.71	75b	0.39	0.41	UWAustralia
LC-14-167c	0.07	0.17	0.10	0.03	0.09	0.25	0.05	71.09	27.69	99.61	31c	0.34	0.22	UWAustralia
LC-14-167c	0.04	0.14	0.05	0.01	0.06	0.25	0.04	71.65	27.76	100.03	32c	0.31	0.18	UWAustralia
LC-14-167c	0.11	0.21	0.14	0.03	0.17	0.24	0.08	70.92	27.80	99.80	33c	0.41	0.29	UWAustralia
LC-14-167c	0.04	0.12	0.01		0.06	0.24	0.04	71.73	27.71	99.98	34c	0.30	0.15	UWAustralia
LC-14-167c	0.05	0.12	0.01		0.06	0.24	0.03	71.59	27.67	99.80	35c	0.30	0.15	UWAustralia
LC-14-167c	0.04	0.11	0.01		0.06	0.24	0.03	71.53	27.63	99.70	36c	0.30	0.14	UWAustralia
LC-14-167c	0.04	0.12	0.02		0.06	0.23	0.03	71.52	27.66	99.74	37c	0.29	0.15	UWAustralia
LC-14-167c	0.06	0.10	0.01		0.17	0.23	0.05	71.48	27.69	99.84	38c	0.40	0.15	UWAustralia
LC-14-167c	0.09	0.13	0.09	0.01	0.07	0.23	0.04	71.57	27.81	100.11	39c	0.30	0.17	UWAustralia
LC-14-167c	0.04	0.08	0.06	0.03	0.06	0.22	0.03	71.74	27.74	100.04	40c	0.28	0.12	UWAustralia
LC-14-167b	0.04	0.08	0.00		0.06	0.21	0.03	71.43	27.54	99.41	91b	0.27	0.11	UWAustralia
LC-14-167b	0.08	0.12	0.06	0.01	0.07	0.22	0.03	71.09	27.57	99.34	92b	0.29	0.15	UWAustralia
LC-14-167b	0.04	0.11	0.01		0.06	0.23	0.03	71.45	27.59	99.53	93b	0.29	0.13	UWAustralia
LC-14-167b	0.05	0.13	0.03		0.06	0.23	0.03	71.48	27.66	99.71	94b	0.30	0.15	UWAustralia

LC-14-167b	0.04	0.10	0.01		0.06	0.23	0.03	71.55	27.63	99.70	95b	0.29	0.13	UWAustralia
LC-14-167b	0.12	0.10	0.02		2.69	0.22	0.21	67.83	28.07	99.28	86b	2.91	0.31	UWAustralia
LC-14-167b	0.07	0.12	0.01		0.31	0.23	0.06	71.24	27.71	99.77	87b	0.54	0.17	UWAustralia
LC-14-167b	0.23	0.09	0.01		2.68	0.21	0.55	67.26	27.99	99.04	88b	2.90	0.64	UWAustralia
LC-14-167b	0.07	0.10	0.00		0.30	0.23	0.05	71.31	27.71	99.79	89b	0.53	0.15	UWAustralia
LC-14-167b	0.08	0.08	0.01		1.67	0.21	0.09	69.31	27.85	99.32	90b	1.87	0.17	UWAustralia
LC-14-167c	0.52	0.45	1.12	0.39	0.17	0.18	0.04	67.21	28.28	99.13	1c	0.36	0.49	UWAustralia
LC-14-167c	0.77	0.61	1.37	0.37	0.17	0.20	0.06	67.28	28.78	100.06	2c	0.37	0.66	UWAustralia
LC-14-167c	0.62	0.58	1.37	0.46	0.21	0.21	0.05	67.07	28.65	99.64	3c	0.41	0.63	UWAustralia
LC-14-167c	0.54	0.53	1.24	0.41	0.20	0.20	0.04	67.27	28.44	99.25	4c	0.40	0.58	UWAustralia
LC-14-167c	0.53	0.44	1.15	0.38	0.17	0.21	0.04	68.19	28.55	99.97	5c	0.38	0.48	UWAustralia
LC-14-167c	0.46	0.40	0.93	0.26	0.15	0.20	0.04	68.84	28.40	99.96	6c	0.36	0.45	UWAustralia
LC-14-167c	0.44	0.42	0.90	0.26	0.17	0.20	0.04	68.42	28.20	99.29	7c	0.37	0.46	UWAustralia
LC-14-167c	0.45	0.36	0.87	0.24	0.14	0.20	0.04	68.88	28.27	99.67	8c	0.34	0.40	UWAustralia
LC-14-167c	0.41	0.36	0.83	0.22	0.14	0.20	0.04	69.01	28.23	99.64	9c	0.34	0.40	UWAustralia
LC-14-167c	0.41	0.35	0.83	0.24	0.14	0.20	0.04	68.87	28.19	99.51	10c	0.34	0.40	UWAustralia
LC-14-167c	0.32	0.26	0.59	0.16	0.35	0.21	0.04	69.35	28.05	99.51	11c	0.56	0.30	UWAustralia
LC-14-167c	0.17	0.18	0.37	0.12	0.10	0.21	0.04	70.09	27.70	99.04	12c	0.30	0.21	UWAustralia
LC-14-167c	0.26	0.18	0.61	0.18	0.09	0.20	0.04	69.65	27.89	99.18	13c	0.28	0.21	UWAustralia
LC-14-167c	0.23	0.18	0.54	0.17	0.10	0.20	0.04	69.87	27.89	99.33	14c	0.29	0.22	UWAustralia
LC-14-167c	0.38	0.29	0.88	0.29	0.13	0.20	0.04	68.84	28.16	99.39	15c	0.33	0.33	UWAustralia
LC-14-167c	0.32	0.28	0.76	0.24	0.12	0.19	0.04	69.30	28.13	99.57	16c	0.31	0.31	UWAustralia
LC-14-167c	0.23	0.20	0.47	0.13	0.09	0.19	0.03	70.22	27.94	99.66	17c	0.28	0.23	UWAustralia
LC-14-167c	0.21	0.16	0.42	0.13	0.08	0.19	0.03	70.35	27.86	99.55	18c	0.27	0.19	UWAustralia
LC-14-167c	0.36	0.26	0.80	0.26	0.12	0.18	0.04	69.26	28.15	99.59	19c	0.30	0.30	UWAustralia

LC-14-167c	0.39	0.38	0.99	0.31	0.15	0.17	0.04	68.53	28.28	99.51	20c	0.32	0.42	UWAustralia
LC-14-167c	0.29	0.30	0.69	0.22	0.13	0.16	0.04	69.44	28.08	99.54	21c	0.29	0.34	UWAustralia
LC-14-167c	0.30	0.27	0.72	0.24	0.12	0.16	0.03	69.70	28.18	99.89	22c	0.28	0.30	UWAustralia
LC-14-167c	0.08	0.09	0.18	0.06	0.06	0.15	0.03	71.35	27.76	99.81	23c	0.21	0.12	UWAustralia
LC-14-167c	0.05	0.10	0.13	0.03	0.06	0.14	0.03	71.41	27.70	99.73	24c	0.20	0.13	UWAustralia
LC-14-167c	0.08	0.17	0.26	0.07	0.08	0.14	0.03	70.81	27.74	99.48	25c	0.22	0.20	UWAustralia
LC-14-167c	0.15	0.29	0.45	0.11	0.10	0.14	0.03	70.34	27.97	99.74	26c	0.24	0.31	UWAustralia
LC-14-167c	0.05	0.10	0.13	0.04	0.06	0.14	0.02	71.44	27.70	99.74	27c	0.20	0.12	UWAustralia
LC-14-167c	0.04	0.07	0.08	0.02	0.05	0.13	0.03	71.76	27.73	99.98	28c	0.18	0.09	UWAustralia
LC-14-167c	0.17	0.30	0.49	0.12	0.11	0.13	0.06	70.00	27.92	99.45	29c	0.24	0.36	UWAustralia
LC-14-167c	0.05	0.09	0.12	0.06	0.06	0.13	0.03	71.34	27.66	99.63	30c	0.19	0.12	UWAustralia
LC-14-167b	0.03	0.05	0.03	0.02	0.05	0.13	0.02	71.89	27.68	99.93	96b	0.18	0.07	UWAustralia
LC-14-167b	0.02	0.05	0.02	0.02	0.05	0.13	0.03	71.81	27.64	99.81	97b	0.18	0.08	UWAustralia
LC-14-167b	0.04	0.05	0.05	0.08	0.04	0.13	0.02	71.28	27.50	99.24	98b	0.18	0.07	UWAustralia
LC-14-167b	0.02	0.05	0.03	0.08	0.04	0.13	0.02	71.29	27.46	99.16	99b	0.17	0.07	UWAustralia
LC-14-167b	0.05	0.09	0.11	0.13	0.05	0.13	0.03	71.40	27.68	99.73	100b	0.18	0.12	UWAustralia
LC-14-167d	0.16	0.20	0.24	0.07	0.13	0.23	0.04	71.38	28.06	100.55	41d	0.36	0.24	UWAustralia
LC-14-167d	0.18	0.22	0.24	0.05	0.10	0.23	0.04	71.42	28.09	100.62	42d	0.33	0.26	UWAustralia
LC-14-167d	0.12	0.18	0.19	0.05	0.09	0.22	0.03	71.67	28.05	100.66	43d	0.31	0.21	UWAustralia
LC-14-167d	0.17	0.16	0.09	0.02	1.38	0.22	0.26	69.78	28.14	100.27	44d	1.60	0.43	UWAustralia
LC-14-167d	0.08	0.18	0.09	0.02	0.15	0.23	0.04	71.76	27.96	100.55	45d	0.37	0.22	UWAustralia
LC-14-167d	0.20	0.21	0.30	0.07	0.08	0.22	0.03	71.40	28.13	100.69	46d	0.30	0.24	UWAustralia
LC-14-167d	0.15	0.20	0.14	0.03	0.81	0.22	0.16	70.73	28.17	100.67	47d	1.03	0.36	UWAustralia
LC-14-167d	0.18	0.21	0.25	0.05	0.61	0.22	0.14	70.54	28.12	100.36	48d	0.83	0.35	UWAustralia
LC-14-167d	0.09	0.23	0.10	0.03	0.08	0.22	0.03	71.69	27.94	100.44	49d	0.30	0.26	UWAustralia

LC-14-167d	0.11	0.19	0.16	0.06	0.07	0.22	0.03	71.52	27.94	100.35	50d	0.29	0.22	UWAustralia
LC-14-167c	0.04	0.06	0.31		0.05	0.10	0.03	71.45	27.83	99.93	61c	0.15	0.09	UWAustralia
LC-14-167c	0.09	0.08	0.46	0.02	0.06	0.07	0.04	71.08	27.91	99.87	62c	0.13	0.12	UWAustralia
LC-14-167c	0.12	0.11	0.48	0.02	0.06	0.07	0.03	71.03	27.97	99.95	63c	0.13	0.14	UWAustralia
LC-14-167c	0.08	0.08	0.36	0.01	0.05	0.08	0.03	71.27	27.85	99.85	64c	0.13	0.11	UWAustralia
LC-14-167c	0.09	0.11	0.60	0.02	0.06	0.09	0.04	70.84	28.03	99.96	65c	0.15	0.15	UWAustralia
LC-14-167c	0.03	0.05	0.01		0.04	0.10	0.03	71.92	27.65	99.87	66c	0.14	0.08	UWAustralia
LC-14-167c	0.07	0.12	0.13	0.03	0.06	0.10	0.02	71.36	27.68	99.62	67c	0.16	0.14	UWAustralia
LC-14-167c	0.05	0.08	0.44	0.03	0.05	0.11	0.03	71.17	27.93	100.00	68c	0.16	0.11	UWAustralia
LC-14-167c	0.04	0.07	0.40	0.01	0.05	0.12	0.03	71.27	27.90	99.99	69c	0.16	0.10	UWAustralia
LC-14-167c	0.02	0.05	0.03	0.00	0.04	0.12	0.02	71.80	27.64	99.83	70c	0.16	0.07	UWAustralia
LC-14-167c	0.11	0.27	0.47	0.14	0.10	0.12	0.03	70.28	27.92	99.61	71c	0.22	0.30	UWAustralia
LC-14-167c	0.15	0.09	0.27	0.03	0.07	0.15	0.05	71.17	27.84	99.87	72c	0.21	0.14	UWAustralia
LC-14-167c	0.13	0.09	0.28	0.03	0.10	0.14	0.05	70.80	27.71	99.41	73c	0.23	0.14	UWAustralia
LC-14-167c	0.15	0.11	0.28	0.03	0.10	0.13	0.05	71.01	27.81	99.74	74c	0.23	0.16	UWAustralia
LC-14-167c	0.17	0.10	0.33	0.04	0.07	0.13	0.03	70.77	27.76	99.44	75c	0.20	0.14	UWAustralia
LC-14-167c	0.22	0.15	0.36	0.05	0.09	0.13	0.04	70.85	27.94	99.94	76c	0.22	0.19	UWAustralia
LC-14-167c	0.19	0.12	0.36	0.05	0.08	0.11	0.04	70.93	27.89	99.83	77c	0.19	0.16	UWAustralia
LC-14-167c	0.23	0.31	0.86	0.14	0.14	0.13	0.04	69.33	28.17	99.56	78c	0.27	0.35	UWAustralia
LC-14-167c	0.14	0.11	0.27	0.11	0.08	0.12	0.03	71.24	27.90	100.07	79c	0.20	0.14	UWAustralia
LC-14-167c	0.43	0.45	1.03	0.38	0.21	0.12	0.05	68.27	28.38	99.66	80c	0.33	0.50	UWAustralia
LC-14-167c	0.23	0.25	0.53	0.16	0.13	0.11	0.03	69.95	27.96	99.51	81c	0.24	0.29	UWAustralia
LC-14-167c	0.41	0.43	0.93	0.30	0.18	0.02	0.05	68.73	28.31	99.68	82c	0.20	0.48	UWAustralia
LC-14-167c	0.48	0.42	1.03	0.35	0.20	0.02	0.06	68.58	28.44	99.93	83c	0.22	0.48	UWAustralia
LC-14-167c	0.47	0.43	1.01	0.34	0.18	0.02	0.05	68.60	28.44	99.96	84c	0.20	0.49	UWAustralia

LC-14-167c	0.43	0.32	0.90	0.33	0.14	0.02	0.05	68.75	28.20	99.52	85c	0.16	0.37	UWAustralia
LC-14-167c	0.38	0.38	0.83	0.30	0.16	0.02	0.05	69.12	28.25	99.74	86c	0.18	0.43	UWAustralia
LC-14-167c	0.48	0.48	1.01	0.30	0.19	0.02	0.06	68.79	28.53	100.21	87c	0.21	0.54	UWAustralia
LC-14-167c	0.47	0.46	1.01	0.31	0.18	0.02	0.06	68.90	28.53	100.26	88c	0.20	0.52	UWAustralia
LC-14-167c	0.50	0.42	1.00	0.30	0.16	0.01	0.06	68.79	28.45	100.03	89c	0.18	0.48	UWAustralia
LC-14-167c	0.49	0.42	0.99	0.33	0.17	0.02	0.06	68.68	28.42	99.92	90c	0.19	0.48	UWAustralia
LC-14-167c	0.06	0.07	0.02		0.05	0.02	0.04	71.88	27.65	99.84	91c	0.07	0.11	UWAustralia
LC-14-167c	0.05	0.07	0.01		0.04	0.02	0.05	72.21	27.76	100.27	92c	0.06	0.11	UWAustralia
LC-14-167c	0.05	0.06	0.00		0.04	0.02	0.04	72.03	27.68	100.00	93c	0.06	0.10	UWAustralia
LC-14-167c	0.06	0.06	0.01		0.04	0.02	0.04	71.88	27.63	99.80	94c	0.06	0.10	UWAustralia
LC-14-167c	0.06	0.06	0.01		0.04	0.02	0.05	72.04	27.69	100.03	95c	0.05	0.10	UWAustralia
LC-14-167c	0.06	0.05	0.01		0.04	0.02	0.04	71.88	27.61	99.77	96c	0.06	0.09	UWAustralia
LC-14-167c	0.06	0.05	0.00		0.03	0.02	0.04	72.06	27.67	100.00	97c	0.05	0.09	UWAustralia
LC-14-167c	0.07	0.05	0.03		0.03	0.02	0.04	71.99	27.69	100.00	98c	0.05	0.10	UWAustralia
LC-14-167c	0.11	0.06	0.10		0.03	0.02	0.05	71.80	27.74	100.00	99c	0.05	0.11	UWAustralia
LC-14-167c	0.06	0.03	0.01		0.02	0.02	0.04	71.98	27.62	99.84	100c	0.04	0.07	UWAustralia
LC-14-167d	0.06	0.03	0.02		0.01	0.02	0.04	71.90	27.60	99.77	1d	0.02	0.07	UWAustralia
LC-14-167d	0.07	0.03	0.03	0.01	0.00	0.01	0.04	71.78	27.57	99.63	2d	0.02	0.07	UWAustralia
LC-14-167d	0.25	0.04	0.42	0.13	0.01	0.01	0.05	71.13	27.96	100.09	3d	0.02	0.09	UWAustralia
LC-14-167d	0.31	0.05	0.57	0.18	0.01	0.01	0.05	70.58	28.00	99.91	4d	0.03	0.10	UWAustralia
LC-14-167d	0.22	0.04	0.36	0.10	0.01	0.02	0.05	71.06	27.84	99.84	5d	0.02	0.09	UWAustralia
LC-14-167d	0.15	0.03	0.21	0.06	0.01	0.01	0.05	71.61	27.81	100.06	6d	0.02	0.08	UWAustralia
LC-14-167d	0.20	0.04	0.28	0.07	0.01	0.01	0.04	71.28	27.80	99.84	7d	0.02	0.08	UWAustralia
LC-14-167d	0.12	0.03	0.14	0.03	0.01	0.01	0.04	71.79	27.75	100.02	8d	0.02	0.07	UWAustralia
LC-14-167d	0.22	0.05	0.38	0.13	0.02	0.01	0.05	71.03	27.87	99.86	9d	0.03	0.09	UWAustralia

LC-14-167d	0.19	0.04	0.30	0.09	0.02	0.01	0.04	71.32	27.85	99.99	10d	0.03	0.08	UWAustralia
LC-14-167d	0.51	0.18	1.12	0.39	0.01	0.01	0.05	68.95	28.38	100.01	11d	0.03	0.23	UWAustralia
LC-14-167d	0.55	0.23	1.14	0.38	0.02	0.01	0.06	68.58	28.35	99.73	12d	0.03	0.29	UWAustralia
LC-14-167d	0.55	0.22	1.11	0.36	0.02	0.01	0.05	68.69	28.33	99.73	13d	0.03	0.27	UWAustralia
LC-14-167d	0.58	0.24	1.18	0.39	0.02	0.01	0.05	68.51	28.42	99.87	14d	0.03	0.29	UWAustralia
LC-14-167d	0.56	0.22	1.22	0.46	0.02	0.02	0.05	68.42	28.43	99.87	15d	0.03	0.27	UWAustralia
LC-14-167d	0.58	0.23	1.16	0.38	0.02	0.01	0.05	68.81	28.48	100.15	16d	0.03	0.28	UWAustralia
LC-14-167d	0.56	0.29	1.05	0.30	0.02	0.01	0.05	69.00	28.44	100.16	17d	0.03	0.34	UWAustralia
LC-14-167d	0.55	0.27	1.08	0.33	0.03	0.01	0.05	68.77	28.40	99.98	18d	0.04	0.33	UWAustralia
LC-14-167d	0.56	0.27	1.15	0.37	0.03	0.01	0.05	68.62	28.41	99.89	19d	0.04	0.32	UWAustralia
LC-14-167d	0.54	0.24	1.12	0.37	0.03	0.01	0.06	68.76	28.40	99.90	20d	0.04	0.30	UWAustralia

Supplementary Information for Chapter 4: "*In-situ* iron isotope analyses reveal igneous and magmatic-hydrothermal growth of magnetite at the Los Colorados Kiruna-type iron oxide - apatite deposit, Chile."

Jaayke L. Knipping, Adrian Fiege, Adam C. Simon, Martin Oeser, Martin Reich[4], Laura D. Bilenker

This supplementary section includes reflected light images of each sample to visualize where exactly data were collected (LA-ICP-MS trace element transects and Fe isotope raster spots). When zoning was observed by these data, additional elemental maps were collected for Al and Ti by EPMA (beam current: 300 nA, accelerating voltage: 20 kV, spot size: 1 µm, counting time: 80 ms/step). No common threshold can be given for trace element concentrations indicating magmatic-hydrothermal or igneous origin, respectively, due to complex interplays that change over depth (higher trace element concentrations are detected with increasing depths). However, discrimination can be conducted by looking at individual samples. Samples that provide a zoning from igneous to hydrothermal parts (sudden changes in trace element concentration) give evidence of how much trace elements can be expected for different origins (igneous vs. magmatic-hydrothermal) at each depths and help to interpret those samples that do not provide distinct zoning. Further, textural appearance helps to estimate different origins. Inclusion-rich crystals/areas are rather indicators for an igneous origin, while pristine magnetite texture implies a magmatic-hydrothermal formation (Knipping et al. 2015a and b). A description is given for each sample to show how their origin (igneous vs. magmatic-hydrothermal) was determined.
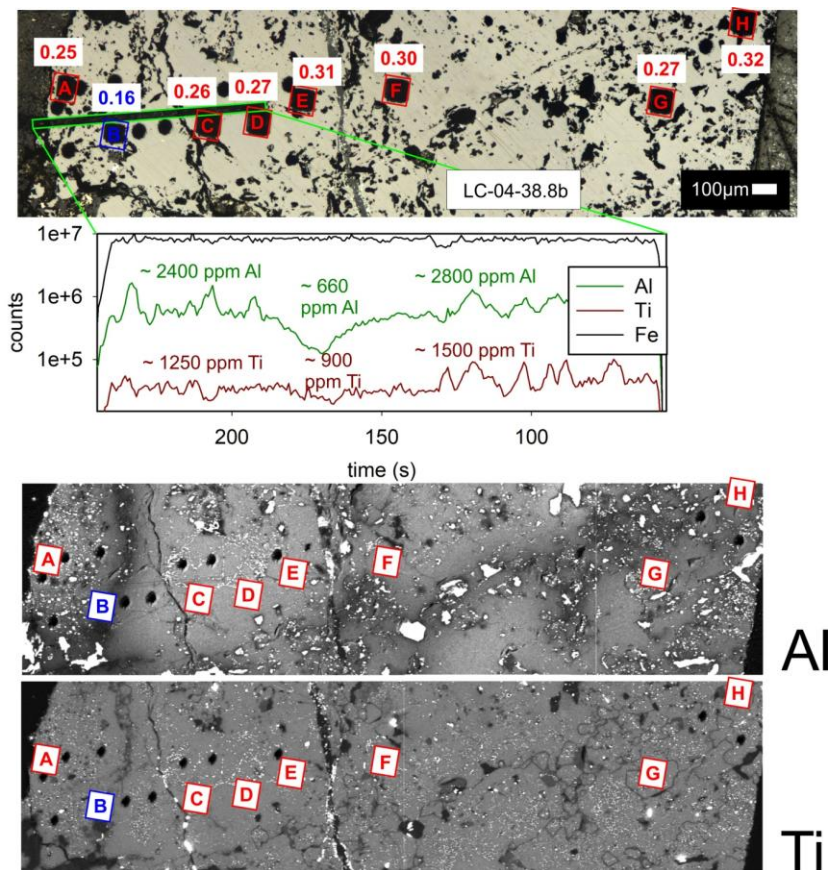
Fig. S4.1: Reflected light image of the shallowest sample of drill core LC-04 (LC-04-38.8b) including location of LA-ICP-MS trace element transect (highlighted in bright green) as well as location and values of in-situ δ^{56}Fe measurements (red or blue). Fe-isotope values were assigned to igneous (red) or hydrothermal origin (blue) based on measured trace element concentration (Ti and Al). A clear drop in Ti and Al concentration at location B indicates a hydrothermal vein between igneous parts with relatively high Al and Ti concentrations. This vein is also visible in the Al and Ti elemental maps measured with EPMA. Therefore, B was interpreted as hydrothermal, while A, C and D were interpreted as igneous magnetite. The remaining raster spots E, F, G and H were also assigned as igneous, since their isotopic values as well as their textural appearance correlate with the raster spots A, C and D.
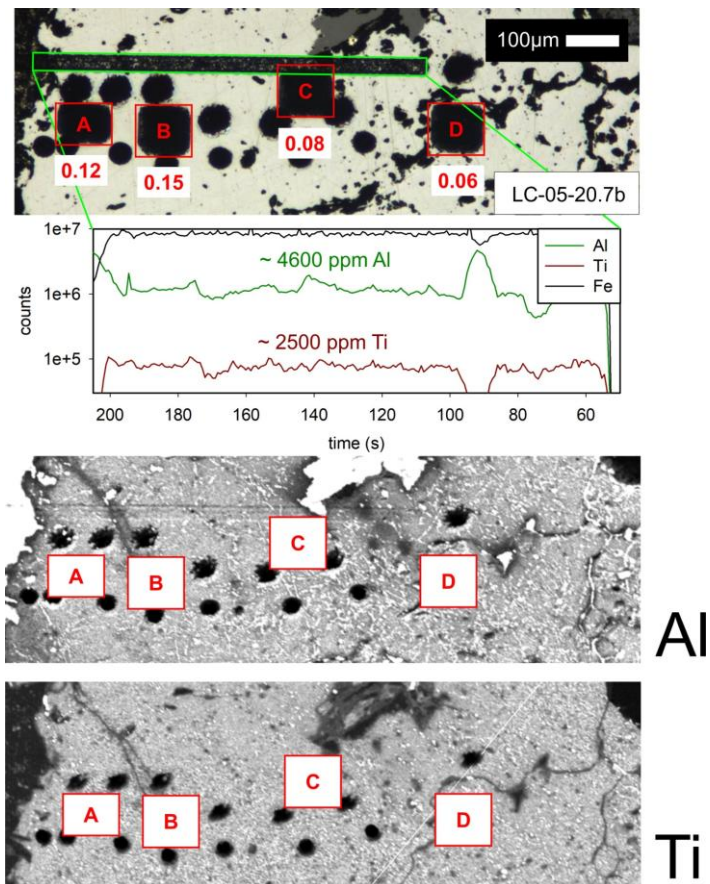
183
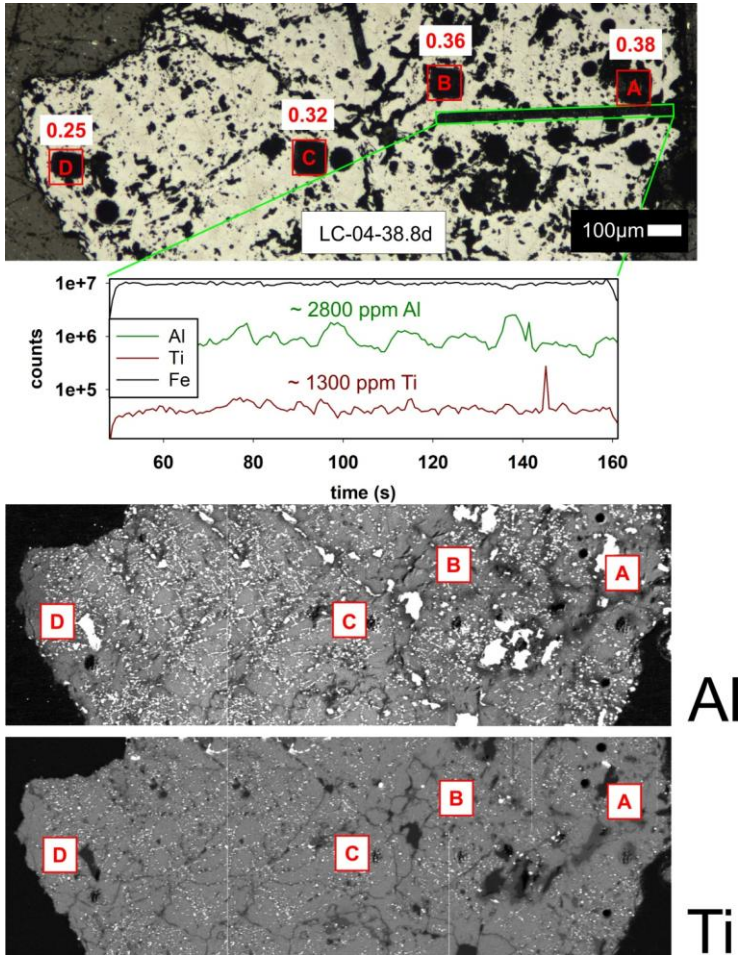
Fig. S4.2: Reflected light image of sample LC-04-38.8d including location of LA-ICP-MS trace element transect (highlighted in bright green) as well as location and values of in-situ δ^{56}Fe measurements (red). Fe-isotope values were assigned to solely igneous (red) origin based on trace element concentration (Ti and Al) comparable to igneous parts of samples from similar depth (LC-04-38.8b). The Al and Ti elemental maps measured with EPMA also indicate a similar texture for all measured spots (A, B, C and D).
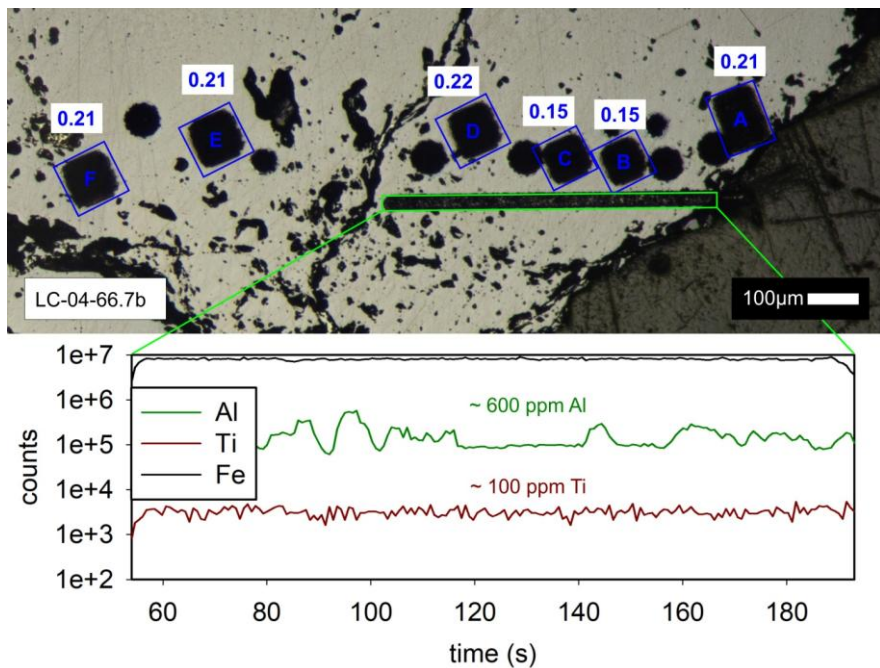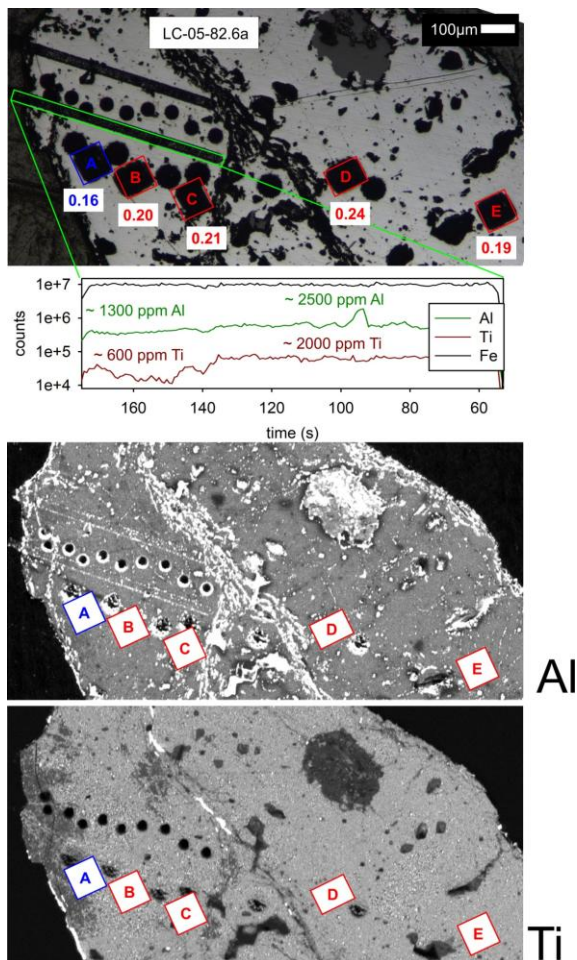
Fig. S4.3: Reflected light image of sample LC-04-66.7b including location of LA-ICP-MS trace element transect (highlighted in bright green) as well as location and values of in-situ $\delta^{56}Fe$ measurements (blue). Fe-isotope values of A, B, C and D were assigned to solely hydrothermal (blue) origin based on very low trace element concentration (Ti and Al) comparable to hydrothermal parts in sample LC-04-38.8b as well as a relatively smooth texture and LA-ICP-MS trace element signal. The remaining raster spots E and F were also assigned as hydrothermal, since their isotopic values as well as their textural appearance correlate with the raster spots A, B, C and D.
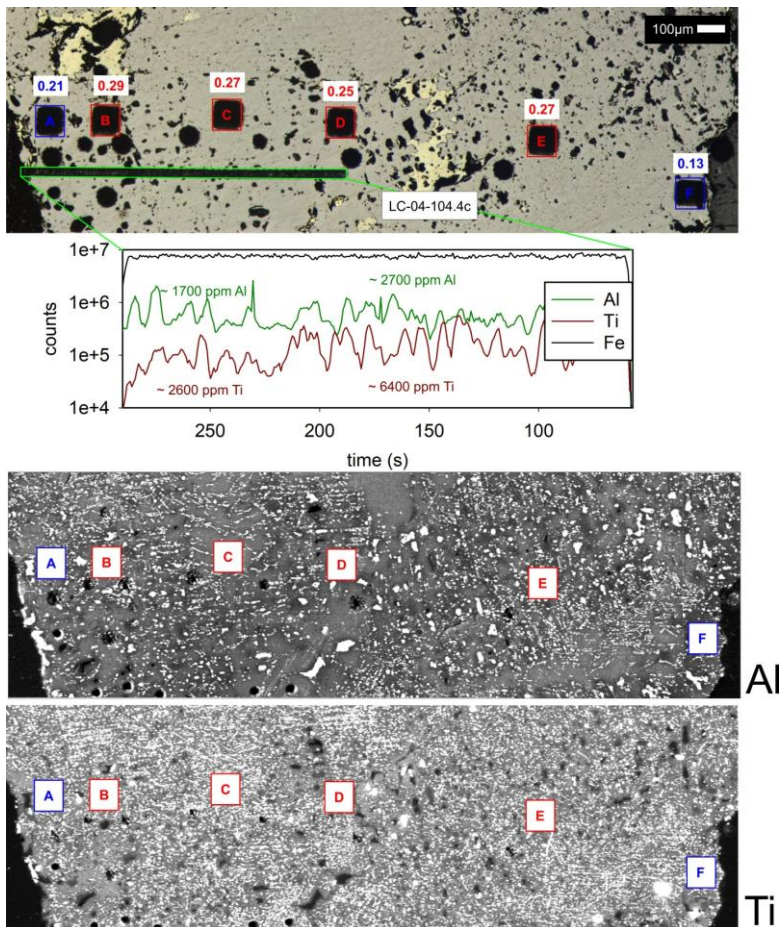
Fig. S4.4: Reflected light image of sample LC-04-104.4c including location of LA-ICP-MS trace element transect (highlighted in bright green) as well as location and values of in-situ $\delta^{56}Fe$ measurements (red or blue). Fe-isotope values were assigned to igneous (red) or hydrothermal origin (blue) based on measured trace element concentration (Ti and Al). A decrease in Ti and Al concentration between location B and A indicates a hydrothermal rim with relatively lower Al and Ti concentrations. This rim is also detectable in the Al and Ti elemental maps measured with EPMA (especially for Al at location F). Therefore, A and F were interpreted as hydrothermal, while B, C and D were interpreted as igneous magnetite. The remaining raster spot E was also assigned as igneous, since its isotopic value as well as its textural appearance correlate with the raster spots B, C and D.
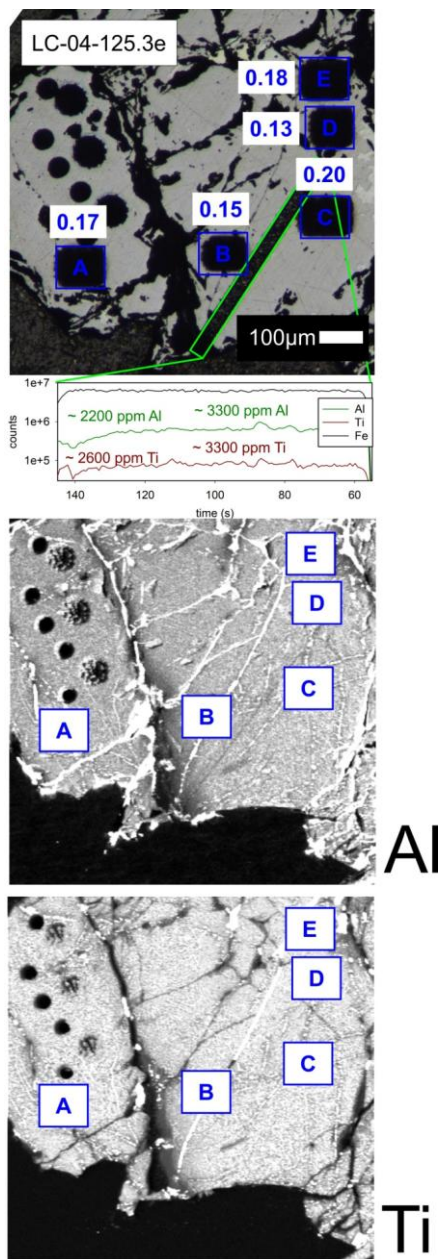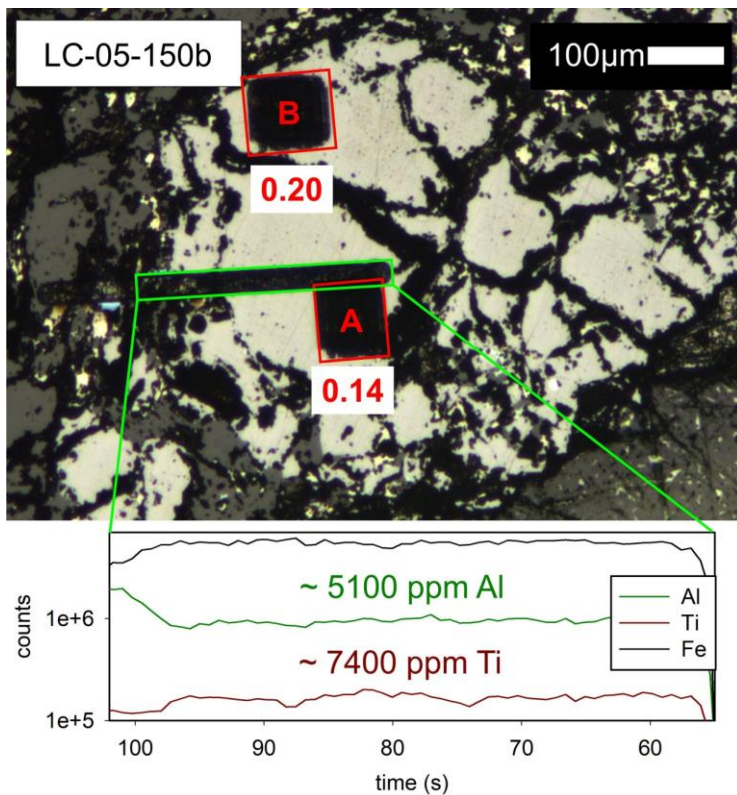
Fig. S4.5: Reflected light image of sample LC-04-125.3e including location of LA-ICP-MS trace element transect (highlighted in bright green) as well as location and values of in-situ δ^{56}Fe measurements (blue). Fe-isotope values of B and C were assigned to solely hydrothermal (blue) origin based on their relatively low Al and Ti concentration comparable to hydrothermal parts in the shallower sample LC-04-104.4c as well as their smooth texture and LA-ICP-MS trace element signal. A decrease in Al and Ti towards the rims may indicate here a cooling history of hydrothermal magnetite. The remaining raster spots A, D and E were also assigned as hydrothermal, since their isotopic values as well as their textural appearance correlate with the raster spots B and C.
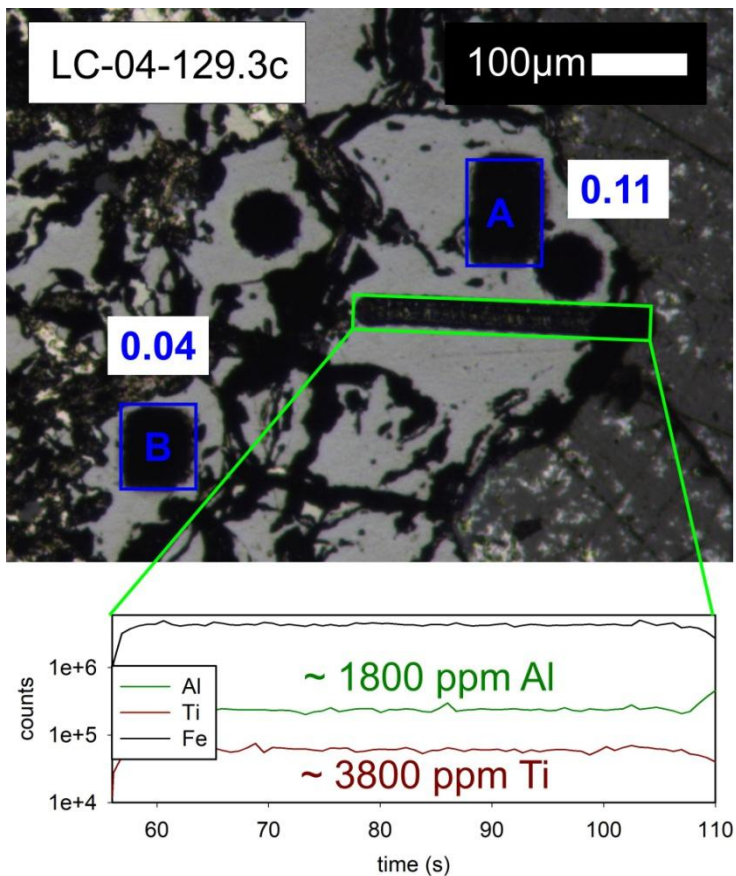
Fig. S4.6: Reflected light image of sample LC-04-129.3c including location of LA-ICP-MS trace element transect (highlighted in bright green) as well as location and values of in-situ δ^{56}Fe measurements (blue). Fe-isotope value of A was assigned to hydrothermal (blue) origin based on its relatively low Al and Ti concentration comparable to hydrothermal parts in shallower samples(LC-04-104.4c and LC-04-125.3e) and in contrast to an igneous sample of the same depth (LC-04-129.3d). The smooth texture and constant LA-ICP-MS trace element signal may also indicate a hydrothermal formation. The remaining raster spot B was also assigned as hydrothermal since its textural appearance correlate with raster spot A.
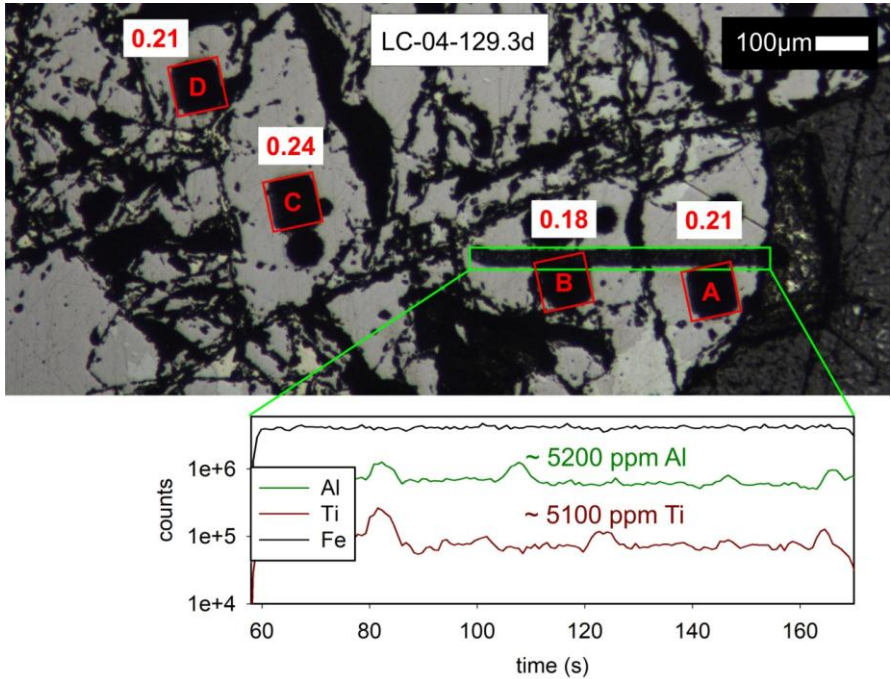
Fig. S4.7: Reflected light image of sample LC-04-129.3d including location of LA-ICP-MS trace element transect (highlighted in bright green) as well as location and values of in-situ $\delta^{56}Fe$ measurements (red). Fe-isotope value of A and B were assigned to igneous (red) origin based on their relatively high Al and Ti concentration in contrast to hydrothermal samples from the same depths (LC-04-129.3c and LC-04-129.3e). The remaining raster spots C and D were also assigned as igneous since their isotopic values as well as their textural appearance correlate with raster spot A and B.
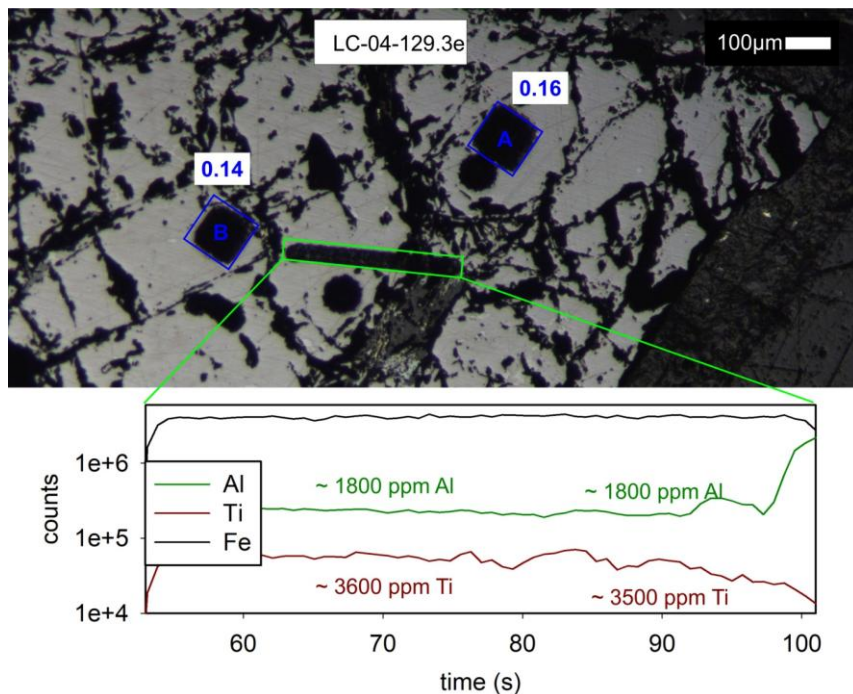
Fig. S4.8: Reflected light image of sample LC-04-129.3e including location of LA-ICP-MS trace element transect (highlighted in bright green) as well as location and values of in-situ δ^{56}Fe measurements (blue). Fe-isotope value of A and B were assigned to hydrothermal (blue) origin based on their relatively low Al and Ti concentration comparable to a hydrothermal sample (LC-04-129.3c) and in contrast to an igneous sample (LC-04-129.3d) from the same depths.

Fig. S4.9: Reflected light image of the shallowest sample of drill core LC-05 (LC-05-20.7b) including location of LA-ICP-MS trace element transect (highlighted in bright green) as well as location and values of in-situ δ^{56}Fe measurements (red). Fe-isotope value of A, B, C and D were assigned to igneous (red) origin based on their relatively high Al and Ti concentration comparable to igneous parts and in contrast to hydrothermal parts in the deeper sample LC-05-82.6a.

Fig. S4.10: Reflected light image of sample LC-05-82.6a including location of LA-ICP-MS trace element transect (highlighted in bright green) as well as location and values of in-situ δ^{56}Fe measurements (red or blue). Fe-isotope values were assigned to igneous (red) or hydrothermal origin (blue) based on measured trace element concentration (Ti and Al). A drop in Ti and Al between location B and A indicates a hydrothermal rim with relatively lower Al and Ti concentrations. This rim is also detectable in the Al and Ti elemental maps measured with EPMA (especially for Ti). Therefore, A was interpreted as hydrothermal, while B and C were interpreted as igneous magnetite. The remaining raster spots D and E were also assigned as igneous, since their isotopic value as well as their textural appearance correlate with the raster spots B and C.
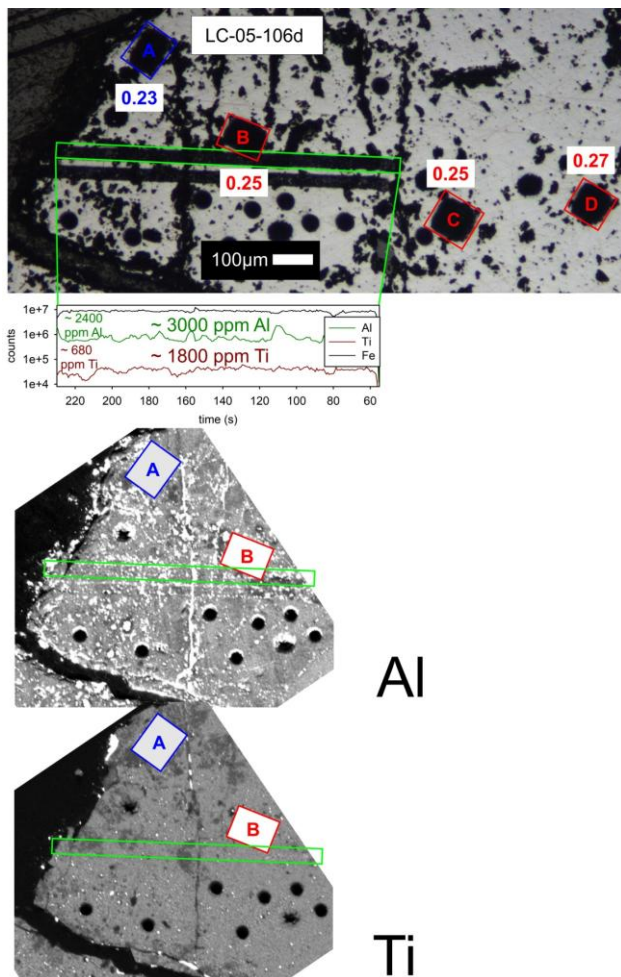
Fig. S4.11: Reflected light image of sample LC-05-106d including location of LA-ICP-MS trace element transect (highlighted in bright green) as well as location and values of in-situ $\delta^{56}Fe$ measurements (red or blue). Fe-isotope values were assigned to igneous (red) or hydrothermal origin (blue) based on measured trace element concentration (Ti and Al). A drop in Ti and Al between location B and A indicates a hydrothermal rim with relatively lower Al and Ti concentrations. This rim is also detectable in the Al and Ti elemental maps measured with EPMA (especially for Ti). Therefore, A was interpreted as hydrothermal, while B was interpreted as igneous magnetite. The remaining raster spots C and D were also assigned as igneous, since their isotopic values as well as their textural appearance correlate with the raster spot B.
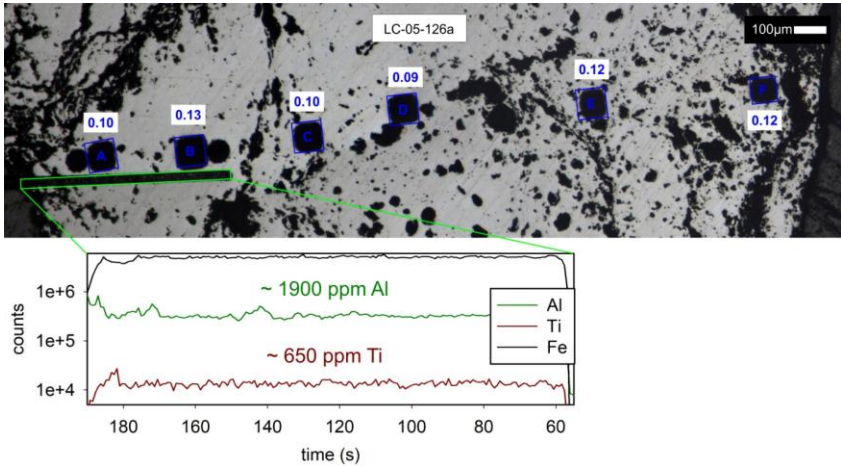
Fig. S4.12: Reflected light image of sample LC-05-126a including location of LA-ICP-MS trace element transect (highlighted in bright green) as well as location and values of in-situ $\delta^{56}Fe$ measurements (blue). Fe-isotope values of A and B were assigned to solely hydrothermal (blue) origin based on very low trace element concentration (Ti and Al) comparable to hydrothermal parts in the shallower samples (LC-05-82.6a and LC-05-106d) as well as a relatively smooth texture and LA-ICP-MS trace element signal. The remaining raster spots C, D, E and F were also assigned as hydrothermal, since their isotopic values correlate very good with the raster spots A and B.

Fig. S4.13: Reflected light image of the deepest sample of drill core LC-05 (LC-05-150b) including location of LA-ICP-MS trace element transect (highlighted in bright green) as well as location and values of in-situ δ^{56}Fe measurements (red). Fe-isotope values of A and B were assigned to igneous (red) origin based on the highest measured Al and Ti concentration when compared to all other samples from Los Colorados.

Supplementary Information for Chapter 5: "Accumulation of magnetite by flotation on bubbles during decompression of silicate magma"

Jaayke L. Knipping, James D. Webster, Adam C. Simon and François Holtz

S5.1: Pressure and temperature range of magnetite flotation

Flotation can happen from the moment of magnetite crystallization and first bubble nucleation; i.e., from the time of fluid exsolution until the density of the magnetite-bubble solution becomes higher than the surrounding melt or until the suspension reaches the top of the melt-rich magma chamber, likely a more crystalline or mushy layer. The depth range is variable and dependent on many parameters:

- water content: The higher the water content, the earlier (deeper) the fluid exsolution begins.

- density of fluid: The densiy of the fluid is dependent on the amount of dissolved $NaCl_{eq}$ and dissolved metals, such as Fe. The lower the content of solutes, the further the suspension can ascend.

- density of the surrounding melt: The density of the surrounding melt is dependent on the melt composition and dissolved water concentration. The more mafic and dryer the melt, the further the suspension can travel. However, less water content means higher viscosity of the melt and may hinder the process.

- amount of magnetite in suspension: The higher the amount of magnetite crystals in the suspension, the more difficult it is for the exsolved fluid bubbles to lift the magnetite. For example, when the abundance of magnetite exceeds 37 vol% of a suspension that contains 35 wt% $NaCl_{eq}$ and 7.2 wt% dissolved Fe in an andesitic melt with a density of 2.27 g/cm^3 (see Knipping et al. 2015a for calculation), the suspension would become negatively buoyant.

- location of the melt-rich magma reservoir in the crust: The more shallow the melt-rich magma reservoir is located (thinned crust), the shallower the suspension can ascend.

In Fig. S5.1, the pressure and temperature range over which magnetite flotation is possible was calculated by using the MELTS software for thermodynamic modeling for an andesite that contains 5.75 wt% H_2O at a fO_2=NNO+3. The model results

indicate that magnetite flotation is possible in magma reservoirs in Earth's upper crust from ~2 to ~10 km assuming a lithostatic geobaric gradient of 28 MPa/km.
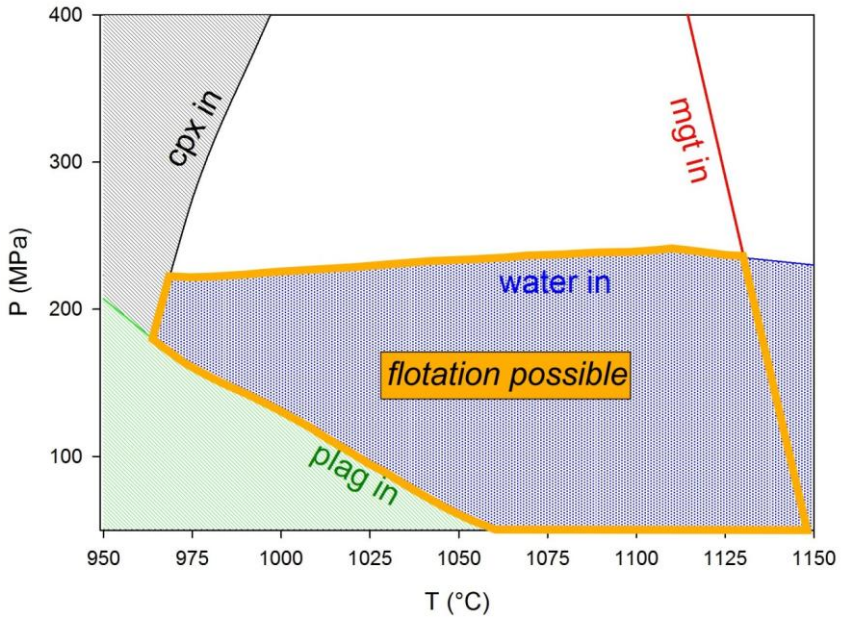
Fig. S5.1: Temperature vs. pressure phase diagram calculated by using MELTS (Ghiorso and Sack 1995; Asimow and Ghiorso, 1998), for the P1D andesitic melt composition of Martel et al. (1999), a water concentration of 5.75 wt% H_2O, and fO_2 = NNO+3. The model results indicate that flotation of magnetite is possible over a wide range of pressures and temperatures equal to a depth range roughly from ~2 to 10 km depending on temperature.

S2: Velocity of magnetite suspension

The velocity of the magnetite suspension can be calculated by using Stoke's law (Eq. S1) due to its dependency on density contrasts, melt viscosity and bubble size.

$$v = \frac{2}{9} \times \frac{(\rho_s - \rho_{m)}}{\eta} \times g \times R^2$$

Eq. S1

ρ_s equals the density of the magnetite-fluid-suspension, which is dependent on the proportion of magnetite (5.2 g/cm^3) and fluid (0.5 g/cm^3) in the suspension, ρ_m equals the melt density (2.27 g/cm^3)[10], η equals melt viscosity (2.1 log kg/m*s) (Giordano et al. 2008), g is the gravitational force (9.81 m/s^2) and R is the bubble radius. Stoke's law usually calculates the sinking velocity of particles. Therefore, positive buoyant particles have a negative velocity. Fig. S2a shows the velocity range for different magnetite and bubble sizes on an experimental scale, while Fig. S2b displays the velocity on a more natural scale; i.e., m per 1000 years. Smaller magnetite grains require smaller bubbles in order to reach the same velocity. In general, magnetite and bubble sizes overlap the observations from the experiments. The results indicate that magnetite grains measuring 10 and 20 µm can be easily lifted by bubbles that are >15 or >32 µm diameter, respectively. Larger magnetite crystals of 50 µm require larger bubbles of > 82 µm.

According to the experiments, re-equilibrium is reached after at least 72 h; i.e., by 72 h all bubbles ascended through the melt column and accumulated between the capsule wall and the melt and no bubbles are anymore existent within the melt. Thus, a minimum velocity of 3000 µm/72 h = 42 µm/h can be assumed for the suspension. This velocity translates to at least 365 m/1000 years on a natural scale. In a 1000 m thick magma reservoir it would take approximately (1000 m / 0.365 m/a =) 2700 years to reach re-equilibrium; i.e., to theoretically float all bubble-magnetite-pairs that could ideally accumulate into a (100 µm/3000 µm * 1000 m =) 33 m thick magnetite layer at the roof. Therefore, magnetite flotation is a very fast and efficient process on a geologic scale.
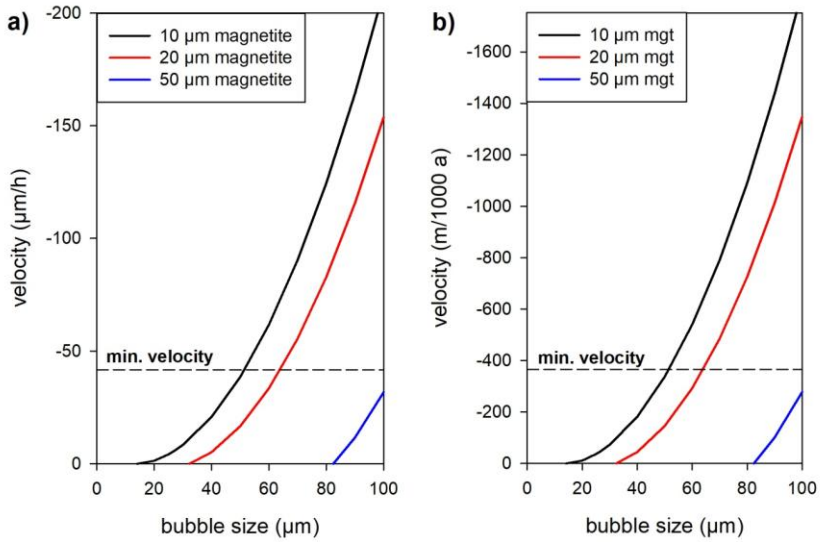
Fig. S5.2: Bubble size vs. velocity of suspension shown for different magnetite sizes. **a)** shows the velocity on an experimental scale (μm/h), and **b)** shows the velocity on a geologic scale (m/1000 a). The horizontal line implies the minimum velocity estimated from the experiments.
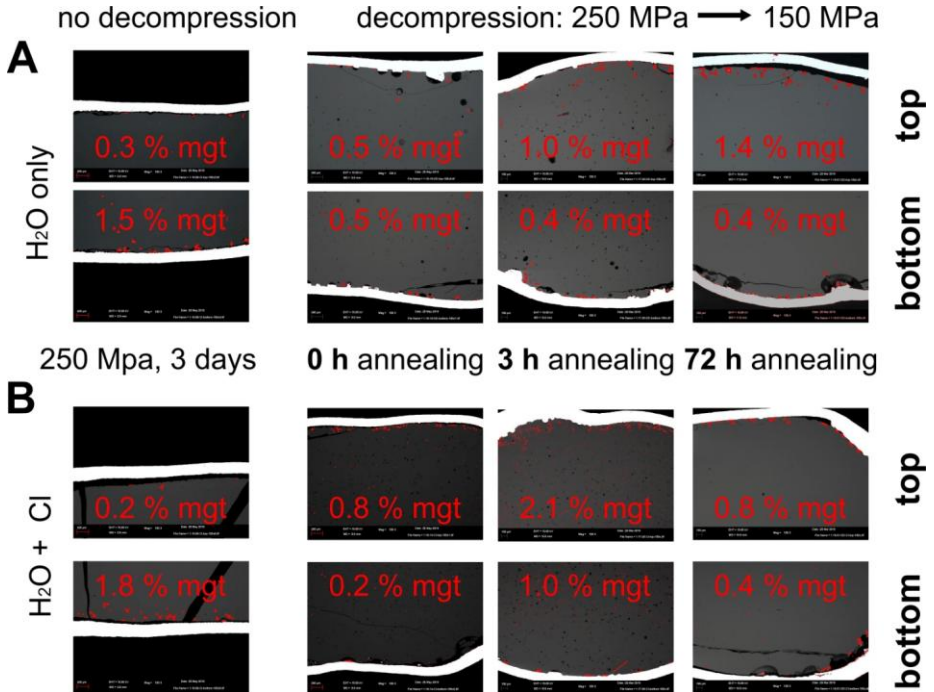
Fig. S5.3: BSE images of top and bottom areas of andesitic glass, vesicles and magnetite in all experimental capsules. Panel (A) shows the H_2O-only runs and panel (B) shows the H_2O+Cl runs. Magnetite (mgt) is highlighted in red and was proportionally counted in the glass (gray) by using the software *imageJ*. For the area calculations, the outer areas such as capsule material (white) and epoxy (black) were excluded from total area. *Noteworthy:* The indicated percentage areas of magnetite cannot be equalized to the actual weight percentage of magnetite present, but they do represent the shifting ratios from the bottom of the melt column to the top of the melt column after decompression and annealing.
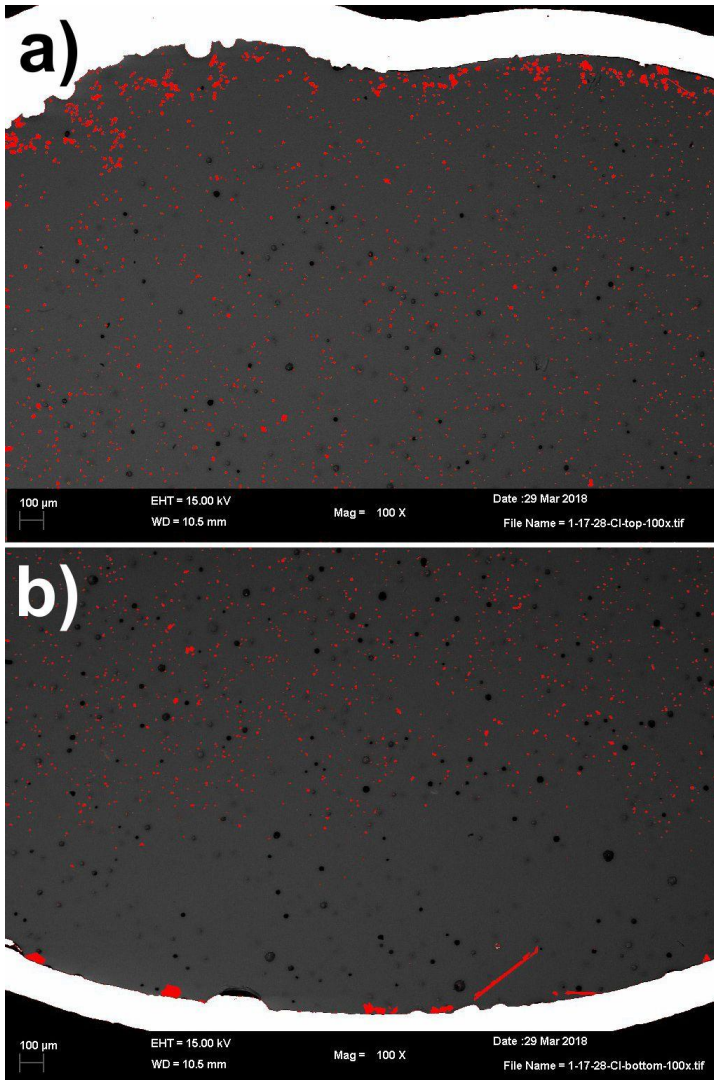
Fig. S5.4: Enlarged BSE images from top **(a)** and bottom **(b)** of the Cl-bearing experiment (Fig. S3B) equilibrated for 3 h. Magnetite is highlighted in red, bubbles are black, capsule wall is white and andesitic glass is grey. After 3 h magnetite has clearly accumulated at the top of the melt column and is depleted in the bottom of the melt column aside from a few large magnetite crystals that settled to the bottom of the melt column.
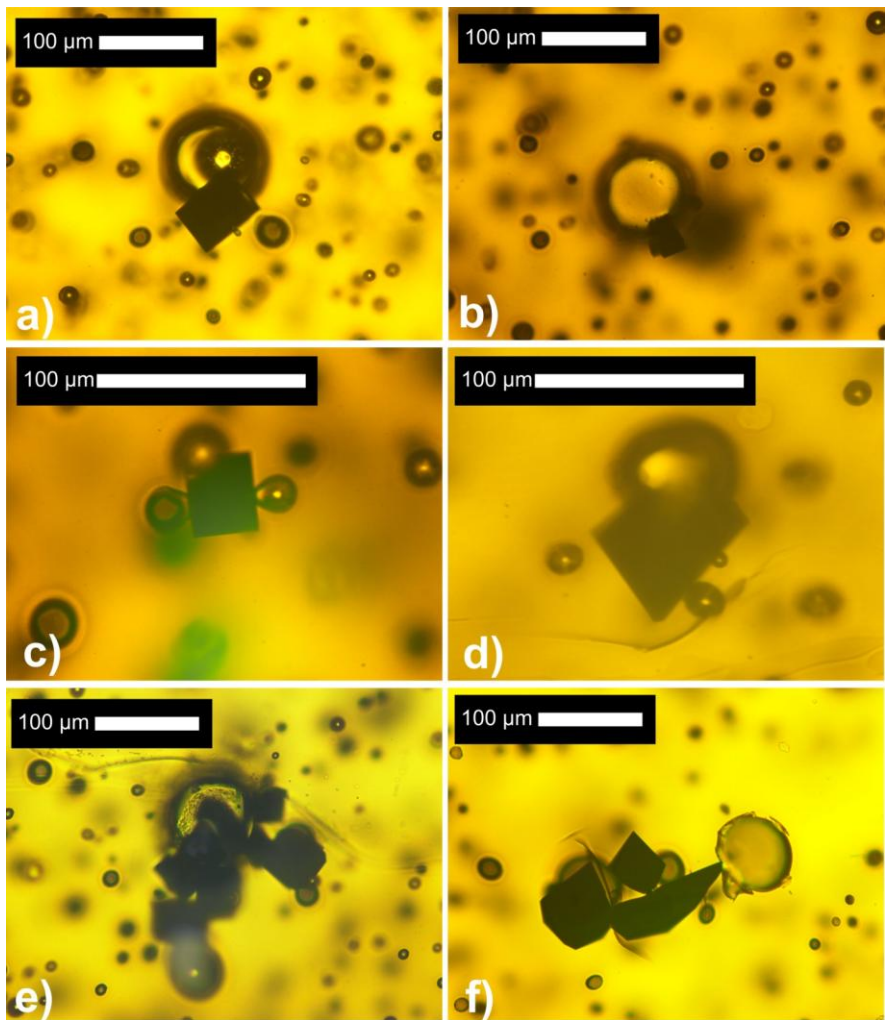
Fig. S5.5: Zoomed-in transmitted light images of the decompressed H$_2$O-only run directly quenched after decompression (in addition to Fig. 4a). Magnetite is either wetted by one bubble **(a,b)**, by several bubbles **(c,d)** or magnetite aggregates are attached to one or more bubbles **(e,f)**.
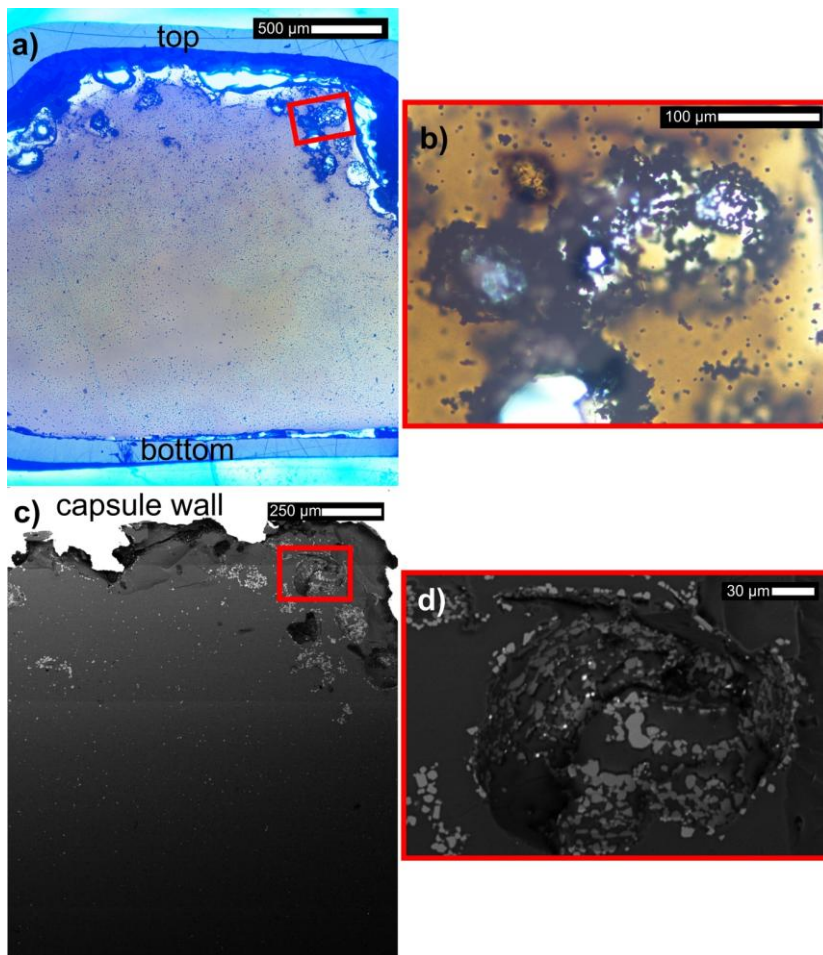
Fig. S5.6: Transmitted light **(a,b)** and BSE **(c,d)** images of an experiment conducted at a constant final pressure of 150 MPa without prior decompression and equilibrated for 3 days. The results reveal a heterogeneous distribution of magnetite and exsolved fluid bubbles. Innumerable small magnetite crystals (< 10 µm) are efficiently attached to the exsolved fluid bubbles that accumulated at the top of the capsule, while the bottom of the capsule is depleted in magnetite. This is in contrast to the fluid-absent static experiment at 250 MPa wherein large magnetite crystals (< 100µm) settled gravitationally to the bottom of the melt column (Fig. 5.3a,e).
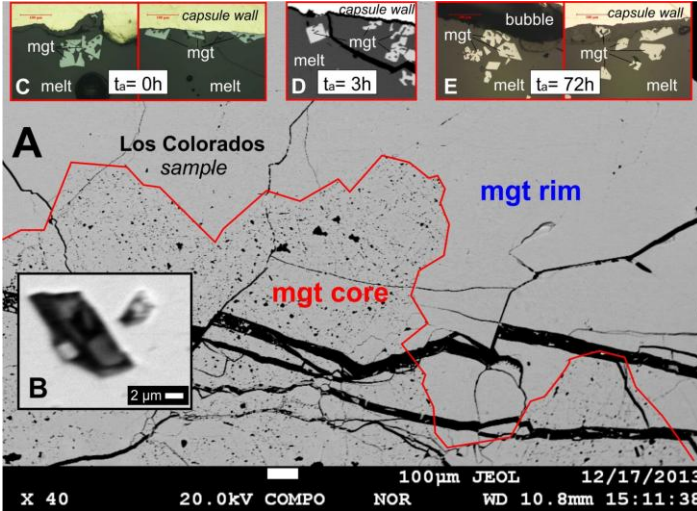
Fig. S5.7: BSE image of a natural magnetite sample from the Los Colorados IOA deposit in comparison with reflected light and/or BSE images of magnetite and glass from decompression experiments of the current study. (A) shows an overview BSE image including a typical inclusion-rich (black spots) magnetite core and pristine magnetite rim discovered at Los Colorados. (B) is the enlargement of an inclusion in the magnetite core and exhibits its polycrystalline nature. The inclusion-rich magnetite cores observed at Los Colorados are interpreted as igneous magnetite, since polycrystalline silicate inclusions only homogenized at magmatic temperatures (T>975 °C) (Knipping et al. 2015b). The experiments of this study (C, D and E) reveal that sudden supersaturation of the melt caused by decompression/degassing results in fast magnetite growth, such as hopper growth[28], where several silicate melt inclusions can be entrapped within euhedral appearing crystals. The size and habitus of the experimental magnetite inclusions are very similar to those in natural samples. This provides further evidence that polycrystalline silicate inclusions in oxides are an igneous growth feature; i.e., magnetite entraps melt as melt inclusions that crystallize during cooling into polycrystalline silicate inclusions.

Table S5.1: Electron probe microanalyses (EPMA) data of experimental glasses.

sample #	P1D	09-H$_2$O	09-Cl	16-H$_2$O	14-Cl	28-H$_2$O	28-Cl	01-H$_2$O	01-Cl
decompression	no	no	no	yes	yes	yes	yes	yes	yes
annealing	-	-	-	0 h	0 h	3 h	3 h	72 h	72 h
Na$_2$O	3.75	3.81	3.61	3.75	3.59	3.62	3.65	3.60	3.54
K$_2$O	1.09	1.14	1.13	1.13	1.13	1.06	1.08	1.05	1.08
MgO	1.93	2.02	1.99	1.99	1.97	2.00	2.01	1.99	1.96
Al$_2$O$_3$	17.49	18.33	18.29	18.26	18.17	18.54	18.52	18.48	18.52
SiO$_2$	62.91	63.92	63.77	64.49	64.00	64.62	64.31	64.69	64.21
CaO	6.16	6.31	6.26	6.38	6.22	6.49	6.43	6.45	6.40
TiO$_2$	0.46	0.36	0.36	0.35	0.36	0.38	0.33	0.36	0.35
FeO	5.59	4.11	4.60	3.65	4.57	3.28	3.69	3.39	3.93
Cl	0.00	0.00	1.20	0.00	1.19	0.00	1.22	0.00	1.03
wt% mgt*	0.00	1.59	1.64	2.08	1.67	2.48	2.62	2.36	2.37

Elemental compositions are normalized to 100 %. P1D represents the composition of the starting glass.
*wt% mgt was calculated by difference to the starting composition. For Cl-bearing experiments the addition of Fe induced by the added fluid as FeCl$_3$ (0.54 wt% Fe addition to the system) was taken into account prior to by-difference calculations.

Table S5.2: FTIR-spectroscopy data of experimental glasses

sample #	09-H$_2$O	09-Cl	16-H$_2$O	14-Cl	28-H$_2$O	28-Cl	01-H$_2$O	01-Cl
decompression	no	no	yes	yes	yes	yes	yes	yes
annealing	-	-	0 h	0 h	3 h	3 h	72 h	72 h
H$_2$O total (wt%)	5.96	5.74	5.24	4.94	5.30	5.32	5.14	4.84
StDev (wt%)	0.07	0.13	0.22	0.12	0.06	0.12	0.08	0.18
Δ wt%	-	-	-0.72	-0.80	-0.66	-0.42	-0.82	-0.90

H$_2$O concentrations were averaged over five measurements across each sample. Δwt% represents the amount of degassed H$_2$O relative to undegassed samples at 250 MPa (09-H$_2$O and 09-Cl).

Curriculum Vitae

PERSONAL DETAILS

Name:	Jaayke Lynn Fiege (née Knipping)
Date of birth:	19.06.1989
Place of birth:	Hamburg, Germany
Family status:	married, 2 children
Nationality:	German
Address:	Reinhold-Frank-Str. 32a, 76133 Karlsruhe
E-Mail:	jaayke.knipping@web.de

EDUCATION

Oct. 2011 - Aug. 2013	M.Sc. in Geosciences at Leibniz Universität (LU) Hannover, GPA 1,1
Oct. 2008 - Jul. 2011	B.Sc. in Geosciences at Leibniz Universität (LU) Hannover, GPA 1,5
Jul. 2008	School-leaving examination (Abitur) at *Meldorfer Gelehrtenschule*

WORK EXPERIENCE

Since Aug. 2014	PhD student at *Institute of Mineralogy*, LU, Hannover, Germany in Cooperation with the *American Museum of Natural History* (AMNH), New York, USA and the *University of Michigan* (UM), Ann Arbor, USA *(Maternity leave from Jul. 2015 – Feb. 2017)*
Nov. 2013 - Aug. 2014	Research Assistant at the *Department of Earth and Environmental Sciences*, UM, USA
Sep. 2009 - Oct. 2013	Student research assistant at *Institute of Mineralogy*, LU, Hannover, Germany

GRANTS/AWARDS

Sep. 2018	*Beate Mocek* Prize (1.000 €)
Jul. 2018	*SEG* Student Research Grant ($2.200)
Dec. 2017	*SEG* Student Research Grant ($ 1.200)
Sep. 2017	*Bernd Rendel* Prize (1.500 €)
Oct.-Dec. 2017	*Annette Kade*-fellow at *AMNH* ($ 9.500), NY, USA
Mar 2017 - 2019	PhD fellow of *Studienstiftung des deutschen Volkes*
Apr. 2015	Poster award at *MGU* conference ($ 300), Ann Arbor, MI, USA

Aug. 2014 - Jun. 2015	*DAAD* PhD grant (12 months at *UM*, USA)
Jun. 2014	*Goldschmidt* Travel Grant, Sacramento, CA, USA
Sep. 2013	Poster award at *DMG/GV* conference (500 €), Tübingen, Germany
Jul. 2013	Poster award at *ZFM Summer School FERRUM*, Goslar, Germany
Feb. - Mar.2012	*DAAD* travel fund (1.200 €), *University of Missouri*, Columbia, MO, USA

INTERNSHIPS AND RESEARCH STAYS

Mar. 2017-Dec. 2018	Research stay (IHPV exp.) at *AMNH*, NY, USA
Nov. 2014	Field work in the Atacama Desert, Chile
Jun. 2014	LA-ICP-MS (Fe ore) at *ETH Zürich*, Switzerland
Oct. 2013	XRF-Diamond Anvil Cell experiments at *APS - Argonne National Laboratory*, IL, USA
Oct.2013-May 2015	Research stay (natural samples) at *UM*, MI, USA
Oct. 2012	SIMS (S-isotopes) at *WHOI*, MA, USA
Feb. - Mar. 2012	Viscometry at *University of Missouri*, MO, USA
Sep. 2011	SIMS (S-isotopes) at *WHOI*, MA, USA
Aug. 2011	4-week internship at *Golder Associates* in Celle
Sep. 2010	3-week internship at *GeoDienste* in Garbsen
Sep. 2008	3-week internship at *Baker Hughes* in Celle
Aug. 2008	2-week internship at *Shell Refinery* in Heide

MEMBERSHIPS, REFEREE AND ADDITIONAL ACTIVITIES

Memberships

DMG (*Deutsche Mineralogische Gesellschaft*), DGGV (*Deutsche Geologische Gesellschaft, Geologische Vereinigung*), SEG (*Society of Economic Geologists*)

Referee

Ore Geology Reviews, *Economic Geology, Contributions to Mineralogy and Petrology*, *Mineralium Depositas*, *Geochimica et Cosmochimica Acta*, *Elements*, *Neues Jahrbuch für Geologie und Paläontologie, International Journal of Earth Sciences, Chemie der Erde – Geochemisty*

Additional Activities

Jul. 2011 – Jul. 2013	Student representative in study commison Geos.
Jan. 2011 – Jan. 2013	Elected member of the student representatives of the Faculty of Sciences, LU Hannover
Oct. 2010 – Apr. 2013	Member of the Student Representatives Geosciences, LU Hannover

List of publications

Journals *(peer-reviewed)*

Knipping, J.L., Webster, J., Simon, A.C. and Holtz, F. (2019) Accumulation of magnetite by flotation on bubbles during decompression of silicate magma. *Scientific Reports,* 9.1, 3852.

Knipping, J.L., Fiege, A., Simon, A.C., Oeser, M., Reich, M. and Bilneker, L.D. (2019) In-situ iron isotope analyses reveal igneous and magmatic-hydrothermal growth of magnetite at the Los Colorados Kiruna-type iron oxide - apatite deposit, Chile. *American Mineralogist,* 104, 471-484.

Simon, A.C.,**Knipping, J.**, Reich, M. , Barra, F., Deditius, A.P., Bilenker, L. and Childress, T. (2018) A holistic model that combines igneous and magmatic-hydrothermal processes to explain Kiruna-type iron oxide – apatite deposits and iron oxide – copper – gold deposits as products of a single evolving ore system. SEG special volume 2018

Deditius, A.P., Reich, M., Simon, A.C., Suvorova, A., **Knipping, J.**, Roberts, M.P., Rubanov, S., Dodd, A. , and Saunders, M. (2018) Nanogeochemistry of hydrothermal magnetite. *Contributions to Mineralogy and Petrology* 173, 6-46.

Welsch, A.M., **Knipping, J.L.** and Behrens, H. (2017) Fe-oxidation state in alkali-trisilicate glasses - a Raman spectroscopic study, *Journal of Non-Crystalline Solids* 471, 28-38.

Stabile, P., Webb., S., **Knipping, J.L.**, Behrens, H., Paris, E. and Giuli, G. (2016) Viscosity of pantelleritic and alkali silicate melts: Effect of Fe redox state and Na/(Na+K) ratio, *Chemical Geology* 442: 73-82;

Reich, M., Simon, A.C., Deditius, A.P., Barra, F., Chryssoulis, S., Lagas, G., Tardani, D., **Knipping, J.**, Bilenker, L., Sanchez-Alfaro, P., Roberts, M.P. and Munizaga, R. (2016) The trace element signature of pyrite from the Los Colorados iron oxide-apatite (IOA) deposit: a missing link between IOA and IOCG systems? Economic Geology 111: 743-761

Knipping, J.L., Bilenker, L.D., Simon, A.C., Reich, M., Barra, F., Deditius, A.P., Wälle, M., Heinrich, C., Holtz, F., Munizaga, R. (2015): Trace elements

209

in magnetitefrom massive iron oxide-apatite deposits indicate a combined formation by igneous and magmatic-hydrothermal processes. *Geochimica et Cosmochimca Acta* 171: 15-38

Knipping, J.L., Behrens, H., Wilke, M., Göttlicher, J., Stabile, P. (2015): Effect of oxygen fugacity on the coordination and oxidation state of iron in alkali bearing silicate melts, *Chemical Geology* 411, 143-154;

Knipping, J.L., Bilenker, L.D., Simon, A.C., Reich, M., Barra, F., Deditius, A.P., Lundstrom, C., Bindeman, I., Munizaga, R. (2015): Giant Kiruna-type deposits form by efficient flotation of magmatic magnetite suspensions, *Geology* 43: 591-594.

Robert, G., **Knipping, J.L.**, Scherbarth, S., Robertson, T.E., Stechern, A., Behrens, H., Whittington, A. (2014): Heat capacity and viscosity of basaltic melts with $\pm H_2O \pm F \pm CO_2$, *Chemical Geology* 418: 51-65

Fiege, A., Holtz, F., Shimizu, N., Mandeville, C.W., Behrens, H., **Knipping, J.L.** (2014): Sulfur Isotope Fractionation between Fluid and Andesitic Melt: An Experimental Study, *Geochimica et Cosmochimca Acta*, 142:501-521

Vetere, F., Iezzi, G., Behrens, H., Cavallo, A., Misiti, V., Dietrich, M., **Knipping, J.**, Ventura, G., Mollo, S. (2013): Intrinsic solidification behaviour of basaltic to rhyolitic melts: A cooling rate experimental study, *Chemical Geology*, 354: 233-242

Bartels, A., Behrens, H., Holtz, F., Schmidt, B.C., Fechtelkord, M., **Knipping, J.**, Crede, L., Baasner, A., Pukallus, N. (2013): The effect of fluorine, boron and phosphorus on the viscosity of pegmatite forming melts, *Chemical Geology*, 346: 184-198

Abstracts *(selection)*

Simon, A.C., **Knipping, J.,** Reich, M., Barra, F., Deditius, A.P., Bilenker, L. and Childress, T. (2018) A magmatic flotation model that genetically links iron oxide-apatite (IOA) and iron oxide-copper-gold (IOCG) deposits. *Pan-American Current Research on Fluid Inclusions Meeting 2018*, Houston, TX, USA

Knipping, J.L., Simon, A.C., Fiege, A., Webster, J.D., Reich, M., Barra, F., Holtz, F. and Oeser, M. (2017) Flotation of magnetite Crystals upon Decompression – A Formation Model for Kiruna-type Iron Oxide-Apatite Deposits, *American Geophysical Union Meeting 2017*, New Orleans, LA, USA

Knipping, J.L., Simon, A.C., Reich, M., Webster, J.D., Fiege, A., Holtz, F. and Oeser, M. (2017) Can magnetite flotation form Kiruna-type IOA deposits? – a new model is tested. *VolcaNYC Meeting 2017*, New York, NY, USA

Knipping, J.L, Simon, A.C., Reich, M., Fiege, A., Deditius, A.P., Webster, J.D., Bilenker, L., Barra, F., Holtz, F. and Oeser, M. (2017) Formation of Kiruna-type deposits – testing a novel model, *Goldschmidt Conference 2017*, Paris, France

Knipping, J.L., Simon, A.C., Reich, M., Holtz, F., Deditius, A.P., Wälle, M. Heinrich, C. (2016): A revolutionary model to explain Kiruna-type iron oxide-apatite deposit formation, *Iron in Functional Materials* Symposium, Hannover, Germany

Simon, A.C, **Knipping, J.L.**, Bilenker, L., Reich, M., Barra, F., Deditius, A.P. (2015): A genetic model that links mafic magma, IOA and IOCG deposits, *Goldschmidt 2015, Prague, Czech*

Knipping, JL., Simon, A.C., Reich, M., Deditius, A.P., Wälle, M., Heinrich, C. (2015): A new magmatic-hydrothermal model for Kiruna-type iron oxide-apatite deposits, *MGU 2015, Ann Arbor, MI, USA*

Simon, A.C., Reich, M., Bilenker, L., **Knipping, J.L.**, Lundstrom, C., Deditius, A.P., Bindeman, I., Barra, F. (2014): Iron and oxygen isotope and element systematics of magnetite from the Los Colorados IOA deposit, Chile: A paradigm shift for IOA deposits?, *SEG 2014, Keystone, CO, USA*

Knipping, J.L., Simon, A., Reich, M. (2014): Evidence for a Magmatic Origin for Iron Oxide-Apatite Deposits, Goldschmidt *2014, Sacramento, CA, USA*

Reich, M., Simon, A., Deditius, A., Bilenker, L., **Knipping, J.**, Barra, F. (2014): Chemical Zoning and Microtexture of Magnetite from Los Colorados Iron Oxide-Apatite Deposit, Chile, Goldschmidt 2014, Sacramento, CA, USA

Knipping, J.L., Behrens, H., Stabile, P., Giuli, G. (2013): Effect of fO$_2$ on the coordination and oxidation state of iron in silicate glasses, *DMG/GV conference 2013*, Tübingen, Germany

Knipping, J.L., Behrens, H., Stabile, P., Giuli, G. (2013): Effect of fO$_2$ on the coordination and oxidation state of iron in silicate glasses, *Summer School Functional Solids-FERRUM, Goslar, Germany*

Stabile, P., Cicconi, M.R.,Giuli,G., Behrens, H., **Knipping, J.**, Paris, E. (2013): The structural role of iron in pantelleritic glasses, *Goldschmidt 2013, Florence, Italy*

Robert, G., Whittington, A.G., **Knipping, J.**, Scherbarth, S., Stechern, A., Behrens, H.(2012): Effect of H$_2$O, and combined effects of H$_2$O + F, H$_2$O + CO$_2$, and H$_2$O + F + CO$_2$ on the viscosity of a natural basalt from Fuego volcano, Guatemala*, AGU 2012, San Francisco, USA*

Knipping, J., Scherbarth**,** S., Robert, G., Behrens, H., Whittington, A., Stechern, A. (2012): Influence of H$_2$O, CO$_2$ and F on the viscosity of a natural basaltic melt, *EMC 2012, Frankfurt, Germany*

Iezzi, G., Vetere, F., Misiti, V., Cavallo, A., Ventura, G., Behrens, H., **Knipping, J.**, Mollo, S. (2012): Compositional variations of clinopyroxene in natural silicate melts induced by cooling rate*, Crystallization in Glasses and Liquids, Goslar, Germany*

Bartels, A., **Knipping, J.**, Behrens, H., Holtz, F., Schmidt, B.C. (2011): The influence of F, P and B content on pegmatitic melt viscosity**,** *Goldschmidt 2011, Prague, Czech*